Reconstruction of momentum density and determination of one-electron reduced density matrix

Thesis · January 2018

CITATION
1

READS
344

1 author:

Zeyin Yan
Southern University of Science and Technology
14 PUBLICATIONS **67** CITATIONS

SEE PROFILE

université PARIS-SACLAY

NNT : 2018SACLC001

CentraleSupélec

Reconstruction of momentum density and determination of one-electron reduced density matrix

Thèse de doctorat de l'Université Paris-Saclay
préparée à CentraleSupélec

INTERFACES (ED 573) : Approches Interdisciplinaires : Fondements, Applications et Innovation
Spécialité de doctorat : Physique

Thèse présentée et soutenue à Gif-sur-Yvette de soutenance, le 19 janvier 2018, par

M. Zeyin Yan

Composition du Jury :

M. Claude Lecomte Professeur Emérite, Université de Lorraine (CRM2)	Président
M. Carlo Gatti Directeur de Recherche, University of Milan (CNR-ISTM)	Rapporteur
M. Enrique Espinosa Professeur, Université de Lorraine (CRM2)	Rapporteur
M. Nour-Eddine Ghermani Professeur, Paris XI (IGPS)	Examinateur
Mme. Béatrice Gillon Directeur de Recherche, CNRS (LLB, CEA-Saclay)	Examinatrice
M. Alessandro Erba Professeur Assistant, University of Torino	Examinateur
M. Jean-Michel Gillet Professeur, CentraleSupélec (SPMS)	Directeur de thèse

Thèse de doctorat

You can look at the world with the p-eye and you can look at the world with a q-eye, but if you want to open both eyes at the same time, you will go crazy.

—Wolfgang Pauli, in a letter to Werner Heisenberg, October 19, 1926

Contents

List of Tables

List of Figures

Abbreviations

1-RDM	1-Electron Reduced Density Matrix
2D-MEMD	2-Dimensional Magnetic Electron Momentum density
AO	Atomic Orbital
BF	Bloch Function
CASSCF	Complete Active Space Self-Consistent Field
CFT	Crystal Field Theory
CI	Configuration Interaction
CPM	Cluster Partitioning Method
CRYSTAL14	Crystal 14 Package
CS	Compton Scattering
DCP	Directional Compton Profile
DFT	Density Functional Theory
DMCP	Magnetic Directional Compton Profile
ECP	Effective Core Potentials
EMD	Electron Momentum Density
FFT	Fast Fourier Transformation
FT	Fourier Transformation
G09	Gaussian 09 Package
GTO	Gaussian Type Orbital
HC	Hansen & Coppens Model
HF	Hartree-Fock
HOMO	Highest Occupied Molecular Orbital
IAM	Independent Atoms Model
LCAO	Linear Combination of Atomic Orbital

LUMO	Lowest Unoccupied Molecular Orbital
MCS	Magnetic Compton Scattering
MEM	Maximum Entropy Method
MEMD	Magnetic Electron Momentum Density
MO	Molecular Orbital
Nit	Nitronyl-Nitroxide
Nit(SMe)Ph	2-(4-Thiomethylphenyl)-4,4,5,5-Tetramethylimidazoline-1-Oxyl-3-Oxide
ONIOM	Own N-layer Integrated molecular Orbital and Mechanics
***p*-NPNN**	*p*-Nitrophenyl Nitronyl Nitroxide
PDF	Probability Density Function
PND	Polarized Neutron Diffraction
RHF	Restricted Hartree-Fock
ROHF	Restricted Open-Shell Hartree-Fock
SCF	Self-Consistent Field
SDD	Static Deformation Density
UND	Unpolarized Neutron Diffraction
UHF	Unrestricted Hartree-Fock
XMD	X-ray Magnetic Diffraction
XRD	X-ray Diffraction

Introduction

Electron density is a fundamental quantity to understand the chemical and physical properties of solids. Electrons have two intrinsic properties, a charge and a spin. Whatever the considered property, charge or spin electron distribution can be described in position or momentum spaces. In position space, electron density can be determined from elastic coherent Bragg scattering observables, the structure factors. The "Spin split" refinement model [1, 2], which makes it possible to efficiently combine X-ray diffraction (XRD) and polarized neutron diffraction (PND), yields access to spin density with unprecedented quality. It thereby confirms that "the whole is more than the sum of its parts" [3]. In momentum space, electron density can be observed by Compton scattering (CS), where the measurement (the directional Compton profiles) are projections of electron density along different scattering directions. Several algorithms have been developed to reconstruct the momentum density from a set of non-equivalent directional Compton profiles [4, 5]. Most of the works reported over the last 40 years focus on position space properties while momentum space observables are generally used as an mere additional source of information. However, Compton scattering is a valuable technique for observing the most delocalized electrons [6]. Numerous investigations show that a simple incoherent addition of (pseudo-)atom centred contributions is not fully adapted to a momentum space description. As a consequence, a general model, exploring beyond the "multipoles on atom model" is required for an efficient exploitation of XRD, PND, CS and MCS data.

One-electron reduced density matrix (1-RDM) is widely accepted to contain all electronic information at a one-electron level. Its diagonal elements are thus electron density in position space, the off-diagonal elements are closely connected to a description in momentum space (as shown below). Today, both theoretical and experimental approaches are used to analyse the electronic properties in position and momentum spaces, using a variety of methods. However, it turns out that a 1-RDM (both diagonal and off-diagonal elements) can hardly be reconstructed from a single experiment.

Obviously, it seems like the exact electronic state cannot be obtained by a given unique experimental technique or even any combination of today's known techniques. This is because each scattering experiment probes a different aspect of the N-electron wave-function. But one

condition must always be fulfilled: independent experiments should be coherent with each other. Moreover, models gathering multiple techniques (especially combining both position and momentum spaces) can yield more precise electronic information. With this goal in mind, our group at SPMS and its collaborators (CRM2 at Nancy, LLB at Saclay, Spring8 in Japan), have been investigating the best strategies to model an experimental 1-RDM by an efficient exploitation of a large variety of scattering data. From this joint effort, it is expected that an ever more accurate description of electronic behaviour in crystal will eventually be obtained.

As a part of the Agence Nationale de la Recherche funded Multiple Techniques Modelling of Electron Density (MTMED) project[a], this thesis work mostly deals with electron density in momentum space through *ab initio* computations and 1-RDM refinements.

The manuscript is divided into three chapters:

- In *Chapter 1*, theoretical and experimental methods are briefly described with an emphasis on their use to investigate $YTiO_3$ electron properties in position and momentum spaces. It is shown that XRD observations can be used to model charge density in position space following the approach developed by Hansen-Coppens [7]. Spin density is obtained by maximum entropy[b] method and atomic orbital model respectively. Pushing a bit further, the joint refinement technique (using XRD and PND) makes use of a more recent "spin split" model [1, 2] to obtain a more precise spin-resolved density with a marked difference with the sole use of PND experimental data. In momentum space, 2D electron spin density is reconstructed from a set of magnetic directional Compton profiles. A propagation error analysis is performed in order to validate the reliability of the reconstruction result and allow for a fair weighting in a later possible refinement. All these experimental results are then compared with a standard periodic DFT computation for the $YTiO_3$ case. Another study is presented on Nit(SMe)Ph as it shows how several types of theoretical computation, with increasing complexity, had to be conducted to reproduce the spin density in a molecular magnet. The problem of approximation in standard DFT computation is discussed based on this case where the role of an accurate experimental spin resolved density is revealed to be of utmost importance.

- In *Chapter 2*, a cluster model, based on a periodic *ab-initio* computation, is proposed to compute crystal properties with an iterative level of accuracy, and opens up the possibility of conducting deeper investigations. In particular, a theoretical 1-RDM is calculated in order to analyse the different roles played by O_1 and O_2 type oxygen atoms in $YTiO_3$ compound and possibly elucidate their respective contributions to the ferromagnetic mechanism. The Moyal function, which can connect the

[a] Mohamed Souhassou, project leader.

[b] This method can also be used for the charge density reconstruction but was not considered in this work.

experimental observation both in position and momentum spaces, is investigated by means of this cluster model. Cross-term contributions between atoms are displayed in position, momentum and phase spaces respectively. This approach allows a better clarification of the different importance of cross terms in different space representations and explains the requirements on a 1-RDM model to absorb information from both origins.

- In *Chapter 3*, a "super position" method based on the spin density work reported in *Chapter 1* is proposed. The goal is to rapidly connect position and momentum spaces with no recourse to a complicated model. Spin density around atoms are superimposed based on nuclei positions by mere translations to eliminate the nuclei "position" effect. The newly constructed electron density (called "**super–position**" density) is used for a convenient qualitative comparison with a momentum space representation density. A new 1-RDM refinement model is presented to reconstruct an experimental 1-RDM based on experimental observations. In order to test this model, theoretical scattering properties, with added random noise, are used to simulate the pseudo experimental observations. The refined 1-RDM thus obtained, is compared with theoretical 1-RDM originating from the cluster model described in *Chapter 2*. This work is still in progress as a long-term project but preliminary results are encouraging enough to be reported in this manuscript. Finally, discussions on models gathering different experimental data and an *ab initio* computation are proposed to estimate possible directions for future model improvements and developments.

Chapter 1

Electron Densities by Experimental & Theoretical Methods

Several types of experiment can be conducted to independently investigate the position and momentum space representations of electron density but scattering of particles (X-rays, gamma, positrons, electrons or neutrons) are probably still those which provide the most detailed information. Experimental results are usefully analysed from a comparison with theoretical computations. But additional, and important, new methods such as those relying on topology indicators have been proven to provide very useful tools to better understand the underlying complex quantum mechanisms responsible for cohesion, electronic or magnetic properties. Discrepancies between ab-initio results and experimental data encourage both experimenters and theoreticians to eventually improve their respective techniques or models and methods. This is what Fermi meant in his famous statement "when the experiment confirms the theory, you have made a measurement. When they do not agree, you have made a discovery".

The first part of this work considers the electron density distribution in a dual space perspective, which is believed to bear more information than a single one.

1.1 Experimental observations

On the experimental side, several approaches are used to observe electron behaviour in fine details. The most popular methods are X-ray diffraction (XRD)[8] and polarized neutron diffraction (PND)[9] in position space or Compton scattering (CS) and magnetic Compton scattering (MCS)[6] in momentum space. The following sections give a brief review on these methods and will serve as a basis to comment on our results.

1.1.1 Observations in position space

The outcome of XRD and PND experiments are respectively structure factors $F(\mathbf{Q})$ and magnetic structure factors $F_{mag}(\mathbf{Q})$[a], where $\mathbf{Q}$ is the scattering vector. For a perfect crystal at the Bragg condition,

$$\mathbf{Q} = h\mathbf{a}^* + k\mathbf{b}^* + l\mathbf{c}^* \tag{1.1}$$

where h, k, l are the Miller indices, and $\mathbf{a}^*, \mathbf{b}^*$ and $\mathbf{c}^*$ are the Bravais reciprocal lattice vectors.

For the ideal case, with an infinite number of (resp. magnetic) structure factors, the electron (resp. spin) density can be written as a Fourier series, the coefficients of which are the structure factors:

$$\rho(\mathbf{r}) = \frac{1}{V}\sum_{\mathbf{Q}}^{\infty} F(\mathbf{Q})e^{-i\mathbf{Q}\cdot\mathbf{r}} \tag{1.2a}$$

$$\rho_{mag}(\mathbf{r}) = \frac{1}{V}\sum_{\mathbf{Q}}^{\infty} F_{mag}(\mathbf{Q})e^{-i\mathbf{Q}\cdot\mathbf{r}} \tag{1.2b}$$

where V is the unit cell volume. However, usual high resolution XRD experiments hardly provide more than a few thousands $F(\mathbf{Q})$, and PND data seldom exceed few hundreds of $F_{mag}(\mathbf{Q})$. The lack of completeness[b] in the Ewald sphere and the necessity of stabilizing the series calls for the use of a model with an adaptable degree of sophistication to reconstruct a precise electron distribution in position space. This is the purpose of the pseudo-atomic constructions which were put forward and used over the last four decades (see *section 1.3.2*).

1.1.2 Observations in momentum space

The observables from CS and MCS[10] are directional Compton profiles (DCP) and directional magnetic Compton profiles (DMCP). For a scattering vector pointing to the direction given by a unit vector $\mathbf{u}$, the signal is related to the electron probability density in momentum space $n(\mathbf{p})$. To be more specific, the (magnetic) Compton scattering signal, for a scattering vector aligned with $\mathbf{u}$, is proportional to DCPs (DMCPs), $J(\mathbf{u}, q)$ ($J_{mag}(\mathbf{u}, q)$):

$$J(\mathbf{u}, q) = \int n(\mathbf{p})\delta(\mathbf{u}\cdot\mathbf{p} - q)d\mathbf{p} \tag{1.3a}$$

$$J_{mag}(\mathbf{u}, q) = \int n_{mag}(\mathbf{p})\delta(\mathbf{u}\cdot\mathbf{p} - q)d\mathbf{p} \tag{1.3b}$$

[a] Flipping ratios are actually provided by PND with $R = \left(\frac{F_N + F_M}{F_N - F_M}\right)^2$. Magnetic structure factors F_M are thus deduced from R's knowing the nuclear structure factors F_N for centro-symmetric space groups. However, for the sake of simplicity, we focus on structure factors to emphasize the similarities between charge and spin investigations.

[b] Maximum entropy methods were precisely developed to circumvent the difficulty of reconstructing an image (here, the electron density) from an incomplete set of data.

The DCP (DMCP) is thus the probability density for an electron of having a momentum with component q along direction $\mathbf{u}$, whatever the values of the other two components. Expression (1.3) shows that the DCP (DMCP) is a projection of $n(\mathbf{p})$ ($n_{mag}(\mathbf{p})$) on a particular vectorial line of momentum space.

Another quantity which is worth considering can be obtained by a Fourier transform of DCPs or the density in momentum space. It is the reciprocal form factor $B(\mathbf{u}, t)$:

$$B(\mathbf{u}, t) = \int J(\mathbf{u}, q) e^{-iq \cdot t} dq \tag{1.4}$$

It is also called an "auto-correlation function" because, for example in a one-electron approach, it is the correlation of system wave-function with itself:

$$B(\mathbf{s}) = \int \Psi(\mathbf{r}) \times \Psi^*(\mathbf{r} + \mathbf{s}) d\mathbf{r} \tag{1.5}$$

where $\mathbf{s}$ is known as the intracular coordinate, i.e. the relative vector between two positions, with $\mathbf{s} = t\mathbf{u}$ in (1.4).

1.2 *Ab-initio* computations

From a strict theoretical perspective, the most complete electron information is contained in the state ket solution of Schrödinger's equation:

$$\widehat{H}|\Psi\rangle = E|\Psi\rangle \tag{1.6}$$

where $\widehat{H}$ is the Hamiltonian and E is the total energy. For a N-electron system, the equation cannot be solved exactly and the wave-function Ψ can be sought using a variety of expressions and strategies. All *ab-initio* methods seek an approximate solution for Ψ by minimizing the system quantum mean energy:

$$E = \langle \Psi | \widehat{H} | \Psi \rangle \tag{1.7}$$

Basically, two main calculation methods are employed: the Hartree–Fock (HF) approach [11] and the Density Functional Theory (DFT)[12, 13] based methods. The HF method assumes that the many-electron wave-function takes the form of a single determinant, i.e. a determinant constructed from the lowest lying electron orbitals of the system. More accurate electron correlation treatment is made possible by using post HF methods to improve these results where repulsion between electrons is considered as a mean field. On the other hand, in the DFT approach, the many-electron wave-function problem is not really addressed and the focus of interest is the electron density. This method relies on the Hohenberg-Kohn theorem which states that the ground state energy solely depends on the electron density and, providing that its expression as a functional of the density is known, the minimization of the energy unambiguously gives the charge density. Kohn and Sham orbitals can thus be considered as mere by products of this process.

As for the different electron spin configurations, closed-shell and open-shell types of computation are applied for non magnetic and magnetic systems respectively. Restricted Hartree-Fock (RHF) [14] is a typical closed-shell method, where orbitals are always doubly occupied (by one alpha and one beta electron, presented on the left diagram in Figure 1.1). However, for systems containing unpaired electrons (with odd number of electrons, ferromagnetic and anti-ferromagnetic solids or molecules), open-shell methods are necessary to get the correct spin eigenfunction. In restricted open shell Hartree-Fock (ROHF) [15] Hamiltonian, orbitals can be doubly occupied (as RHF method), singly occupied and unoccupied (shown as middle diagram in Figure 1.1). Unrestricted Hartree-Fock (UHF) [16] is another type of open-shell method where alpha and beta levels are treated separately and, at most, singly occupied (presented on the right-part of diagram Figure 1.1). As there is no such thing as a free lunch, all these methods have an increasing need of computational resources.

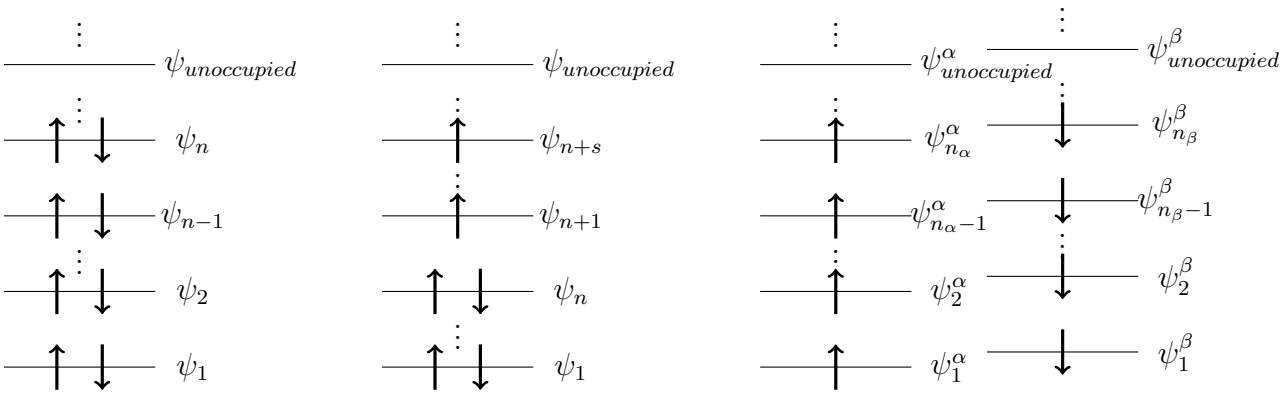

Figure 1.1: Molecular orbitals diagram for RHF (left), ROHF (middle) and for UHF (right)

Depending on the system being considered, molecular and periodic computations are used to calculate the molecule (or cluster) and the crystal respectively. For this work, the Gaussian 09 package (G09)[17] and Crystal 14 code (CRYSTAL14)[18, 19] were used to address with a comparable point of view (LCAO orbitals with Gaussian type-orbital contractions on atomic centres) the molecular and periodic computations respectively.

The one-electron reduced density matrix (1-RDM)[20] $\Gamma(\mathbf{r}, \mathbf{r}')$ contains all the information at the one-electron level. The 1-RDM is the simplest quantity that is common to position and momentum spaces. It is a convenient and more economic way to model one electron behaviour than the full N-electron wave-function. The 1-RDM is constructed from the N-electron wave-function according to:

$$\Gamma(\mathbf{x}, \mathbf{x}') = N \int \Psi(\mathbf{x}, \mathbf{x_2}, \ldots, \mathbf{x_N}) \times \Psi^*(\mathbf{x}', \mathbf{x_2}, \ldots, \mathbf{x_N}) d\mathbf{x_2} \ldots d\mathbf{x_N} \tag{1.8}$$

where $\mathbf{x}$ gathers the spin and position variables. By splitting the up and down electron spin

populations, the spin-resolved 1-RDM can be used to obtain:

$$\Gamma(\mathbf{r},\mathbf{r}') = \Gamma^{\uparrow}(\mathbf{r},\mathbf{r}') + \Gamma^{\downarrow}(\mathbf{r},\mathbf{r}') \tag{1.9a}$$

$$\Gamma_{mag}(\mathbf{r},\mathbf{r}') = \Gamma^{\uparrow}(\mathbf{r},\mathbf{r}') - \Gamma^{\downarrow}(\mathbf{r},\mathbf{r}') \tag{1.9b}$$

Obviously, similar to (1.9), the 1-RDM can also be given in a momentum representation.

$$\Gamma(\mathbf{p},\mathbf{p}') = \int \Gamma(\mathbf{r},\mathbf{r}') e^{i\mathbf{r}\cdot\mathbf{p}} e^{-i\mathbf{r}'\cdot\mathbf{p}'} d\mathbf{r} d\mathbf{r}' \tag{1.10}$$

and the spin-resolved 1-RDM in momentum representation is similarly used as:

$$\Gamma(\mathbf{p},\mathbf{p}') = \Gamma^{\uparrow}(\mathbf{p},\mathbf{p}') + \Gamma^{\downarrow}(\mathbf{p},\mathbf{p}') \tag{1.11a}$$

$$\Gamma_{mag}(\mathbf{p},\mathbf{p}') = \Gamma^{\uparrow}(\mathbf{p},\mathbf{p}') - \Gamma^{\downarrow}(\mathbf{p},\mathbf{p}') \tag{1.11b}$$

1.2.1 Molecular or periodic computations

HF and DFT methods are used to obtain the system orbitals[a] [21]. In both cases, and in G09 or in CRYSTAL14, orbitals are expressed as a linear combination of atomic orbitals (LCAOs). In turn, atomic orbitals are described by a contraction of Gaussian type orbitals (GTOs). The solution to (1.6) boils thus down to determining MO coefficients $\{c_{ij}\}$ in (A.1). For a closed shell system, each orbital is occupied by two electrons, which only differ by their spin states α and β(according to the Pauli exclusion principle). As a consequence, the $\{n_i\}$ are thus 2 or 0. For UHF cases, α and β electrons are considered separately so that $\{n_i^{\alpha}\}$ and $\{n_i^{\beta}\}$ are 1 or 0. The 1-RDM can be written as

$$\Gamma(\mathbf{r},\mathbf{r}') = \sum_{k}^{occ.} \sum_{i,j=1}^{i,j=N} n_k c_{ik} c_{jk}^{*} \chi_i(\mathbf{r}) \chi_j^{*}(\mathbf{r}) \tag{1.12}$$

where χ represents the atomic orbitals (see (A.2)). To simplify the expression, the population matrix[b] P is often used:

$$P_{ij} = \sum_{k}^{occupied} n_k c_{ik} c_{jk}^{*} \tag{1.13}$$

Therefore, P is a $N \times N$ matrix. Using the population matrix and its associated basis set, all one-electron properties can be calculated. However the method to obtain the population matrix is different for molecular and periodic computations. Here, the G09 and CRYSTAL14 cases will be briefly presented as examples with an emphasis on their similarities and differences. Other quantum-chemistry programs using LCAOs are usually similar with the notable exception of those making use of plane-waves.

[a] Actually, single electron wave-functions are obtained from HF but DFT makes use of only Kohn–Sham orbitals which are justified for a mere computational purpose.

[b] It is nothing but the density matrix in a discrete basis functions set representation. Hence the unfortunate name of "density matrix" in both computational code outputs.

Molecular Computations[22] Molecular-type computations concern systems with a limited number of atoms, such as isolated molecules or clusters. The input information for such a computation contains only nuclei coordinates, a choice of basis set, and *ab-initio* methods, the so-called "quantum-chemistry model". The molecular orbitals are constructed as a linear combination of atomic contractions of GTOs (as presented in A.1), and the population matrix is a square symmetric matrix for the whole system. For G09, the basis set information and population matrix (as well as MOs coefficients) are given in a ".fch" file, the structure of which is nowhere near to self-obvious. Hence another file, with less details (and numerical precision) known as ".log" or ".out" files.

Periodic Computations[23] Periodic computations assume an infinite crystal (3D), an infinite slab (2D) or an infinite polymer (1D). The input information for the computation requires the cell parameters, symmetries, non-equivalent atoms coordinates in the primitive cell, a choice of basis set and the *ab-initio* method. As the ideal crystal is periodic and infinite, Bloch functions (BF) $\phi(\mathbf{r}, \mathbf{k})$ are constructed by linear combinations of local AOs, themselves expressed as a contraction of GTOs. The orbitals (called crystalline orbitals) $\psi_i(\mathbf{r}, \mathbf{k})$ are linear combinations of BF.

$$\psi_i(\mathbf{r}, \mathbf{k}) = \sum_{\mu}^{N} c_{\mu,i}(\mathbf{k})\phi_\mu(\mathbf{r}, \mathbf{k}) \tag{1.14a}$$

$$\phi_\mu(\mathbf{r}, \mathbf{k}) = \sum_{\mathbf{g}} \varphi_\mu(\mathbf{r} - \mathbf{A}_\mu - \mathbf{g})e^{i\mathbf{k}\cdot\mathbf{g}} \tag{1.14b}$$

$$\varphi_\mu(\mathbf{r} - \mathbf{A}_\mu - \mathbf{g}) = \sum_{j}^{N_{GTOs}} d_j g_j(\mathbf{r} - \mathbf{A}_\mu - \mathbf{g}) \tag{1.14c}$$

where $\mathbf{A}_\mu$ denotes the relative nucleus coordinate in the cell on which φ_μ is centered, $\mathbf{g}$ are the lattice vectors, $\mathbf{k}$ is the Bloch vector in reciprocal space. Equations (1.14) are very similar to (A.1), except for the periodic computation which is carried out in the $\mathbf{k}$-space.

In a matter of fact, the periodic computation is not stricly speaking infinite, but carried out on a pseudo-macroscopic scale [24]. In direct space, the global wave-function would be too complicate using BF form, and the 1-RDM is more conveniently expressed in the Gaussian type orbitals (GTOs) form:

$$\Gamma(\mathbf{r}, \mathbf{r}') = \sum_{\mathbf{g},\mathbf{l}}^{N_{cells}} \sum_{i,j}^{N_{AOs}} P_{ij}^{\mathbf{gl}} \chi_i^{\mathbf{g}}(\mathbf{r})\chi_j^{\mathbf{l}}(\mathbf{r}) \tag{1.15}$$

where the χ_j are defined on basis sets, just like in molecular computations, and there should be N_{cells} population matrices. Since all the cells are identical, the N_{cells} population matrices are those between the center cell and all the other cells. For CRYSTAL14, the basis set and population matrix information can be obtained by using the keyword *CRYAPI_OUT* and an official utility code made available on the website[a].

[a] Utilities part are retrieved from http://www.crystal.unito.it/documentation.php

The molecular and periodic computations are used for different types of system. Considering the usual weakness of interaction between the molecules for many molecular crystals, both molecular (monomer, dimer, trimer etc.) and periodic computations can be used to investigate individual properties. For metallic crystals, a molecular computation is obviously not a pertinent choice, mostly because of strong interactions and electron delocalization between atoms[a]. Even if both types of computation use GTOs, molecular computations are focused on a limited number of atoms in space and the basis set is usually more diffuse than in periodic cases for the same atom, because crystalline atomic basis sets are built starting from an atomic basis set optimized for molecules. The exponents of the most diffuse GTOs are then re-optimizing (see example of $Si(p_x)$ orbital [b] presented in Figure 1.2).

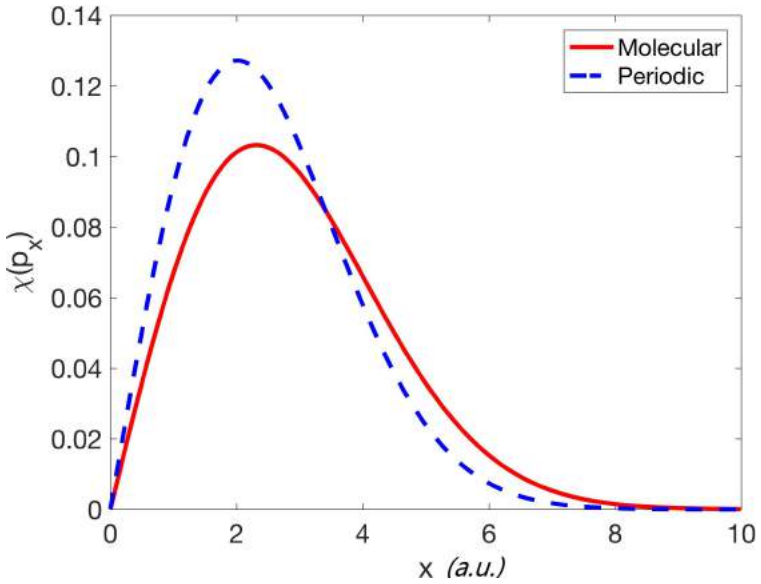

Figure 1.2: Molecular and periodic atomic basis set
Orbital $Si(p_x)$ defined by Si, pople 6-21G [25] split valence basis set: red solid line and modified for crystalline calculation in CRYSTAL14: blue dashed line.

1.2.2 Complete active space self-consistent field

The complete active space SCF method (CASSCF)[26–28] plays an important role in understanding molecular structures and properties [29]. It is a combination of an SCF computation with a full configuration interaction (CI)[30] involving a subset (the so called "active space") of the eigen orbitals. Electron correlation between electrons is better accounted for than at the HF level which only makes use of mean field interactions and introduces correlations via the mere exchange term.

[a] Clusters with atoms or point charges creating the crystal environment to study the key part is a possible alternative but not trivial to carry out by any means.

[b] More detailed information is available from http://www.theochem.unito.it/crystal_tuto/mssc2008_cd/tutorials/basis_set/basis_set_tut.html

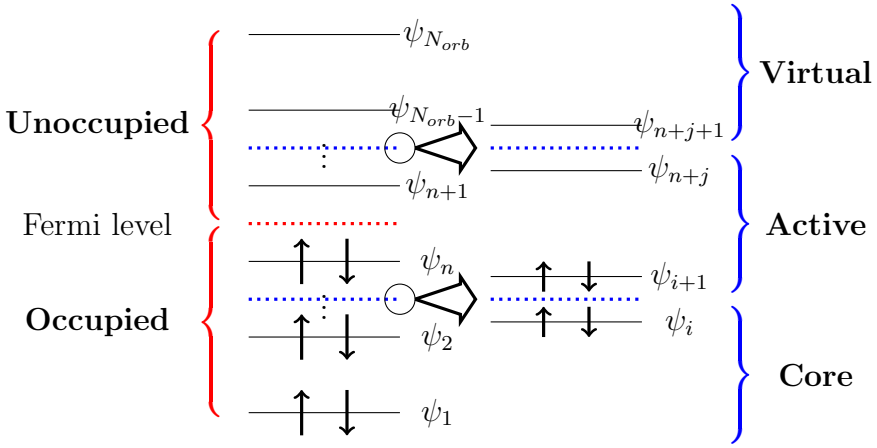

Figure 1.3: CASSCF orbitals regrouping
Red brace for standard occupation scheme; Blue brace for CASSCF method.

The complete active space method calls for a classification of molecular orbitals. From an initial SCF computation, orbitals are divided into two types: occupied orbitals and virtual orbitals (in red for Figure 1.3). CASSCF then considers the orbitals as separated into three distinct classes:

- core orbitals, which always bear two electrons. From ψ_1 to ψ_i in Figure 1.3.
- active orbitals, taken from several of the highest occupied molecular orbitals (HOMOs) and several of lowest unoccupied molecular orbitals (LUMOs), from ψ_{i+1} to ψ_{n+j} in Figure 1.3.
- virtual, always bear zero electron. From ψ_{n+j+1} to $\psi_{N_{orb}}$ in Figure 1.3.

After this classification, a new computation focuses on the active space. A given number of electrons (those from the HOMOs taken from the active space), are used to repopulate all the active orbitals in appropriate combinations, resulting in a new electron configuration in the active space. The active classification can, in principle (and at great expense), be extended to all the molecular orbitals, to obtain the so-called "full CI" treatment. In practice, this choice is rather limited, due to the high computational cost needed to optimize a large complete active space wave-function on medium size and large molecular systems.

In G09, CASSCF creates an active space by the $CASSCF(N, M)$ command, where N is the number of electrons and M is the number of orbitals in the active space. For a closed-shell system, the number of HOMOs is $\lceil \frac{N}{2} \rceil$ ($\lceil x \rceil = min\{n \in \mathbb{Z} | x \leq n\}$), $\mathbb{Z}$ is the integer number, and the number of LUMOs is $M - \lceil \frac{N}{2} \rceil$. The optimization of electronic configuration is then conducted in the active space to obtain a new approximation to a new eigenstate of the system. For open shell systems, the unrestricted Hartree-Fock (UHF) calculation can be also used as a basis for a subsequent CASSCF calculation. It is obviously a more expensive option because α and β orbitals have now different shapes and occupations. The Restricted

Open-Shell Hartree-Fock (ROHF)[15], using doubly occupied orbitals for paired electrons and singly occupied orbitals for unpaired electrons, is a possible alternative choice as it can significantly reduce the need for computational resource.

Unlike HF or CI computations which, to some extent, could be used blindly, the CASSCF is by no means a black box. The creation of an appropriate active space (i.e. the number of HOMOs and LUMOs to be kept) requires a good understanding of the system under investigation.

In this work, for Nit(SMe)Pt, molecular computations were carried out with G09, periodic computations with CRYSTAL14, and CASSCF was (suggested and) conducted by A. Genoni and M. Marazzi, from SRSMC Lab. –Nancy– using MOLCAS [31]. For $YTiO_3$, periodic computations were performed by means of CRYSTAL14.

1.3 Electron density in position space

1.3.1 Theoretical method

On the theoretical side, the electron density (charge/spin) can be obtained from the 1-RDM in its position representation (1.9)

$$\rho(\mathbf{r}) = \rho^{\uparrow}(\mathbf{r}) + \rho^{\downarrow}(\mathbf{r}) = \Gamma(\mathbf{r},\mathbf{r}')_{\mathbf{r}=\mathbf{r}'} \qquad \textbf{charge density} \tag{1.16a}$$

$$\rho_{mag}(\mathbf{r}) = \rho^{\uparrow}(\mathbf{r}) - \rho^{\downarrow}(\mathbf{r}) = \Gamma_{mag}(\mathbf{r},\mathbf{r}')_{\mathbf{r}=\mathbf{r}'} \qquad \textbf{spin density} \tag{1.16b}$$

As $\rho(\mathbf{r})$ is the modulus square of the wave-function, it is positive definite. Conversely, $\rho_{mag}(\mathbf{r})$ can be negative because it is the difference between up $\rho^{\uparrow}(\mathbf{r})$ and down $\rho^{\downarrow}(\mathbf{r})$ electron densities.

To understand electron migration in the system, another relevant quantity, the "static deformation density" (SDD) $\rho_{deformation}(\mathbf{r})$ is often used. It is the difference between the total electron probability distribution $\rho(\mathbf{r})$ in the system and that of the so called "pro-molecule" (or pro-crystal density), $\rho_{isolated}(\mathbf{r})$. Therefore:

$$\rho_{deformation}(\mathbf{r}) = \rho(\mathbf{r}) - \rho_{isolated}(\mathbf{r}) \tag{1.17}$$

$\rho_{isolated}(\mathbf{r})$ is the sum of all the isolated atoms contributions.

$$\rho_{isolated}(\mathbf{r}) = \sum_{i}^{atoms} \rho_i(\mathbf{r} - \mathbf{r}_i)$$

For a pure theoretical computation, it is obtained using a basis set similar to that of molecular (or periodic) SCF computation[a].

[a] Clementi atomic functions can be also used to calculate the isolated atoms contributions with the risk of introducing basis set bias in the resulting deformation density.

1.3.2 Experimental refinement models

Charge density refinement Models

The independent atoms model (IAM) is the simplest charge density model,

$$\rho_{\text{static}}(\mathbf{r}) = \sum_{i}^{atoms} \rho_i(\mathbf{r} - \mathbf{R}_i) \tag{1.18}$$

where $\mathbf{R}$ is the atomic nucleus position. This model which only assumes spherical local distributions cannot account for any polarization of the electron cloud. Improvements of non-spherical contributions were later suggested by Dawson[32], Stewart[33–35] and Hirshfeld[36, 37]. Finally, the multipole model (also called Hansen & Coppens model (HC)) has been proposed by Niels Hansen and Philip Coppens in 1978[7] and was an essential breakthrough in electron density reconstruction. Programs such as *MOLLY*[7], *MoPro*[38], *XD*[39] and *JANA*[40] are based on this model to accurately determine the charge density from XRD data. According to this model, the charge density in a unit cell is the sum of pseudo-atom contributions. Each atomic contribution ρ_i is divided into three components: core, spherical valence and non-spherical valence as

$$\rho_i(\mathbf{r}) = \underbrace{P_{i,core}\rho_{i,core}(\mathbf{r})}_{\text{core}} + \underbrace{\underbrace{P_{i,val}\kappa^3\rho_{i,val}(\kappa\mathbf{r})}_{\text{spherical valence}} + \underbrace{\sum_{l=0}^{l_{max}} \kappa'^3 R_{i,l}(\kappa'\mathbf{r}) \sum_{m=0}^{l} P_{i,lm\pm}Y_{i,lm\pm}(\theta,\varphi)}_{\text{non spherical valence}}}_{\text{valence electrons}} \tag{1.19}$$

where P are the respective populations, κ and κ' are the radial scaling factors, $R(\kappa'\mathbf{r})$ is a Slater-type radial function, often based on Clementi's table [41][b]. Usually spherical density functions for core and valence parts, $\rho_{i,core}(\mathbf{r})$ and $\rho_{i,val}(\mathbf{r})$, are initially given by *ab-initio* atomic functions taken from Clementi-Roetti's tables [42]. Real spherical harmonic functions, $Y(\theta,\varphi)$, serve to model the deviation from sphericity, with l and m the orbital and magnetic quantum numbers, respectively.

To account for thermal effects, each atomic charge density is convoluted by the displacement probability density function (PDF) $P(\mathbf{u})$, where $\mathbf{u}$ is the displacement from the atom's mean position.

$$\begin{aligned} \rho_j(\mathbf{r}) &= \rho_j(\mathbf{r}) \otimes P_j(\mathbf{u}) \\ &= \int \rho_j(\mathbf{r}+\mathbf{u}) \cdot P_j(\mathbf{u}) d\mathbf{u} \end{aligned} \tag{1.20}$$

Structure factors can thus be calculated as:

$$\begin{aligned} F(\mathbf{Q}) &= \sum_{j=1}^{N_{\text{atoms}}} \int \rho_j(\mathbf{r}+\mathbf{u}) \cdot P_j(\mathbf{u}) d\mathbf{u} e^{i\mathbf{Q}\cdot\mathbf{R}_j} \\ &= \sum_{j=1}^{N_{\text{atoms}}} f_j(\mathbf{Q}) e^{i\mathbf{Q}\cdot\mathbf{R}_j} \times e^{-T_j(\mathbf{Q})} \end{aligned} \tag{1.21}$$

[b] as an initial guess, it can be optimized during the refinement process

where, for atom j centred at $\mathbf{R}_j$, $f_j(\mathbf{Q})$ is the form factor evaluated at scattering vector $\mathbf{Q}$, and $T_j(\mathbf{Q})$ is the "Debye-Waller factor", which is the Fourier transform of $P_j(\mathbf{u})$. The above mentioned parameters in this model can be refined by minimizing an objective function (the χ^2 criterion) which quantifies the overall difference between the sets of experimental and model structure factors:

$$\chi^2 = \sum_i^N \omega_i (\frac{|F_i^{obs}|}{K} - |F_i^{cal}|)^2 \tag{1.22}$$

where F_{obs} and F_{cal} are the experimental and model structure factors. N is the number of data points, K is a scale factor between experiment and model data, ω_i is the weight of each structure factor.

Just like multipolar refinement models, the atom-centered multipolar expansion has some limitations[3]:

(a) The interaction contribution between atoms (also called "two-center electron density") is not included. Orbitals centred on two distinct atoms could result in a more accurate electron density[43]. This interaction contribution is weak and is often discarded in position space, while it turns out to be much more significant in momentum space (for more information about cross-term between atoms see *section 2.4*).

(b) The angular expansion is necessary limited. As a general rule, the more spherical harmonics, the better the description of electron density. However, the number of parameters is limited by the experimental data number and can severely hinder the convergence of a least-squares refinement process.

(c) The radial function for the anisotropic contribution is rather poorly described. Since a single Slater radial function is used for each l (in (1.19)) value, it could be imprecise, especially for valence orbitals. On the theoretical side, the double, triple-zeta basis sets are used to obtain an accurate orbital description, even if the highest orbital quantum number of polarization functions is usually coupled with a quite limited number of gaussians (often a single one).

(d) Core electrons are frozen. To reduce the number of refined parameters, only core electron populations are considered. This has already been identified as a possible source of difficulty to accurately describe heavy element contributions (such as in the $YTiO_3$ case).

The residual density is the Fourier transform of the difference between the observed structure factors F_{obs} and calculated structure factors F_{cal}.

$$\rho_{res}(\mathbf{r}) = \frac{1}{V} \sum_{\mathbf{Q}} \left(\frac{|F_{obs}(\mathbf{Q})|}{K} - |F_{cal}(\mathbf{Q})| \right) e^{i\varphi_{calc}} e^{-i\mathbf{Q}\cdot\mathbf{r}} \tag{1.23}$$

where V is the volume of the unit cell, φ_{calc} is the calculated phase. The residual density is thus an indicator of the quality of the refinement. The fewer structures in the residual density (random-like distribution), the less information content left unexploited from the data. This thus means that we can be fairly confident that the structure factors calculated using the model correctly account for the information available from the experimental data. In a way much similar to the theoretical description, the SDD makes it possible to visualize the electron migration upon the chemical bond formation:

$$\rho_{deformation}(\mathbf{r}) = \rho(\mathbf{r}) - \rho_{IAM}(\mathbf{r}) \tag{1.24}$$

using (1.19)

$$\rho_{deformation}(\mathbf{r}) = P_{valence}\kappa^3\rho_{valence}(\kappa\mathbf{r}) - N_{valence}\rho_{valence}(\mathbf{r}) + \sum_{l=0}^{l_{max}} \kappa'^3 R_l(\kappa'\mathbf{r}) \sum_{m=0}^{l} P_{lm\pm} Y_{lm\pm}(\theta,\varphi) \tag{1.25}$$

where $N_{valence}$ is the number of valence electrons for each atom. The difference can be calculated with neutral atoms or ions depending on the effect that needs to be evidenced. Eventually, as it emphasizes how electrons participate in the formation of chemical bonds, it is often informative to compare the experimental SDD with those obtained through an *ab-initio* calculation. Of course, more sophisticated functions of the electron density contain a wealth of information to better characterize and elucidate the nature of chemical bonds such as the Laplacian or even the source function [44]. But a topological approach has not yet been explored in momentum space and will therefore not be addressed here.

Spin density refinement models

Much like in the charge density case, the Fourier series (1.2b) would legitimately be expected to give a reconstructed spin density. However, as PND usually provides a very limited number of magnetic structure factors, a mere use of (1.2b) can only yield an unsatisfactory result. Even more than for the charge density, a refinement model is required to constrain the reconstruction of a precise spin probability distribution in the crystal.

Another "direct" reconstruction strategy is based on the maximum entropy method (MEM) [45]. This method has been generalized for non centro-symmetric system by Schleger et al [46]. The entropy is defined by

$$S = -\sum_{i=1}^{M} q_i^{\uparrow} \ln(q_i^{\uparrow}) - \sum_{i=1}^{M} q_i^{\downarrow} \ln(q_i^{\downarrow}) \tag{1.26}$$

where M is the number of sample points in the unit cell. Because the spin density can take negative values (and the ln function in the MEM expression requests positive quantities), two channel grids of M points for alpha ($q_i^{\uparrow} = \rho_i^{\uparrow}/\sum_i \rho_i^{\uparrow}$) and beta ($q_i^{\downarrow} = \rho_i^{\downarrow}/\sum_i \rho_i^{\downarrow}$) are

respectively used. The $F_{mag}^{cal}(\mathbf{Q})$ can be calculated to compare with the experimental observations:

$$\chi^2(S) = \frac{1}{N}\sum_{\mathbf{Q}} \frac{|F_{mag}^{obs}(\mathbf{Q}) - F_{mag}^{cal}(\mathbf{Q})|^2}{\sigma^2(\mathbf{Q})} \tag{1.27}$$

where N is the number of observations, σ is the experimental error bar. The objective is to obtain a maximum entropy with $\chi^2 = 1$. The MEM is model free, the reconstructed result is totally dominated by the large magnetization density peaks and, as a consequence, the weak ones tend to be neglected. Therefore refinement models are often necessary to obtain detailed magnetic information on the studied compounds.

An atomic orbital model [47] using the unrestricted Hartree-Fock (UHF) method-like scheme is often considered to account for spin polarization effects, which are responsible for negative spin density regions. The spin density is the difference between $n^{\uparrow}$ alpha (majority) and $n^{\downarrow}$ beta (minority) electrons described by different MOs $\varphi^{\uparrow,\downarrow}$ respectively [48]:

$$\rho_{mag}(\mathbf{r}) = \rho^{\uparrow}(\mathbf{r}) - \rho^{\downarrow}(\mathbf{r}) = \sum_{i}^{n^{\uparrow}} |\varphi_i^{\uparrow}(\mathbf{r})|^2 - \sum_{i}^{n^{\downarrow}} |\varphi_i^{\downarrow}(\mathbf{r})|^2 \tag{1.28}$$

The new MOs are linear combinations of the N_{atoms} Clementi atomic orbitals $\chi_i(\mathbf{r})$ centered on atom i.

$$\varphi_i^{\uparrow,\downarrow}(\mathbf{r}) = \sum_{j}^{N_{atoms}} c_j^{\uparrow,\downarrow}\chi_j(\mathbf{r}) \tag{1.29}$$

where $\chi_j(\mathbf{r})$ can be described as follows:

$$\chi_j(r) = Nr^{n-1}e^{-\xi_L^i r}\sum_{M=-L}^{L} \alpha_{LM}^i Y_{LM}(\theta_i, \varphi_i)$$

here $Nr^{n-1}e^{-\xi_L^i r}$ are Slater functions, n, L and M are the quantum numbers ($L = 0$ to $N-1$, $L = 0$ for s orbitals, 1 for p orbitals and 2 for d orbitals, $M = -L$ to L), $Y_{LM}(\theta_i, \varphi_i)$ are spherical harmonics, ξ_L^i is the Slater radial exponent and α_{LM}^i are the atomic orbital coefficients with the normalization condition:

$$\sum_{M=-L}^{L} |\alpha_{LM}^i|^2 = 1$$

Making use of the independent atom approximation, inter-atomic cross terms are once again ignored, and the spin density simplifies to

$$\rho_{mag}(\mathbf{r}) = \sum_{j}^{N_{atoms}} p_j|\chi_j(\mathbf{r})|^2 \tag{1.30}$$

where p_j is the spin population on atom j,

$$p_j = \sum_{i}^{n^{\uparrow}} c_j^{\uparrow 2} - \sum_{i}^{n^{\downarrow}} c_j^{\downarrow 2} \tag{1.31}$$

As a consequence, each population can be positive or negative, while their sum is constrained to match the number of unpaired electrons in the system.

Another refinement model is based on the Hansen & Coppens model (HC) [7], adapted to spin density refinement[49, 50]. Similar to (1.18) and (1.19):

$$\rho_{mag}(\mathbf{r}) = \sum_{i}^{atoms} \rho_{i,mag}(\mathbf{r} - \mathbf{R}_i) \tag{1.32}$$

where the atomic spin density is described by means of the multipolar terms:

$$\rho_{i,mag}(\mathbf{r}) = P_{i,valence}\kappa^3 R_{i,0}(\kappa\mathbf{r}) + \sum_{l=0}^{l_{max=4}} \kappa'^3 R_{i,l}(\kappa'\mathbf{r}) \sum_{m=0}^{l} P_{i,lm\pm} Y_{i,lm\pm}(\theta,\varphi) \tag{1.33}$$

Hence, no core contribution is accounted for, because unpaired electrons are expected to generally originate from the valence shells.

Much like the charge density refinement model, parameters of this model can be refined from the minimization of an objective function quantifying the difference between experimental and model magnetic structure factors (expression (1.22)).

Joint refinement strategy

To this day, the best suited model for a joint refinement of spin resolved electron density in position space using XRD & PND data is called the "spin-split" pseudo-atom model. It is an adaptation of the HC model ((1.19), (1.33)), was proposed by Deutsch et al [1, 2] and implemented in $MOLLYNX$. Splitting the electron density into up and down contributions gives:

$$\rho_i^{\uparrow}(\mathbf{r}) = P_{i,core}^{\uparrow}\rho_{i,core}(\mathbf{r}) + P_{i,valence}^{\uparrow}\kappa^{\uparrow 3}\rho_{i,valence}(\kappa^{\uparrow}\mathbf{r}) + \sum_{l=0}^{l_{max}} \kappa'^{\uparrow 3} R_{i,l}(\kappa'^{\uparrow}\mathbf{r}) \sum_{m=0}^{l} P_{i,lm\pm}^{\uparrow} Y_{i,lm\pm}(\theta,\varphi) \tag{1.34a}$$

$$\rho_i^{\downarrow}(\mathbf{r}) = P_{i,core}^{\downarrow}\rho_{i,core}(\mathbf{r}) + P_{i,valence}^{\downarrow}\kappa^{\downarrow 3}\rho_{i,valence}(\kappa^{\downarrow}\mathbf{r}) + \sum_{l=0}^{l_{max}} \kappa'^{\downarrow 3} R_{i,l}(\kappa'^{\downarrow}\mathbf{r}) \sum_{m=0}^{l} P_{i,lm\pm}^{\downarrow} Y_{i,lm\pm}(\theta,\varphi) \tag{1.34b}$$

the sum and difference of these two expressions yield the charge and spin densities, respectively as in (1.19) and (1.33):

$$\rho(\mathbf{r}) = \sum_{i}^{N_{atoms}} (\rho_i^{\uparrow}(\mathbf{r}) + \rho_i^{\downarrow}(\mathbf{r})) \quad \text{and} \quad \rho_{mag}(\mathbf{r}) = \sum_{i}^{N_{atoms}} (\rho_i^{\uparrow}(\mathbf{r}) - \rho_i^{\downarrow}(\mathbf{r})) \tag{1.35}$$

Because it is widely admitted that only valence electrons significantly contribute to the spin density, $P_{i,core}^{\uparrow}$ is usually set equal to $P_{i,core}^{\downarrow}$. Moreover, splitting into up and down

contributions is limited to those atoms which are suspected to play a non-negligible role in the global magnetic properties. Parameters $P^{\uparrow}_{valence}/P^{\downarrow}_{valence}$, $\kappa^{\uparrow}/\kappa^{\downarrow}$, $\kappa'^{\uparrow}/\kappa'^{\downarrow}$ and $P^{\uparrow}_{lm\pm}/P^{\downarrow}_{lm\pm}$ are used to describe "split atoms" up and down multipoles just as if they pertained to different atoms (but on the same site). All other atoms use a single set of multipoles and will therefore cancel out in the spin density expression.

Experimental observations include both XRD and PND data sets with their respective error bars. Nevertheless, it must be emphasized that conducting a refinement with fair balance of both sets of data is quite a challenge (and probably explains why few -if any- attempts have been reported). In the χ^2 case, PND data contribution is weak because of their limited number compared with the XRD data. To fairly balance the weights of different data for minimization, a **NLOG** scheme based on χ^2 for individual experiments has been proposed by Bell et al[51] and independently by Gillet et al [52, 53].

$$L = N_{XRD}\log[\sum_{i=1}^{N_{XRD}} \frac{|F^{obs}_{XRD}(\mathbf{Q}_i) - F^{cal}_{XRD}(\mathbf{Q}_i)|^2}{\sigma^2(\mathbf{Q}_i)}] + N_{PND}\log[\sum_{j=1}^{N_{PND}} \frac{|F^{obs}_{XRD}(\mathbf{Q}_j) - F^{cal}_{PND}(\mathbf{Q}_j)|^2}{\sigma^2(\mathbf{Q}_j)}] \tag{1.36}$$

where N_{XRD} is the number of XRD data (several thousands), and N_{PND} is the number of PND data (several hundreds). The estimated standard deviation for each measurement is σ. Such an expression is derived from Bayes maximum likelyhood considerations, assuming that the standard deviations correspond to a normal distribution law of errors and are known within an overall scale factor.

1.3.3 Applications to Nit(SMe)Ph & $YTiO_3$

Application to Nit(SMe)Ph [54]

The first application case is on Nit(SMe)Ph [a] (Figure 1.4). It belongs to the nitronyl-nitroxide (Nit) free radical family. The magnetic property of this radical is due to an unpaired electron mainly delocalized over the two NO groups ($S = \frac{1}{2}$) as depicted on figure 1.4. XRD and PND investigations have been conducted by Pillet [55] and Pontillon [56, 57], respectively. Electron transfer from O–N–C–N–O fragment and the role of hydrogen bonds have been examined by means of topological analysis tools. Joint refinement aims at revisiting, from a more global perspective, the XRD data previously published by Pillet and co-workers [55] together with those from PND [56, 57]. It was carried out with *MOLLYNX* by the *CRM2* collaborators in Nancy. To serve as theoretical reference, three types of *ab-initio* computations were considered: on the molecular side, computations (DFT, UHF and ROHF[15]) were carried out using G09 with M06-2X [58], CAM-B3LYP [59] and B3LYP[60] hybrid functionals and the standard basis set cc-pVDZ[61]. To reach a better grasp on possible solid state effects, periodic DFT

[a] 2-(4-thiomethylphenyl)-4,4,5,5-tetramethylimidazoline-1-oxyl-3-oxide

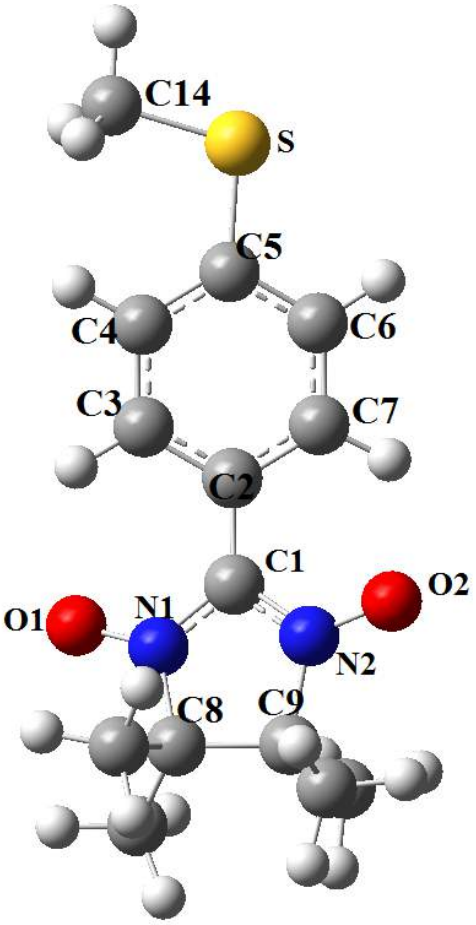

Figure 1.4: The Nit(SMe)Ph molecular magnet
Space group $P2_1/c$, a=9.6586 Å, b=19.482 Å, c=9.34 Å, $\beta = 125.972°$

computations were conducted using CRYSTAL14 with M06-2X [58], PBEXC[62], PBE0-1/3[63] and B3LYP[60] hybrid functionals and Pob-TZVP[64] basis set. CASSCF calculations were performed using *MOLCAS* by A. Genoni and M. Marazzi, Lab. SRSMC, using the cc-pVDZ[61] basis set at the $CASSCF(7,8)$ and $CASSCF(10,10)$ levels (see *section 1.2.2*).

For the figures and tables, only the M06-2X DFT computations are presented. More information can be found in the Appendix A [a] *and article [54].*

The almost structureless residual electron density in Figure 1.5 is evidence of the high quality of the final result obtained by joint refinement from both experimental data. Firstly, both experimental static deformation densities (SDD) in the C–N–O planes (Figure 1.6) and vertical planes (perpendicular to the molecular plane) (Figure 1.7) confirm the asymmetry between the two NO groups evidenced by experimental results, and polarization of O atoms (6 and 5 blue contours around O1 for N1–O1 group, 3 and 6 blue contours around O2 for N2–O2 group in Figure 1.6, while 0 and 3 blue contours around O1 for N1–O1 group, 8 and

[a] Table A.4 for Mulliken spin populations of periodic computations with different functional. Table A.5 and Table A.6 for the monomer Mulliken spin populations with different functional by G09 and MOLCAS respectively.

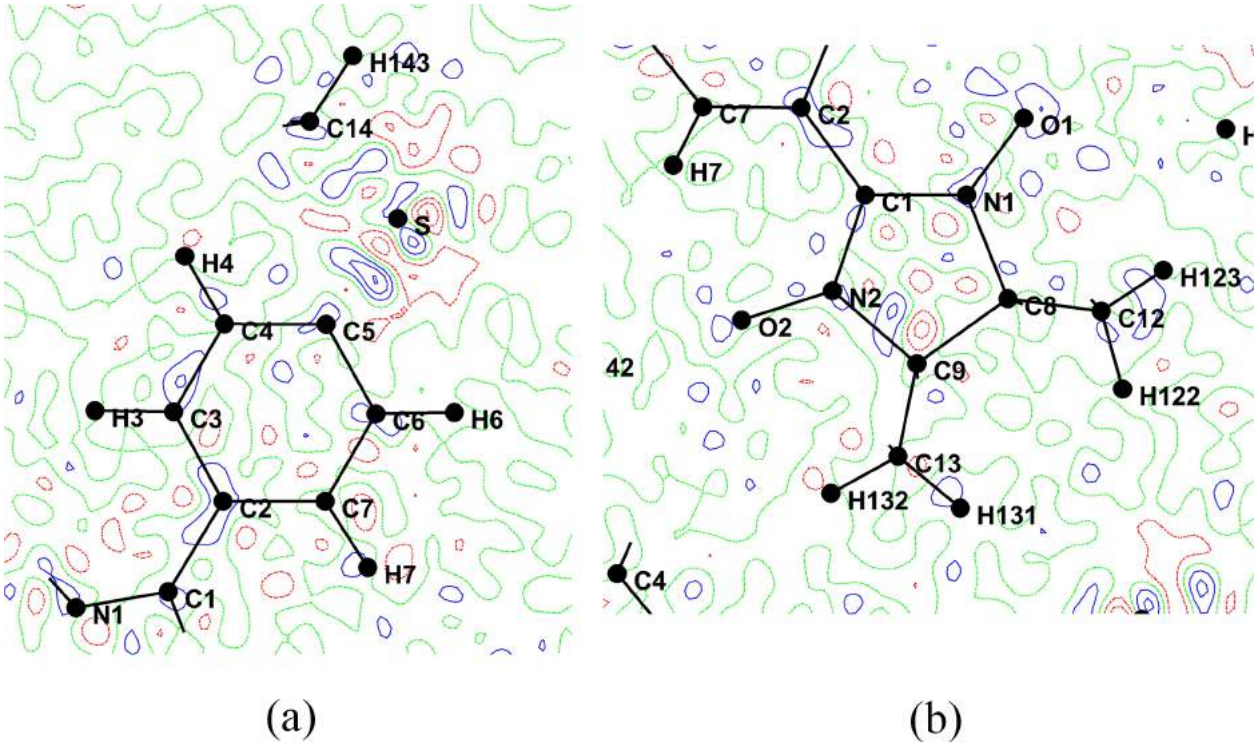

Figure 1.5: Nit(SMe)Ph residual electron density maps
(a) Phenyl ring plane and (b) Nit ring plane. Contour intervals of 0.05 eÅ^{-3}, positive (blue), negative (red) and neutral (green) lines.

0 blue contours around O2 for N2–O2 group in Figure 1.7). This observation contradicts the symmetric results obtained by *ab-initio* methods at the DFT level (for any functional) in both vacuum (G09) and crystalline environment (CRYSTAL14). For the SDD around nitrogen atoms in the vertical planes (perpendicular to the molecular plane), the joint refinement density shows negative contours (red), while G09 and CRYSTAL14 predict an excess of electrons (blue) (Figure 1.7). The same results are found in the SDD of vertical planes containing the C-N bond (Figure A.1). Rather unexpectedly, G09 results are closer to the experiment than those from CRYSTAL14 (6 blue contours for experimental, 5 blue contours for G09 and only 1 blue contour for CRYSTAL14 results between N and O atoms).

Based on the charge density obtained in position space, a topological analysis can be conducted. Isolated molecules (G09) are computed by means of the AIMALL package[65] while CRYSTAL14 has an embeded TOPOND package [66–68]. On the experimental side, the similar analysis is performed with the utility included in *MOLLYNX* from the joint refinement results. Elements of topology analysis are displayed in Table 1.1[a]. Information on critical points show a fair agreement between experimental, G09 and CRYSTAL14 results, except for the Laplacian $\Delta\rho$ at the critical points between N and O atoms (see red numbers in Table 1.1). In this particular case, the experimental results are positive where a depletion of negative charge occurs, while the standard DFT computations produce

[a]see Table A.7 for complete topology results.

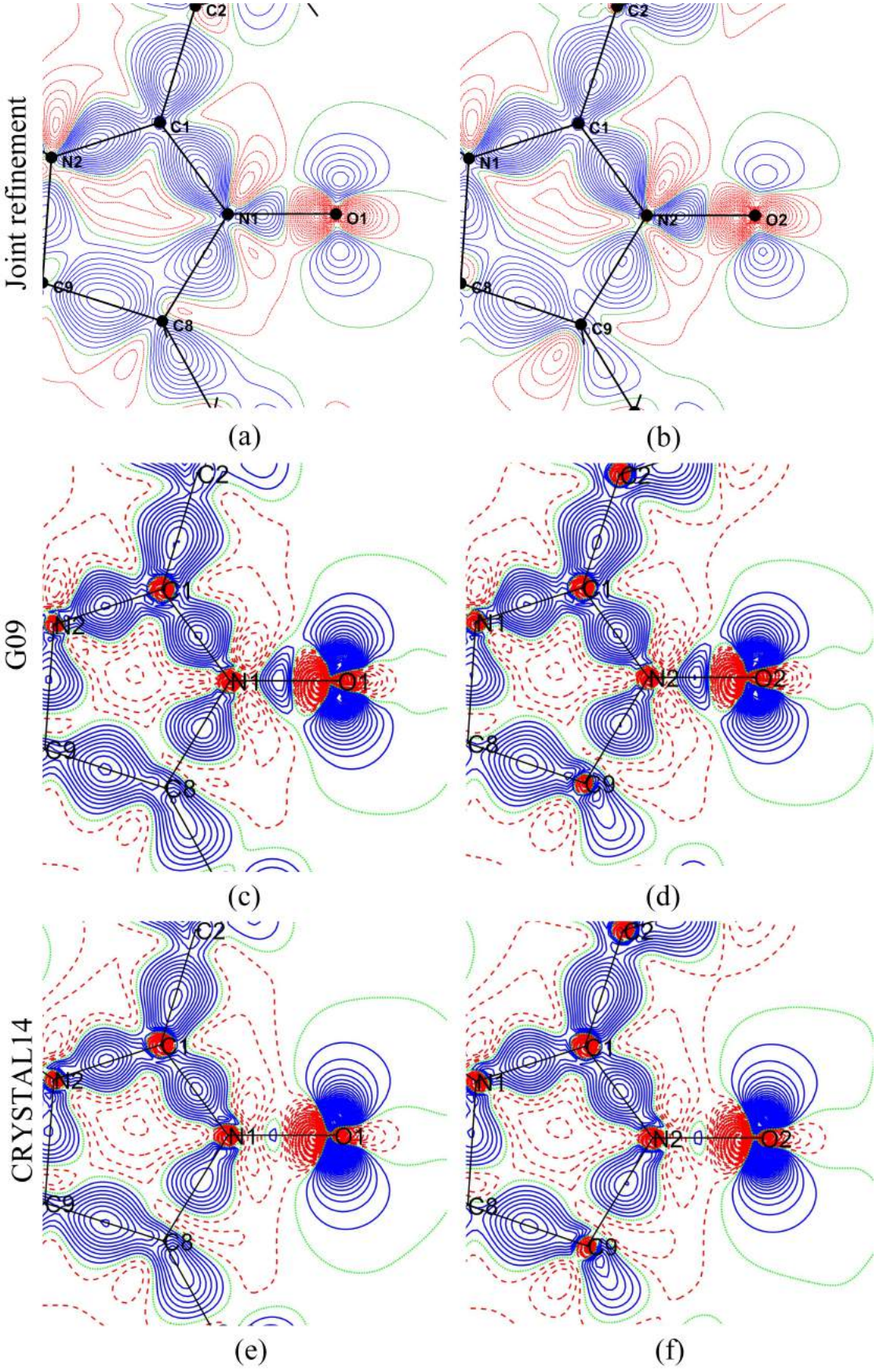

Figure 1.6: Nit(SMe)Ph deformation density
C1–N1–O1 plane (left) and C1–N2–O2 plane (right). Each row corresponds different methods: (a,b) joint refinement, (c,d) G09 (monomer), (e,f) CRYSTAL14. Contour intervals of 0.05 eÅ^{-3}, positive (blue), negative (red) and neutral (green) lines.

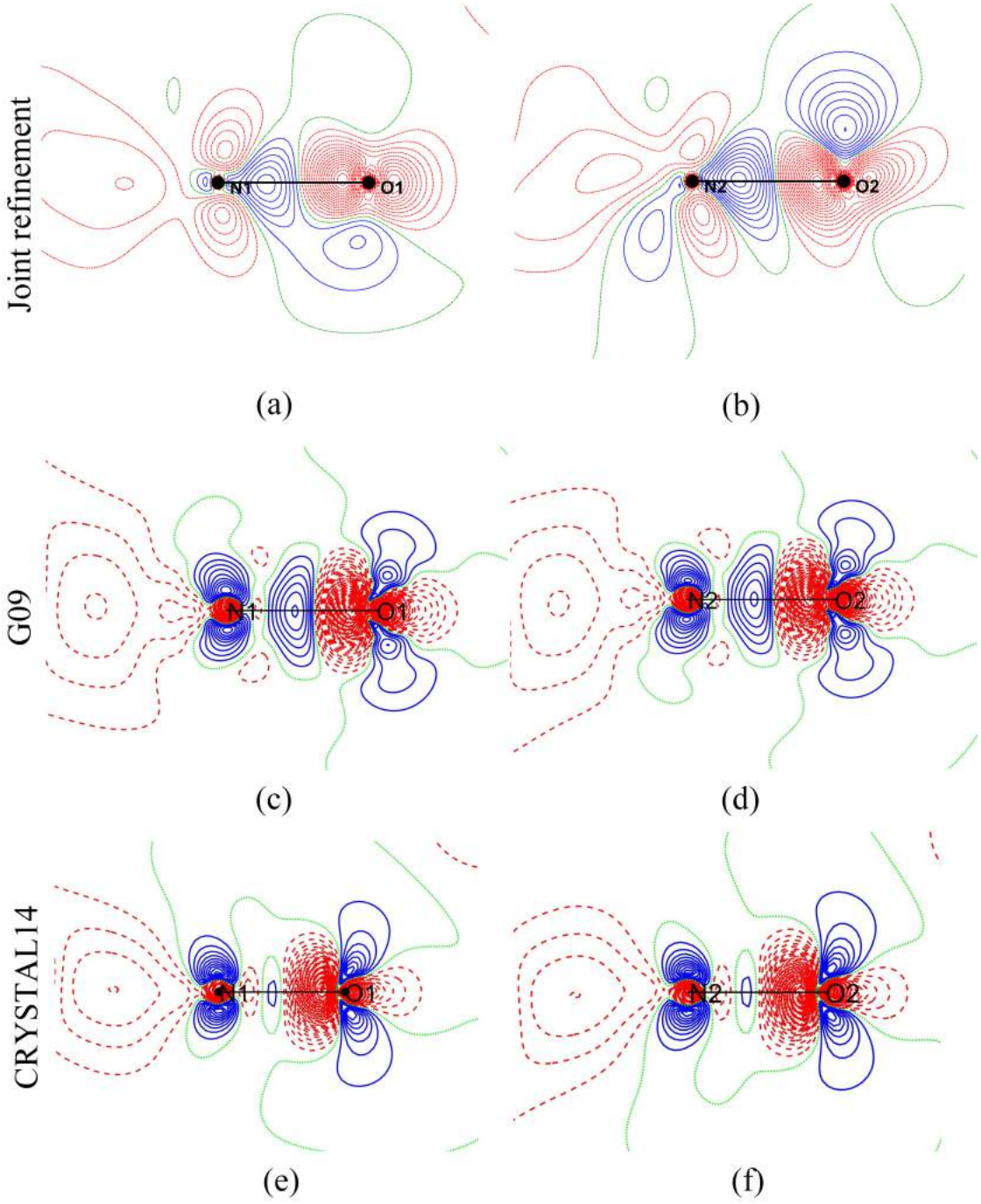

Figure 1.7: Nit(SMe)Ph deformation density
in the perpendicular planes to cycle and containing N–O bond perpendicular to C1–N1–O1 plane (left) and C1–N2–O2 plane (right). Each row corresponds to different methods: (a,b) joint refinement, (c,d) G09 (monomer), (e,f) CRYSTAL14. Contour intervals of 0.05 eÅ^{-3}, positive (blue), negative (red) and neutral (green) lines.

Bonding(x-y)	$d_{(x-y)}$ Å	$d_{(x-CP)}$ Å			$d_{(CP-y)}$ Å		
		EXP	G09	CRYSTAL14	EXP	G09	CRYSTAL14
O2—N2	1.28	0.63	0.67	0.66	0.65	0.61	0.62
N1—O1	1.28	0.64	0.61	0.62	0.64	0.67	0.66
C1—N2	1.35	0.54	0.47	0.50	0.81	0.88	0.85
C1—N1	1.36	0.55	0.47	0.52	0.81	0.88	0.83
Bonding(x-y)		$\Delta\rho(e\text{Å}^{-5})$			$\rho(e\text{Å}^{-3})$		
		EXP	G09	CRYSTAL14	EXP	G09	CRYSTAL14
O2—N2		4.64	-18.21	-10.16	2.68	2.89	2.62
N1—O1		5.98	-18.05	-9.99	2.59	2.88	2.61
C1—N2		-19.30	-20.44	-22.54	2.19	2.18	2.19
C1—N1		-19.16	-21.24	-22.39	2.22	2.16	2.19

Table 1.1: Nit(SMe)Ph Laplacian and density values at the bond critical points (monomer for G09)

negative values, where negative charge is concentrated.

For the spin density in the molecular plane (Figure 1.8), the theoretical results exhibit weaker spin values than those from the experiment (6 and 7 blue contours for N and O atoms respectively from experimental results, but 4 blue contours for N and O atoms from DFT results in Figure 1.8). However, an inverse result is presented on the vertical planes (Figure 1.9 and Figure A.2) (6 and 7 blue contours for N and O atoms respective from experimental results, but 7 and 8 blue contours for N and O atoms respective from DFT results). It can thus be claimed that the mean field tends to prefer $sp(\sigma)^{+}p^{\perp}$ orbitals to sp^3 hybridization and computations yield different distribution weights for the molecular and perpendicular planes.

From these results, the comparison between experiment and computations shows the different spin distribution in and perpendicular to the molecular planes. Standard DFT computations are not able to reproduce the asymmetry between the two NO groups. The possible reason is that mean field interaction used by DFT computations yields an approximate electron distribution. However, from the experimental perspective, possible electron correlations make electron transfer from perpendicular plane to molecular plane. Therefore, electron correlation approximation as described by DFT methods are not fully adapted to the detailed orbital information of the two NO groups as observed by experiments.

Compared with the spin density maps published by Pontillon and co-workers [57] (Figure 1.10), the joint refinement strategy provides a spin density with significantly more details. The large amount of XRD data now allows to define more atoms as magnetic and enable better radial description for atoms. The joint refinement can access the different electron behaviour with their respective spin dependence by 'spin split' construction.

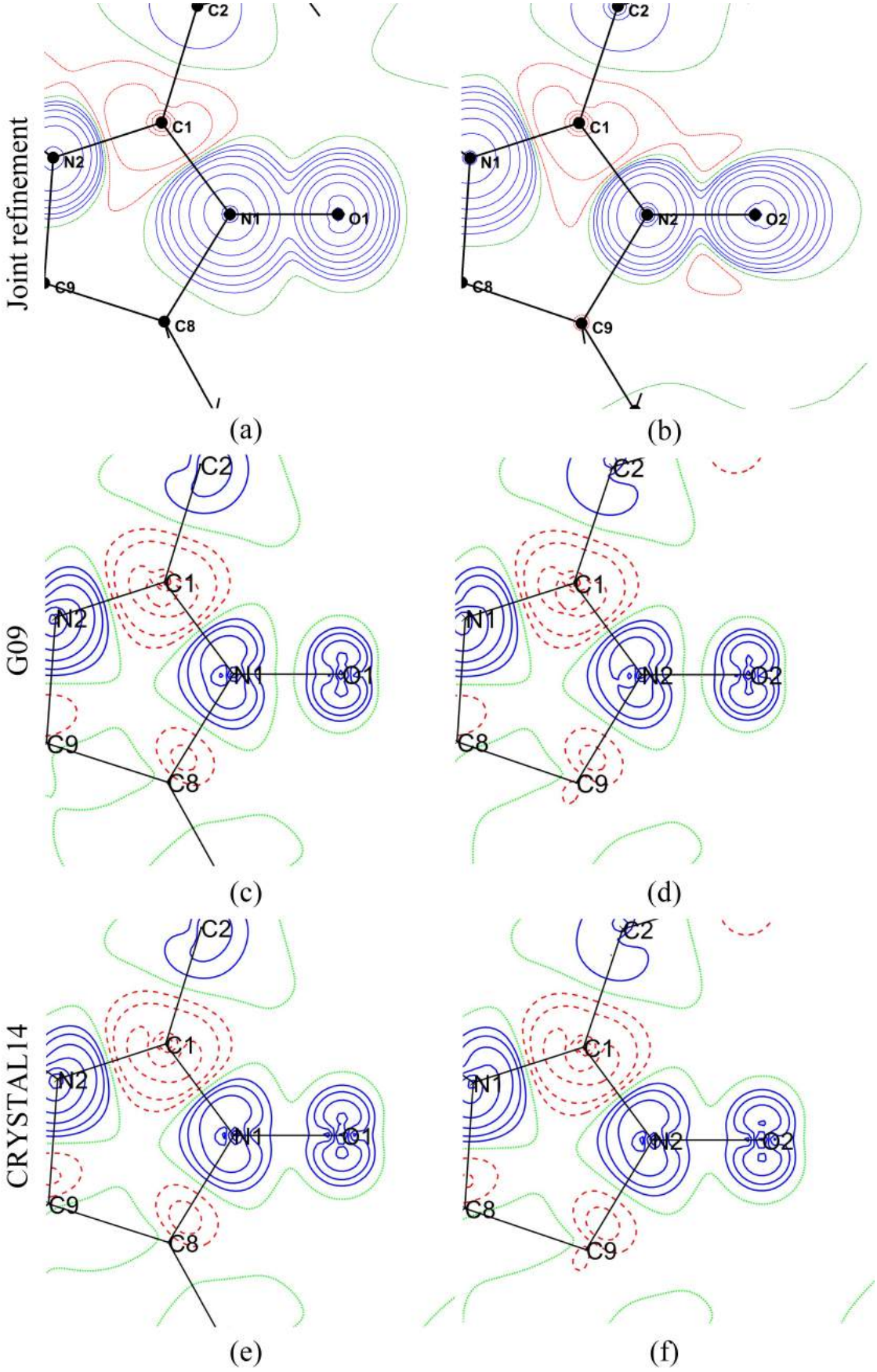

Figure 1.8: Nit(SMe)Ph spin density
C1–N1–O1 plane (left) and C1–N2–O2 plane (right). Each row corresponds to a different method: (a,b) joint refinement, (c,d) G09 (monomer), (e,f) CRYSTAL14. Contour at 0.01 $\times 2^n$, $(n = 0, \ldots, 12)$ $\mu_B \cdot$ Å^{-3}, positive (blue), negative (red) and neutral (green) lines.

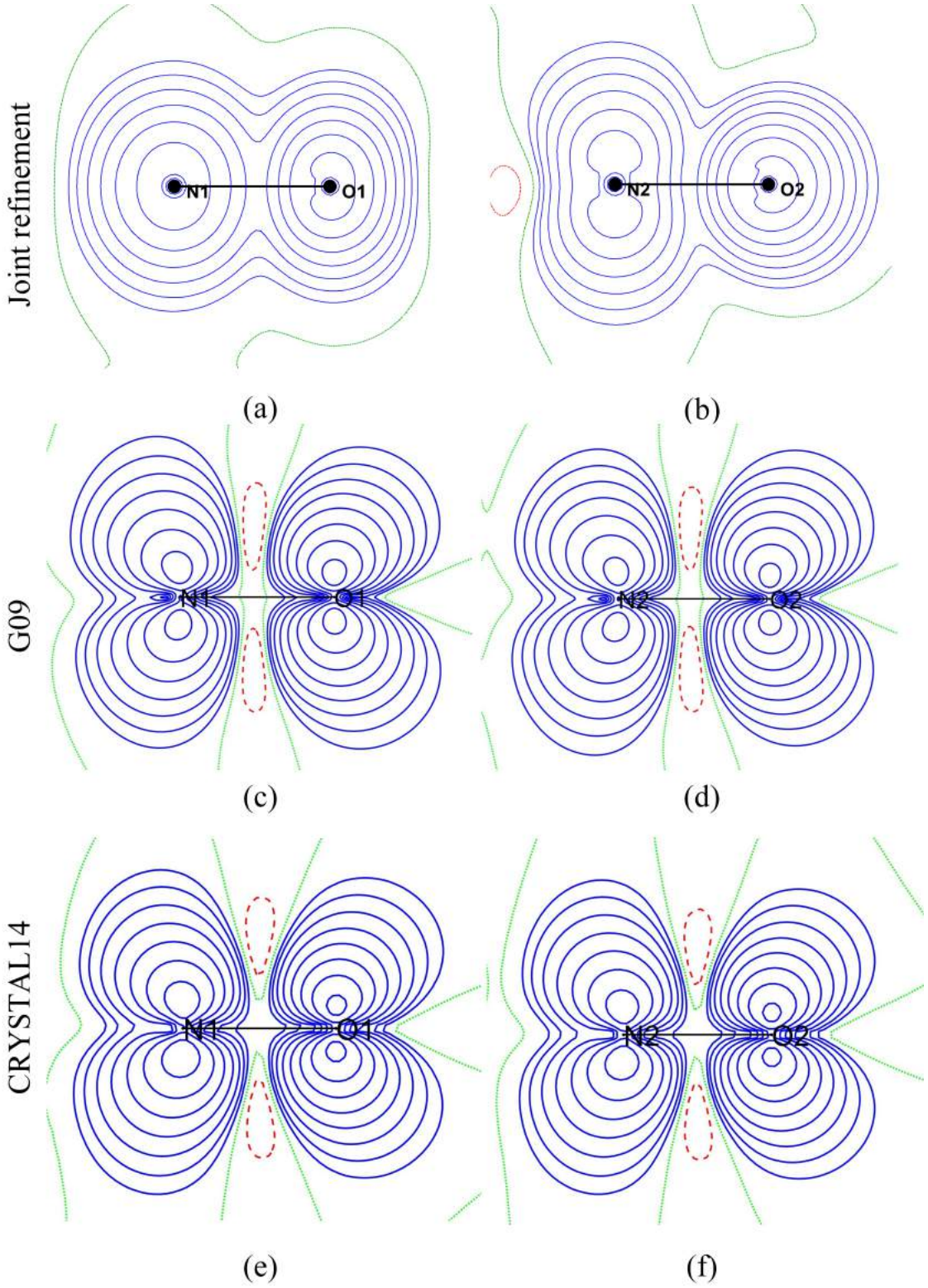

Figure 1.9: Nit(SMe)Ph spin density in the vertical plane containing bond N–O perpendicular to C1–N1–O1 plane (left) and perpendicular to C1–N2–O2 plane (right). Each row corresponds to a different method: (a,b) joint refinement, (c,d) G09 (monomer), (e,f) CRYSTAL14. Contour at 0.01 $\times 2^n$, $(n = 0, \ldots, 12)$ $\mu_B \cdot$ Å^{-3}, positive (blue), negative (red) and neutral (green) lines.

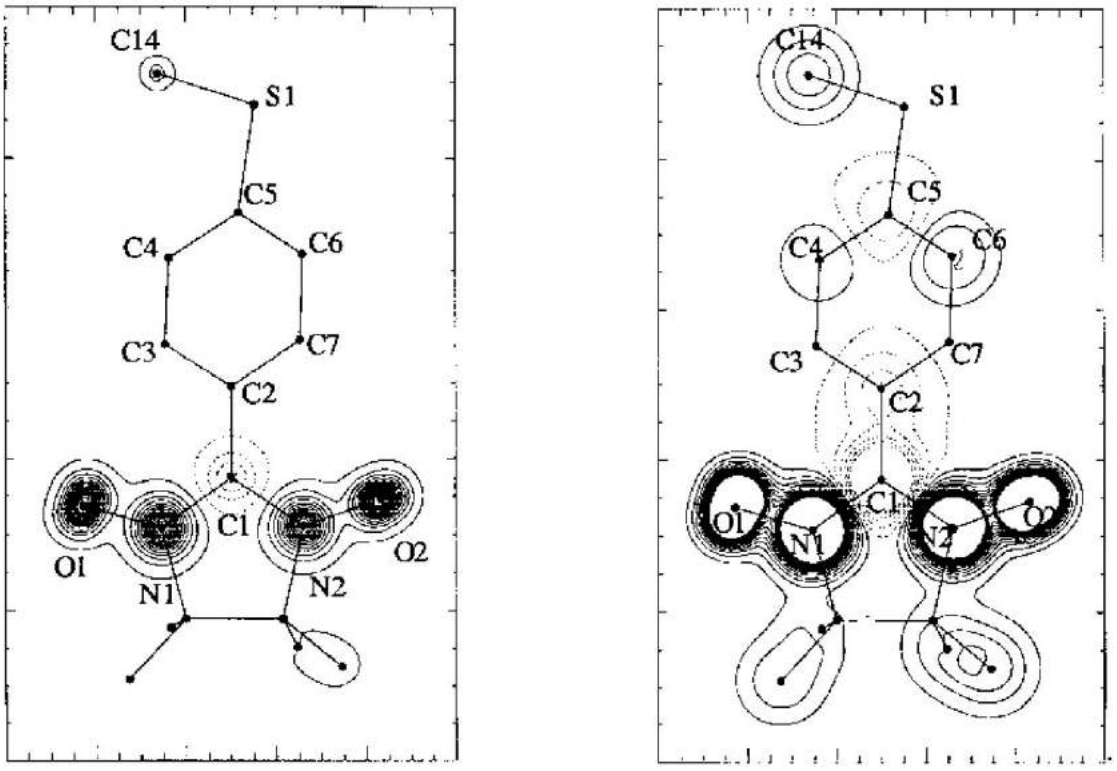

Figure 1.10: Nit(SMe)Ph spin density
Projection of the spin density as analyzed by wave-function modelling onto the nitroxide mean plane (Nit(SMe)Ph). Negative contours are dashed: Left: high-level contours (step 0.04 μ_BÅ^{-2}); right: low-level contours (step 0.006 μ_BÅ^{-2}).

CASSCF computations were conducted by A. Genoni and M. Marazzi to evaluate to what extent a configuration interaction treatment can impact these discrepancies. From the 3D point of view (Figure 1.11), it yields an obvious difference between the molecular and perpendicular planes. Moreover, the negative (green) distribution on the NO_2 (right) side now shows the asymmetry between two NO groups. More detailed information can be observed from the 2D spin density in the C1-N-O planes and their translations along perpendicular directions (Figure 1.12, A.3, A.4). The spin density distribution is weak in the molecular plane, the negative (red) distributions appear when translation distances equal to $0.4 \sim 0.9$ Å on the NO_2 side.

The topology analysis is subsequently conducted to access the atomic basin charge and spin populations as reported in Table 1.2 and Table 1.3, respectively. The Bader spin population of CASSCF is calculated by charge and spin cubes (with a step < 0.05 Å), using the *Code: Bader Charge Analysis*[a] [69] (formerly called *BaderWin*). The spin population is the integration of a spin density *cube*[b] file in the respective basin defined by the zero-flux surface of the total charge density.

The integrated spin atomic populations, of experimental and CASSCF origins, now display

[a] http://theory.cm.utexas.edu/henkelman/code/bader/
[b] a formatted 3D grid of data file. More information is available from http://gaussian.com/cubegen/.

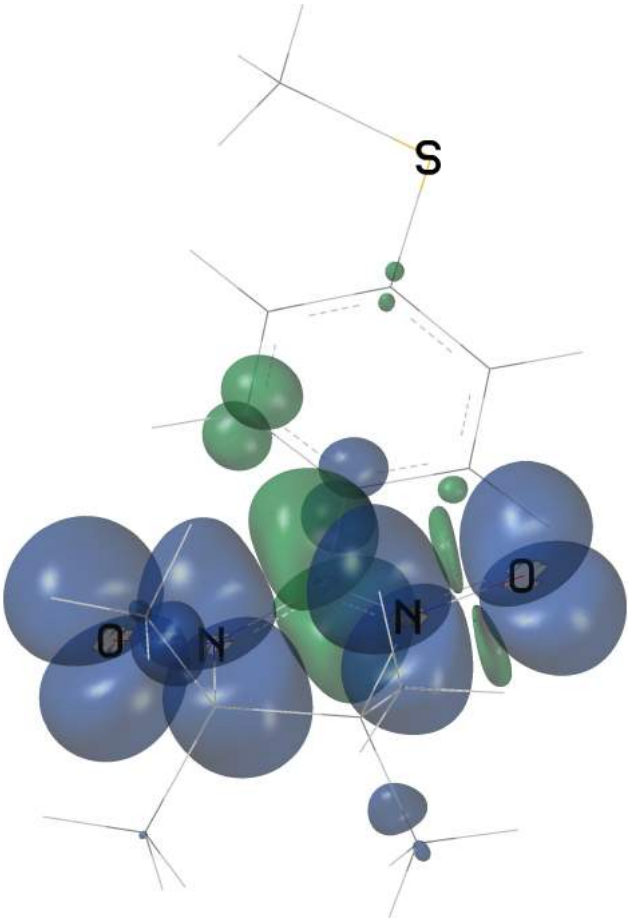

Figure 1.11: Nit(SMe)Ph 3D spin density from CASSCF
Iso-surface value 0.0068 μ_BÅ^{-3} positive (blue) and negative (green).

	ΔP^{val}	*Mulliken populations*			*Bader populations*			
Atoms	Refinement	G09	CRYSTAL14	CASSCF	Refinement	G09	CRYSTAL14	CASSCF
O1	-0.08(2)	-0.335	-0.180	-0.406	-0.3	-0.512	-0.547	-0.541
N1	-0.08(2)	-0.058	-0.460	-0.160	-0.5	-0.388	-0.455	-0.620
C1	-0.15(2)	0.339	0.502	0.568	0.5	-0.826	0.837	1.074
N2	-0.05(2)	-0.046	-0.449	-0.138	-0.4	-0.389	-0.456	-0.609
O2	-0.02(2)	-0.339	-0.167	-0.401	-0.2	-0.515	-0.547	-0.551
N1+O1	-0.16(4)	-0.393	-0.640	-0.566	-0.8	-0.900	-1.002	-1.161
N2+O2	-0.07(4)	-0.385	-0.616	-0.538	-0.6	-0.904	-1.003	-1.160

Table 1.2: Nit(SMe)Ph charge population (monomer for G09 and CASSCF)

	ΔP^{val}	*Mulliken populations*			*Bader populations*			
Atoms	Refinement	G09	CRYSTAL14	CASSCF	Refinement	G09	CRYSTAL14	CASSCF
O1	0.24(1)	0.37	0.33	0.30	0.27	0.35	0.32	0.29
N1	0.33(1)	0.28	0.33	0.30	0.27	0.26	0.30	0.28
C1	-0.15	-0.27	-0.27	-0.17	-0.08	-0.19	-0.19	-0.12
N2	0.29(1)	0.27	0.32	0.27	0.25	0.25	0.28	0.25
O2	0.21(1)	0.36	0.32	0.29	0.23	0.34	0.31	0.28
N1+O1	0.56(2)	0.66	0.65	0.60	0.54	0.62	0.61	0.57
N2+O2	0.50(2)	0.63	0.64	0.56	0.48	0.60	0.60	0.54

Table 1.3: Nit(SMe)Ph spin population (monomer for G09 and CASSCF)

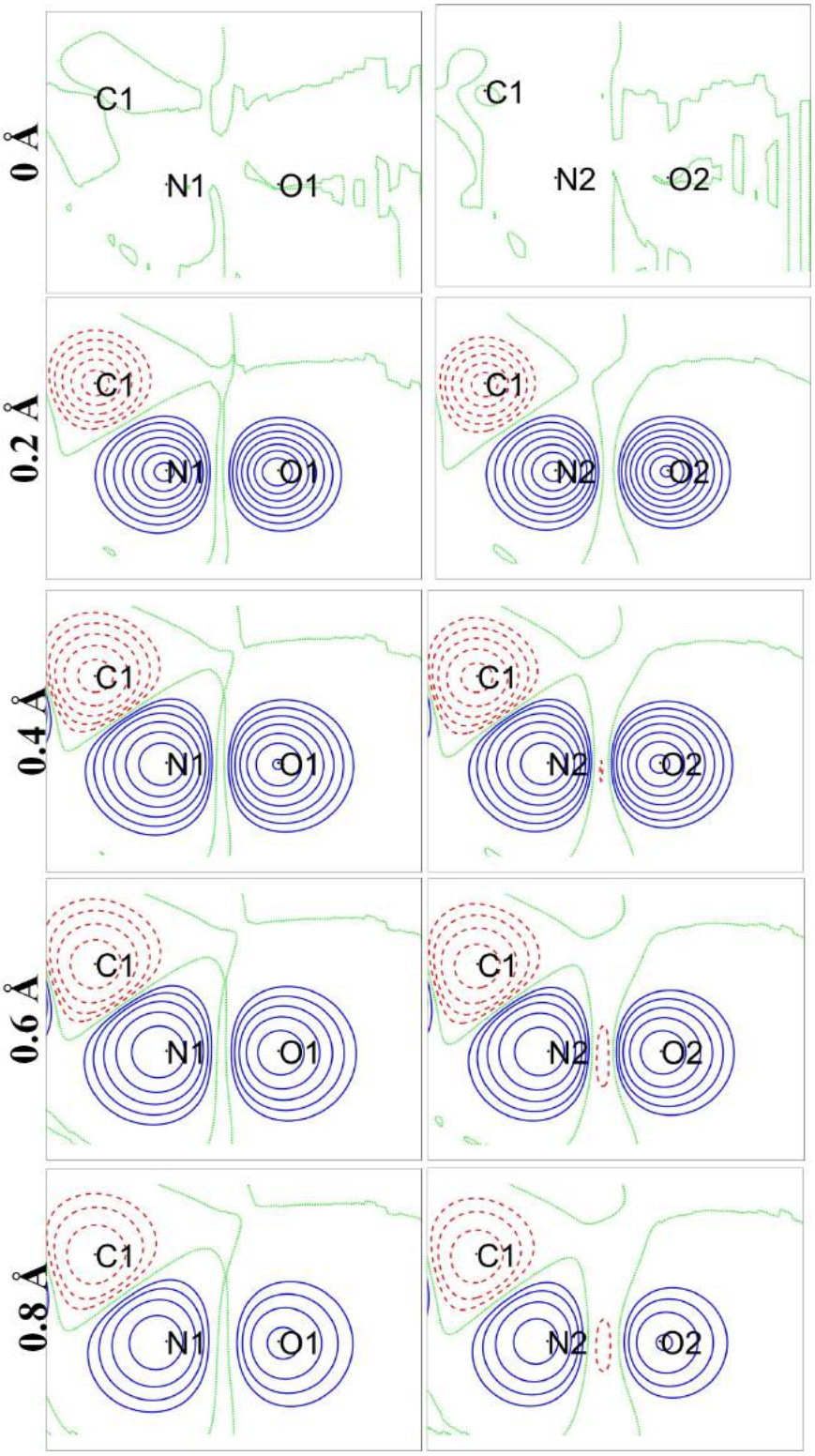

Figure 1.12: Nit(SMe)Ph spin density from CASSCF
C1–N1–O1 plane (left) and C1–N2–O2 plane (right). Each row corresponds to a different distance from the plane.Contour at 0.01 $\times 2^n$, $(n = 0, \ldots, 12)$ $\mu_B \cdot$ Å^{-3}, positive (blue), negative (red) and neutral (green) lines.

the asymmetry between both *NO* groups while standard DFT approaches (G09 and CRYSTAL14) had proved to be insensitive to this rather weak effect. A similar behaviour was recently confirmed on a independent study conducted by Gatti for the di-copper

molecular magnets $[Cu_2(t\text{-Bupy})_4(N_3)_2](ClO_4)_2$ [t-Bupy $= p - tert$-butylpyridine] and $Cu_2L_2(N_3)_2$ (L = 7-dimethylamino-1,1,1-trifluoro-4-methyl-5-azahept-3-en-2-onato) [70]. To understand the influence of inter-molecule interaction, dimer computations have been performed by G09 and CASSCF (retrieved from molecules with fractional coordinates: $(\bar{x}, \bar{y}, \bar{x})$ and $(\bar{x}, y + \frac{1}{2}(+1), z + \frac{1}{2})$ in space group $P\ 2_1/c$ [71] shown in Figure 1.13).

Atom	G09		CASSCF	
	Dimer (mol 1)	Dimer (mol 2)	Dimer (mol 1)	Dimer (mol 2)
O1	0.36	0.34	0.32	0.29
N1	0.27	0.27	0.28	0.29
C1	-0.18	-0.18	-0.12	-0.12
N2	0.26	0.26	0.28	0.29
O2	0.33	0.33	0.23	0.23
N1+O1	0.62	0.61	0.58	0.60
N2+O2	0.59	0.59	0.52	0.50

Table 1.4: Nit(SMe)Ph dimer Bader spin population by G09 and CASSCF

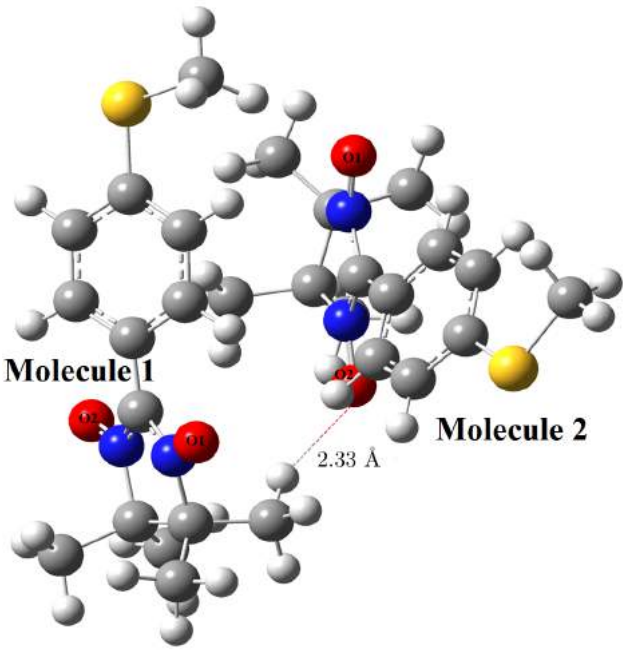

Figure 1.13: Nit(SMe)Ph dimer structure
Inter-molecule hydrogen bond O_2–H distance is 2.33 Å.

Bader spin population analysis conducted in Table 1.4) show a clear asymmetry between two NO groups by CASSCF, while it remains close for G09. The difference between two NO is amplified compared to the monomer case. This is clear evidence that the asymmetry effect is a complex phenomenon created by both intra and inter molecular interactions.

From these results, the joint refinement strategy combining XRD and PND data clearly demonstrates that it can provide a more sophisticated orbital description than previous (separated) attempts. This unexpected result shows to what extent state of the art

experimental measurements, and subsequent electron density modeling, can challenge theoretical methods and that the experiment-theory interplay is still an essential key to a better understanding of physical and chemical processes at stakes.

Obviously, standard DFT calculations using mean field interactions or more sophisticated functionals, are efficient at reducing the computational cost and more often than not give very accurate results. Nevertheless, in some particular cases, peculiar electronic configuration in Nit(SMe)Ph (especially that on the two *NO* groups) are reluctant to a fair description by such methods. In this respect it is quite recomforting to know that a more detailed configuration interaction (such as that offered by CASSCF) can be helpful to fit the *NO* orbitals and break the symmetry barrier.

When experimental and theoretical results do not agree, it may be the refinement problem, but also possibly the choice of quantum chemistry model for *ab-initio* computation. There is no such thing as a real *ab-initio* computational method which would be totally free of approximation. DFT methods, with their wealth of possible functionals, each adapted to a particular case, show the difficulty to predict accurate spin densities in a solid [72, 73]. This is why a more detailed treatment of electron correlation should be considered usually by means of post-HF methods.

Application to $YTiO_3$

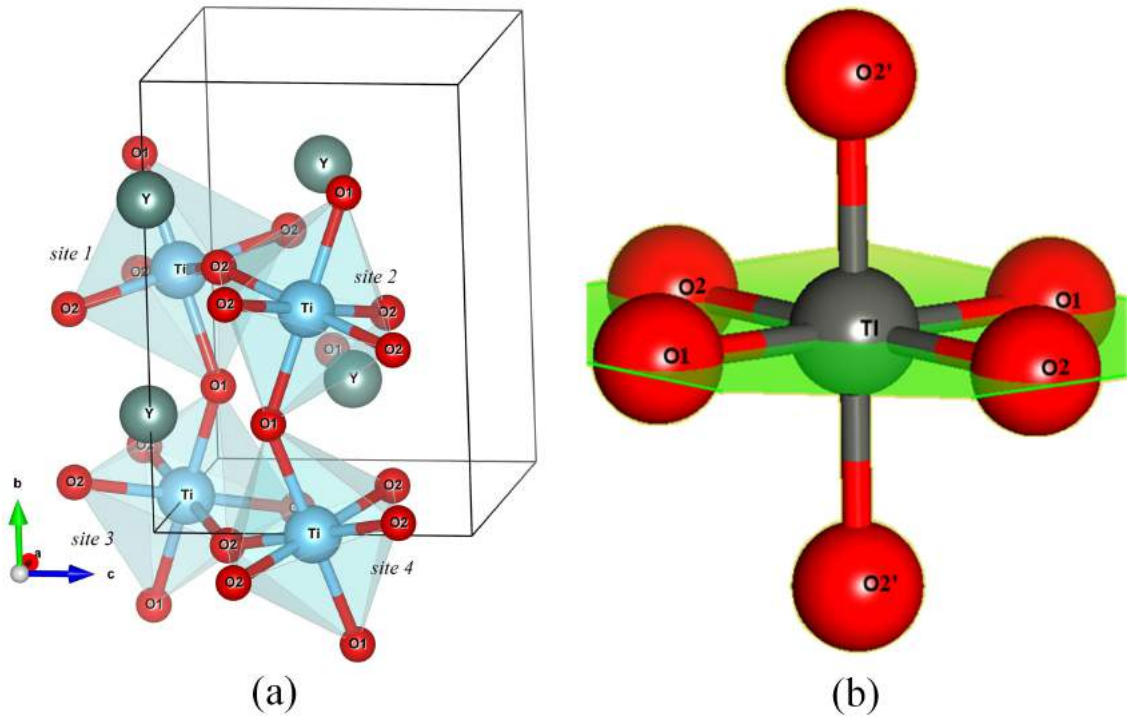

Figure 1.14: Perovskite $YTiO_3$
(a) geometry structure, (2) TiO_6 octahedron structure

Ti–O_1	2.024 Å
Ti–O_2	2.025 Å
Ti–O_2'	2.080 Å
∡ (O_2'–Ti–O_1)	93.03°, 86.77°
∡ (O_2'–Ti–O_2)	90.47°, 89.53°
∡ (O_2–Ti–O_1)	90.55°, 89.45°
∡ (Ti–O_2–Ti)	143.58°
∡ (Ti–O_1–Ti)	140.19°

Table 1.5: $YTiO_3$ octahedron structure

Perovskite $YTiO_3$ (Figure 1.14(a)) is a ferromagnetic compound at low temperature (below 30K)[74]. It has been investigated both theoretically [75, 76] and experimentally [77, 78]. The TiO_6 unit has a distorted octahedron structure (Figure 1.14(b)), where the $3d$ electrons of Ti atoms separate into two levels t_{2g} and e_g states, under the influence of the crystal field (CFT)[79]. The single t_{2g} state electron is widely accepted to be responsible for the magnetic properties [80]. The oxygen atoms connect two neighbouring octahedras. Two types of oxygen atom are defined according to the Ti–O distance and none of the ∡(O–Ti–O) angles are exactly 90°, nor 180°for the ∡(Ti–O–Ti) angles (shown in Table 1.5). The Ti($3d$) electron transfer is believed to be dominated by the interaction via O($2p$) rather than a mere direct Ti($3d$)−Ti($3d$) hopping [81].

Because of strong interactions and electron transfer between atoms, molecular computations using a $YTiO_3$ cluster[a] is not adapted to yield correct electronic states compared with experimental observations. Periodic DFT computations were carried out with CRYSTAL14 using PBE0-1/3 [63] hybrid functional and optimized effective core potentials (ECP) basis set for Y [b] and Ti[83]. A more standard basis set for O[84] is used. The cell parameters are taken from the experimental geometry without optimization in order to avoid any additional bias in the comparison of magnetic structure factors. A 1 μ_B spin value per Ti atom was attributed as an initial guess. Resulting Mulliken and Bader populations are presented in the Table 1.8 and Table 1.12. The Bader population analysis was performed from the TOPOND package already referred to in the previous section [66].

Standard basis set for Y[85] and Ti[84] have also been tested. Core electrons for heavy elements (Y atom) are difficult to describe, especially as far as SDD properties are concerned. SDD in Figure 1.15 exhibits striking differences between real distribution and sum of Y^{3+}, Ti^{3+} and O^{2-} isotropic contributions. It is clear that the distribution around the Y atom is awkward, even if the two types of computation yield similar atomic effective charge populations on this site. A possible explanation is that a portion of core electron transfers to high energy orbitals, and must be held responsible for the negative contour

[a] A macro cluster using Own N-layer Integrated Molecular orbital and mechanics (ONIOM) method [82] or cluster with point charges around were considered.

[b] unpublished data, offered by the CRYSTAL14 site http://www.crystal.unito.it/Basis_Sets/yttrium.html

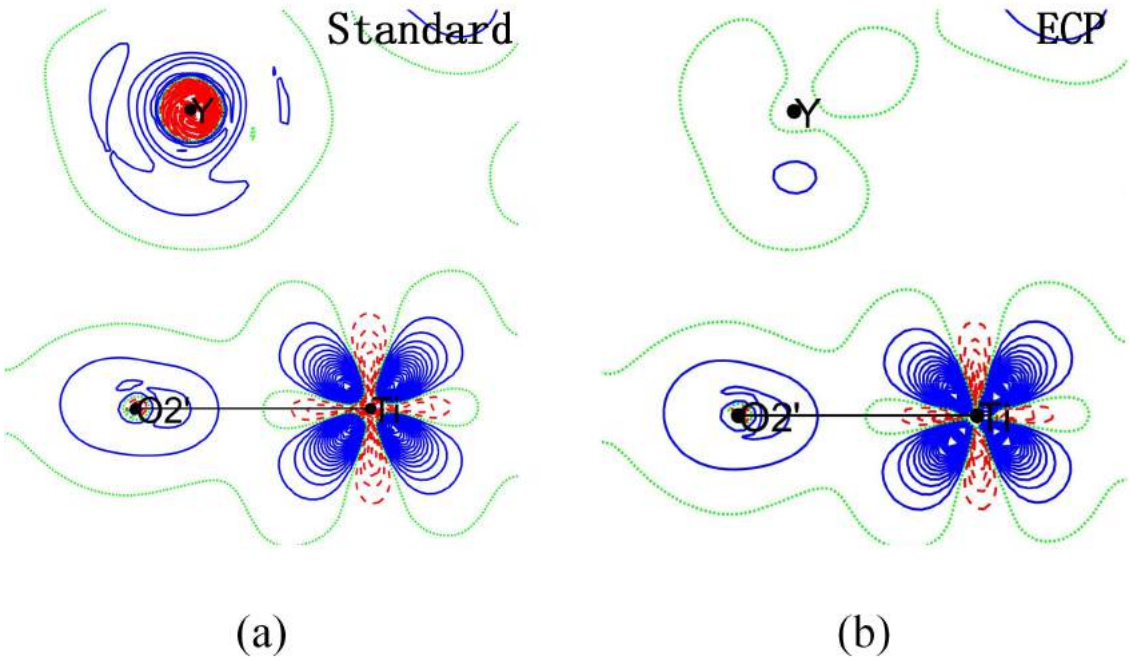

Figure 1.15: $YTiO_3$ *ab-initio* SDD results with different basis set
(a) standard basis set, (b) ECP basis set. Contour intervals of 0.1 eÅ^{-3}, positive (blue), negative (red) and neutral (green) lines.

close to the nuclei and positive further around, for the standard basis set computation. An effective core potentials (ECP) basis set obviously solves this problem by constraining the core electrons behaviour. This region is replaced by a core potential function with the additional advantage that it can reduce computational cost on systems with many metalic centers (1400374 h CPU time for ECP and 349059 h CPU time for normal basis set both with 12 × 12 CPU cores for $YTiO_3$ case).

Charge density refinements High resolution X-ray diffraction experiments were conducted using the CMOS PHOTON 2 detector in Bruker application laboratory, Karlsruhe, Germany, by our CRM2 collaborators. As presented in Table 1.6, a small single crystal ($0.021 \times 0.100 \times 0.109 mm^3$) was cooled down to 100 K, the x-ray wavelength is $\lambda = 0.56086$ Å using the Ag source. There are 1963 (unique) reflections after merging with $\sin\theta/\lambda < 1.25$ Å^{-1}. The geometry was firstly refined and resulted in the cell parameters $a = 5.6956(1)$Å, $b = 7.5963(1)$Å, $c = 5.3287(1)$Å, $\alpha, \beta, \gamma = 90°$, atomic fractional coordinates are presented in Table A.8.

The charge density is then refined by the HC model implemented in *Mopro* using these high-resolution XRD data. From the residual density (Figure 1.16 with $\sin\theta/\lambda < 0.8$Å^{-1}), structures around Ti and Y atoms are clear evidence that not all the available information is accounted for by the first refinement model. It exhibits negative values around Ti and Y, and positive values between Ti–O_2 positions. Negative value contours around O_1 in the O_1–Ti–O_2 plane continue towards to the Y direction. It is possible that absorption and extinction effects are not perfectly corrected for.

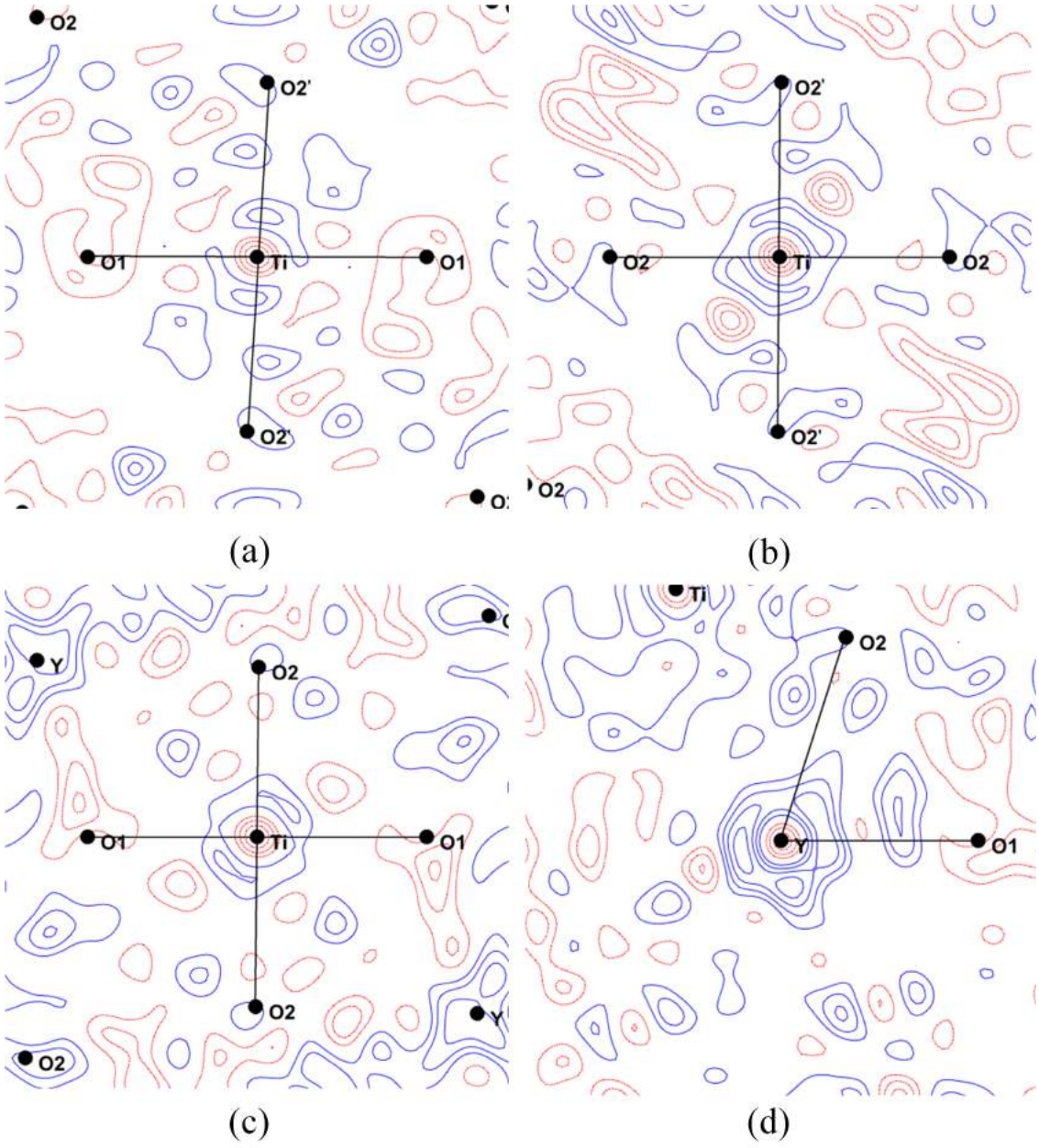

Figure 1.16: $YTiO_3$ residual electron densities
(a) plane O'_2–Ti–O_1, (b) plane O'_2–Ti–O_2, (c) plane O_2–Ti–O_1, (d) plane O_2–Y–O_1.
Contour intervals of 0.1 eÅ^{-3}, positive (blue), negative (red) and neutral (green) lines.

Detector	PHOTON 2
Space group	*Pnma*
a, b, c (Å)	5.6956(1), 7.5963(1), 5.3287(1)
X-ray source / wavelength (Å)	Ag/0.56086
Temperature (K)	100
$(sin\theta/\lambda)_{max}$ Å^{-1}	1.25
No. of reflections (unique)	1963
R_w(%)	4.48

Table 1.6: $YTiO_3$ XRD experimental data

The SDD, defined by the difference with Y, Ti^{3+} and O, are compared with theoretical predictions. XRD and theoretical maps are in reasonable qualitative agreement in O'$_2$–Ti–O_2 and O_2–Ti–O_1 planes. The negative deformation density indicates a Ti depletion along Ti–O bonds, while the positive deformation density decreases in the diagonal directions (between Ti–O bonds). With the local axis (x: Ti→ O_1, y: Ti→ O_2 and z: Ti→ O_2'), the negative deformation density represents the depopulation of e_g state orbitals ($d_{x^2-y^2}$ and d_{z^2}) , while the positive part is the signature of an increase in the population of t_{2g} state orbitals (d_{xz} d_{yz} and d_{xy}). In this perovskite, the Ti d_{xy} orbital is weak comparing to d_{xz} and d_{yz}, as shown in Table 1.7 [86]. The deformation density around O atoms is polarized towards the Ti atoms. The experimental deformation density along Ti–O bonds, in the order of $0.3 \sim 0.4e \times$ Å^{-3}, is larger than that given by DFT calculations $0.2 \sim 0.3\ e \times$ Å^{-3}.

Orbital	d_{z^2}	d_{xz}	d_{yz}	$d_{x^2-y^2}$	d_{xy}
Population	0.21	0.94	0.88	0.22	0.56
Relative pop. (%)	7.4	33.5	31.4	7.7	20

Table 1.7: $YTiO_3$ Ti $3d$ populations from XRD

The largest discrepancies with DFT are found in the O_1–Ti–O_2 plane. Theoretical results confirm the depletion of $d_{x^2-y^2}$ orbitals as evidenced by the negative deformation densities in the bond directions. However the clear increase of the population of d_{xy} orbitals as evidenced by XRD refinement is not at all reproduced. Another point of obvious mismatch is the Y atom site. Theoretical maps display an almost isotropic distribution, from strongly negative to positive close to the nucleus, while experimental density is very anisotropic and consistent with the electron deformation density seen on neighbouring oxygen atoms: the negative region on Y atomic sites points towards positive deformation density around the nearest O_1 atoms. To understand the details around Y atoms, other SDD planes and atomic charge population analysis were undertaken.

From the Figure 1.18, experimental results around Y and O are significantly more anisotropic. The deformation density around Y is obviously influenced by the neighbouring O_1 atoms, but it cannot be observed from the theoretical maps[a]. Atomic charge values or populations

[a]see Chapter 2 for Y-O cross term contribution.

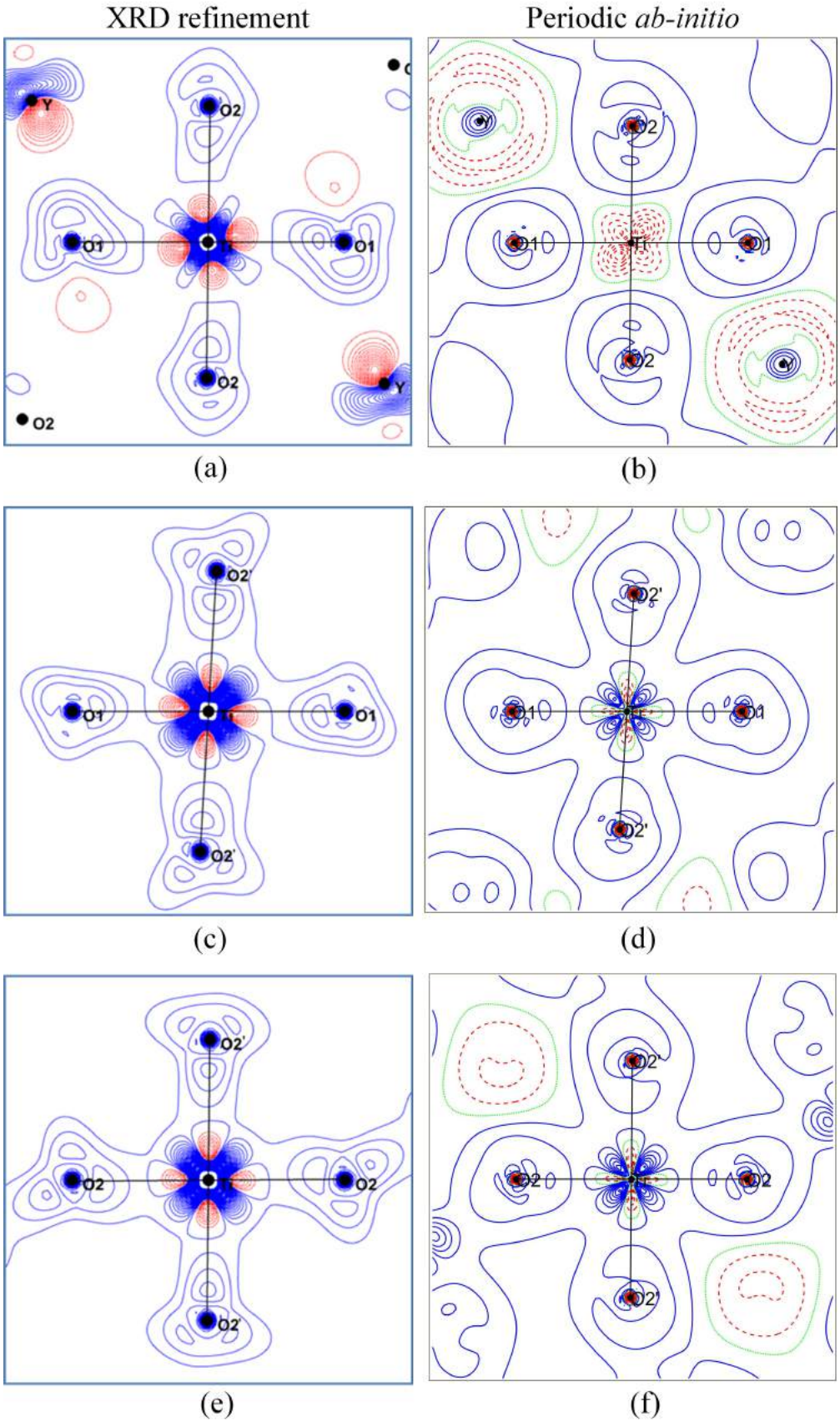

Figure 1.17: $YTiO_3$ static deformation densities around Ti
Left column by XRD refinement and right column by *ab-initio* computation. Each row corresponds to a plane: (a,b) the O_1–Ti–O_2 plane, (c,d) the O_1–Ti–O'$_2$ plane, (e,f)the O_2–Ti–O'$_2$ plane. Contour intervals are 0.1 eÅ^{-3}, positive (blue), negative (red) and neutral (green) lines.

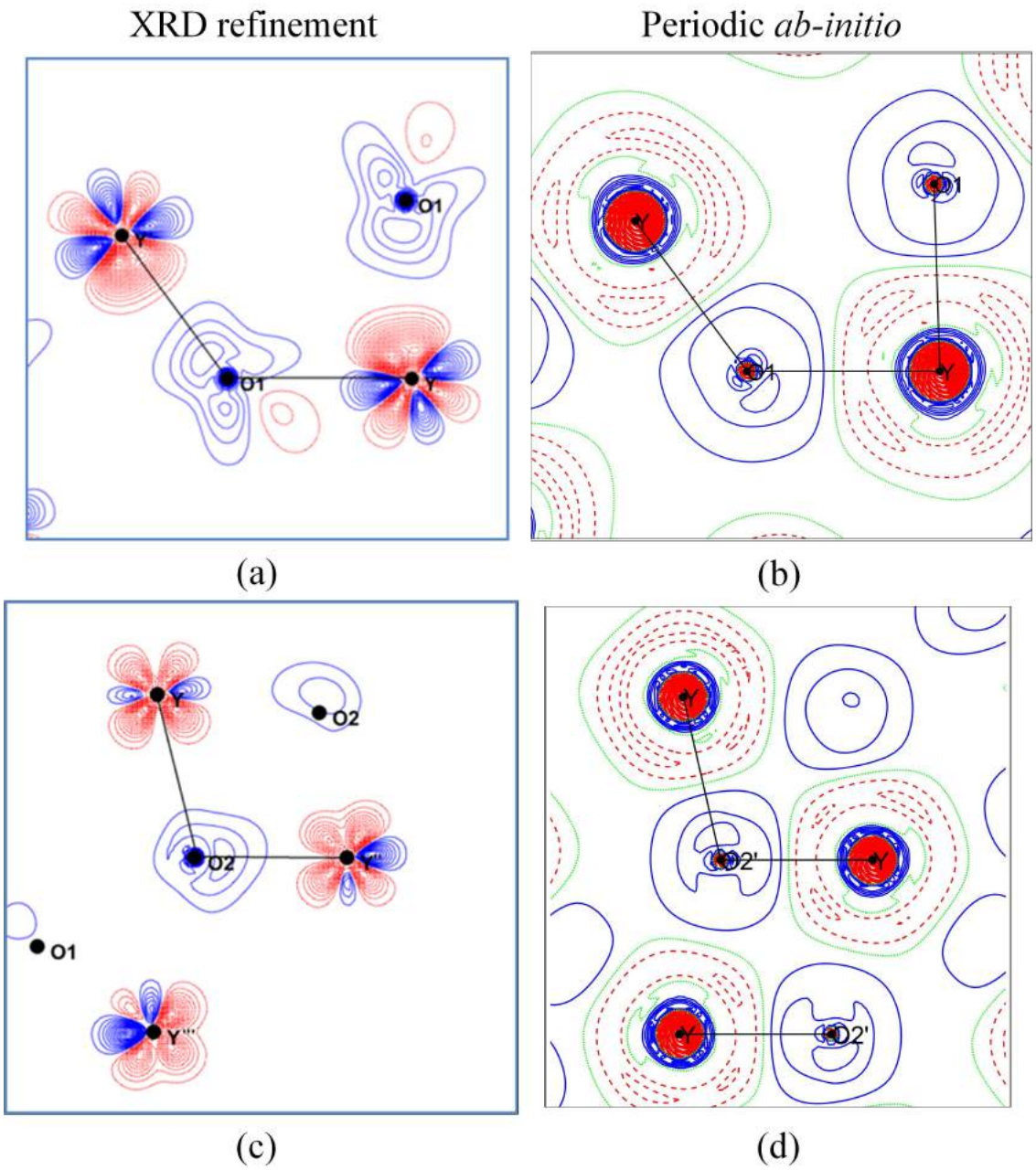

Figure 1.18: $YTiO_3$ static deformation densities around Y
Left column by XRD refinement and right column by *ab-initio*. Each row corresponds to a plane: (a,b) the Y–O_1–Y plane, (c,d) the Y–O_2–Y plane. Contour intervals of 0.1 eÅ^{-3}, positive (blue), negative (red) and neutral (green) lines.

in Table 1.8 show that their contrasts, i.e. the experimental gains and losses of electrons for atomic sites, are weaker than predicted on a theoretical basis. As the Mulliken population is known to be heavily basis set dependent [87], there is a significant difference for the Mulliken results with two different basis sets (normal and ECP basis sets). This difference is nevertheless confirmed by the Bader basin population analysis.

To compare with experimental topological analysis, properties at the charge density bond critical points are conducted (presented in Table 1.9). There is a good agreement between

Atoms	XRD		Normal basis set		ECP	
	ΔP_{val}	Bader	Mulliken	Bader	Mulliken	Bader
Y	0.90(10)	1.40	0.77	2.37	2.47	2.32
Ti	1.19(8)	1.18	1.86	2.10	2.20	2.08
O1	-0.69(4)	-0.90	-0.84	-1.49	-1.53	-1.46
O2	-0.69(3)	-0.83	-0.89	-1.50	-1.57	-1.47

Table 1.8: $YTiO_3$ charge populations
Experimental results by refinement parameter P_{val} and integration in the atomic basins, theoretical methods use standard and ECP basis sets, respectively

Bonds(x-y)	d(x—y) Å	d(x—cp) Å		d(y—cp) Å		$\nabla^2\rho(e\cdot\text{Å}^{-5})$		$\rho(e\cdot\text{Å}^{-3})$	
		EXP	CRYSTAL14	EXP	CRYSTAL14	EXP	CRYSTAL14	EXP	CRYSTAL14
O_1—Ti	2.0198(2)	0.993	1.021	1.027	0.999	9.48	10.09	0.58	0.56
O_2—Ti	2.0220(5)	0.993	1.023	1.030	1.000	8.81	10.20	0.60	0.56
O_2'—Ti	2.0816(6)	1.035	1.058	1.047	1.024	7.22	8.91	0.57	0.47
O_1—Y'	2.2372(6)	0.991	1.076	1.247	1.161	7.47	6.86	0.77	0.44
O_2—Y"	2.2817(5)	1.003	1.102	1.279	1.180	6.26	6.13	0.68	0.41
O_1—Y	2.3142(6)	1.012	1.119	1.318	1.196	5.45	5.67	0.55	0.38
O_2—Y	2.5047(5)	1.106	1.228	1.412	1.277	3.89	3.49	0.38	0.25
O_2—Y"'	2.6825(5)	1.186	1.324	1.512	1.359	2.84	2.36	0.24	0.17

Table 1.9: $YTiO_3$ topological properties at the charge density bond critical points

theoretical and experimental results. Closed shell interactions are characterized by the positive laplacian and low electron density values for all the O–Ti (Y) bonds.

Spin density refinements Polarized neutron diffraction experiments were performed at the thermal polarized neutron lifting counter diffractometer 6T2[a][88], by our collaborators at LLB [89]. As presented in Table 1.10, a single crystal ($1\times2\times3.5mm^3$) was cooled down to 5 K and embedded in a 5 T magnetic field. The $\lambda = 1.4$ Å neutrons were monochromatized by a vertically focusing graphite crystal and polarized by a super-mirror bender. The crystal structure parameters were first determined by unpolarized neutron diffraction (UND) at 40 K. The results are very close to that obtained by means of X-ray diffraction (Table A.9) with $a = 5.6844(31)$Å, $b = 7.5873(44)$Å, $c = 5.3104(47)$Å. A possible explanation for the slight difference is that both experiments are conducted at two different temperatures.

Detector	6T2
Wavelength (Å)	1.4
Temperature (K)	5
Magnetic field (T)	5
No. of reflections (unique)	286

Table 1.10: $YTiO_3$ PND experimental data

The spin density refinement is performed from PND data[b] using both previously mentioned

[a]LLB-Orphée, Saclay, France. See http://www-llb.cea.fr/fr-en/pdf/6t2-llb.pdf for more information

[b]In fact, the XMD data is used also for spin density refinement, see Appendix A.3

different methods. MEM and atomic orbital model refinement results can finally be compared to the outcome of *ab-initio* computations.

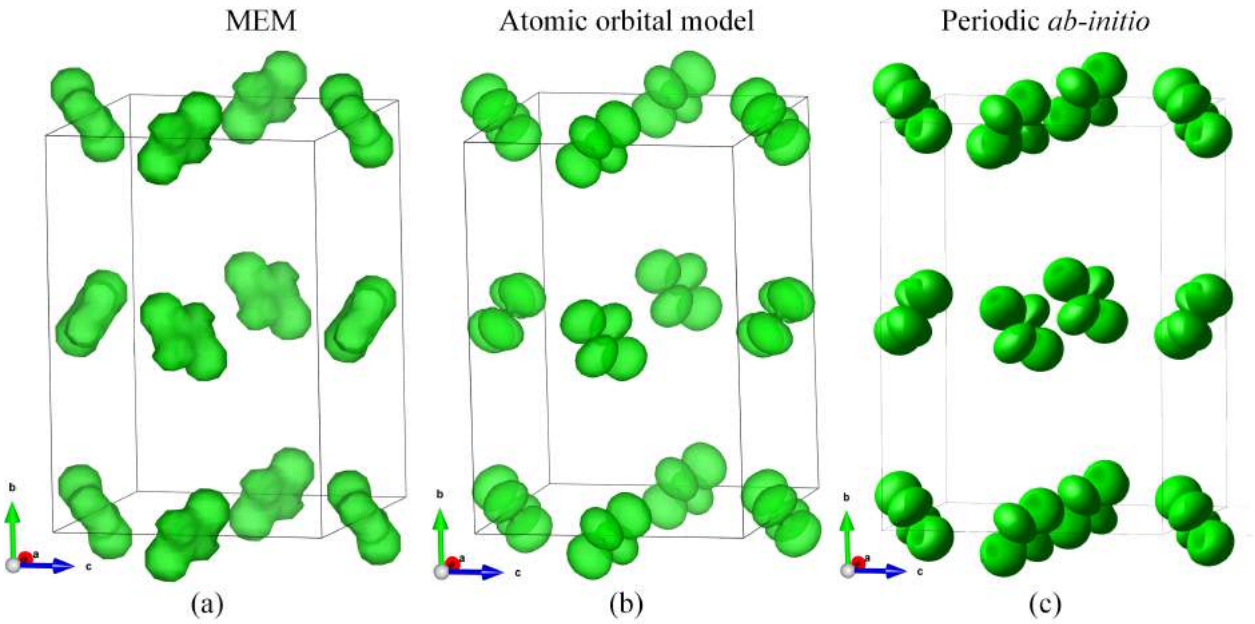

Figure 1.19: $YTiO_3$ 3D spin densities refined only from PND data
Left column by MEM, middle column by atomic orbital model and right column by *ab-initio*. Isosurface value 1.216 $\mu_B/\text{Å}^3$.

From the 3D spin density representation (Figure 1.19), the three methods show very similar resulting shapes for a 1.216 $\mu_B/\text{Å}^3$ isosurface value envelop. They are quantitatively coherent with the orbital ordering state proposed by Akimitsu [77]. On the experimental side, the Ti atomic orbital is defined using a system of local axes (Figure 1.20), where the local z direction is defined by the Ti–O_2' bond, while the local x and y directions are set approximately along the Ti–O_1 and the Ti–O_2 bonds respectively. For Akimitsu the local Ti $3d$ orbitals are defined by

$$|\psi_{1,2}\rangle = \sqrt{0.6}|yz\rangle - \sqrt{0.4}|xz\rangle \tag{1.37a}$$
$$|\psi_{3,4}\rangle = \sqrt{0.6}|yz\rangle + \sqrt{0.4}|xz\rangle \tag{1.37b}$$

In our case, a noticeable difference is that the local y and z axes are reversed for site 1 and 2 with fractional coordinates: (0.5, 0.5, 0) and (0, 0.5, 0.5) respectively (see Figure 1.20). It thus makes it possible to use a unique Ti $3d$ orbital format defining the four sites Ti orbitals.

$$|\psi_{1,2,3,4}\rangle = \sqrt{0.61(6)}|yz\rangle + \sqrt{0.39(3)}|xz\rangle \tag{1.38}$$

On the *ab-initio* computation side, orbitals are described with a global set of cartesian axes, the relative orientations of the octahedron structures are therefore different. It is thus more complicate to recover the Ti $3d$ detailed orbitals information. Another indirect method makes use of the experimental refinement method to refine theoretical local orbital populations. The procedure is similar to that employed in the usual experimental case except that the structure

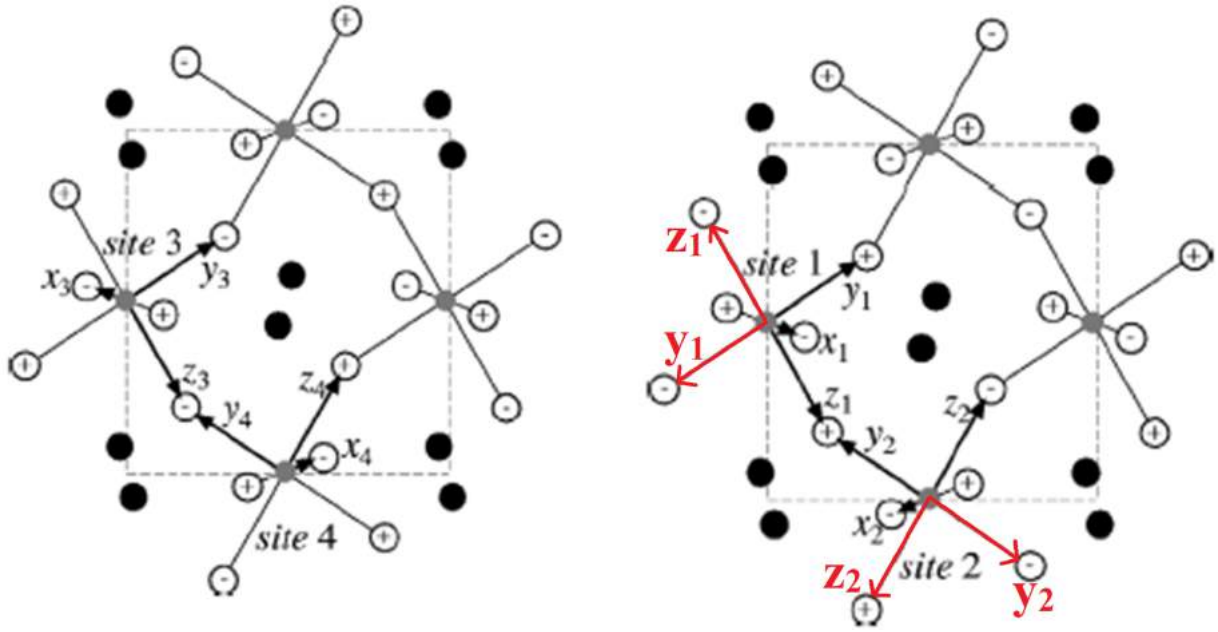

Figure 1.20: $YTiO_3$ Ti sites local axis
Black: definition used in the ref[77]. Red: axis at the site 1 and 2 from our new definition [89]. Left: fractional coordinate $y = 0$; Right: fractional coordinate $y = 0.5$.

factors are those computed from the ab-initio density[a]. From the $3d$ orbital populations in

	PND	CRYSTAL14
P(xy)	0.0	0.0
P(xz)	0.39(3)	0.46(1)
P(yz)	0.61(6)	0.54(2)
P(z^2)	0.001(1)	0.002(1)
P($x^2 - y^2$)	0.0005(7)	0.0000(1)

Table 1.11: $YTiO_3$ Ti $3d$ populations from PND and CRYSTAL14

Table 1.11, it clearly appears that the orbital of interest is almost a linear combination of $|yz\rangle$ and $|xz\rangle$. The detailed $3d$ orbital information can also be observed from the 2D spin density in the planes respectively defined by O_1–Ti–O_2, O_1–Ti–O'$_2$, and O_2–Ti–O'$_2$.

	PND refinement populations	CRYSTAL14 Bader populations
Y	-0.058(4)	0.015
Ti	1.033(4)	0.852
O_1	0.023(4)	0.036
O_2	0.006(3)	0.049

Table 1.12: $YTiO_3$ atomic spin populations
PND refinement results have been normalized to 1 electron.

Firstly, the three methods show similar qualitative results (Figure 1.21). Obviously, the

[a] refinement is conducted by I. A. Kibalin

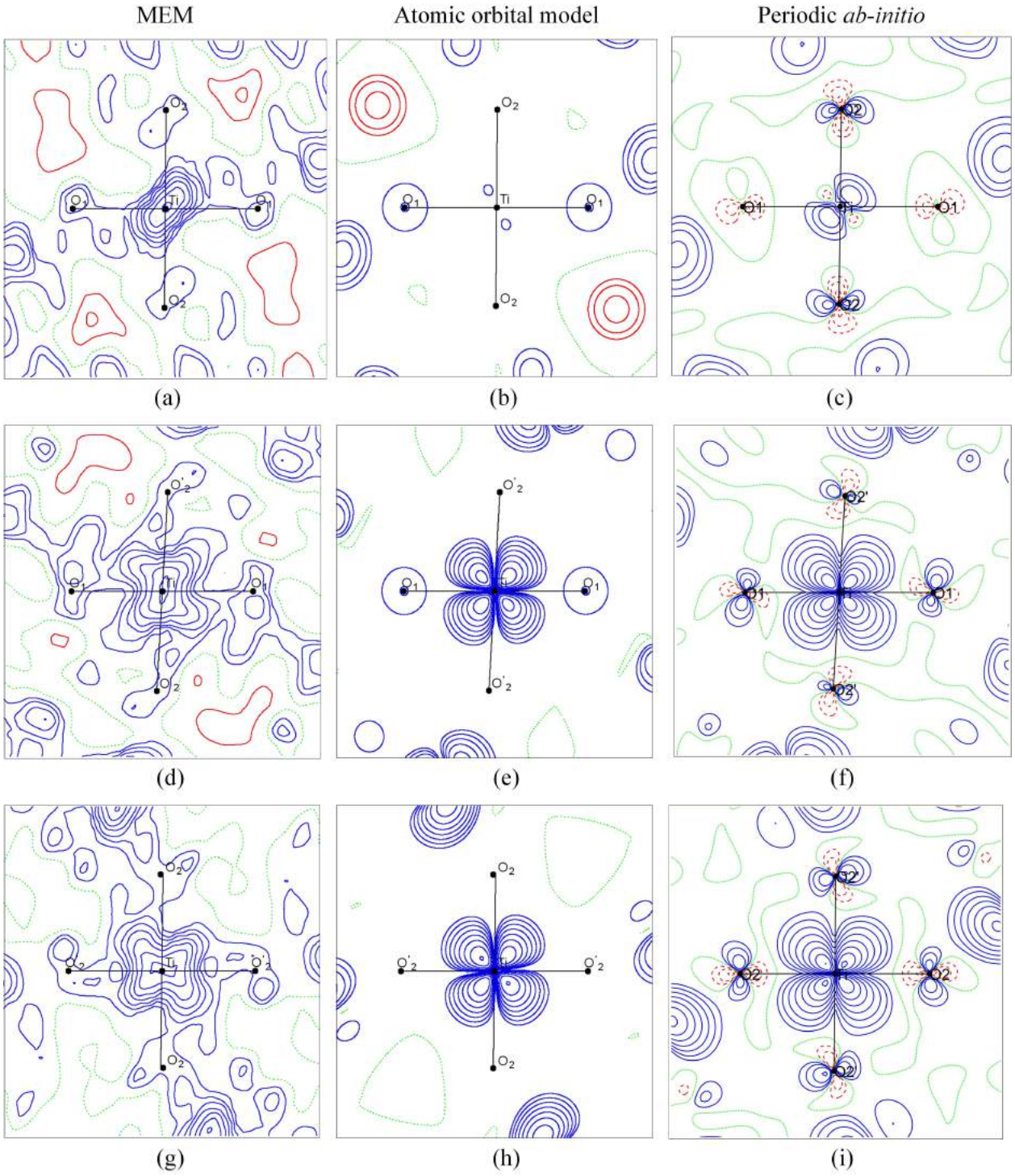

Figure 1.21: Sections of $YTiO_3$ spin density refined only from PND data
Left column by MEM, middle column by atomic orbital model and right column by *ab-initio*. Each row corresponds a plane: (a,b,c) the O_1–Ti–O_2 plane, (d,e,f) the O_1–Ti–O'$_2$ plane, (g,h,i) the O_2–Ti–O'$_2$ plane. Contour at $0.01\times2^n, (n = 0, \ldots, 12)$ μ_BÅ^{-3}, positive (blue), negative (red) and zero (green) lines.

atomic orbital model shows a more detailed electronic information and a better orbital description. Secondly, the spin distributions in O_1–Ti–O'$_2$ and O_2–Ti–O'$_2$ planes, around the Ti site mostly come from $|yz\rangle$ and $|xz\rangle$ orbitals, which agrees with the XRD observations (Figure 1.17). As no significant magnetic moment is observed on O_2 and a rather weak value on O_1, there is no contour around the O_2 or O_2' atoms. In the O_1–Ti–O'$_2$ plane, the spin density around the Ti nucleus is negligible, because of the zero $|xy\rangle$ population, while the MEM and CRYSTAL14 results show only a weak distribution. The atomic spin populations (in Table 1.12) show that the Ti atoms retain most unpaired electrons. Yttrium atoms have a weak spin value, but the signs are opposite between theoretical and experimental values. The DFT spin population on O_2 seems overestimated compared to the PND results. A possible reason which has previously been put forward is that DFT methods are not always optimal for estimating spin distributions[72, 73].

The different spin values derived from the PND refinement results, for O_1 and O_2 in $YTiO_3$ compound, are likely to be relevant for a better understanding of the spin coupling mechanism between neighbouring TiO_6 octahedra. It can be argued that the Ti $3d$ electron couples via the O $2p$, and the Ti–O_1–Ti path is more probable than that through a Ti–O_2–Ti path. Two possible reasons can be evoked: the $\measuredangle$ (Ti–O–Ti) angles between neighbouring TiO_6 octahedra is 143.58° for O_2 and 140.19° for O_1. The smaller the angle, the shorter the distance between Ti atoms, and the stronger Ti-Ti interaction. In addition, the chain Ti–O_1–Ti involves two 2.024 Å successive bonds that are symmetric with respect to O_1. For the O_2 case, the bond lengths are different (2.025 Å and 2.080 Å). As a consequence the Ti–O_1 interaction is stronger than the Ti–O_2 case.

1.4 Electron density in momentum space

Electron density in momentum space ($n(\mathbf{p})$ or $n_{mag}(\mathbf{p})$) represents the electron behaviour in a momentum representation. It is sensitive to the most diffused electrons, which in turn are allowed to have a stronger contribution in the low velocity region. These diffuse electrons play a significant role for the bond formation and delocalized magnetic properties.

1.4.1 Theoretical method

On the theoretical side, the electron momentum density (EMD) and magnetic electron momentum density (MEMD) are:

$$n(\mathbf{p}) = \Gamma(\mathbf{p}, \mathbf{p}')_{\mathbf{p}=\mathbf{p}'} \qquad \textbf{EMD} \tag{1.39a}$$

$$n_{mag}(\mathbf{p}) = \Gamma_{mag}(\mathbf{p}, \mathbf{p}')_{\mathbf{p}=\mathbf{p}'} \qquad \textbf{MEMD} \tag{1.39b}$$

The directional (magnetic) Compton profiles are projections of the (magnetic) electron momentum density (as shown in (1.3)), and can be measured by Compton scattering and magnetic Compton scattering.

Generally, the purpose of DFT methods is not the computation of momentum space properties[90, 91] and such results have been shown to have recurrent flaws. Conversely, the Hartree-Fock method often performs better[92, 93], because it aims at optimizing a wave-function model. For large system computations (such as $YTiO_3$), a HF approach turns out to bear several convergence difficulties and it was found that DFT converges much faster to a robust solution. Moreover, the momentum space properties, computed from the Fourier transform of Kohn-Sham orbitals, provide very satisfactory results[94]. Lam-Platzman [90] pointed out that the momentum density as deduced from Fourier transform of Kohn-Sham orbitals needs a correction, which takes correlation into account. Such a patch to the DFT derived Compton spectra can significantly reduce the discrepancy between theory and experiment profiles. Nevertheless, no such correction was strongly needed here and all properties are directly computed from Kohn-Sham orbitals

1.4.2 Electron momentum density reconstruction from DCPs

On the experimental side, after the measurement of several DCPs, the directions of which span the irreducible fraction of the Brillouin zone, 2-dimensional[95–97] or 3-dimensional[98–103] EMD can be reconstructed from a set of such projections. The strategy is similar to that used for image reconstructions (such as Computed Tomography scan imaging) (Figure 1.22). Sampling projections (a set of DCPs) are used to reconstruct the 3D distribution by an interpolation method in the Fourier space. The algorithm details are presented in the following part.

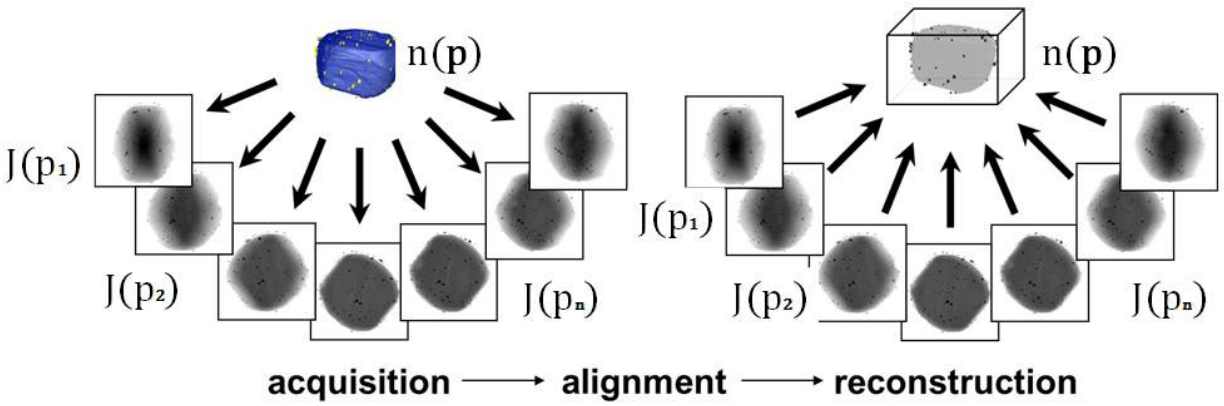

Figure 1.22: Reconstruction strategy

Reconstruction algorithms have been discussed by Hansen and Dobrzynski[4, 5]. In the most

popular method, each DCP is used to compute the corresponding directional reciprocal form factor $B(\mathbf{u},t)$ by Fourier transform as given in (1.4). The auto-correlation function $B(\mathbf{u},t)$ can also be calculated from the 1-RDM (with $\mathbf{r}=\mathbf{u}t$) according to

$$B(\mathbf{r}) = \int \Gamma(\mathbf{s},\mathbf{s}+\mathbf{r})d\mathbf{s} \tag{1.40}$$

where $\mathbf{u}$ is the unit vector collinear to the scattering vector and t is known as the "intracular position coordinate[a] " along $\mathbf{u}$. The EMD is the inverse Fourier transform of $B(\mathbf{u},t)$,

$$n(\mathbf{p}) = \frac{1}{(2\pi)^3}\int B(\mathbf{r})e^{i\mathbf{p}\cdot\mathbf{r}}d\mathbf{r} \tag{1.41}$$

This is enough to reconstruct EMD (MEMD) from a set of DCPs (DMCPs) as it now will be explained.

From a limited set of directional $B(\mathbf{u},t)$ corresponding to several non equivalent scattering directions $\mathbf{u}$, an interpolated function $B(\mathbf{r})$ can be estimated. The momentum density can thus be obtained by inverse Fourier transform (1.41). There are three steps for the reconstruction process in the general 3D case:

(1) Use a discrete Fourier transform equivalent of (1.4) in order to obtain the directional $B(\mathbf{u},t)$ from directional $J(\mathbf{u},q)$.

$$B(\mathbf{u},j\Delta r) = 2\Delta p{\sum_{k=0}^{n}}' J(\mathbf{u},k\Delta q)\cos(j\Delta r\cdot k\Delta q) \quad j=0,1,2\ldots n \tag{1.42}$$

(2) Grid values $B(j_x,j_y,j_z)$ are generated by the following interpolation scheme:

$$\begin{aligned} B(j_x,j_y,j_z) &= u_1B(\mathbf{u_1},r)+u_2B(\mathbf{u_2},r)+u_3B(\mathbf{u_3},r) \\ \text{with}\quad r &= \Delta r\sqrt{j_x^2+j_y^2+j_z^2}, \quad u_1+u_2+u_3=1 \end{aligned} \tag{1.43}$$

The interpolation weights u_1, u_2 and u_3 are proportional to the spherical areas of the triangles the vertices of which are $B(j_x,j_y,j_z)$ and two amongst ($B(\mathbf{u_1},r)$, $B(\mathbf{u_2},r)$, $B(\mathbf{u_3},r)$) (see Figure 1.23).

(3) Finally, use discrete inverse Fourier transform (1.41) to obtain the EMD, $n(\mathbf{p})$.

$$\begin{aligned} &n(k_x\Delta p,k_y\Delta p,k_z\Delta p) = \\ &(\frac{2\Delta r}{\pi})^3{\sum_{j_x=0}^{n_1}}'{\sum_{j_y=0}^{n_2}}'{\sum_{j_z=0}^{n_3}}' B(j_x,j_y,j_z)\cos(k_x\Delta p\cdot j_x\Delta r+k_y\Delta p\cdot j_y\Delta r+k_z\Delta p\cdot j_z\Delta r) \end{aligned} \tag{1.44}$$

The $\sum'$ denotes a sum with the first and last term multiplied by $\frac{1}{2}$.

[a] As a reminder the intracular vector is the relative vector between two positions of the same particle. The extracular vector is the mean vector for these two positions.

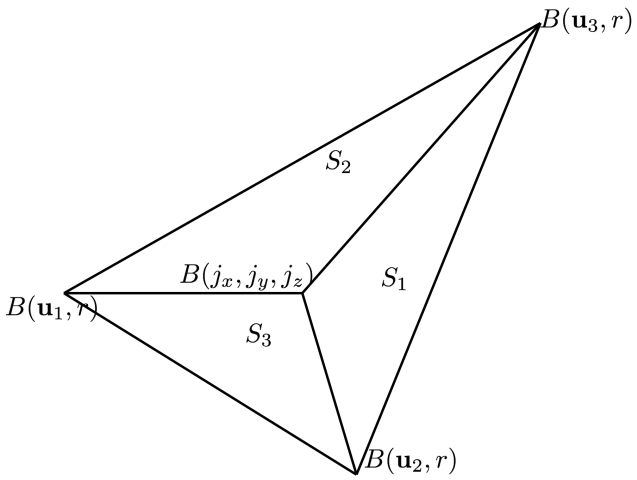

Figure 1.23: Interpolation between three points

Practically, the Fast Fourier Transform (FFT) is of course used to improve the computational efficacy. However, reconstructed results close to $\mathbf{p} = \mathbf{0}$ are inaccurate, because the weakest fluctuations are amplified by the Fourier transform. This problem will be further discussed when the propagated error analysis will have been explained.

The 2D reconstruction method to obtain the 2 dimensional (magnetic) electron momentum density (2D-(M)EMD) is a simplified case of the operation which has just been described.

The EMD anisotropies, defined as the difference between EMD, $n(\mathbf{p})$, and the isotropic (angular averaged) EMD, $n_{iso}(\mathbf{p})$, emphasize the directional differences in a given distribution:

$$n_{aniso}(\mathbf{p}) = n(\mathbf{p}) - n_{iso}(\mathbf{p}) \tag{1.45}$$

An error propagation analysis is necessary to assess the reliability of the experimental reconstruction and evaluate the significance of a discrepancy with theoretical results. Experimental error bars on DCPs are expected to impact the corresponding EMD [104] and the following method has been used to simulate error propagation in the reconstruction process.

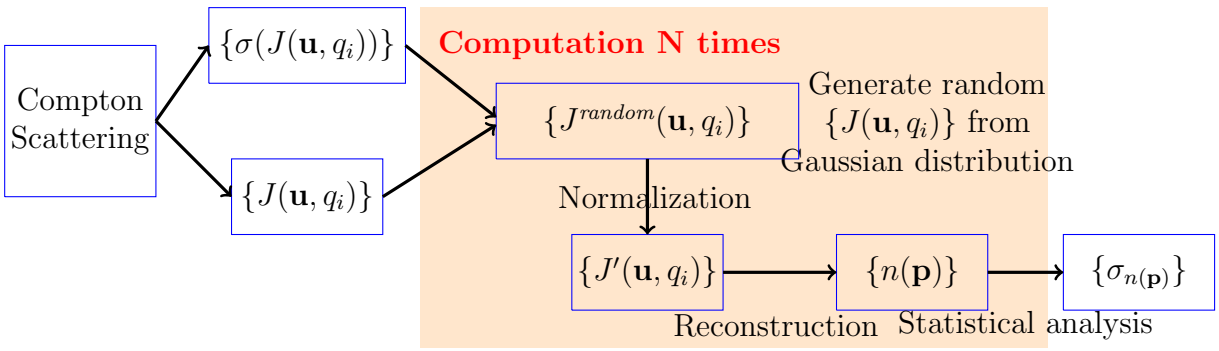

Figure 1.24: Process of statistical error propagation analysis

Each experimental DCPs $\{J(\mathbf{u}, q_i)\}$ data points and associated error bars $\{\sigma(J(\mathbf{u}, q_i))\}$ are

the respective mean value and root mean square error (RMSE) of a measurement. A Gaussian random distribution law is assumed, the mean value and standard deviation of which are set to the experimental value $\{J_{\mathrm{mag}}(\mathbf{u}, q_i)\}$ and associated error bar $\{\sigma(J_{\mathrm{mag}}(\mathbf{u}, q_i))\}$ respectively. The error propagation is thus estimated as follows (Figure 1.24):

(1) Generate random DCPs $\{J^{random}(\mathbf{u}, q_i)\}$ following such a Gaussian distribution centred on mean value.

(2) Re-normalize (to one electron) each DCP to obtain $\{J'(\mathbf{u}, q_i)\}$ for each direction.

(3) Apply the reconstruction process to obtain a new EMD $n'(\mathbf{p})$.

(4) Repeat N times steps 1 to 3, and perform a statistical analysis over the large ensemble $\{n'(\mathbf{p})\}$ to evaluate a propagated error distribution $\sigma_{n(\mathbf{p})}$ for each plane of interest.

In order to assess the quality of the error propagation estimate, a simple test can be carried out using theoretical DCPs and their corresponding EMD. For both quantities, theory-experiment agreement factors can be defined as:

$$\chi^2_{J(\mathbf{u},q)} = \frac{1}{N_{J(\mathbf{u},q)}} \sum_{\mathbf{u},q} \frac{[J^{theo}(\mathbf{u}, q) - J^{exp}(\mathbf{u}, q)]^2}{\sigma^2_{J(\mathbf{u},q)}} \tag{1.46a}$$

$$\chi^2_{n(\mathbf{p})} = \frac{1}{N_{n(\mathbf{p})}} \sum_{\mathbf{p}} \frac{[n^{theo}(\mathbf{p}) - n^{exp}(\mathbf{p})]^2}{\sigma^2_{n(\mathbf{p})}} \tag{1.46b}$$

where $N_{n(\mathbf{p})}$ and $N_{J(\mathbf{u},q)}$ are the EMD and DCPs respective numbers of data points. These expressions indicate the extent of the discrepancy relative to the experimental standard deviations. The same value for $\chi^2_{J(\mathbf{u},q)}$ and $\chi^2_{n(\mathbf{p})}$ will confirm that a reliable error reconstruction has been conducted with this process. It is well known that for an unbiased theoretical model, if the errors are distributed according to a normal law, the χ^2 estimator is expected to reach a value of 1 (if the model is parameter free). If the model does not match the expected mean value of the data points the χ^2 is greater than 1. This is why 1 is the expected asymptotic limit for an unbiased model. If χ^2 is lower than 1, it is usually the sign that either the errors do not follow a Gaussian law or that their magnitude (as a mean square deviation) has been underestimated. Obviously, if any two functions of the data are used, the respective χ^2 estimators should coincide providing that the errors have been correctly estimated.

1.4.3 Application to $YTiO_3$

DMCPs

In 2008, Tsuji and coworkers [105] first investigated the $3d$ electron orbital ordering using magnetic Compton scattering (MCS). The spin moment value was directly measured and

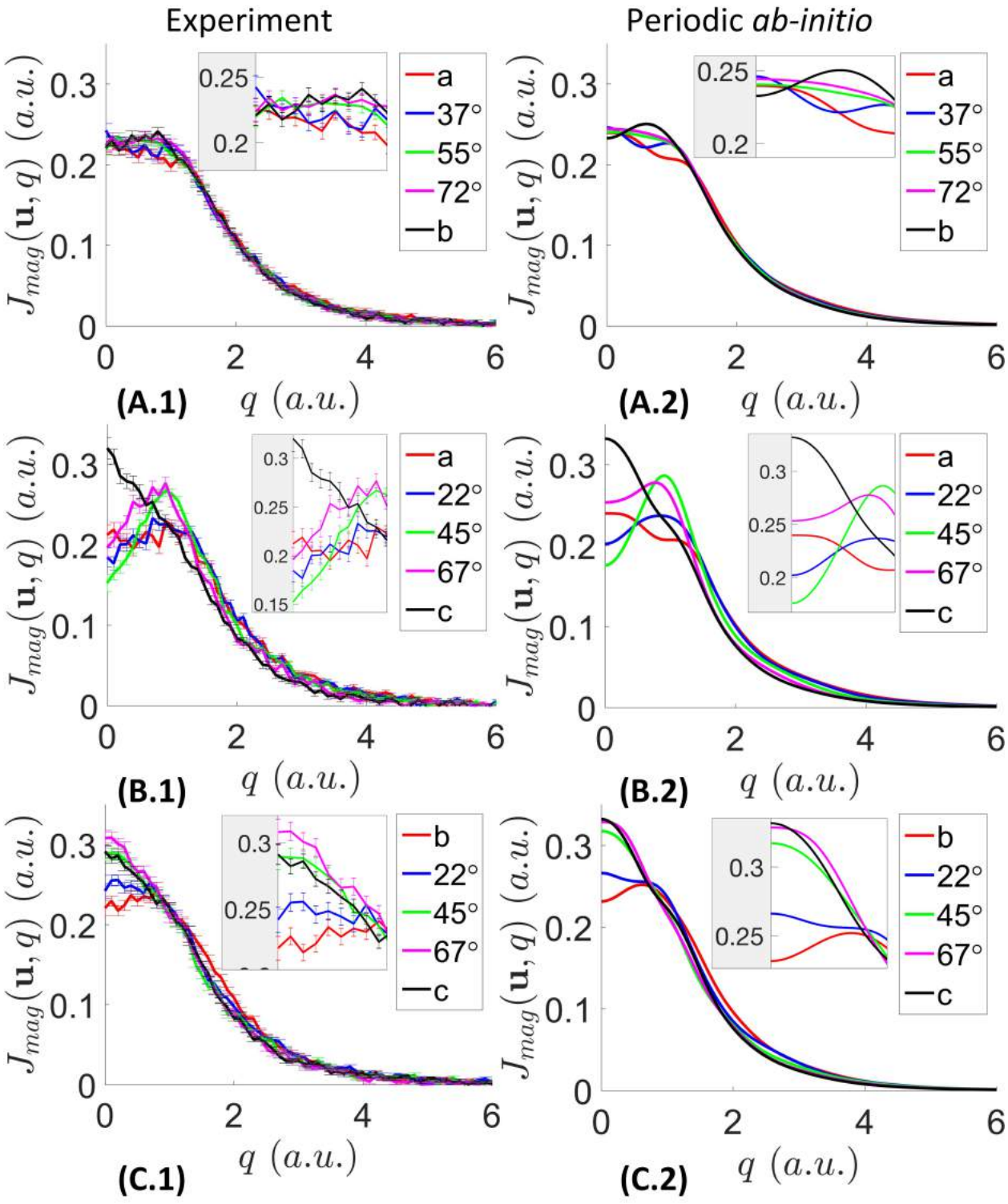

Figure 1.25: $YTiO_3$ DMCPs
Directional magnetic compton profiles (DMCP) $J_{mag}(\mathbf{u}, q)$ for $YTiO_3$ for five non equivalent directions $\mathbf{u}$ in each plane. Each row corresponds to a set of DMCPs in a given plane: (A) (ab) plane; (B) (ac) plane; (C) (bc) plane. The spectra are in atomic units (One a.u. of momentum is $\hbar/a_0 = 1.99 \times 10^{-24} kg \cdot m \cdot s^{-1}$) and normalized to one electron. Left column: experimental DMCP's data points, given with their estimated error bars. Right column: periodic *ab-initio* DMCP, convoluted by a 0.4 a.u. wide Gaussian resolution function.

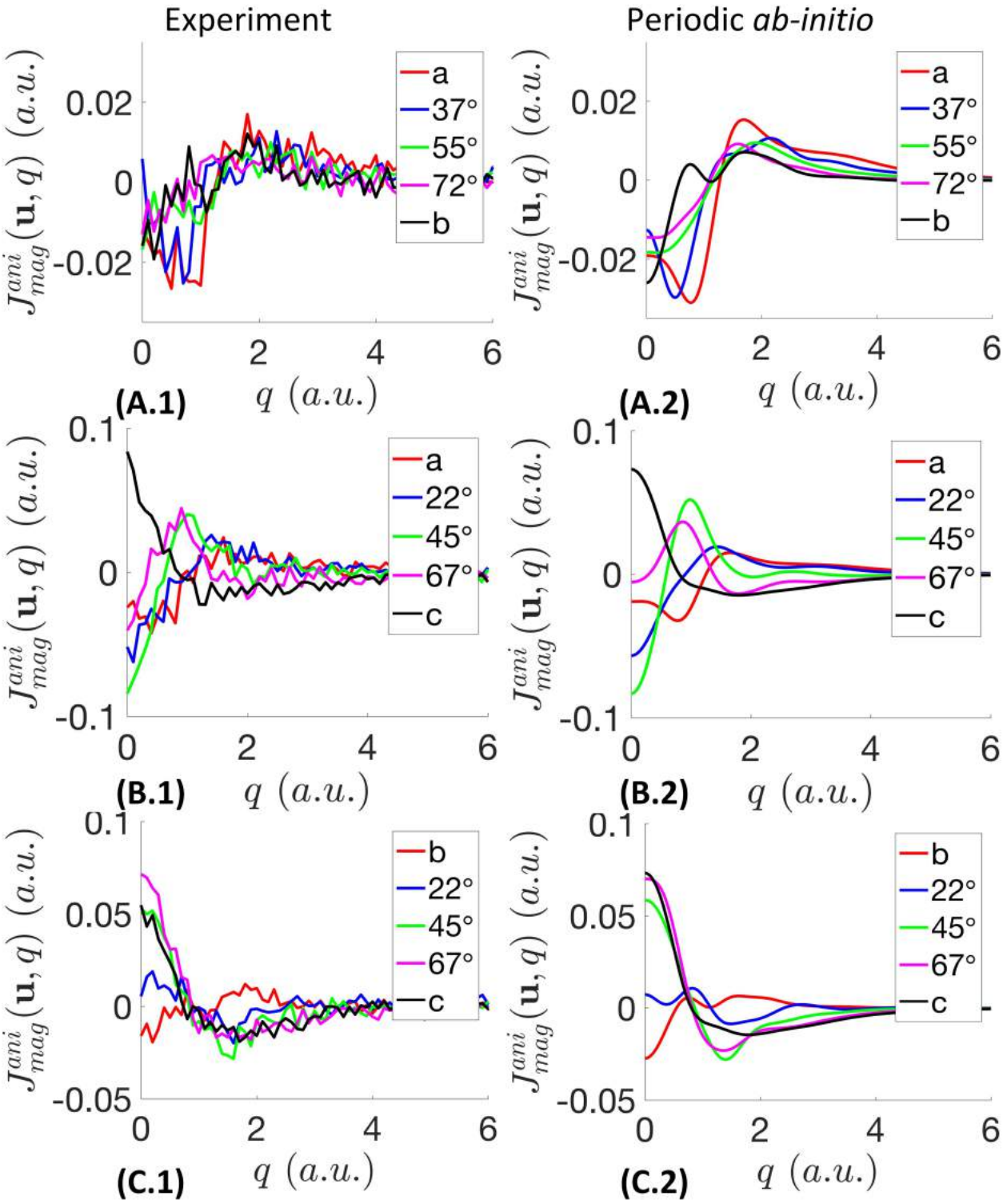

Figure 1.26: $YTiO_3$ MCP anisotropies
MCP anisotropies $J^{ani}_{mag}(\mathbf{u}, q)$ for $YTiO_3$ for five non equivalent directions $\mathbf{u}$ in each plane. Each row corresponds to a set of DMCPs in a given plane: (A) (ab) plane; (B) (ac) plane; (C) (bc) plane. The spectra are in atomic units. Left column: experimental. Right column: periodic *ab-initio* results.

the t_{2g} state role of Ti $3d$ electrons was established. Our goal is to explore the possibility to enrich information available from polarized neutron diffraction (PND) and use a momentum perspective to clarify not only the state of Ti $3d$ electrons, but also the roles of Ti–O–Ti chemical bonds in ferromagnetic coupling. The experiment was conducted using the MCS spectrometer on the high energy inelastic scattering beam-line, BL08W, at Spring8 synchrotron facility in Japan[a]. Polarized X-rays are emitted from an elliptical multipole wiggler and monochromatized to 175 keV before reaching the sample (a single crystal of size $(1 \times 2 \times 3.5)mm^3$ for $YTiO_3$). The energy of scattered X-rays at an angle of 178.5° is analyzed by a 10-segmented Ge solid state detector. During the measurement, a ±2.5 T external magnetic field was alternately applied along the measuring direction in order to reverse the sample magnetization while keeping a 10 K $\sim$ 18 K temperature range. Each DMCP was extracted as the difference between the two Compton profiles measured on the same sample magnetized in the opposite directions with a fixed photon helicity[b]. The width of the elastic peak provides an estimate of 0.4 atomic unit for the momentum resolution of the magnetic Compton spectrometer. In the present work, a total of 12 DMCPs were measured: along the principal axes, 37.7°, 55.1° and 72.5° from the axes in (ab) plane and 22.5°, 45° and 67.5° from the axes in (ac) and (bc) planes. To serve as a reference and better analyse, theoretical DMCPs have been computed at the DFT level, using the PBE0-1/3 [63] hybrid functional and optimized atomic basis sets [84, 85] as provided by CRYSTAL14 [18].

$$J(\mathbf{u}, q) = \frac{1}{2\pi} \int B(\mathbf{u}, r) e^{iq \cdot r} dr \tag{1.47a}$$

$$\begin{aligned} B(\mathbf{r})_{\mathbf{r}=\mathbf{u}r} &= \int \Gamma(\mathbf{s}, \mathbf{s}+\mathbf{r}) d\mathbf{s} \\ &= \int \sum_{\mathbf{g}}^{N_{cells}} \Phi(\mathbf{s}) P^{\mathbf{g}} \Phi^{\mathbf{g}}(\mathbf{s}+\mathbf{r}) \end{aligned} \tag{1.47b}$$

To emphasize directional specific behaviours, it is often convenient to construct anisotropic directional magnetic Compton profiles (DMCPs), defined by:

$$J^{ani}_{mag}(\mathbf{u}, q) = J_{mag}(\mathbf{u}, q) - J^{iso}_{mag}(q) \tag{1.48}$$

where $J^{iso}_{mag}(q)$ is the mean value of all the DMCPs (12 non-equivalent DMCPs for $YTiO_3$ case).

As shown in Figure 1.25[a] and Figure 1.26, theoretical and experimental DMCPs compare extremely well considering that less than 2% of the total electron population contribute to

[a]5 directions in (ac) plane were measured by SPring8 collaborators M. Ito and the data treatment was conducted by M. Brancewicz. All other Compton measurement were performed by the CRM2 and SPMS group with the help of the SPring8 team.

[b]The technique used in magnetic Compton scattering is thus the exact opposite of PND where the magnetic field is static and the neutron spin orientation is alternatively reversed

[a]Non-convoluted theoretical DMCPs are presented in Appendix Figure A.5

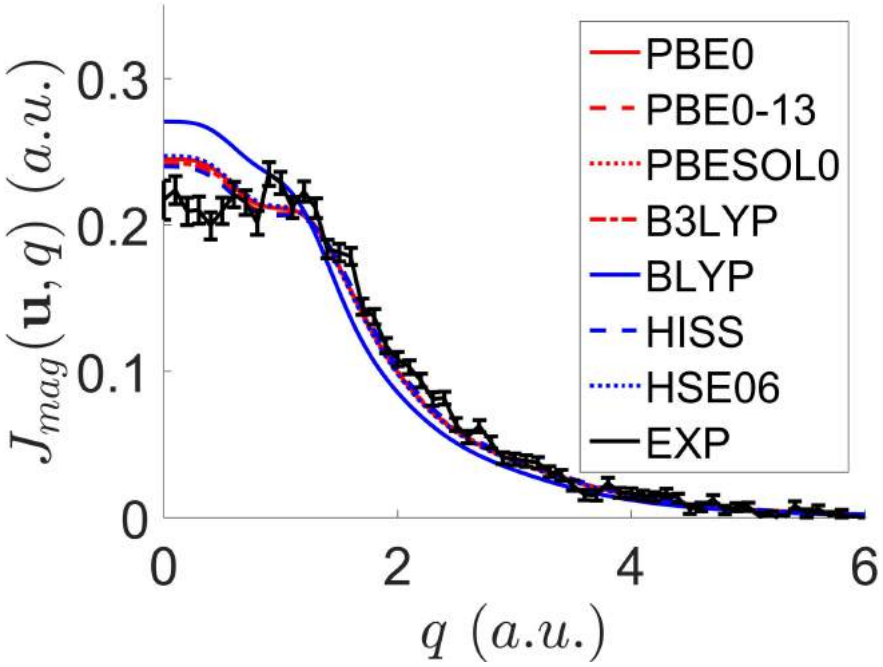

Figure 1.27: $YTiO_3$ DMCP with different functionals
$J(\mathbf{a}, q)$ with PBE0, PBE-1/3, PBESOL0, B3LYP, HISS, HSE06, BLYP functionals and experimental result.

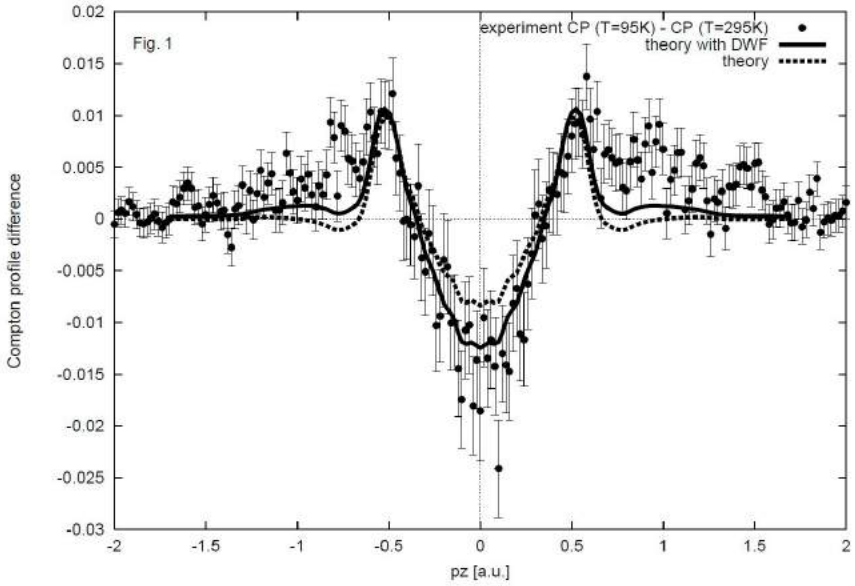

Figure 1.28: Thermal influence on Compton profile on lithium
Experimental valence Compton profile difference $J_{p_z}(T = 95K) - J_{p_z}(T = 295K)$(points with error bars) compared to the difference of calculated profiles using an empirical pseudo-potential scheme (solid line). The temperature influence is included via Debye–Waller factor and variation of the lattice constant. The dashed line shows the result of the calculation without Debye–Waller factor, where only the temperature dependence of the lattice constant is considered.

the inelastic magnetic signal. While all the electrons contribute to the background noise. As a general observation, for each direction of momentum space, the theoretical distributions are systematically more contracted than their experimental counterparts. Two

reasons have previously been put forward: a possible functional effect on electron correlations has been proposed by Huotari[106] and thermal disorder. In the $YTiO_3$ case, a range of functionals (PBE0, PBE-1/3, PBESOL0, B3LYP, HISS, HSE06, BLYP) [62, 63, 107–112] have been tested and, except for BLYP, all result in very similar DMCP (as shown in Figure 1.27). Thermal smearing at low temperature usually yields more contracted distributions in momentum space [113] (points with error bars in Figure 1.28), because the thermal effects tend to promote electrons to high energy states, yielding more low momenta electrons. It is thus legitimate to also rule out this second source of broadening. A possible source of discrepancies can be attributed to the DFT computation method itself. DFT aims at obtaining a precise electron density in position space, not a wave-function of the system and, as a consequence, no particular constraint is put on its momentum space representation.

DMCPs (Figure 1.25) reflect the unpaired electrons distribution in momentum (velocity) space. The (ab) plane exhibits the most isotropic results. This is because it contains the largest variety of chemical bonds as seen in the projection plane ((a) in Figure 1.29 where Y atoms are ignored). Conversely the (ac) plane shows greater anisotropy. In particular, the projection plane ((b) in Figure 1.29), only Ti–O_2 chemical bonds exist in the plane from vertical view, for which the contribution mostly comes from the Ti–O_2–Ti chemical bonds. The bisecting direction is the lowest at low momenta, while it increases to reach a maximum around $q = 1$ a.u.. This implies that, in position representation, the electrons are delocalized along the (ac) 45° direction, and more localized along the $\boldsymbol{a}$ or $\boldsymbol{c}$ directions. The (bc) plane exhibits a significant difference between the $\boldsymbol{b}$ and $\boldsymbol{c}$ directions ($\boldsymbol{b}$ corresponds Ti–O_1–Ti directions and $\boldsymbol{c}$ corresponds to Ti–O_2–Ti directions in the projection plane ((c) in Figure 1.29)), with lower $J_{mag}(\mathbf{u}, q)$ values at low momenta in the $\boldsymbol{b}$ direction.

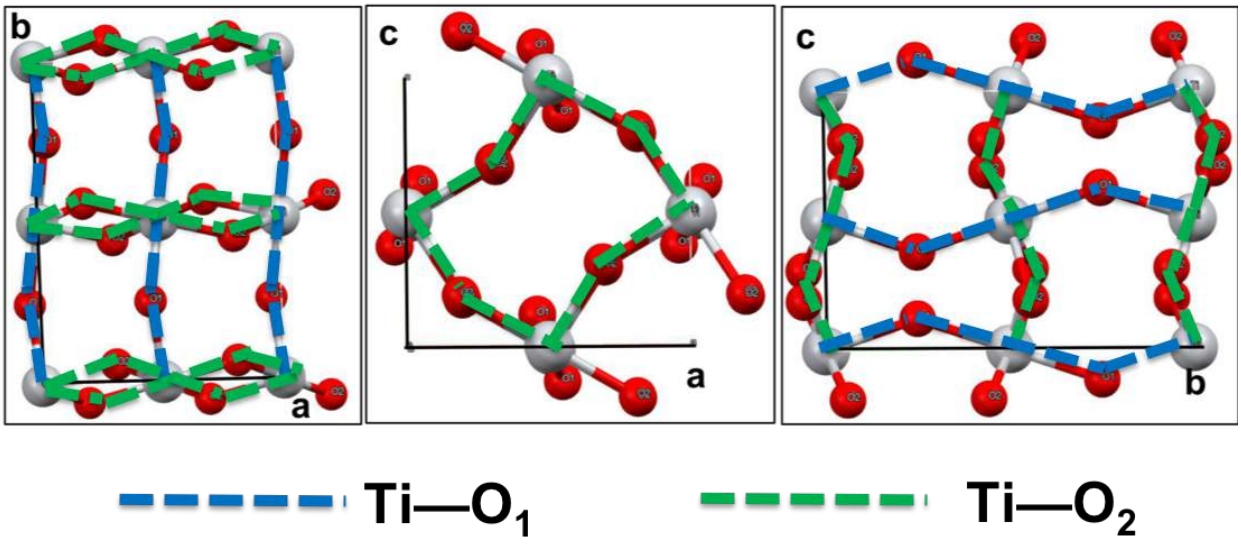

Figure 1.29: $YTiO_3$ vertical views from the three principal crystallographic axes: Ti–O_1 marked by blue and Ti–O_2 marked by green colors.

2D-MEMD

For this work, the 12 DMCPs have been used to conduct 2D-MEMD reconstructions as projections of the magnetic momentum density in each of the above mentioned planes. To avoid any interpretation bias in comparing theoretical and experimental 2D-MEMD, it was decided that both quantities should be reconstructed from their respective set of DMCPs by the same reconstruction procedure[a].

2D-MEMD anisotropies, defined as the difference between magnetic momentum density $n_{\mathrm{mag}}(\mathbf{p})$ and the angular averaged isotropic density $n^{iso}_{\mathrm{mag}}(|\mathbf{p}|)$, can be calculated in each plane.

$$n^{ani}_{mag} = n_{mag}(\mathbf{p}) - n^{iso}_{mag}(|\mathbf{p}|) \tag{1.49}$$

As expected, these anisotropies are characteristic of the unpaired electron distribution upon the chemical bond formation. If electrons on Ti sites are described in a pure crystal field perspective, the spin momentum density can be seen to bear many features of the occupied atomic orbitals (in momentum representation) [97]. Results of Figure 1.30 and Figure 1.31 (left and middle columns) confirm the analysis of Figure 1.25: the (ab) plane is the most isotropic with also the least informative features. In contrast, the (ac) plane displays a strong anisotropy, the projected momentum density is concentrated in regions ($\pm$1.3, 0) and (0, $\pm$1.05), and the momentum density favours the $\boldsymbol{a}$ direction over $\boldsymbol{c}$. A possible reason is the influence of Ti–O_1–Ti bonds, whose projections on (ac) plane are close to $\boldsymbol{c}$ direction (see (b) in Figure 1.29), the d_{xz} (local x corresponds Ti–O_1) orbital contributes more along $\boldsymbol{a}$ than $\boldsymbol{c}$ directions. Likewise, the (bc) plane exhibits a clear difference between $\boldsymbol{b}$ and $\boldsymbol{c}$ directions. From the crystal geometry, the $\boldsymbol{b}$ direction approximately corresponds to the Ti–O_1–Ti interactions, while Ti–O_2–Ti mostly lies in the (ac) planes.

Error Analysis

For each direction, 1000 sets of normalized random DMCPs, following a Gaussian distribution law, were generated. As a result, 1000 reconstructions could be carried out and saved as a statistical set for estimating the influence of experimental uncertainty of the final 2D reconstruction of spin density in momentum space.

The (ac) plane yields the highest propagated error, because original data of 5 DMCPs are measured with $\mathbf{p} \in [0, 6]$ *a.u., while the other two planes (ab) and (bc) are on a wider range* $\mathbf{p} \in [0, 12]$ *a.u.*

From Table 1.13, theory-experimental agreement factors of DMCP (1.46a) and 2D-MEMD (1.46b) are very consistent. For example, in the $p \in [-6, 6]$ range, $\chi^2_{J(\mathbf{u},q)}$ yields a value of 3.09,

[a] Even if 2D-MEMD could have been directly computed from ab-initio results.

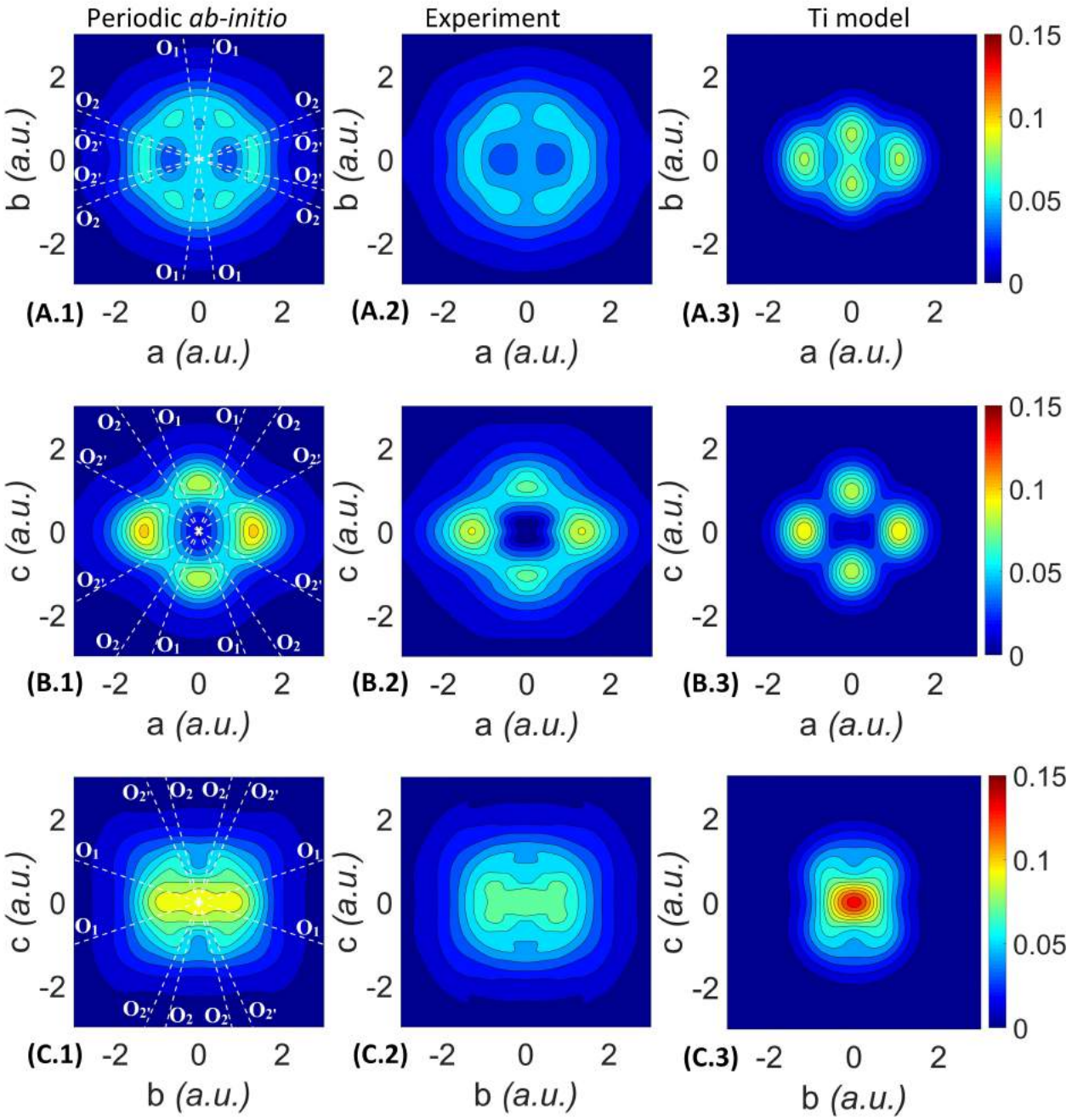

Figure 1.30: $YTiO_3$ 2D-MEMD
Reconstructed spin density in momentum space (in a.u.), projected onto the three main crystallographic planes (2D-MEMD). Each row corresponds to a plane: (A) (ab) plane; (B) (ac) plane; (C) (bc) plane. Left column: periodic *ab-initio* results using convoluted MDCPs, with white dashed lines indicating the projections of Ti–O directions in momentum space. Middle column: experimental results. Right column: the same quantity obtained by the "single Ti model" (see section 3.1). Contour at intervals of 0.01 a.u. Color bar scaling from 0 to 0.15 a.u.

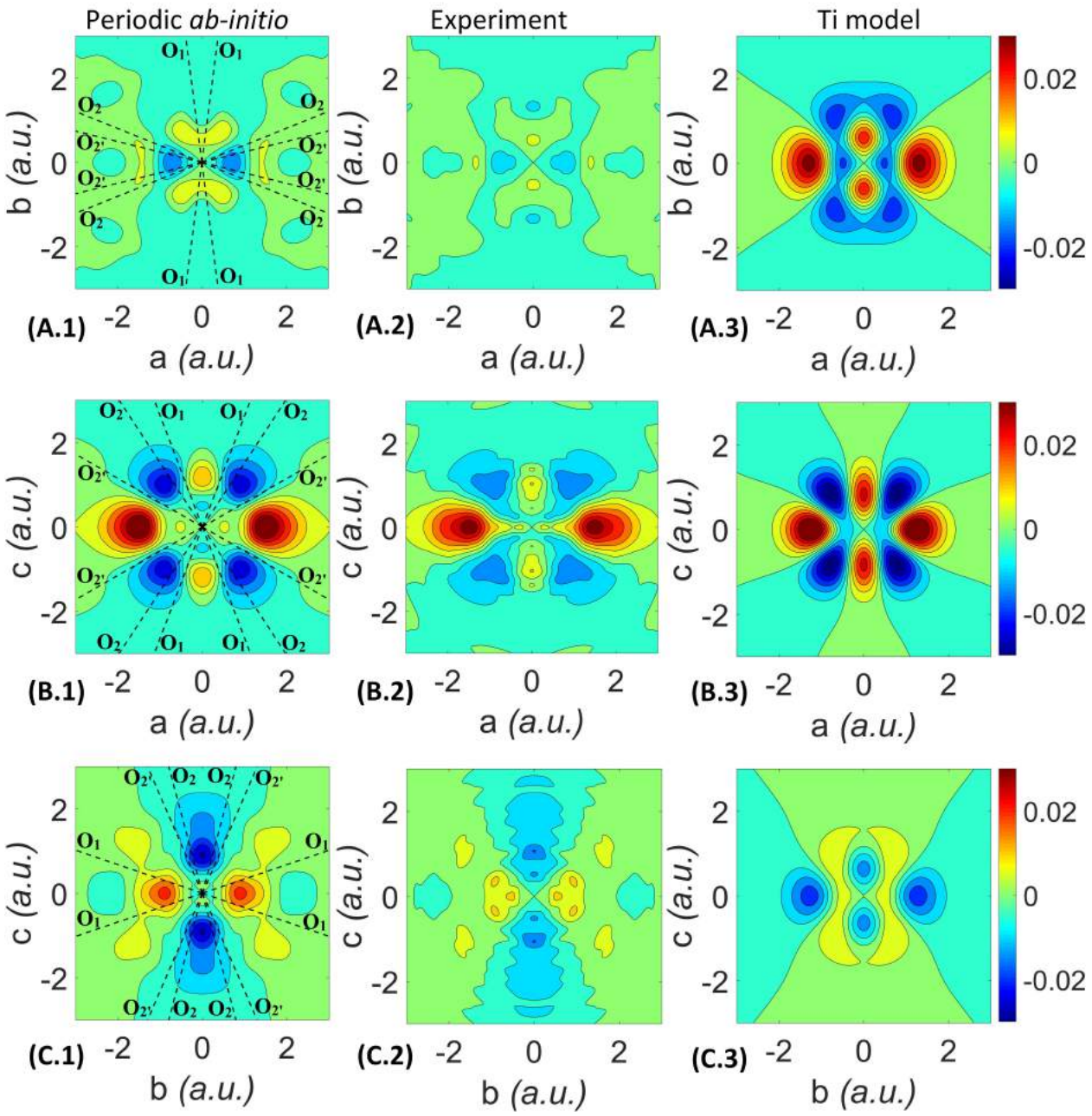

Figure 1.31: $YTiO_3$ 2D-MEMD anisotropies
Anisotropies of 2D-MEMD in each plane (in a.u.). Each row corresponds to a plane: (A) (ab) plane; (B) (ac) plane; (C) (bc) plane. Left column: periodic *ab-initio* results using convoluted MDCPs, with black dashed lines indicating the projections of Ti–O directions in momentum space. Middle column: experimental results. Right column: the same quantity obtained by the single Ti orbital model (see also section 3.1). Contour at intervals of 0.005 a.u. Color bar scaling from -0.03 to 0.03 a.u.

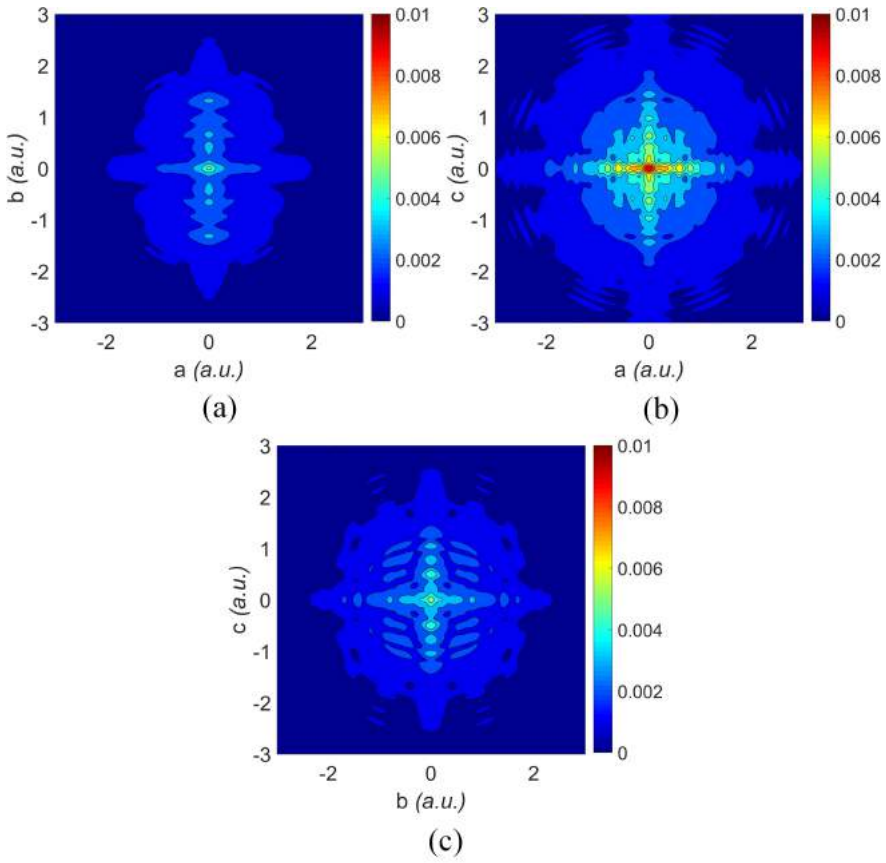

Figure 1.32: $YTiO_3$ Error Analysis
Propagation error $\sigma_{n(\mathbf{p})}$ of 2D-MEMD (in a.u.), $N_{times} = 1000$ for reconstruction in (a) plane (ab), (b) plane (ac) and (c) plane (bc), with an adapted color bar scaling from 0 to 0.01 a.u. Contour at intervals of 0.001 a.u.

	(ab)			(ac)			(bc)		
p (a.u.)	$[-2,2]$	$[-3,3]$	$[-6,6]$	$[-2,2]$	$[-3,3]$	$[-6,6]$	$[-2,2]$	$[-3,3]$	$[-6,6]$
$\chi^2_{J(\mathbf{u},q)}$	3.81	3.80	2.44	5.37	4.89	3.09	7.29	6.35	4.16
$\chi^2_{n(\mathbf{p})}$	9.86	5.65	2.05	9.20	6.28	3.02	13.82	7.66	2.89

Table 1.13: $\chi^2_{J(\mathbf{u},q)}$ and $\chi^2_{n(\mathbf{p})}$ values
For different p ranges in the three principal planes

and $\chi^2_{n(\mathbf{p})}$ amounts to 3.02. It clearly indicates that the order of magnitude for reconstructed $\sigma_{n(\mathbf{p})}$ is trustworthy. Therefore, the reconstructed error reported in Figure 1.32 shows very weak values compared with that of the experimental 2D-MEMD. As expected, the largest contribution is mostly concentrated in the $[-1,+1]$ a.u. range.

Additionally, it can be noted that a (theory-experiment agreement factor) $\chi^2 > 1$ value is an evidence that *ab-initio* DMCPs or 2D-MEMD significantly deviate from experimental results.

A refined model is thus necessary to make full use of experimental data, to identify the origin of discrepancies and reconnect with position space information.

1.5 Summary

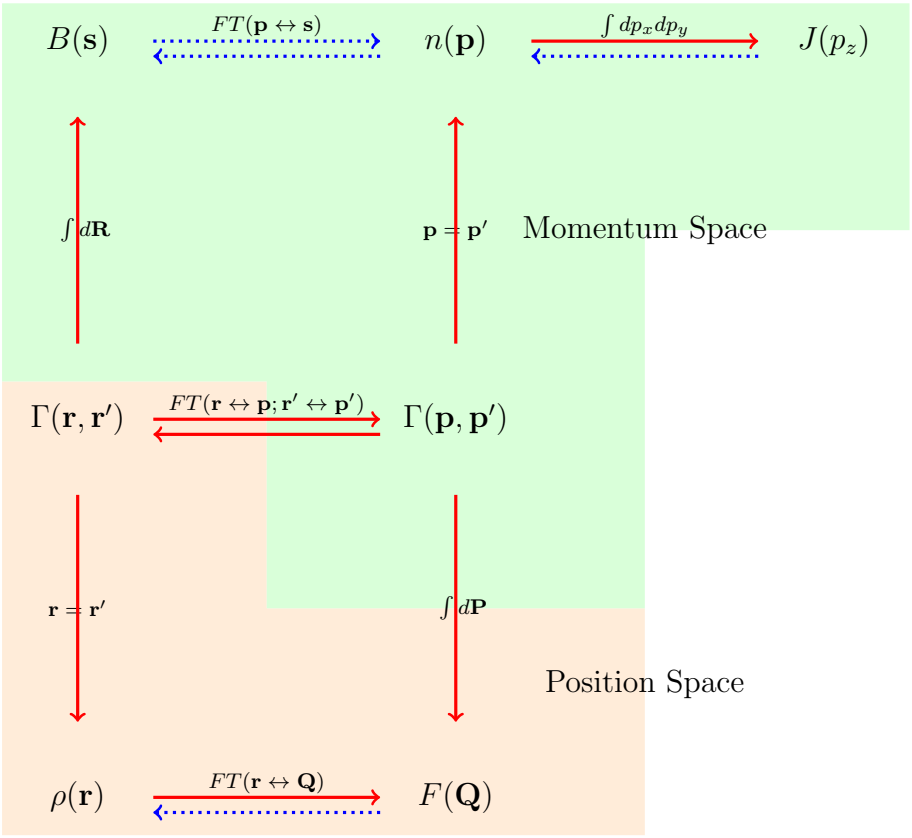

Figure 1.33: Electron representations and related variables
red arrow for theoretical directions, and blue arrow for experimental refinement.

As shown in Figure 1.33, this chapter has introduced the theoretical (red arrows) and experimental refinement models (blue dashed arrows) in position and momentum spaces respectively. On the theoretical side, 1-RDM from the *ab-initio* computation can be used to calculate electron densities and related quantities in both spaces. On the experimental side, the electron density and spin density in position space can be reconstructed separately from XRD and PND (also XMD) experimental data $F(\mathbf{Q})$ or $F_{mag}(\mathbf{Q})$, but can also be gathered in a joint refinement process of a common model using both sets of data. In momentum space, the DCPs (DMCPs) can be used to perform 3D or 2D charge and spin density reconstructions.

Several conclusions can be drawn from the applications on Nit(SMe)Ph and $YTiO_3$:.

- The spin split model gives more accurate spin density reconstruction than when the sole PND data are used. While XRD data allow a fine description of the possible pseudo-atomic orbitals, a few hundreds PND data bring the information on their respective spin occupations and polarizations. The joint refinement (XRD & PND) therefore yields a better spin density description.

- A critical comparison of experimental and theoretical approaches helps to improve models on both sides. In the Nit(SMe)Ph case, the standard DFT (molecular and periodic) cannot reproduce the asymmetry between two *NO* groups. However, a post-HF method (e.g. CASSCF), considering a more detailed electronic configuration interaction, can be used to overcome this problem.

- Electron density in momentum space can be reconstructed from the DCPs without recourse to a model but a mere interpolation scheme in direct space. The technique shows a fair reliability and, despite the bias introduced by DFT or the incoherent nature of scattering, theory and experimental momentum space densities (or DMCP) compare very well.

Separated investigations, in position (PND) and momentum (MCS) spaces, aim at describing the electron states in the solid from different points of view, and can be compared with *ab-initio* derived results, respectively. Nevertheless, it is a minimal pre-requisite that experimental data should be coherent between independent scattering techniques, even if they are relevant to different space representations. This is simply because those observable quantities originate from the same electron cloud in the same solid. From these simple comments, several questions can be raised on the basis of this work:

- Can experimental results addressing different spaces representations be cross-checked directly, without recourse to an *ab-initio* computation intermediation? For example: is there a method to cross check the (XRD *vs* CS) or (PND *vs* MCS) results.

- Can quantities, such as the 1-RDM, be directly refined from the experimental observations?

- What are the roles played by the cross-terms between different atoms in both spaces?

It is the main purpose of this work to explore each of these problems and study to what extent the gathering of different experiments can enrich our knowledge of electron behaviour. Theoretical investigations based on the 1-RDM computation and an analysis of its cross-term contribution will be presented in Chapter 2. Experimental investigations using a "single atom model" and a 1-RDM refinement model will be discussed in Chapter 3.

Chapter 2

A Cluster Construction for the Periodic 1-RDM

2.1 Introduction

Crystal property computations are implemented in many *ab-initio* programs (CRYSTAL14 in our case). However, position and momentum spaces are usually calculated separately, the quantities such as the 1-RDM or other phase space oriented functions are not included. Obviously, detailed information on the orbitals separate contributions to the above-mentioned properties[b] are not given either. This type of computation is rather complicated and CPU costly for periodic cases. A new approach reducing the computational time and adapted to calculate these quantities and analyse cross-term contribution by orbitals separation is needed for a better understanding. It is our belief that this step is necessary so that it becomes possible to construct an adequate 1-RDM model suited to a fruitful further refinement.

Using a cluster to simulate the crystal is one possible method to reduce computational cost. A periodic computation is not strictly speaking an infinite computation but a macroscopic cluster computation with boundary conditions[23]. A simulation of two-cluster computations has been conducted to simulate a two-atom type crystal (crystal with two atoms A and B per unit cell) by Gillet et al[101, 114, 115]. This method was proven to be adapted to ionic compounds (MgO, LiH etc.), and for semi-conductors (Si)[116]. Similar ideas have also been applied for large molecule computations. The Own N-layer Integrated molecular Orbital and Mechanics (ONIOM)[82] method is used for large clusters, especially for protein computations. The "Divide and Conquer" method proposed by Yang et al[117] and Cluster Partitioning Method (CPM) by Courcot (PhD thesis of Blandine Courcot 2006) are also in

[b]For example, the density matrix computation is a "developers only" function in CRYSTAL14, and there is problem for complex system (such as $YTiO_3$). There is no other phase space function, nor the orbitals separation available.

the same line of thoughts.

Building up onto these ideas, a cluster construction is now proposed to access phase space quantities and analyze cross-term contribution [43] in different spaces by means of explicit orbitals separation. Phase space distribution functions allow a convenient combination of the position and momentum spaces. Cross-term, i.e. those which involve two different atoms, are often discarded in position space, but they play an important role in momentum space. Such a systematic choice is not necessarily legitimate and needs to be further investigated. The fact is that cross-term mostly corresponds to diffuse electrons. This contribution in different spaces may help us better understand the electron behaviours and properties in the solid.

2.2 Construction and validation

2.2.1 Construction of Cluster

The idea of cluster construction is to simulate the crystal environment of each of its components. The purpose of our construction is also to help the computations of properties, after an SCF computation was performed by CRYSTAL14. Much like in the two-atom type crystal method, the unit of our model is no longer an atom, but a unit cell. A cluster of 27 cells is retrieved from the crystal. The center cell is where the property computation is performed. The 26 neighbouring cells are used to mimic the immediate crystal environment for the center cell (shown as Figure 2.1).

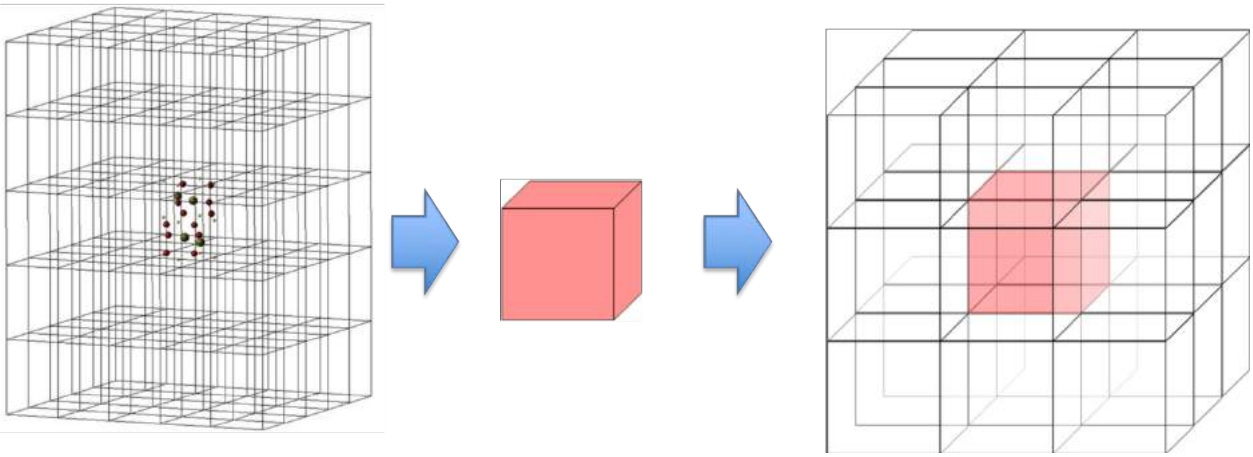

Figure 2.1: Cluster construction

This construction method can be applied to different types of crystal. When the first neighbouring cells are not enough, the cluster can be expanded to the second or third shells.

2.2.2 Data Treatment

As the cluster construction is based on CRYSTAL14 output, the wave-function information (nucleus positions, basis set and population matrices) need to be extracted and re-formatted to conduct further computations (For technical details, see Appendix A).

Cells Definition

While all cells are, by definition, identical in the crystal, each cell plays a different role in the cluster. A position G-vector is defined by three integers.

$$G = [m \quad k \quad l] \tag{2.1}$$

and the position of the cell origin can be expressed as

$$\mathbf{R_G} = m\mathbf{a} + k\mathbf{b} + l\mathbf{c} \tag{2.2}$$

where $\mathbf{a}$, $\mathbf{b}$ and $\mathbf{c}$ are the Bravais lattice vectors. Therefore $G = [0 \quad 0 \quad 0]$ is the center cell position, and the other cells in cluster correspond to m, k, $l \in \{-1, 0, 1\}$.

The G vector list is ranked by the module value of R_G, the method to obtain the G-vectors list is presented in Appendix B.1.

Basis set and population matrix

As the computation of a cluster construction is conducted in a limited portion of direct space, the orbitals information is conveniently described using GTOs. In much the same way as (A.3), the GTOs function in the $\mathbf{g}$ cell take the form

$$g_{ip}^{\mathbf{g}}(\mathbf{r}) = c(x - X_0 - R_x^{\mathbf{g}})^{l_1}(y - Y_0 - R_y^{\mathbf{g}})^{l_2}(z - Z_0 - R_z^{\mathbf{g}})^{l_3} e^{-\alpha_{ip}(\mathbf{r}-\mathbf{R}-\mathbf{R_g})^2} \tag{2.3}$$

where $\mathbf{R_g}$ is represented as (2.2), and $R_x^{\mathbf{g}}$, $R_y^{\mathbf{g}}$ and $R_z^{\mathbf{g}}$ are its 3 components. CRYSTAL14 uses a population matrix relative to AOs described just as (A.2). The N (the number of G-vectors) population matrices can be retrieved from the output file where their order follows the G-vectors list. The original population matrices assume the use of pure functions. To simplify the computation these population matrices can be transformed to new Cartesian ("impure") population matrices P_c using a standard transformation matrix M_{TM}.

More detailed information about Cartesian population matrices is presented in Appendix B.2

Population matrices for connecting functions in different cells require a specific treatment. As our cluster contains 27 cells, 27 population matrices need to be considered. They represent

the population matrices between the center cell and the 26 cells (plus the center cell with itself). Because the cells are identical in the crystal, the population matrices only depend on the relative lattice vector which makes the connection. There are five types of cell connection depending on their positions relative to the center cell[a] in the cluster (as shown in Figure 2.2). The first four types can be found in the 27 population matrices with center cell which

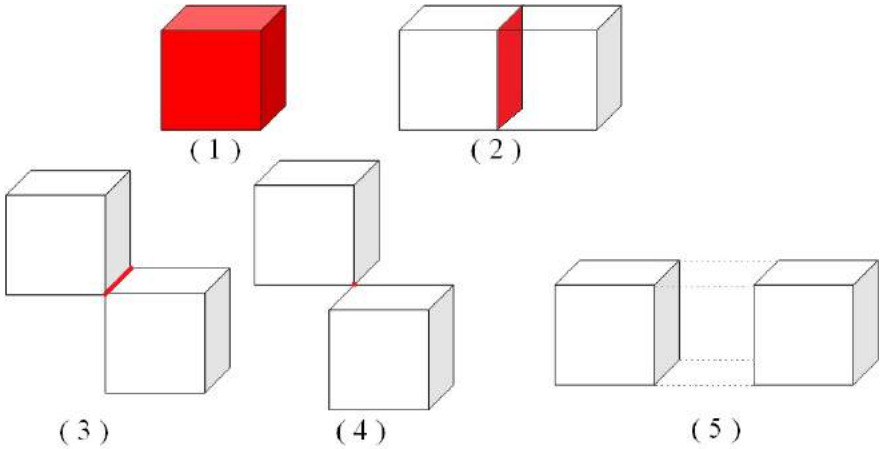

Figure 2.2: Cell relative positions in the cluster
(1) cell with itself, (2) connection by faces, (3) connection by edges, (4) connection by vertex, (5) no connection

arise from our limited cluster. The interaction between two cells is weak for the fifth type and, for our purpose, the population matrix is approximated to zero. Then, for the cluster, the population matrix P_{ij} where $i, j \in \{1, \ldots, 27\}$ can be either found in the 27 population matrices or approximated to zero (the algorithm is presented in Appendix B.3).

With the treated Cartesian basis sets and Cartesian population matrices, the 1-RDM formula for the cluster can be written,

$$\Gamma(\mathbf{r}, \mathbf{r}') = \sum_{\mathbf{g},\mathbf{l}}^{N_{cells}} \Phi^{\mathbf{g}}_{Cart}(\mathbf{r}) P_c^{gl} \Phi^{\mathbf{l}}_{Cart}(\mathbf{r}') \tag{2.4}$$

The properties based on the 1-RDM can then be calculated.

2.2.3 Validation

Before starting the computation of new properties, this approximated construction should be validated using a comparison with the CRYSTAL14 results whenever it is appropriate. The spin density in position space and Compton profiles are the closest available observables to the density matrix and are therefore chosen as useful and pertinent indicators.

[a] Obviously there are more types for the construction of a larger cluster

For the electron density in position space,

$$\begin{aligned}\rho(\mathbf{r}) &= \Gamma(\mathbf{r},\mathbf{r}) \\ &= \sum_{\mathbf{g},\mathbf{l}}^{N_{cells}} \Phi^{\mathbf{g}}_{Cart}(\mathbf{r}) P_c^{\mathbf{gl}} \Phi^{\mathbf{l}}_{Cart}(\mathbf{r})\end{aligned} \tag{2.5}$$

where $\sum_{\mathbf{g},\mathbf{l}}^{N_{cells}}$ contains a double sum so that all the crystal is accounted for. For the electron density in momentum space,

$$\begin{aligned}n(\mathbf{p}) &= \Gamma(\mathbf{p},\mathbf{p}) \\ &= \sum_{\mathbf{g}}^{N_{cells}} \Phi_{Cart}(\mathbf{p}) P_c^{\mathbf{g}} \Phi^{\mathbf{g}}_{Cart}(\mathbf{p})\end{aligned} \tag{2.6}$$

Unlike $\rho(\mathbf{r})$, where electron distribution in direct space is obtained by double sum (2.5), integration over the center cell volume yields N electrons. However, integration over momentum space of double sum results $N_{cells} \times N$ electrons, this can be solved by single sum[a]. In our model, the DCPs are calculated by Fourier transform of directional reciprocal form factors $B(\mathbf{r})$ which can be obtained by expression[b] (1.40) and:

$$\begin{aligned}B(\mathbf{r}) &= \int \Gamma(\mathbf{s},\mathbf{s}+\mathbf{r})d\mathbf{s} \\ &= \int \sum_{\mathbf{g}}^{N_{cells}} \Phi_{Cart}(\mathbf{s}) P_c^{\mathbf{g}} \Phi^{\mathbf{g}}_{Cart}(\mathbf{s}+\mathbf{r})d\mathbf{s}\end{aligned} \tag{2.9a}$$

$$J(\mathbf{u},p) = \frac{1}{2\pi}\int B(\mathbf{u},r)e^{ip\cdot r}dr \tag{2.9b}$$

where $\mathbf{u}$ in (2.9b) is the unit vector along the scattering direction, and $B(\mathbf{u},r)$ could be calculated by $B(r\mathbf{u})$ in (2.9a).

For our test system $YTiO_3$, and with $N_{cells} = 27$, the spin density in O_2–Ti–O_1 plane and DMCPs along the 3 principal crystallographic directions are considered. They are calculated

[a] For the "infinite case":

$$\begin{aligned}n_{double}(\mathbf{p}) &= \sum_{\mathbf{g},\mathbf{l}}^{N_{cells}} \Phi^{\mathbf{g}}_{Cart}(\mathbf{p}) P_c^{\mathbf{l}} \Phi^{\mathbf{g}}_{Cart}(\mathbf{p}) \\ &= \sum_{\mathbf{l}}^{N_{cells}} n_l(\mathbf{p})\end{aligned} \tag{2.7}$$

with $\int n_{double}(\mathbf{p})d\mathbf{p} = N_{cells} \times N$ and

$$n_l(\mathbf{p}) = \sum_{\mathbf{g}}^{N_{cells}} \Phi^{l}_{Cart}(\mathbf{p}) P_c^{\mathbf{lg}} \Phi^{\mathbf{g}}_{Cart}(\mathbf{p}) \tag{2.8}$$

For infinite case, all the $n_l(\mathbf{p})$ are identical and represent a unit cell contribution N. This is why single sum in (2.6) is used to calculate center cell contribution in momentum space.

[b] see Appendix B.4 for computation details

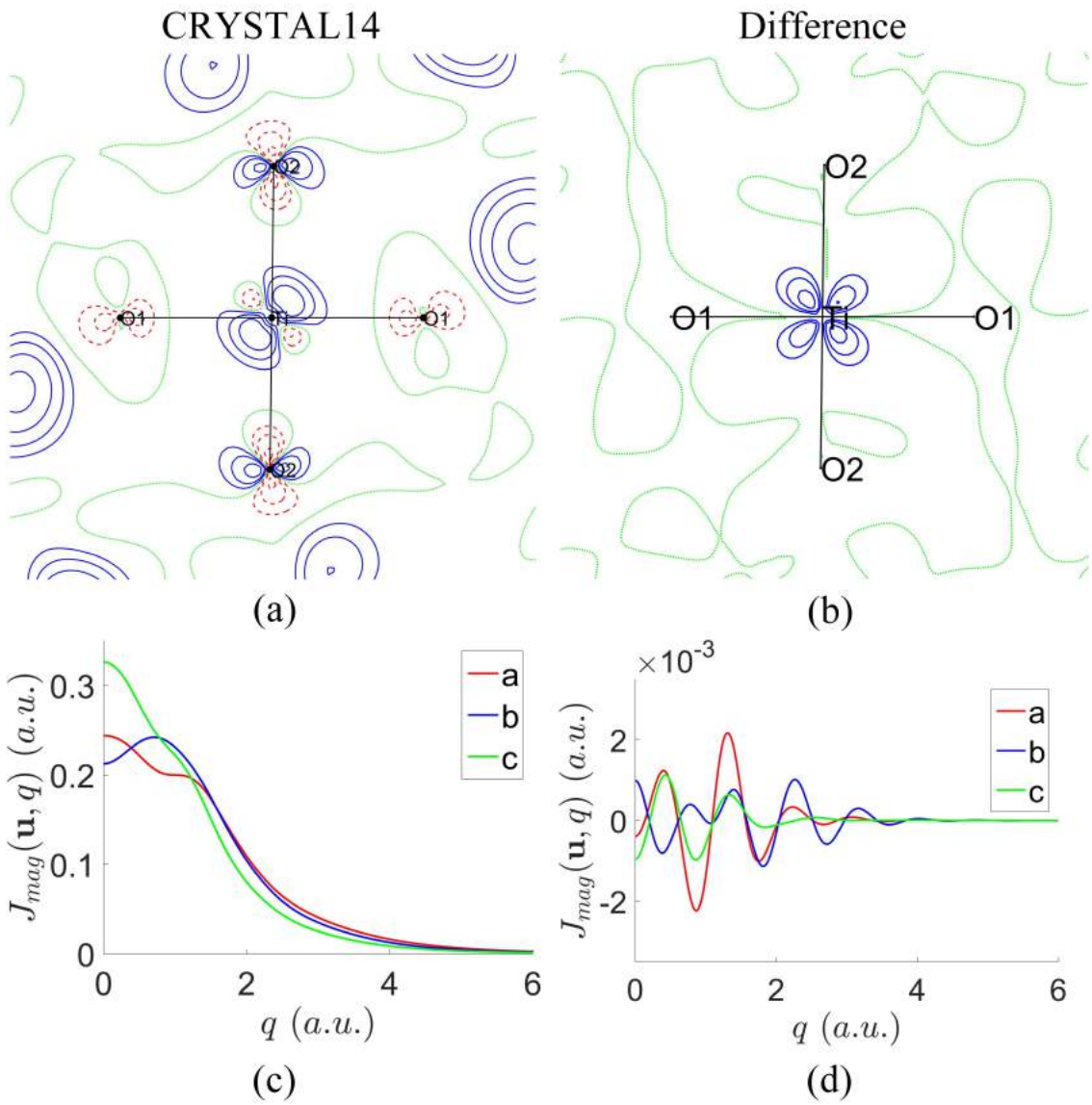

Figure 2.3: Comparison of CRYSTAL14 and cluster reconstruction properties. Validations by spin density and DMCPs
(a) spin density by Crystal 14, contours at $\pm 0.01 \times 2^n$ $(n = 0, ..., 12)$ $\mu_B \cdot \text{Å}^{-3}$ and (b) difference of spin density in O_2–Ti–O_1 plane. Contours at $\pm 0.001 \times 2^n$ $(n = 0, ..., 12)$ $\mu_B \cdot \text{Å}^{-3}$, positive: blue lines, negative: red dashed lines and neutral: green dashed; (c) DMCPs by Crystal 14 and (d) difference of DMCPs along the 3 principal crystallographic directions.

and compared with the CRYSTAL14 results as reported in Figure 2.3. In both position and momentum spaces, the differences are extremely weak: $|\delta\rho_{\text{mag}}| < 0.005$ $\mu_B \cdot \text{Å}^{-3}$ in position space and $|\delta J_{\text{mag}}| < 0.003$ $a.u$ in momentum space.

The first neighbour contributions can be clarified from a comparison of DMCPs obtained using a single cell, a 27-cell cluster and CRYSTAL14 (Figure 2.4). It turns out that a significant portion of electron contribution is missed with the center-cell-only calculation. The 27 cells cluster almost yields a result identical to that from a macroscopic cluster ($16 \times 11 \times 17$ unit cells in this case) as routinely performed by CRYSTAL14. It emphasizes

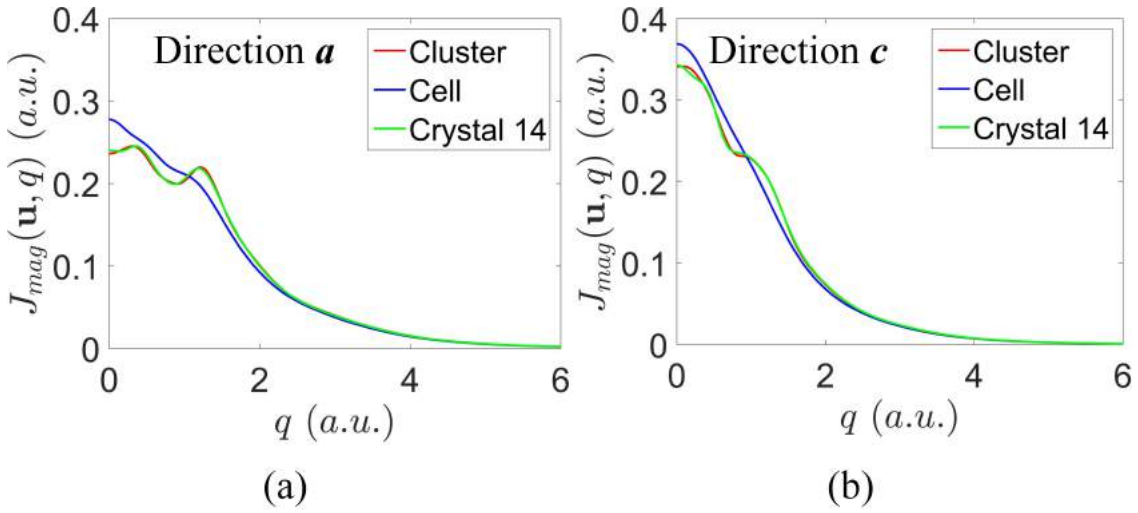

Figure 2.4: DMCPs of center cell, cluster and Crystal 14 results
(a) along direction $\boldsymbol{a}$; (b) along direction $\boldsymbol{c}$. DMCPs are normalized to one electron.

that the interaction between two atoms more distant than a minimal lattice vector can often be neglected. It thus demonstrates that considering interactions between first neighbouring cells can usually fulfill the accuracy requirements for the computation of 1-RDM derived properties.

2.3 Electron representations in phase space

Now that the pertinence of a minimal cluster construction has been validated, several electron representations in phase space can be considered. All of them are equivalent and their choice is only a matter of personal preference, depending on whether they are meant to be mostly used for chemical purpose (1-RDM), for connecting to classical physics (Wigner function [118]) or to have a direct link with scattering experiments (Moyal function [119]).

2.3.1 1-RDM

As previously mentioned, the 1-RDM $\Gamma(\mathbf{r}, \mathbf{r}')$ contains all the information at the one-electron level. If a simple path along a chemical bond is considered, the usual 6D representation space of a 1-RDM $\Gamma(r, r')$ is conveniently reduced to two dimensions[a].

As presented in *section 1.3.3*, the Ti–O–Ti chemical bonds play an important role in electron transfer and spin coupling. The chemical bond paths O_1–Ti–O_1–Ti–O_1 and O_2–Ti–O_2–Ti–O_2 are chosen to calculate and display the 1-RDM (for charge and spin, respectively) (Figure 2.5).

[a]see Appendix B.5 for computation details

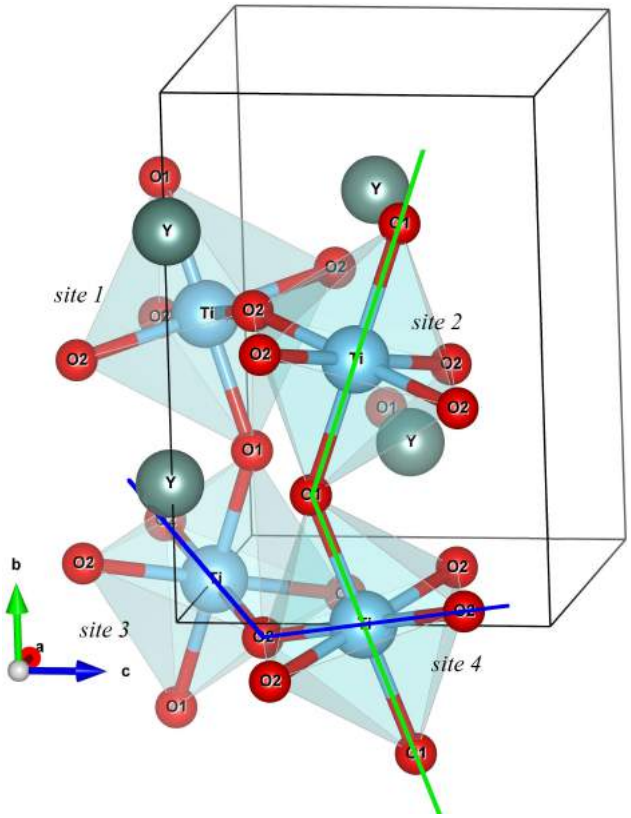

Figure 2.5: 1-RDM paths in YTiO3
green line for O_1–Ti–O_1–Ti–O_1, blue line for O_2–Ti–O_2–Ti–O_2.

In Figure 2.6, the distance for Ti–O_1 is always 2.024 Å ((a) and (b), indicated by black arrows), and there are two types of distance for Ti–O_2 (from left to right the distance for the first Ti is 2.08 Å (blue arrow), and the other is 2.025 Å (orange arrow)). The O atoms for the first Ti are noted O_2' and the second are labelled O_2. The total 1-RDM for the two paths ((a) and (c)) are qualitatively similar. Note that for (a) the regions of rectangle 1 and 2 which correspond to the interaction densities between the O_1 oxygen and its two Ti first neighbours are exactly the same. For (c) there is a small difference between regions marked by rectangles 5 and 6. However, by removing the paired electron contributions, the spin-resolved 1-RDM show a more obvious difference. Regions identified by rectangles 3 and 4 remain the same because O_1 is identical for both neighbouring Ti atoms. Conversely, rectangles 7 and 8 are quite different. It is likely that the different Ti–O_2 distances (2.025 Å for O_2 and 2.08 Å for O_2') is at the origin of this effect.

More than Ti($3d$)–O($2p$)–Ti($3d$) spin coupling, the 1-RDM results indicate difference of Ti–$O_{1,2}$–Ti chemical bonds, where Ti–O_1 yields a stronger interaction with a shorter distance (comparison of intensities in rectangles 3, 4, 7 and 8).

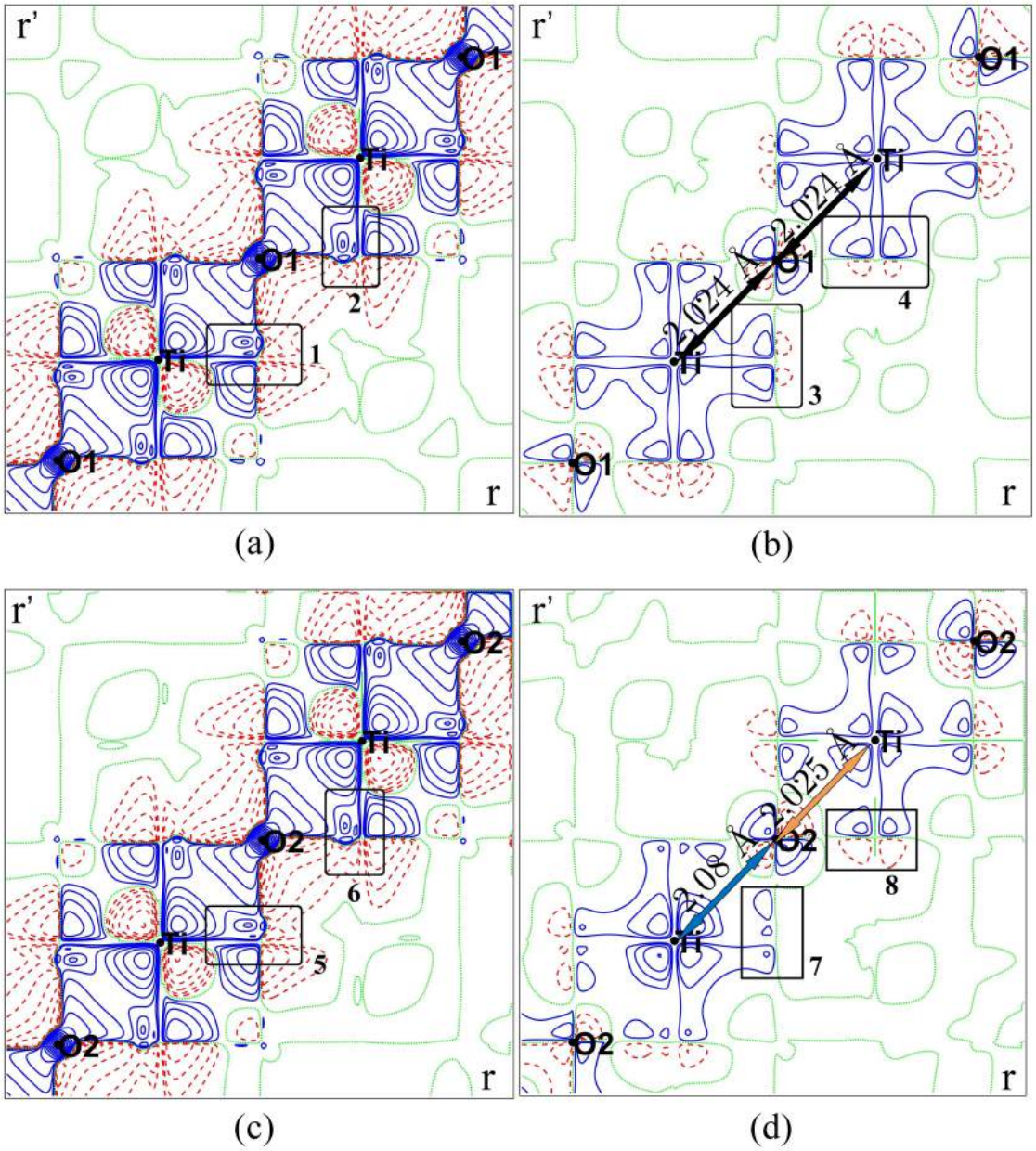

Figure 2.6: 1-RDM in $YTiO_3$
(a) total 1-RDM and (b) spin 1-RDM along O_1–Ti–O_1–Ti–O_1, (c) total 1-RDM and (d) spin 1-RDM along O_2–Ti–O_2–Ti–O_2. Contours at $\pm 0.1 \times 2^n$ $(n = 0, ..., 20)$ $e{\cdot}\text{Å}^{-3}$ for total 1-RDM and $\pm 0.01 \times 2^n$ $(n = 0, ..., 20)$ $e{\cdot}\text{Å}^{-3}$ for spin 1-RDM, positive: blue lines, negative: red dashed lines and neutral: green dashed.

2.3.2 Phase space functions

The one-electron density matrix is directly derived from the N-electron wave-function. Equivalent representations can be derived in both position and momentum spaces. It is also possible to modify its representations to adapt to different circumstances. The change of coordinate notations and Fourier transforms can yield other types of phase space functions such as Wigner [118] and Moyal [119] functions. They are respectively given by:

$$W(\mathbf{r},\mathbf{p}) = (2\pi)^{-3} \int \Gamma(\mathbf{r}-\frac{\mathbf{s}}{2},\mathbf{r}+\frac{\mathbf{s}}{2})\ e^{i\mathbf{p}\cdot\mathbf{s}} d\mathbf{s} \tag{2.10a}$$

$$A(\mathbf{s},\mathbf{k}) = \int \Gamma(\mathbf{r}-\frac{\mathbf{s}}{2},\mathbf{r}+\frac{\mathbf{s}}{2})\ e^{i\mathbf{k}\cdot\mathbf{r}} d\mathbf{r} \tag{2.10b}$$

where $\mathbf{s} = \mathbf{x}' - \mathbf{x}$ is called the intracule coordinate, and $\mathbf{r} = \frac{\mathbf{x}+\mathbf{x}'}{2}$ is the extracule coordinate[a].

The four functions $W(\mathbf{r},\mathbf{p})$, $A(\mathbf{s},\mathbf{k})$, $\Gamma(\mathbf{r}-\frac{\mathbf{s}}{2},\mathbf{r}+\frac{\mathbf{s}}{2})$ and $\Gamma(\mathbf{p}-\frac{\mathbf{k}}{2},\mathbf{p}+\frac{\mathbf{k}}{2})$ can be derived from each other by various Fourier transforms (Figure 2.7).

$$W(\mathbf{r},\mathbf{p}) = (2\pi)^{-3} \int \Gamma(\mathbf{p}-\frac{\mathbf{k}}{2},\mathbf{p}+\frac{\mathbf{k}}{2})\ e^{-i\mathbf{k}\cdot\mathbf{r}} d\mathbf{k} \tag{2.11a}$$

$$A(\mathbf{s},\mathbf{k}) = \int \Gamma(\mathbf{p}-\frac{\mathbf{k}}{2},\mathbf{p}+\frac{\mathbf{k}}{2})\ e^{-i\mathbf{p}\cdot\mathbf{s}} d\mathbf{p} \tag{2.11b}$$

$$A(\mathbf{s},\mathbf{k}) = \int\int W(\mathbf{r},\mathbf{p})\ e^{i(\mathbf{k}\cdot\mathbf{r}-\mathbf{s}\cdot\mathbf{p})} d\mathbf{r}d\mathbf{p} \tag{2.11c}$$

2.3.3 Wigner function

$W(\mathbf{r},\mathbf{p})$ is a function combining position $\mathbf{r}$ and momentum $\mathbf{p}$ variables directly. Integration of Wigner function over position or momentum variables yields the N-normalized momentum or position electron density, respectively.

$$\int W(\mathbf{r},\mathbf{p})d\mathbf{r} = \rho(\mathbf{r}) \tag{2.12a}$$

$$\int W(\mathbf{r},\mathbf{p})d\mathbf{p} = n(\mathbf{p}) \tag{2.12b}$$

$$\int\int W(\mathbf{r},\mathbf{p})d\mathbf{r}d\mathbf{p} = N \tag{2.12c}$$

The Wigner function links to the electron densities in one space by integration over the other space. Such a function is thus a pseudo-density function in phase space since it respects the Heisenberg uncertainty principle, that it is impossible to measure accurate electron coordinates both in position and momentum spaces simultaneously.

[a] Here variables do not account for the spin.

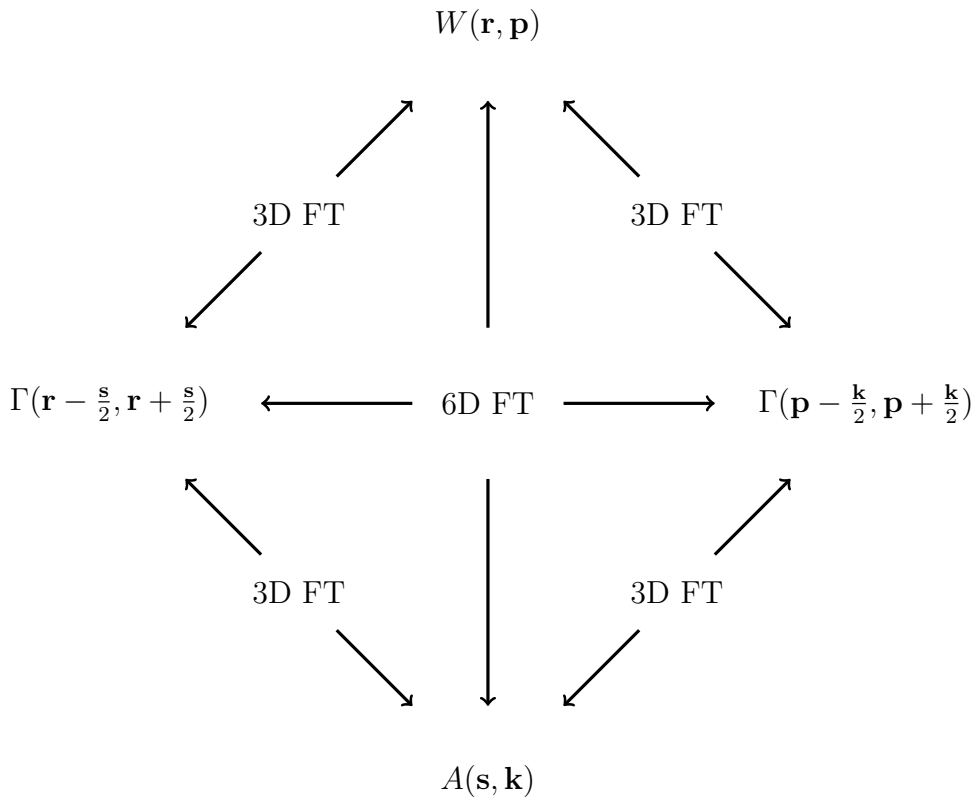

Figure 2.7: Relationship between phase space functions

The Wigner function value is always real but can be negative [120]. This function connects not only position and momentum spaces, but also the classical and quantum physics. However, because of the complexity of associating directly the Wigner function to experimental observations, the difficulties of using such a description to connect both position and momentum space is quite a challenge.

On the theoretical side, the Wigner function is calculated as:

$$\begin{aligned} W(\mathbf{x},\mathbf{p}) &= \sum_{n,m} P_{n,m} \int \varphi_n(\mathbf{x}+\frac{\mathbf{s}}{2})\varphi_m(\mathbf{x}-\frac{\mathbf{s}}{2})e^{i\mathbf{ps}}d\mathbf{s} \\ &= \sum_{n,m} P_{n,m} W_{n,m}(\mathbf{x},\mathbf{p}) \end{aligned} \tag{2.13}$$

where $W_{n,m}(\mathbf{x},\mathbf{p})$ takes a simple expression

$$W_{n,m}(\mathbf{x},\mathbf{p}) = \int \varphi_n(\mathbf{x}+\frac{\mathbf{s}}{2})\varphi_m(\mathbf{x}-\frac{\mathbf{s}}{2})e^{i\mathbf{ps}}d\mathbf{s} \tag{2.14}$$

and φ is the expression of atomic orbital functions, possibly described by linear combination of GTOs.

For molecular computations, the $P_{n,m}$ are again the global population matrix elements. The Wigner function could be calculated as presented in Appendix B.6, but for the periodic case (as well as our minimal cluster construction), the interaction terms between cells for position and momentum parts is another computational difficulty.

2.3.4 Moyal function

Unlike Wigner, Moyal function is more directly connected to experimental quantities. It bridges two experimental observations directly, diffraction of X-rays (or polarized neutrons), via the structure factors $F(\mathbf{k})$, and incoherent inelastic scattering, via the reciprocal structure factors $B(\mathbf{s})$:

$$A(\mathbf{0},\mathbf{k}) = \int \Gamma(\mathbf{p}-\frac{\mathbf{k}}{2},\mathbf{p}+\frac{\mathbf{k}}{2})d\mathbf{p} = F(\mathbf{k}) \tag{2.15a}$$

$$A(\mathbf{s},\mathbf{0}) = \int \Gamma(\mathbf{r}-\frac{\mathbf{s}}{2},\mathbf{r}+\frac{\mathbf{s}}{2})d\mathbf{r} = B(\mathbf{s}) \tag{2.15b}$$

$$A(\mathbf{0},\mathbf{0}) = F(\mathbf{0}) = B(\mathbf{0}) = N \tag{2.15c}$$

As presented previously, $F(\mathbf{k})$ and $B(\mathbf{s})$ are linked to the electron densities in the complementary two spaces, respectively. The Moyal function can also be used for interpreting the electronic structure as explained in the simple H and H_2 cases in Ref [121]. For an isolated atom H,

$$A_H(\mathbf{s},\mathbf{k}) = \int \widetilde{\psi}_H(\mathbf{p}-\frac{\mathbf{k}}{2})\widetilde{\psi}^*_H(\mathbf{p}+\frac{\mathbf{k}}{2})\, e^{-i\mathbf{s}\cdot\mathbf{p}}d\mathbf{p} \tag{2.16}$$

where ψ_H and $\widetilde{\psi}_H$ are the ground-state wave function in position and momentum representations respectively. The isolated atom H is spherical so that the Moyal function can thus conveniently be limited to a three dimension representation using $|\mathbf{s}|$, $|\mathbf{k}|$ and the angle between the two vectors. By using the symmetric wave function[122]:

$$A_H(\mathbf{s},\mathbf{k}) \approx 2(2\pi)^{3/2}\psi_H(s)\widetilde{\psi}_H(k)\cos(\mathbf{s}\cdot\mathbf{k}/2) \tag{2.17}$$

For a large system, the Moyal function can take a much more complicated form.

Another point is that the Moyal function $A(\mathbf{s},\mathbf{k})$ with $\mathbf{k} = \mathbf{Q}_{hkl}$ is directly accessible via Compton scattering at Bragg position as put forward by Schülke[123–125].

$$J(\mathbf{u},q,\mathbf{k}) = \int \Gamma(\mathbf{p}+\mathbf{k},\mathbf{p})\delta(\mathbf{u}\cdot\mathbf{p}-q)d\mathbf{p} \tag{2.18}$$

However, it is still difficult to separate the non-diagonal $\Gamma(\mathbf{p}+\mathbf{k},\mathbf{p})$ and diagonal $\Gamma(\mathbf{p},\mathbf{p})$ contributions on a pure experimental basis. Compared to (1.3), $J(\mathbf{u},q,\mathbf{k})$ is the integral of momentum represented density matrix off-diagonal elements by a shifted reciprocal lattice vector $\mathbf{k}$:

$$B(\mathbf{u},s,\mathbf{k}) = \int e^{-is\cdot q}J(\mathbf{u},q,\mathbf{k})dq \tag{2.19a}$$

$$B(\mathbf{u},s,\mathbf{k}) = e^{-i\mathbf{s}\cdot\mathbf{k}/2}A(\mathbf{s},-\mathbf{k}) \tag{2.19b}$$

where $\mathbf{s} = \mathbf{u}\cdot s$, and $\mathbf{u}$ is the unit vector collinear to the scattering vector.

Directional Moyal function at Bragg position $\mathbf{k}$ can be defined to access from DCPs at Bragg position:

$$A(\mathbf{u}, s, -\mathbf{k}) = e^{i\mathbf{s}\cdot\mathbf{k}/2} \int e^{-is\cdot q} J(\mathbf{u}, q, \mathbf{k}) dq \tag{2.20}$$

Once more, on the theoretical side, the Moyal function is calculated as:

$$\begin{aligned} A(\mathbf{s}, \mathbf{k}) &= \sum_{n,m} P_{n,m} \int \varphi_n(\mathbf{r} + \frac{\mathbf{s}}{2}) \varphi_m(\mathbf{r} - \frac{\mathbf{s}}{2}) e^{i\mathbf{kr}} d\mathbf{r} \\ &= \sum_{n,m} P_{n,m} A_{n,m}(\mathbf{s}, \mathbf{k}) \end{aligned} \tag{2.21}$$

where $A_{n,m}(\mathbf{s}, \mathbf{k})$ takes a simple expression

$$A_{n,m}(\mathbf{s}, \mathbf{k}) = \int \varphi_n(\mathbf{r} + \frac{\mathbf{s}}{2}) \varphi_m(\mathbf{r} - \frac{\mathbf{s}}{2}) e^{i\mathbf{kr}} d\mathbf{r} \tag{2.22}$$

The theoretical computation of $A_{n,m}(\mathbf{s}, \mathbf{k})$ can be readily obtained using GTOs (see Appendix B.7). For molecular computations, it is found that:

$$A(\mathbf{s}, \mathbf{k}) = \sum_{n,m} P_{n,m} A_{n,m}(\mathbf{s}, \mathbf{k}) \tag{2.23}$$

where $P_{n,m}$ is the global population matrix and, for periodic or our limited cluster model computations

$$A(\mathbf{s}, \mathbf{k}) = \sum_{n,m} \sum_{\mathbf{g}}^{N} P^{\mathbf{g}}_{n,m} A^{\mathbf{g}}_{n,m}(\mathbf{s}, \mathbf{k}) \tag{2.24}$$

where $\mathbf{g}$ indicates the cell order, N is the number of cells; infinite for a perfect crystal and 27 for the limited cluster construction.

In the present work, where the unpaired electrons are the focus of interest, the magnetic Moyal function can be calculated by means of the cluster construction. To display the Moyal function, 2D sections are defined by two vectors in 6-dimensional space $(\mathbf{s}, \mathbf{k})$ with the origin $(\mathbf{0}, \mathbf{0})$. To better emphasize the connection to DMCPs at Bragg positions (2.20), the 1D Moyal function can be represented with an intracular position vector $\mathbf{s}$, and a Bragg reciprocal vector $\mathbf{k} = \mathbf{Q}_{hkl}$.

The 2D magnetic Moyal function for $YTiO_3$ in planes $(\mathbf{s}_x\ \mathbf{k}_x)$, $(\mathbf{s}_y\ \mathbf{k}_y)$ and $(\mathbf{s}_y\ \mathbf{k}_y)$ are presented in the Figure 2.8. The 2D magnetic Moyal function is a section, with the other vectors set to zeros. To validate unpaired electrons number in primitive cell, the value at the origin should be 4 (between 0.01×2^8 and 0.01×2^9 in the figures). Which can be observed in the 1D magnetic Moyal function at Bragg positions (blue lines $A(\mathbf{0})$ at 000 is exactly 4).

From Figure 2.8, it can be seen that the 2D Moyal function on the three planes exhibit different behaviours. As $\mathbf{s}$ is the intracule coordinate and $\mathbf{k}$ is a vector in reciprocal space,

the connection with chemical properties can be difficult to extract. The 1D case is probably a better choice. $YTiO_3$ is a centrosymmetric orthorhombic crystal, and

$$\mathbf{a}^* = [0.58434, 0, 0] \quad \mathbf{b}^* = [0, 0.43695, 0] \quad \mathbf{c}^* = [0, 0, 0.62323] \quad (a.u.)$$

For the space group $Pnma$, the Miller indices with conditions:

$$\begin{aligned} 0kl: &\quad k + l = 2n \\ hk0: &\quad h = 2n \\ h00: &\quad h = 2n \\ 0k0: &\quad k = 2n \\ 00l: &\quad l = 2n \end{aligned}$$

are the available reflections[71], even indices cases are presented in the (d,e,f) of Figure 2.8. The blue curves with 000 index are the Fourier transform of DMCPs, which can be measured by magnetic Compton scattering. The others can be observed by magnetic Compton scattering at Bragg positions.

However, as it turns out, more information is difficult to be retrieved from the Moyal function. Here Figure 2.8 is displayed to show the possibility to calculate this type of function but further development is needed to make full use of the specificity of probability distribution functions in phase space. This point has so far been amply unexplored and to what extent these functions represent meaningful alternatives to the 1-RDM is a question which remains to be answered.

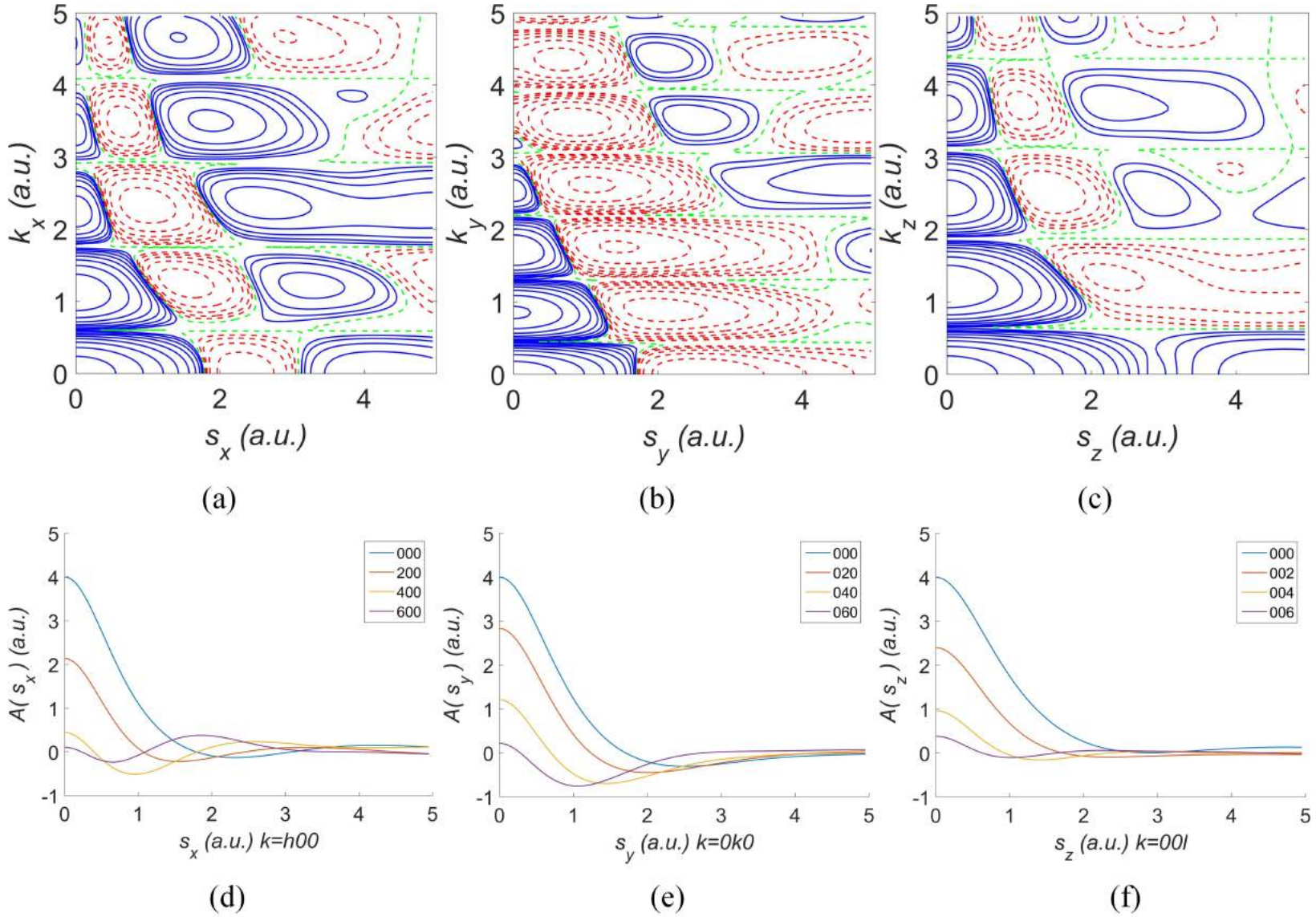

Figure 2.8: $YTiO_3$ magnetic Moyal functions
2D magnetic Moyal function in plane (a) ($\mathbf{s}_x$ $\mathbf{k}_x$), (b) ($\mathbf{s}_y$ $\mathbf{k}_y$) and (c) ($\mathbf{s}_z$ $\mathbf{k}_z$). Contours at $\pm 0.1 \times 2^n$ $(n = 0, ..., 20)$ $e{\cdot}\text{Å}^{-3}$, positive: blue lines, negative: red dashed lines and neutral: green dashed. Directional magnetic $A(\mathbf{u}, s, -\mathbf{k})$ at Bragg positions (d) $A(s_x)$ at $h00$, (e) $A(s_y)$ at $0k0$ and (f) $A(s_z)$ at $00l$

2.4 Orbital resolved RDM

The density matrix relates to the product of wave-functions at two different positions and it is thus interesting to study how each orbital contributes to the total spin RDM. For clarity, the molecular orbitals of a $YTiO_3$ cluster can be separated into atomic-type contributions as

$$\psi_i(\mathbf{r}) = \sum_j c_{ij}^{Y}\chi_j^{Y}(\mathbf{r}) + \sum_k c_{ik}^{Ti}\chi_k^{Ti}(\mathbf{r}) + \sum_l c_{il}^{O_1}\chi_l^{O_1}(\mathbf{r}) + \sum_m c_{im}^{O_2}\chi_m^{O_2}(\mathbf{r}) \tag{2.25}$$

To get a better grasp at the Ti($3d$)–O($2p$)–Ti($3d$) electron transfer, various TiO, TiO_1 and TiO_2 interaction terms are calculated:

$$\Gamma^{TiO_1}(\mathbf{r},\mathbf{r}\,') = \sum_i n_i \left(\sum_{k,l} c_{ik}^{Ti} c_{il}^{O_1,*} \chi_k^{Ti} \chi_l^{O_1,*} + \sum_{k,l} c_{ik}^{Ti,*} c_{il}^{O_1} \chi_k^{Ti,*} \chi_l^{O_1} \right)$$
$$\Gamma^{TiO_2}(\mathbf{r},\mathbf{r}\,') = \sum_i n_i \left(\sum_{k,m} c_{ik}^{Ti} c_{im}^{O_2,*} \chi_k^{Ti} \chi_m^{O_2,*} + \sum_{k,m} c_{ik}^{Ti,*} c_{im}^{O_2} \chi_k^{Ti,*} \chi_m^{O_2} \right)$$
$$\Gamma^{TiO}(\mathbf{r},\mathbf{r}\,') = \Gamma^{TiO_1}(\mathbf{r},\mathbf{r}\,') + \Gamma^{TiO_2}(\mathbf{r},\mathbf{r}\,')$$

To illustrate the cross-term contribution, we propose the following table (Figure 2.9) where the atomic orbitals χ_i are gathered according to the types of atom, the diagonal blocs are the atomic contributions, and off-diagonal blocs are cross-term contributions. Especially, the cross-term contributions between Ti and O are our interests, and also TiO_1 and TiO_2 cross-term contributions.

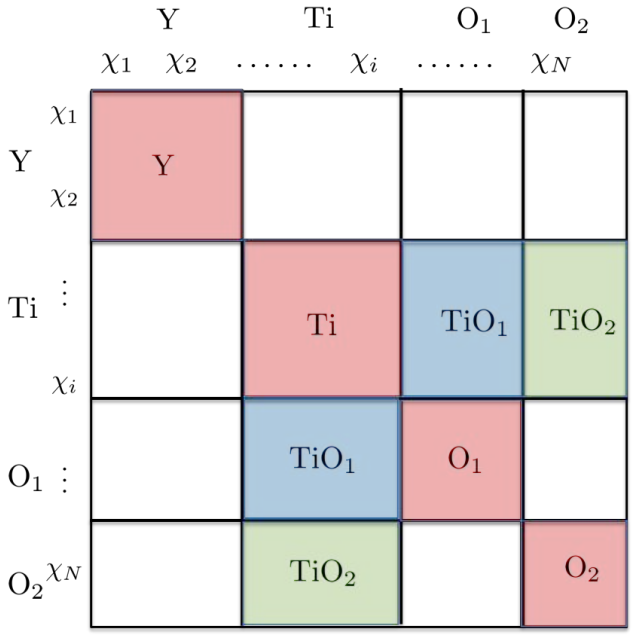

Figure 2.9: Atomic contributions and cross-term contributions

Detailed information on the procedure for orbital separation is presented in Appendix B.8

In this work, the cross-term contribution is calculated in pure position, pure momentum and phase spaces.

2.4.1 Position space

The Ti and O atoms cross-term contribution in position space is calculated in the three usual planes (shown in Figure 2.10 and 2.11). Firstly, the cross-term contribution in position is weak compared to the charge densities or spin densities. For the charge density case (Figure 2.10), obviously, the total charge density is always positive and mostly concentrates around the atoms, but cross-term contribution dominates inter-atomic regions. Total charge density shows many more contours (even divided by 100) than cross-term contributions. The weakness of cross-term contributions also appears for the spin density case where 7 or 8 blue contours can be seen for total spin density and hardly 2 for the cross-term contribution around Ti in the O_1–Ti–O_2' and O_2–Ti–O_2' planes (3 and 1 for O_1–Ti–O_2 plane). It confirms the legitimacy of IAM or even a pseudo-atomic approach. Cross-terms can often be ignored and their absence be corrected by an extended distortion of the valence part of each atomic contribution. Alternative (but more expensive) compromises have successfully been proposed and put into practice by Stewart [43]. Secondly, cross-term contributions represent the most diffuse electrons, and a slight difference between the different Ti–O bonds can be observed from the charge density results. There are 9 blue contours between Ti and O_1, but 8 contours between Ti–O_2 (also O_2'). This difference is possibly an evidence of different Ti–O (O_1 and O_2) chemical bonds in the solid.

As the cross-term mostly corresponds to diffuse electrons, the unbalance charge densities for both sides of O atoms appear perpendicular to the Ti–O bonds. It can also be influenced by the Y atoms, as presented in the XRD refinement, in the plane O_1–Ti–O_2. Therefore, the Y and O atoms cross-term contribution was calculated in the plane O_1–Ti–O_2.

From Figure 2.12, polarization is shown around O_1 and influenced by Y. It is however quite weak when compared with the total charge density. The respective influences of the distribution around O_1 by Ti–O and Y–O cross-term are shown to be opposite (compared to the (b) in Figure 2.12). This can also contribute to limit the polarization behaviour in the total charge distributions.

2.4.2 Momentum space

The Ti and O atoms cross-term contribution in momentum space (magnetic Compton profiles along the 3 principal crystallographic directions) was calculated and compared to the O atoms

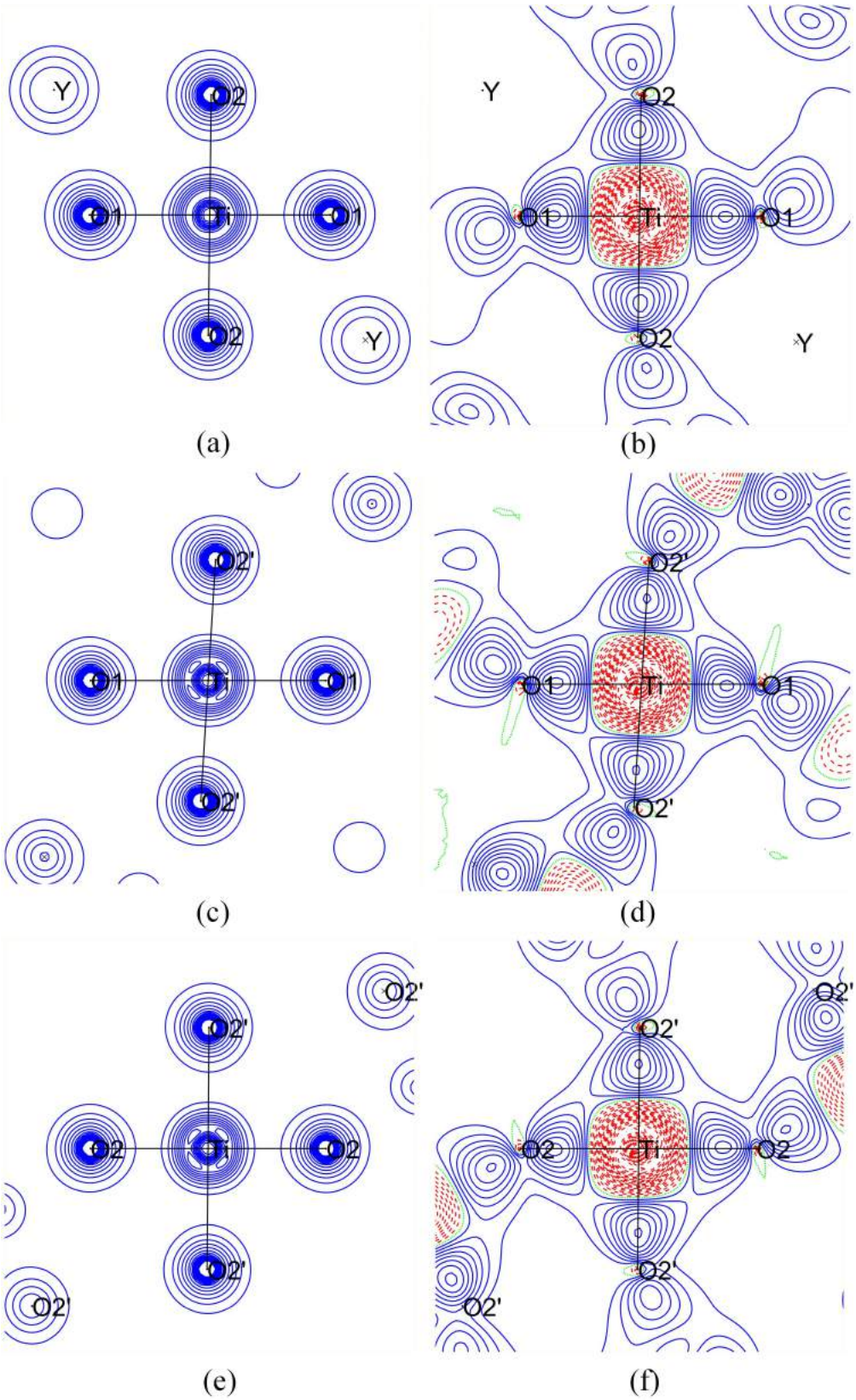

Figure 2.10: $YTiO_3$, TiO cross-term charge density in position space
Total charge densities (left column) and cross-term contribution (right column) in plane (a,b) O_1–Ti–O_2, (c,d) O_1–Ti–O_2' and (e,f) O_2–Ti–O_2'. Contours intervals of $0.01e{\cdot}\text{Å}^{-3}$ with total charge density values divided by 100, positive: blue lines, negative: red dashed lines and neutral: green dashed.

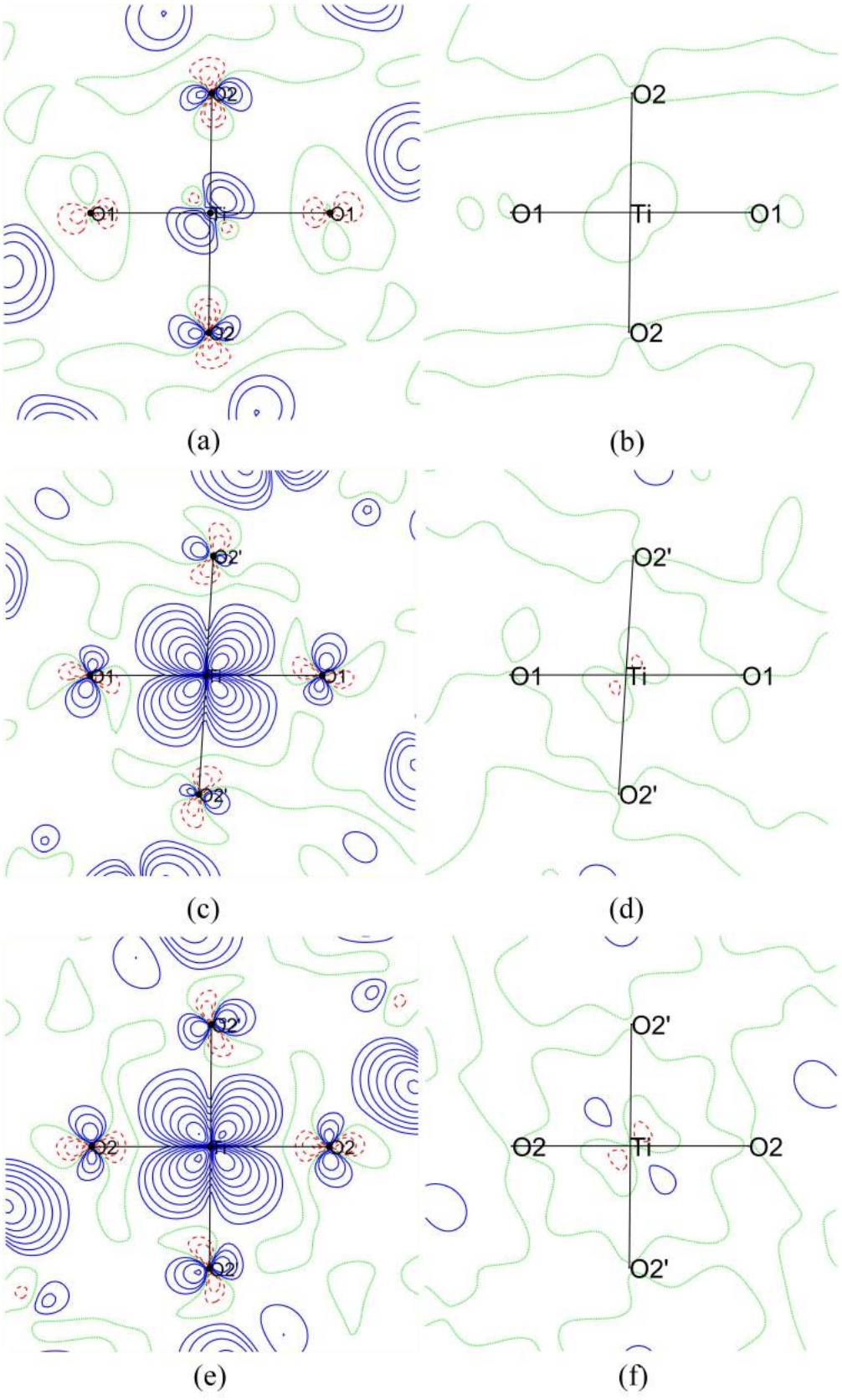

Figure 2.11: $YTiO_3$, TiO cross-term spin density in position space
Spin densities (left column) and cross-term spin densities (right column) in plane (a,b) O_1–Ti–O_2, (c,d) O_1–Ti–O_2' and (e,f) O_2–Ti–O_2'. Contours at $\pm 0.01 \times 2^n$ $(n = 0, ..., 12)$ $\mu_B \cdot \text{Å}^{-3}$, positive: blue lines, negative: red dashed lines and neutral: green dashed.

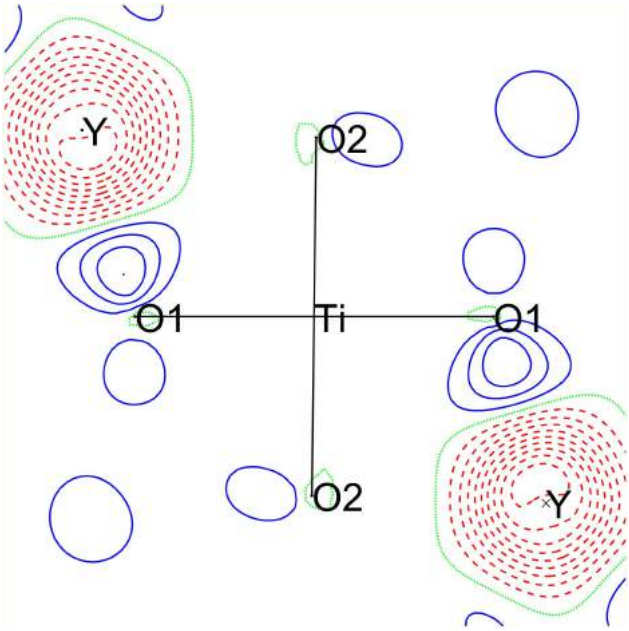

Figure 2.12: YO cross-terms in position space in $YTiO_3$. Charge densities in plane O_1–Ti–O_2. Contours at intervals of $\pm 0.01 \times 2^n (n = 0, ..., 12)$ e $\cdot$ Å^{-3}. Positive: blue lines, negative: red dashed lines and neutral: green dashed.

contribution.

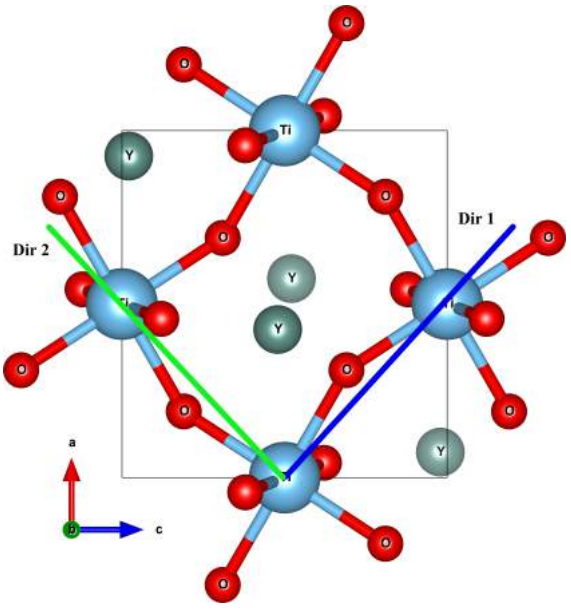

Figure 2.13: Directions in $YTiO_3$ approximately corresponding to Ti–O_2–Ti are close to $(\boldsymbol{a}, \boldsymbol{c})$ (blue) and $(\boldsymbol{a}, -\boldsymbol{c})$ (green).

Unlike the position space case, a comparison with the oxygen atom contributions (Figure 2.14) shows that TiO cross-term cannot be ignored in momentum space. It turns out that their contributions are as important as those from pure single oxygen site origin. Figure 2.14 (a) and (c) show that the cross-term amplitude is larger than that of O atoms, where crystallographic directions $\boldsymbol{a}$ and $\boldsymbol{c}$ both include Ti–O_2–Ti chemical bonds. Figure 2.14 (b)

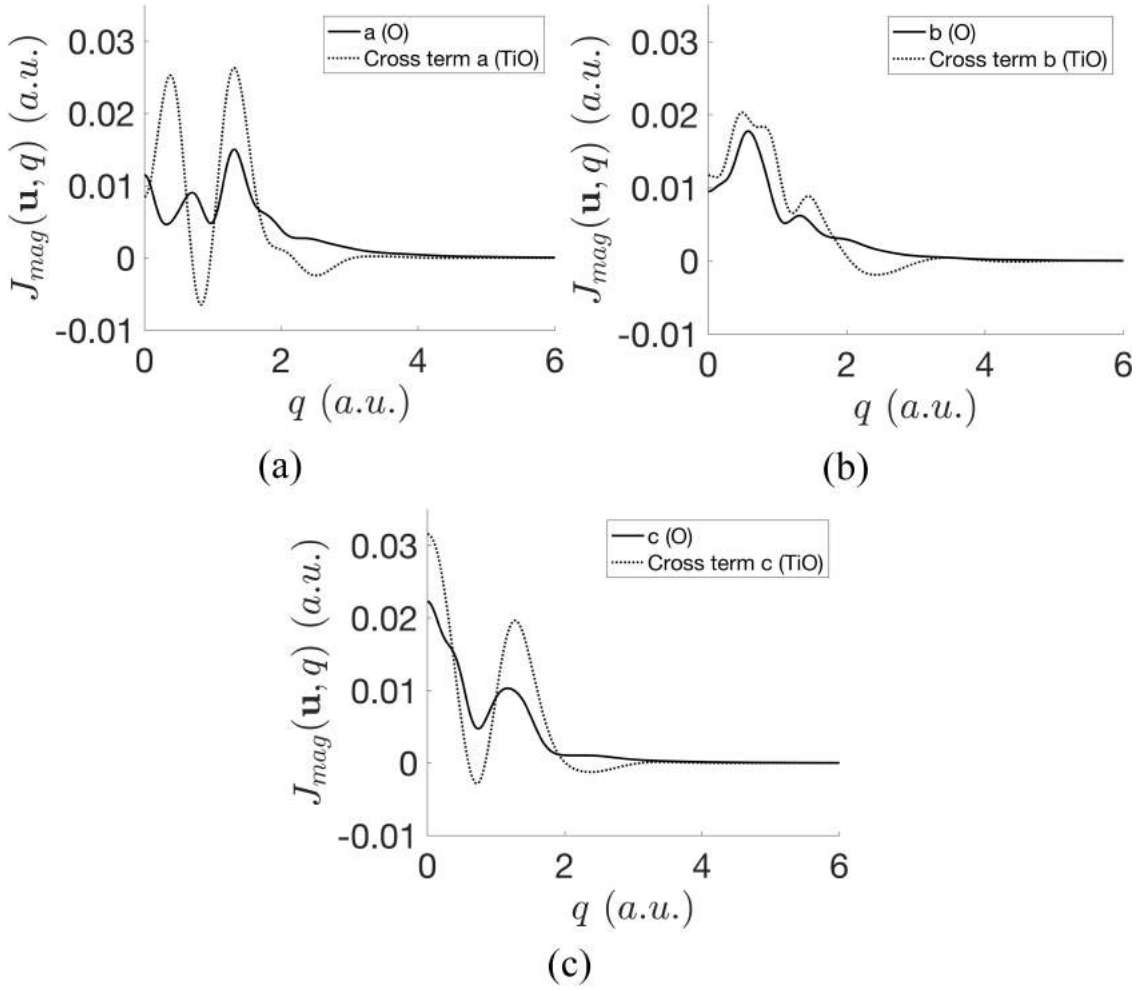

Figure 2.14: $YTiO_3$, TiO cross-term in momentum space
Magnetic Compton profiles of TiO cross-term (solid lines) and O atoms (dashed lines) along the crystallographic directions (a) $\boldsymbol{a}$, (b) $\boldsymbol{b}$ and (c) $\boldsymbol{c}$

shows that in this direction the cross-term brings a contribution similar to that of pure O atoms. This is also true for Figure 2.14 (c). In this case, the $\boldsymbol{b}$ direction corresponds to the Ti–O_1–Ti chemical bonds. In order to obtain a clearer representation of Ti–O_2–Ti contributions, the focus is put onto two special directions as shown in Figure 2.13. The Ti–O_2–Ti is composed by a Ti–O_2 (2.03 Å) and a Ti–O_2' (2.08 Å). As expected from Figure 2.15, the two directions results are very similar. This obviously indicates the same type of chemical bonds. Compared with Figure 2.14, along the directions of TiO chemical bonds, the cross-term is clearly more sensitive to momentum representation and the amplification is larger than the O atoms contributions.

When the O atom contributions, corresponding to Ti–O_1–Ti (Figure 2.14 (b)) are compared with those of Ti–O_2–Ti (Figure 2.15), it appears that the unpaired electron of O_1 is more diffused than that of O_2 along the Ti–O chemical bonds (as shown in Figure 2.16) (considering the number of Ti–O_2 bonds (8) is the double of Ti–O_1 bonds in a unit cell, therefore, there is a difference of intensity), while the cross-term TiO_1 and TiO_2 show a different tendency. To understand the role of O (O_1 and O_2) atoms in cross-term, cross-term TiO_1, TiO_2 and Ti

independent contributions along different directions are calculated and reported in Figure 2.17. The intensities of the two cross-term contributions are conditioned by the number of Ti–O_1 and Ti–O_2 bonds in a unit cell, this is why the amplitude of TiO_2 is larger than TiO_1. Shape comparison between cross-term and single atomic site curves (Ti or O_1, O_2) can help clarify the different weight of atomic contributions in such cross-terms. The shape of cross-term TiO_2 is similar to that of the Ti curve (b), while cross-term TiO_1 is similar to the O_1 curve (a). It means that Ti plays an important role in the TiO_2 cross-term, while the O_1 gives the major contribution to the TiO_1 cross-term. The O_1 diffused electrons are more likely to bridge Ti $3d$ electrons leading a Ti($3d$)–O($2p$)–Ti($3d$) electron coupling. It can thus be concluded that the unpaired electrons of O_1 are more diffused than O_2 and are the best candidates to play an important role into ferromagnetic properties of the solid.

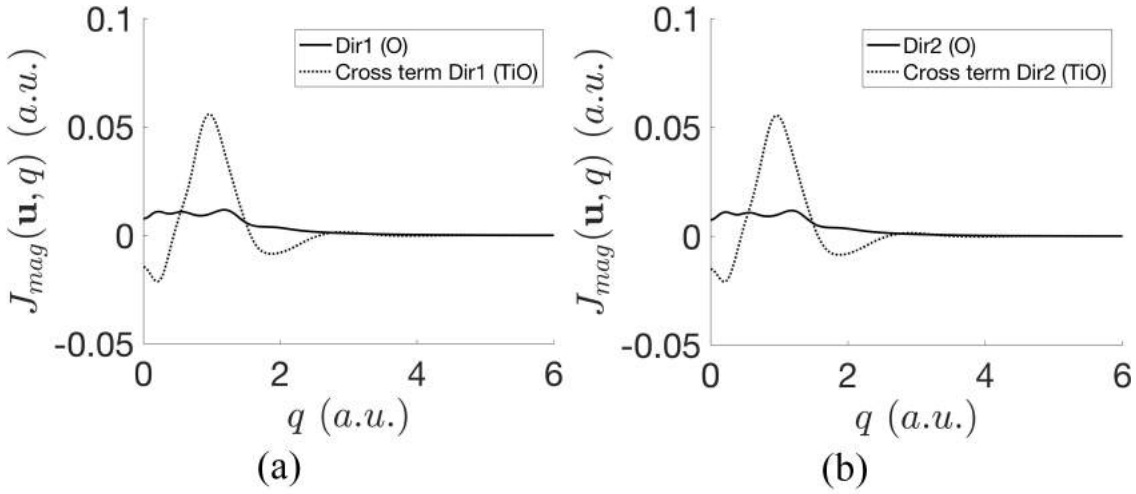

Figure 2.15: $YTiO_3$ TiO cross-term in momentum space corresponds Ti–O_2–Ti directions
Magnetic Compton profiles of TiO cross-term (solid lines) and O atoms (dashed lines) along the Ti–O_2–Ti directions (a) Dir 1 (blue line) in Figure 2.13 and (b) Dir 2 (green line) in Figure 2.13

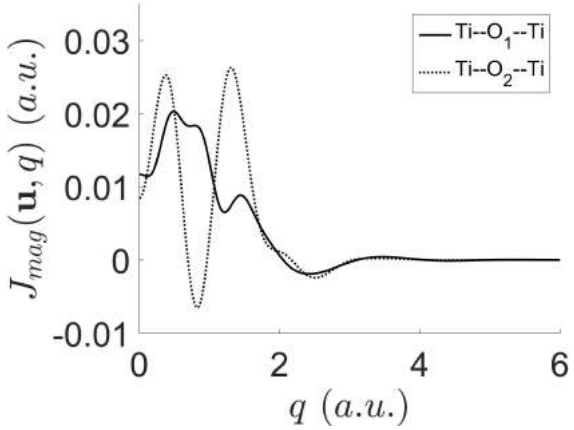

Figure 2.16: $YTiO_3$, TiO cross-term in momentum space
Magnetic Compton profiles of TiO cross-term along Ti–O_1–Ti direction (solid line) and Ti–O_2–Ti direction (dashed line)

As the cross-term represents the most diffuse electrons (or the interaction between the atoms), the electron transfer (similar to the SDD) can be clarified in position space, but

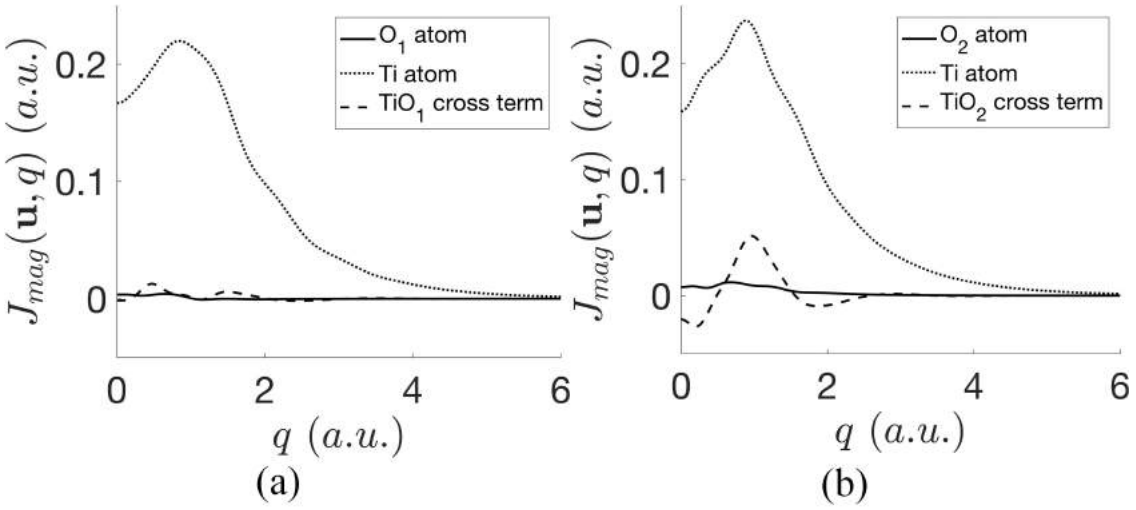

Figure 2.17: $YTiO_3$ TiO cross-term (dashed lines) in momentum space comparing with Ti (dotted lines) and O (solid lines) contributions
(a) along the Ti–O_1–Ti and (b) along the Ti–O_2–Ti.

the value is so weak that it is often neglected. Conversely, in momentum space, the diffuse electrons possess higher momenta. Much like in the Compton profile anisotropies case, it is sensitive to the chemical bond directions.

2.4.3 1-RDM

It has just been seen that cross-terms bear different importance depending on whether they are considered from a position or momentum representation perspective. Their role in total and spin resolved 1-RDM in the vicinity of Ti and O atoms is now evaluated and displayed in Figure 2.18.

Cross-term contribution in 1-RDM can readily be seen in Figure 2.18. Obviously, some of the cross-terms participate to the construction of the 1-RDM to a level as important as that of individual atoms. According to Figure 2.18, the difference between Ti–O_1–Ti and Ti–O_2–Ti for the total 1-RDM are not strikingly obvious, even with elimination of individual atom contributions. The total electron (charge) behaviour between Ti and O atoms for O_1, O_2 and O_2' cases (the same observation as in the static deformation densities figures) appears very similar and the difference between O_1 and O_2 becomes clearer by removing the paired electrons. As a result, magnetic electron density interactions between Ti and O_2' are weaker than in the two other cases and, in turn, spin coupling along Ti–O_1–Ti is much stronger than Ti–O_2–Ti case. It thus confirms the hypothesis formulated from polarized neutron diffraction and magnetic Compton scattering results [89, 126]. Intensities between Ti and O atoms range as $O_1 > O_2 > O_2$', and O_1 and O_2 are quite similar because of their close distances to titanium. It can be concluded that the most possible reason of different O role can be attributed to the Ti–O distances.

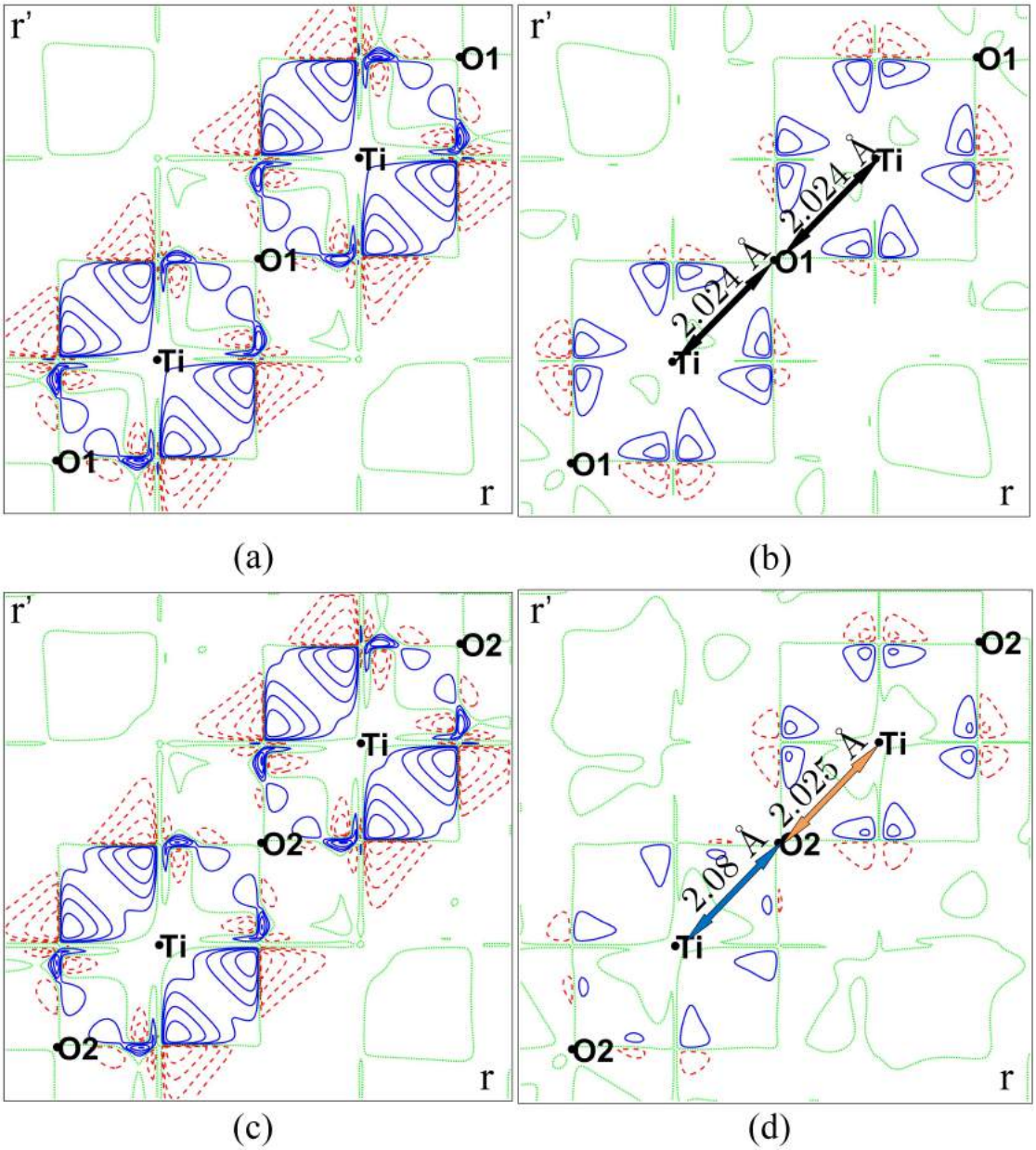

Figure 2.18: $YTiO_3$ TiO cross-term in 1-RDM
(a) total 1-RDM and (b) spin 1-RDM along O_1–Ti–O_1–Ti–O_1, (c) total 1-RDM and (d) spin 1-RDM along O_2–Ti–O_2–Ti–O_2. Contours at $\pm 0.1 \times 2^n$ $(n = 0, ..., 20)$ $e{\cdot}\text{Å}^{-3}$ for total 1-RDM and $\pm 0.01 \times 2^n$ $(n = 0, ..., 20)$ $e{\cdot}\text{Å}^{-3}$ for spin 1-RDM, positive: blue lines, negative: red dashed lines and neutral: green dashed.

2.4.4 Phase space

The Moyal function[a] can also be calculated and used to analyse the cross-term contribution. The directional Moyal functions of TiO cross-term (a) $A(s_x)$ at $h00$, (b) $A(s_y)$ at $0k0$ and (c) $A(s_z)$ at $00l$ are compared with O individual atom contributions (shown in Figure 2.19). Moyal functions with 000 are exactly the auto-correlation function, i.e. the inverse Fourier transform of directional Compton profiles, which can be observed in momentum space.

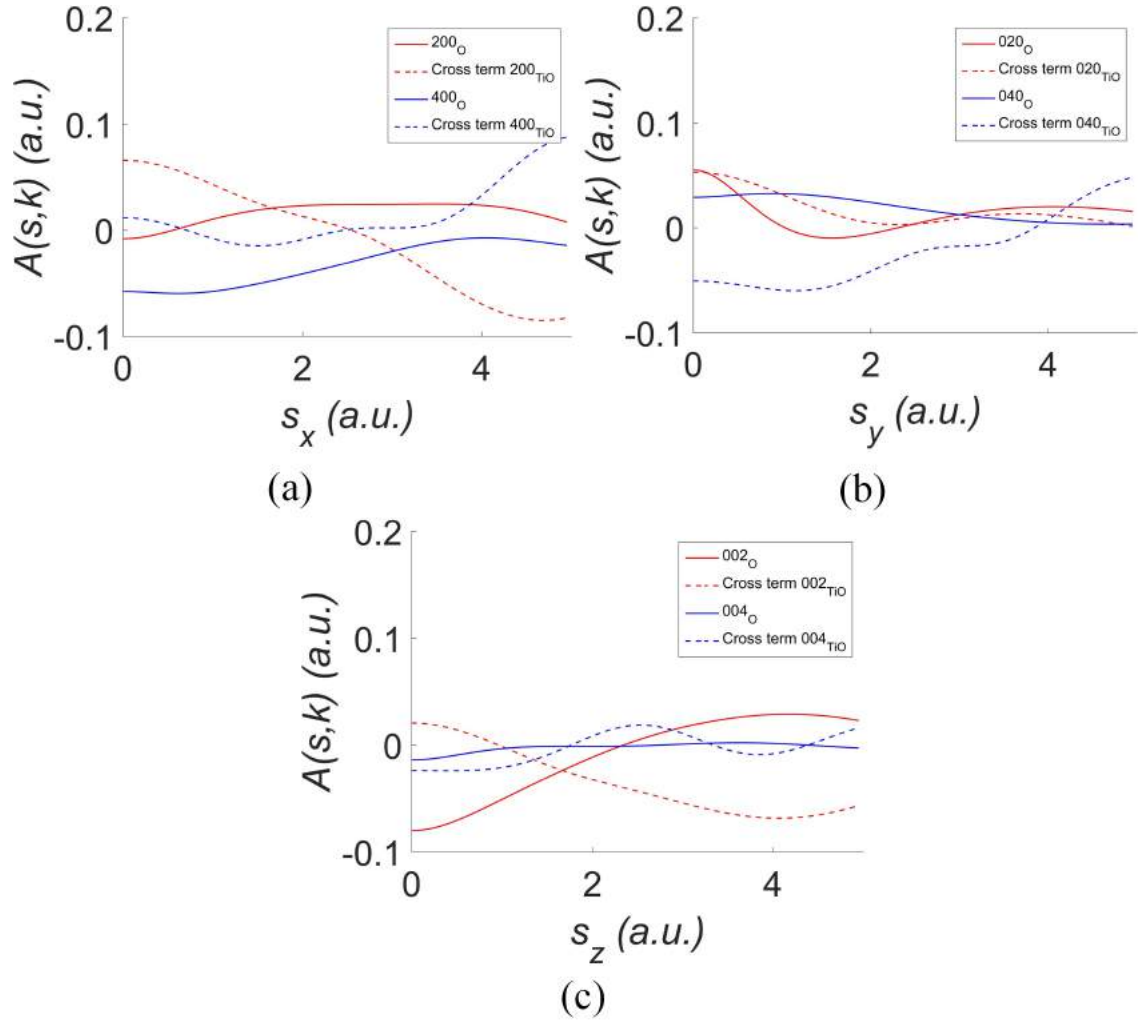

Figure 2.19: $YTiO_3$ TiO cross-term in Moyal function
Directional magnetic Moyal function of TiO cross-term (dashed lines) and O atoms (solid lines) at Bragg positions (a) $A(s_x)$ at $h00$, (b) $A(s_y)$ at $0k0$ and (c) $A(s_z)$ at $00l$

Two directional Moyal functions are presented in each plane (defined by $(\mathbf{s_i}, \mathbf{k_i})$ with $i \in \{x, y, z\}$). In $YTiO_3$ case, as evidenced from Figure 2.19, the result is significantly more complicated as the cross-term directional Moyal function depends both on the direction of $\mathbf{s}$ and $\mathbf{k}$. It can be close to the O atoms contribution (eg: 004 in (c)), but can also be significantly different (040 in (b)). From Figure 2.19, the relation between $\mathbf{k}$ values and directional Moyal functions is not clear, and requests more investigations.

[a]Wigner functions have shown to suffer from computational difficulties in the case of the limited cluster re-construction and also, perforce, of periodic systems.

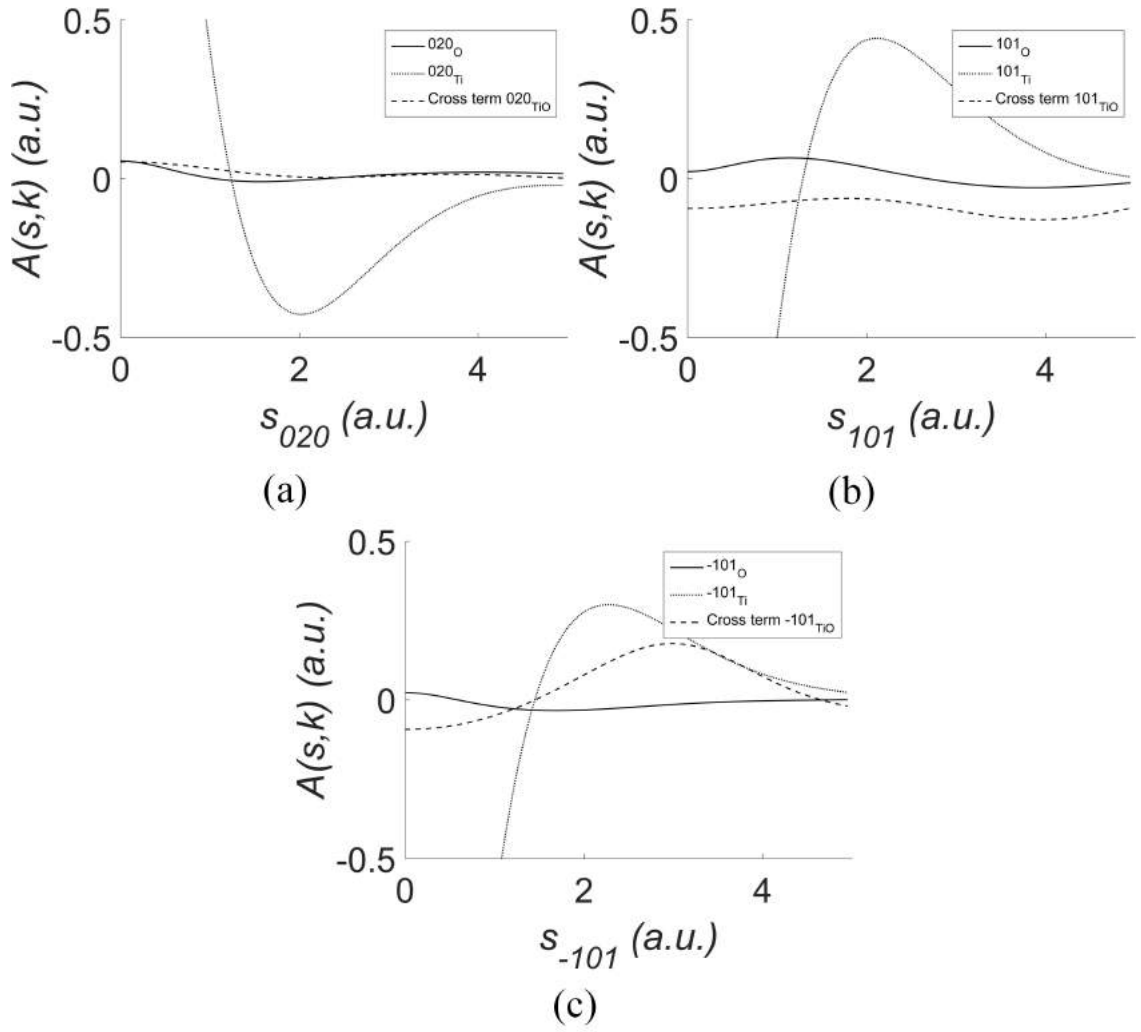

Figure 2.20: $YTiO_3$ TiO cross-term in Moyal function along Ti–O–Ti directions
Directional magnetic Moyal function of TiO cross-term (dashed lines) and O atoms (solid lines) and Ti atoms (dotted lines) at Bragg positions (a) $A(s_{020})$ at 020, (b) $A(s_{101})$ at 101 and (c) (b) $A(s_{-101})$ at 101

Because the chemical bonds Ti–O_1–Ti and Ti–O_2–Ti are the possible ferromagnetic interaction pathways, the directional Moyal function along these two directions may be of some relevance (Figure 2.20). For $A(s_{020})$ at 020 (a), the curves of cross-term and of O atoms are almost superimposed. While the two curves in (b) (direction 101) just have different amplitudes with similar shapes, the cross-term curve in (c) (direction -101) changes significantly and seems to be affected more by the Ti atoms contributions. Because of **s** is intracule coordinate in direct space, directional Moyal function with the same **k** shows the correspondence with chemical bond directions. However, qualitative analysis to indicate the type of chemical bond also requests further exploration.

As a conclusion, cross-term is proven to play an important role in Moyal function from both the **s** and **k** aspects. This can, of course, be connected to position and momentum representations. However, the complexity of mixing both space representations induces a significant difficulty of conducting qualitative and quantitative analysis. Here, it thus

becomes more challenging to disentangle the two space contributions. To our best knowledge, a quantitative analysis of the Moyal function has never really been explored, and probably deserves further developments as the relevant experiments can more easily be accessible and considered on a similar footing.

Finally, it is important to acknowledge the fact that no pseudo-atom based model (as a direct transposition of Hansen-Coppens construction) can be considered in the long term for correctly reproducing a valid experimental Moyal function. The same statement applies to Wigner function and 1-RDM for which a mere incoherent superposition of atomic contributions can only be envisaged as a mere starting point.

2.5 Summary

In this chapter, a minimal cluster construction is put forward to allow for the computation of new properties and the analysis of (often discarded) cross-terms. The cluster construction is based on a periodic self-consistent computation carried out with CRYSTAL14. The model considers the contributions of a center cell (primitive cell) and its 26 first neighbours. The electronic properties can be recovered both in position and momentum spaces (as well as phase space). The 1-RDM and Moyal functions are shown to be valuable tools for observing (and possibly analysing) the subtle behaviours of electrons (charge and spin) in the solid.

- The 1-RDM emphasizes chemical bond aspects and links the position and momentum spaces. Individual atom and two-center interaction contributions are gathered in the same 1-RDM representation. In $YTiO_3$, it clarifies the respective roles of O_1 and O_2, which are difficult to observe from the sole electron density in position space or momentum space.
- The Moyal function is a potentially useful but complex observable. Its primary virtue is that it is directly connected to the most familiar experimental quantities $F(\mathbf{k})$ and $B(\mathbf{s})$.
- The directional Moyal function can be directly retrieved from Compton scattering in Bragg positions and, albeit technical difficulties, it provides an additional experimental resource which should not be neglected.

Cross-term analysis by orbitals separation (regrouping orbitals according to the type of atom) can shed light on the interaction between atoms in different spaces.

- While cross-term contribution is often considered negligibly weak in position space, it contains information about electron coupling between atomic sites. Conversely,

cross-term contribution is proven to be more important than some individual atom contributions in momentum space.

- As the cross-term mostly represents the diffuse electrons, it is quite natural that they give a significant contribution in momentum space related quantities such as the directional Compton profiles, especially along particular chemical bonds. From a comparison between cross-term and individual atom contributions, the role of particular atoms in the electron transfer and spin coupling can be clarified. For example, the cross-term magnetic Compton profile analysis supports the conclusion from magnetic 1-RDM, that the O_1 role is dominant in spin coupling.

- Moyal cross-term is difficult to analyse because of their simultaneous dependence in $\mathbf{s}$ and $\mathbf{k}$ which mixes both spaces. A further application of Moyal function needs additional developments. Similar to the atomic form factor, the individual atomic Moyal contributions would be a promising starting model.

The minimal cluster construction is a mere technical process for computing *ab-initio* derived properties that need to be compared with experimental observations. The multipolar refinement models in position space and reconstruction method in momentum space have been developed with tremendous successes for many years. However, models combining both spaces are just at their beginning and a more complete electronic description is expected by gathering a large number of experiments such as XRD, PND, CS and MCS , XMD or NMR. In the next chapter, the "super-position" method and premises of a 1-RDM refinement model will be presented to connect two spaces and open the possibility for new investigations.

Chapter 3

Joint Model: Position and Momentum Spaces

Electron densities in position and momentum spaces describe the electron behaviour in a solid from different aspects. Electron position space representation is usually considered to conduct QTAIM analysis to better characterise atomic charges and chemical bonds. However, it is difficult to analyse the physical and chemical properties solely from a momentum perspective. In point of fact, most reported researches make use of Compton scattering as a mere additional contribution to conduct a model refinement [52] or a simple comparison with more or less sophisticated *ab-initio* computations. More general models, considering both representations on equal footing deserve further exploration. In this work, several methods have been put forward to compare and possibly combine both spaces.

3.1 Super-position space

3.1.1 Introduction

The first method is the so-called "super-position" approach. As the position concept is irrelevant in momentum space, the concept of "super-position" stems from the idea of superimposing "atomic electron densities" using only translation operations. The new superimposed electron distribution in a limited region of position space is called the "super-position" electron density. This method works well providing that a condition is met: a single type[b] of atom bears the great majority of unpaired electrons[c] in the crystal. What follows makes use of $YTiO_3$ as an illustration of the "super-position" method.

[b] If more atoms are involved, with no clear directional chemical bond, it is likely that the result will be highly isotropic and most of the information content will be lost.

[c] The above condition (footnote [b]) is more easily met when unpaired electrons are considered because of the usual limited number of magnetic atomic sites.

3.1.2 Super-position construction

As a first approximation to the theoretical atomic spin population of $YTiO_3$, a Mulliken analysis [127] yields the following results {Y: 0.043, Ti: 0.967, O_1: -0.006 and O_2: -0.002}. On the experimental result side[89], polarized neutron diffraction (PND) (as well as magnetic X-ray diffraction (XMD)) data have permitted to reconstruct the spin density distribution using an atomic orbital model[128]. Parameters of the model include spin populations for all atoms Y, Ti and O. While the contribution of Ti clearly dominates with 0.974 electron, experiments confirm the weak addition from O_1 with an estimated value of 0.026. No value is found on the Y site because this atom was not included in the analysis and therefore no function was attached to it.

To emphasize the coherence of experimental results between both position and momentum space representations, we put forward a new procedure. The respective dominant contributions of the four Ti atoms in the primitive cell are superimposed in position space. The resulting averaged spin density is hereafter denoted as the "super-position construction (or representation)" of the spin density, $\langle \rho_{\mathrm{mag}}(\mathbf{r}) \rangle_{\mathrm{Ti}}$, and computed as

$$\langle \rho_{\mathrm{mag}}(\mathbf{r}) \rangle_{\mathrm{Ti}} = \frac{1}{4} \sum_{n=1}^{4} \rho^{n}_{\mathrm{mag}}(\mathbf{r} + \mathbf{R}_n) \tag{3.1}$$

where $\mathbf{r}$ is in a 2 Å cube, with -1 Å $\leq \{x, y, z\} \leq 1$ Å, and $\mathbf{R}_n$ are the Ti nuclei positions at different sites (as shown in Figure 3.1). The construction of a "super-position" cube is a two-step process[a]:

(a) For a given unit cell, extract 4 cubes with 2 Å edges, centred on each Ti nucleus (4b positions generated by space group symmetries [71]).

(b) Add up (and divide by 4) the respective spin density distributions in the 4 cubes to obtain the "super-position" density cube for $YTiO_3$.

The 2-dimensional projections of the "super-position" spin density for the three planes perpendicular to the three crystallographic axes can then be respectively computed and displayed on Figure 3.2. They can thus be compared with two-dimensional magnetic electron momentum density (2D-MEMD) results.

For each plane, the *ab-initio* projected "super-position" spin density is slightly larger than its experimental counterpart. As previously mentioned, this can be attributed to the larger theoretical unpaired population on the Ti sites. A comparison of Figure 3.2 and Figure 3.3 highlights the striking similarity of projected "super-position" spin density with 2D-MEMDs

[a] This method works better for the crystal where a single type of atom is responsible for the major part of the spin density.

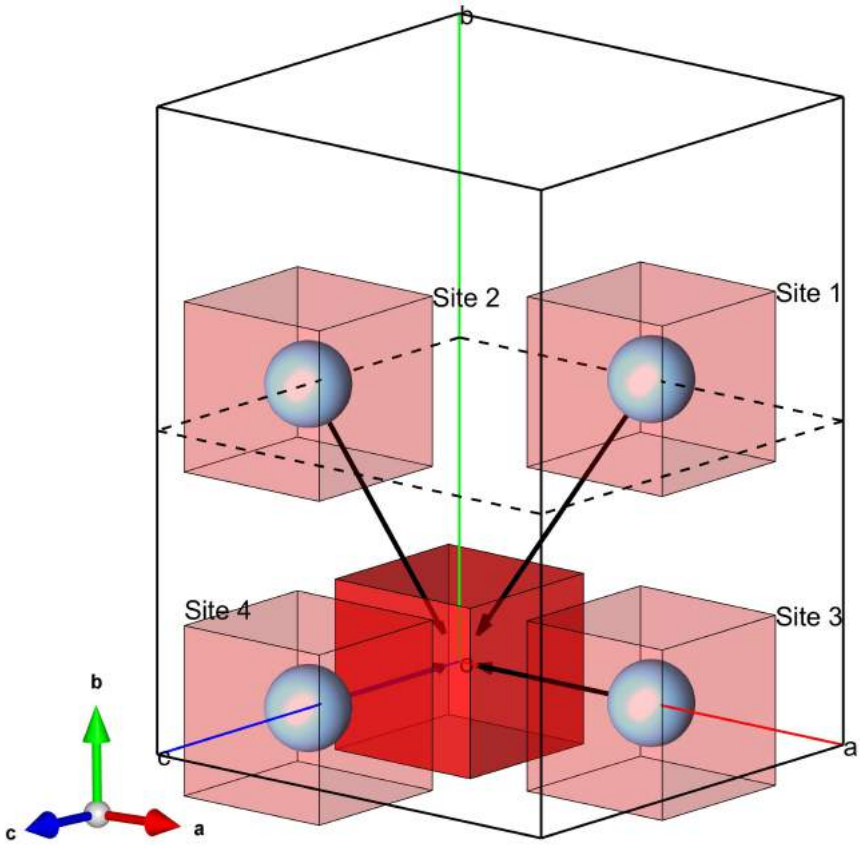

Figure 3.1: $YTiO_3$ super-position cube construction

for all planes. This method thus provides a possible means of a fast qualitative checking of the coherence between PND and magnetic Compton scattering (MCS) experiments. Moreover, this is visual confirmation that observing orbitals [129] in momentum space (using Compton scattering data) is possible in much the same way as it is (more commonly) done in position space [97].

3.1.3 Single atom model

To provide a qualified explanation of geometric similarity between two space representations, an "single Ti model" can be used. It is first considered that the dominant contribution to the spin density comes from an unpaired electron on a Ti $3d$-type orbital. Following a combination of symmetries suggested by Akimitsu and co-workers [77], the local wave-function can be written as

$$|\psi\rangle = \sqrt{0.61}|yz\rangle + \sqrt{0.39}|xz\rangle \tag{3.2}$$

where the coefficients have been determined by the pseudo-atomic wave-function refinement on PND data [89]. Such a d orbital population anisotropy is also in excellent agreement with our recent electron density modeling based on high resolution X-ray diffraction data (presented in *chapter 1* and as part of the Voufack's thesis work (to be published)). A noticeable difference with the construction brought forward by Akimitsu et al.[77] is that

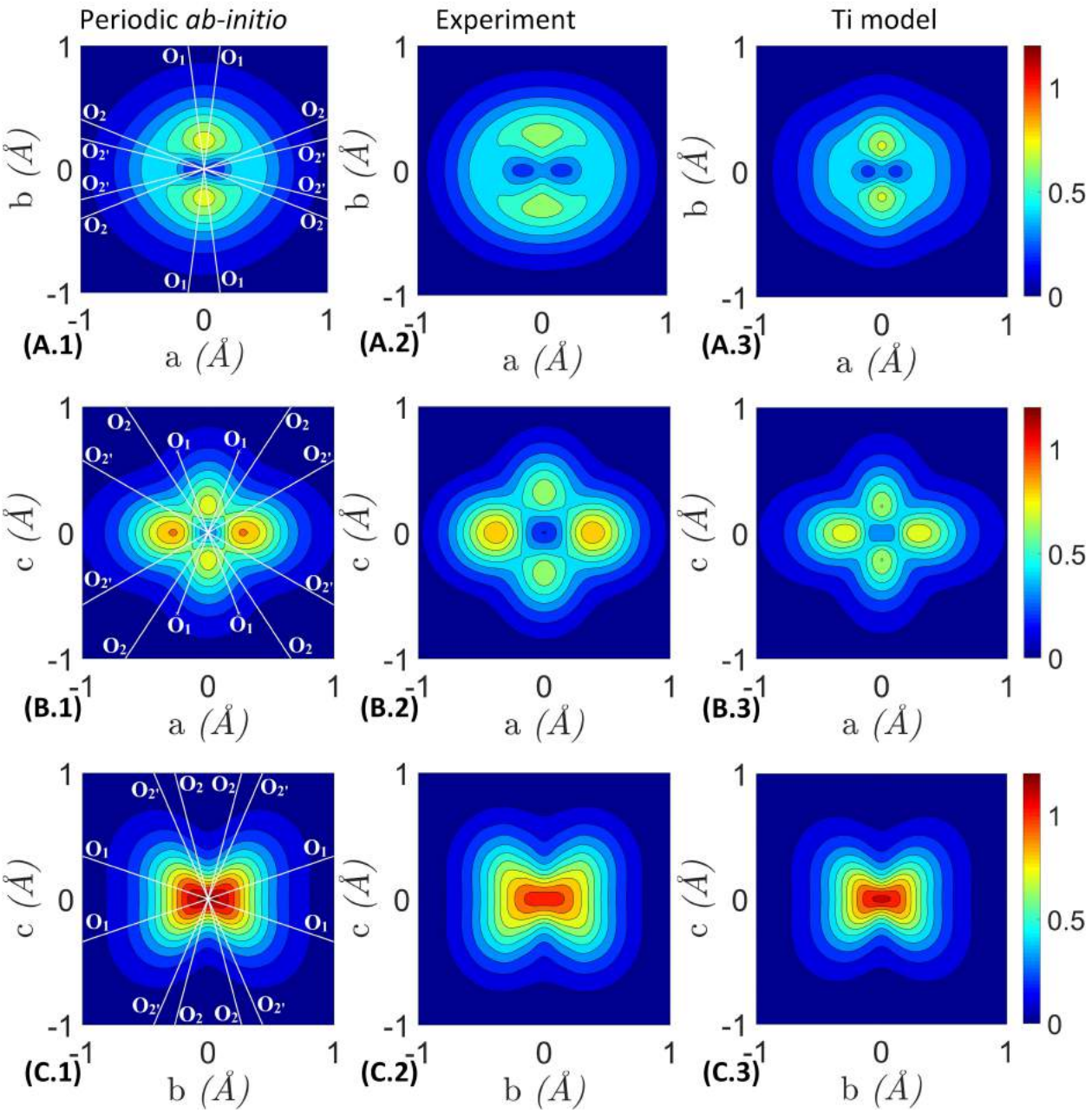

Figure 3.2: $YTiO_3$ 2D super position spin density
Projections of the "super-position" spin density (in $\mu_B \cdot$ Å^{-2}) onto the three main crystallographic planes. Each row corresponds to a plane: (A) (ab) plane; (B) (ac) plane; (C) (bc) plane. Left column: periodic *ab-initio* results, with white solid lines indicating the projections of oxygen positions in "super-position" space. Middle column: experimental data. Right column: "single Ti model". Contours at intervals of 0.1 $\mu_B \cdot$ Å^{-2}. Colour bar scaling from 0 to 1.2 $\mu_B \cdot$ Å^{-2}.

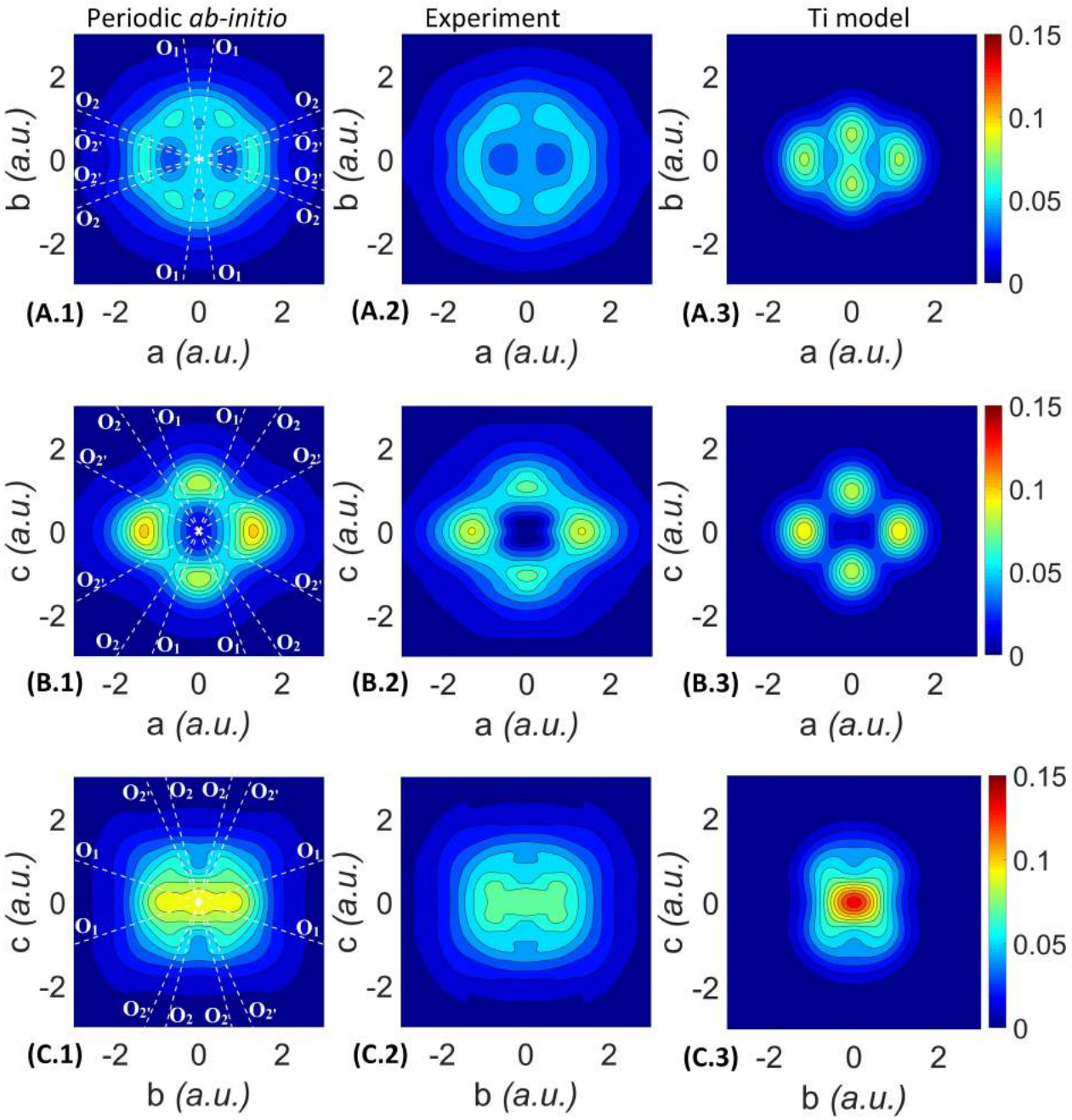

Figure 3.3: $YTiO_3$ 2D-MEMD
Reconstructed spin density in momentum space (in a.u.), projected onto the three main crystallographic planes (2D-MEMD). Each row corresponds to a plane: (A) (ab) plane; (B) (ac) plane; (C) (bc) plane. Left column: periodic *ab-initio* results using convoluted MDCPs, with white dashed lines indicating the projections of Ti–O directions in momentum space. Middle column: experimental results. Right column: the same quantity obtained by the "single Ti model" (see section 3.1). Contour at intervals of 0.01 a.u. Color bar scaling from 0 to 0.15 a.u.

here the local y and z axes are reversed for site 1 and 2 with fractional coordinates: (0.5, 0.5, 0) and (0, 0.5, 0.5) respectively (see Figure 1.20 in *chapter 1* for detailed information). The 4 Ti atoms are identical by symmetries (4b positions in *Pnma*)[71], but cannot be superimposed by translations only. The local z direction is defined by the Ti–O_2' bond, while the local x and y directions are set approximately along the Ti–O_1 and the Ti–O_2 bonds respectively (Figure 1.20).

In this "single Ti model", the Ti atomic radial function for $|yz\rangle$ and $|xz\rangle$ is described by a Slater type function (STF)[130] given by Clementi[42] and expressed, for computational convenience, as a contraction of Gaussians. Here we use 3 GTOs given in the theoretical d orbital basis set for Ti[84] to fit the Clementi atomic orbital.

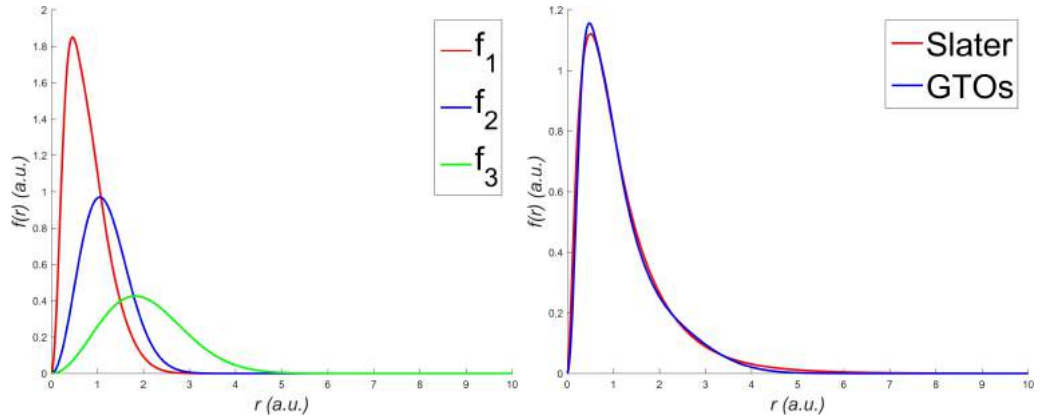

Figure 3.4: Fit of Ti STF $3d$ atomic radial function by GTOs
Left, three GTOs. Right, STF and linear combination of three GTOs

In the three GTOs (left in Figure 3.4), f_3 is more diffuse than f_2 and than f_1. The combination coefficients are such that

$$f_{STF}(r) = 0.60 f_1(r) + 0.03 f_2(r) + 0.45 f_3(r) \tag{3.3}$$

Obviously, as seen in Figure 3.4, the STF has been fairly well reproduced by the GTO contraction. This linear combination is used in the following computations.

The model "super-position" density using expression (3.2), for each Ti contribution, can then be computed as mentioned in (3.1). Similarly, the total spin density in momentum space results from a mere addition of the Ti sites contributions. The projections of "super-position" and momentum densities obtained by this simple model will be used for comparison with *ab-initio* and experimental 2D-MEMDs and "super-position" spin density.

Figure 3.2[a] and Figure 3.3[b] (right column) confirm the strong geometrical similarities between "super-position" and momentum distributions. More importantly, a comparison of

[a] "Super-position" spin density accounting O_1 contribution has also been conducted (Figure C.1)

[b] Considering the error bar of PND refinement result, computations using expression (3.2) with different coefficients are conducted, see Figure C.2 and Figure C.3

this result with the two other columns supports the dominant belief that a pseudo-atomic model often gives a fair account of observations in position space. However, for Figure 3.3, it is essential to note that the single Ti model is not fully adapted to reproduce momentum space properties. While the model's 2D-MEMD (Figure 3.3) and its anisotropy (Figure 1.31) exhibit features which are quite comparable in the (ac) plane to those found from experiment (or *ab-initio* results), this is no longer true for the momentum space spin density projected onto the (ab) or (bc) planes. Obviously, the single Ti simple model is dominantly affected by discrepancies along the $\boldsymbol{b}$ direction for which the lack of coupling with O_1 (4c position) atom appears to have the strongest impact. It can thus be reasonably claimed that momentum space properties, which are known to be more sensitive to delocalized electrons, support the role played by the coupling along Ti-O_1-Ti chemical bond for the unpaired electron. Therefore, it qualifies this bond as a possible ferromagnetic pathway in $YTiO_3$.

In order to validate such a mechanism, it becomes necessary to go beyond the single Ti picture for elaborating a local wave-function. The use of both PND and MCS data will thus be essential to refine a more sophisticated model accounting for the coupling between the metal and its oxygen atomic neighbors.

3.2 1-RDM refinement

3.2.1 Introduction

1-RDM contains all electronic information at one electron level and it connects position and momentum spaces by diagonal and off-diagonal elements respectively. It is thus a natural quantity to gather both space representations. Cluster approximation models (*Chapter 2*) make it possible to reproduce crystal properties including the 1-RDM. However, a 1-RDM based on the experimental observations (Bragg and Compton scattering data) requests further exploration before it can be compared with a theoretical (*ab-initio*) 1-RDM.

Few attempts to refine 1-RDM models have been carried out[131–136], all them using exclusively x-ray diffraction (XRD) data since, again:

$$F(\mathbf{Q}) = \int_v \langle \Gamma(\mathbf{r}, \mathbf{r}')_{\mathbf{r}=\mathbf{r}'} \rangle e^{i\mathbf{Q}\cdot\mathbf{r}} d\mathbf{r} \tag{3.4}$$

where v is the unit cell volume. From expression (3.4), XRD data gives a dominant contribution to the diagonal elements of 1-RDM refinement. The off-diagonal elements should be considered by using Compton scattering (CS) data:

$$J(\mathbf{u}, q) = \frac{1}{2\pi} \int \langle \Gamma(\mathbf{r}, \mathbf{r} + s\mathbf{u}) \rangle e^{iq\cdot s} d\mathbf{r} ds \tag{3.5}$$

where **u** is a unit vector collinear to the inelastic scattering vector.

A coupled pseudo-atom model using XRD and directional Compton profile (DCP) data to refine the 1-RDM has been proposed by Gillet[137]. This model considers the independent atomic contributions, and also the interaction between neighbouring atoms.

$$\Gamma(\mathbf{r},\mathbf{r}') = \underbrace{\sum_{i} \Gamma_i(\mathbf{r},\mathbf{r}')}_{\text{atomic contribution}} + \underbrace{\sum_{(i,j)} \Gamma_{ij}(\mathbf{r},\mathbf{r}')}_{\text{couple of close neighboring atoms}} \tag{3.6}$$

where the couple of close neighboring atoms is determined by using the nearsightedness principle[138, 139]. The reported work also confirms that joint refinements are more sensitive to the quality and flexibility of the model than when a unique type of experiment is considered. Nevertheless, this model suffers from a major inconvenient: the N-representability of the resulting 1-RDM is not automatically guaranteed and needs to be checked a posteriori.

Theoretical computation and experimental refinement are two principle methods for investigating electron density in a solid. Ideally, the difference between theoretical predictions and experimental observations should be as small as possible. On the other hand, there are many theories and experiments cross-contributions. For example: atomic form factors used for the modelling of structure factors originate from the Dirac-Fock wave-functions computed for isolated atoms[140]. In the multipolar electron density refinement model (1.19), functions, describing core and valence electron density models, are based on the atomic orbitals calculated on isolated atoms at the HF level or Dirac-Fock level including the relativistic effects[41, 42]. Another method is the X-ray constrained wave-function refinement approach strengthening the connection between experimental observations and calculations[136, 141–145]. It gives an approximate wave-function by using a modified SCF approach. In brief, it is thus difficult to separate theories from experiments, especially since experimental refinements using theoretical functions often yield high quality results.

In this work, a method based on *ab-initio* computation as an initial guess is proposed to refine the spin-resolved 1-RDM using PND and MCS data[a] (unpaired electrons are our focus of interest). Basis set (only radial functions) optimization and orbital occupation refinements can be conducted separately by minimization of difference between experimental and calculated observables (magnetic structure factors and directional magnetic Compton profiles (DMCPs)). The advantages of this method are:

- Firstly, the N-representability of the resulting 1-RDM is guaranteed by the *ab-initio* computation stage.

[a] the code is implemented by S. Gueddida

- Secondly, this model is adapted to various experimental scattering data such as XRD, PND, CS, MCS and XMD.

3.2.2 Refinement model

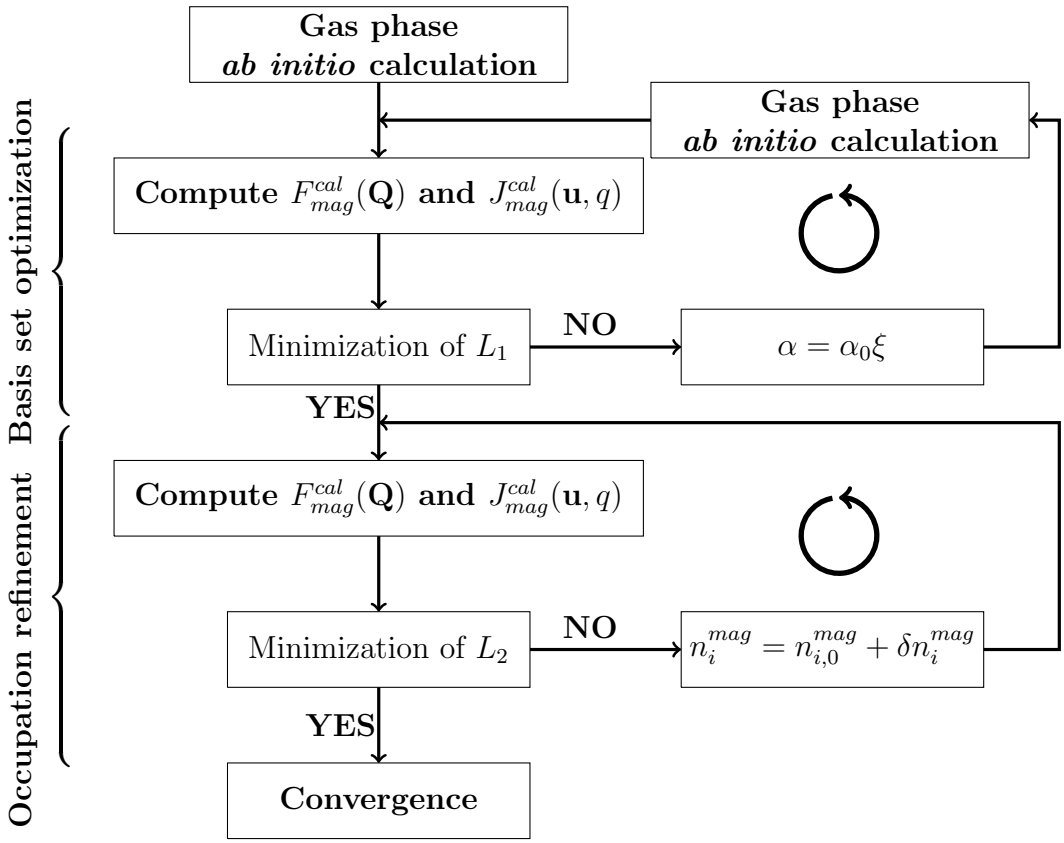

Figure 3.5: 1-RDM refinement process

The current 1-RDM refinement strategy is presented in Figure 3.5. An initial guess is prepared by the gas phase *ab initio* calculation (with G09 for this work), a simple quantum model (HF with simple, minimal standard basis set) is chosen. The construction of cluster or molecule depends on the crystal parameters, and it is obviously different for molecular or metallic crystals: monomer or dimer (or larger cluster) can be chosen for molecular crystals. It becomes more complicated for the metallic crystal case, where electrons of interest are highly delocalized and no obvious frontiers can be drawn. The key atoms, structure, magnetic coupling path (the magnetic properties are our focus of interest) should be accounted for in the cluster, and point charges at nuclei positions around the cluster can be used to simulate the crystal environment. Refinement is separated into two parts:

Basis set optimization

As presented in *section 1.2.1*, crystalline atomic basis sets are built starting from an atomic basis set optimized for molecules, and re-optimizing the exponent of the most diffuse GTOs.

Basis set optimization is similar to the κ refinement as used in the HC multipolar model (1.19). Optimized orbitals can be obtained by a rescaling of exponential coefficients α, $\alpha = \alpha\xi$, in the Gaussian basis set based on (A.3):

$$g_{ip}(\mathbf{r}) = c_{ip}(x - X_0)^{l_1}(y - Y_0)^{l_2}(z - Z_0)^{l_3} e^{-\xi\alpha_{ip}(\mathbf{r}-\mathbf{R})^2} \tag{3.7}$$

where $\sqrt{\xi}$ is thus similar to κ in the standard HC refinement model (1.19), and the following restrain was set $0.8 \leq \xi \leq 1.2$. The first step is the computation of scattering observable values ($F_{mag}(\mathbf{Q})$ and $J_{mag}(\mathbf{u}, q)$) following the *ab initio* molecular-like (cluster type) calculation based on (3.4) and (3.5). This is the basis of the first comparison with the observation. Quantification of the difference is evaluated by means of L_1 expressed in LOG scheme (for faster convergence) according to

$$L_1 = Log[\sum_{i=1}^{N_{PND}} \frac{|F_{mag}(\mathbf{Q}_i)^{obs} - F_{mag}^{cal}(\mathbf{Q}_i)|^2}{\sigma^2(\mathbf{Q}_i)}] + Log[\sum_{j=1}^{N_{Dir}} \sum_{k=1}^{N_{MCS}} \frac{|J_{mag}^{obs}(\mathbf{u}_j, q_k) - J_{mag}^{cal}(\mathbf{u}_j, q_k)|^2}{\sigma^2(\mathbf{u}_j, q_k)}] \tag{3.8}$$

where L_1 is thus the objective function, N_{PND} is the number of magnetic structure factors, N_{Dir} is the number of non-equivalent directions for DMCPs, N_{MCS} is number of sample points along each direction, $\sigma(\mathbf{Q}_i)$ and $\sigma(\mathbf{u}_j, q_k)$ are the error bars of both experimental observations, respectively. If $L > min$, the current α value is replaced by $\alpha\xi$, and a new calculation with the new basis set is conducted by G09. The normalization of basis set is done by G09 as presented in *Section A.1*. This process is repeated until minimization of L, and an optimal ξ is obtained.

The objective of basis set optimization is to achieve a better molecular orbital description based on the experimental observations. Thereby, a portion of the crystal environment effects is included in the optimized basis set.

Occupation refinement

The occupation refinement process consists in fitting the electron occupation of the SCF optimized orbitals (defined by means of the newly optimized basis set) based on the experimental observations.

As presented in (1.12), the spin-resolved 1-RDM can be written:

$$\Gamma_{mag}(\mathbf{r}, \mathbf{r}') = \Gamma^{\uparrow}(\mathbf{r}, \mathbf{r}') - \Gamma^{\downarrow}(\mathbf{r}, \mathbf{r}') = \sum_{i=1,j=1}^{i=N,j=N} P_{ij}^{mag} \chi_i(\mathbf{r}) \chi_j^*(\mathbf{r}) \tag{3.9}$$

where P_{ij}^{mag} is the spin population matrix from:

$$P_{ij}^{mag} = \sum_{k}^{k=N} n_k^{\uparrow} c_{ik}^{\uparrow} c_{jk}^{\uparrow} - \sum_{k}^{k=N} n_k^{\downarrow} c_{ik}^{\downarrow} c_{jk}^{\downarrow} \tag{3.10}$$

where N is the number of molecular orbitals. In single determinant HF approach $n_k^{\uparrow}$ and $n_k^{\downarrow}$ are equal to 1 for occupied orbitals, and 0 for unoccupied orbitals.

It is difficult to modify all orbital occupations, because of the large number of parameters and high computational cost. A CASSCF-like approach is used for the occupation number refinement. An active space containing LUMOs and HOMOs is created, where a limited number of orbital occupations above and below the Fermi level need to be refined.

In the refinement process, the final result of basis set optimization is the initial guess of occupation refinement. The population matrix is thus modified by varying the occupation number:

$$n_i^{\uparrow,\downarrow} = n_{i,0}^{\uparrow,\downarrow} + \delta n_i^{\uparrow,\downarrow} \tag{3.11}$$

and it should satisfy the conditions:

$$0 \leq n_i^{\uparrow,\downarrow} \leq 1 \qquad \text{Pauli principle} \tag{3.12a}$$

$$\sum_i^N (n_i^{\uparrow} + n_i^{\downarrow}) = N_{electron} \qquad \text{charge value conservation} \tag{3.12b}$$

$$\sum_i^N (n_i^{\uparrow} - n_i^{\downarrow}) = N_{spin} \qquad \text{spin value conservation} \tag{3.12c}$$

The new spin population matrix can then be obtained:

$$P_{ij}^{mag} = P_{ij,0}^{mag} + \delta P_{ij}^{mag} \tag{3.13}$$

with

$$P_{ij,0}^{mag} = \sum_k^{k=N} n_{k,0}^{\uparrow} c_{ik}^{\uparrow} c_{jk}^{\uparrow} - \sum_k^{k=N} n_{k,0}^{\downarrow} c_{ik}^{\downarrow} c_{jk}^{\downarrow} \tag{3.14a}$$

$$\delta P_{ij}^{mag} = \sum_k^{k=N} \delta n_k^{\uparrow} c_{ik}^{\uparrow} c_{jk}^{\uparrow} - \sum_k^{k=N} \delta n_k^{\downarrow} c_{ik}^{\downarrow} c_{jk}^{\downarrow} \tag{3.14b}$$

where only $n_i^{\uparrow,\downarrow}$ for the chosen set of LUMOs and HOMOs are modified to minimize the objective function L_2 (3.15) while fulfilling the conditions (3.12).

$$L_2 = L_1 - \mu_1 (\sum_{i=1} n_i^{\uparrow} - N_{electron}^{\uparrow}) - \mu_2 (\sum_{i=1} n_i^{\downarrow} - N_{electron}^{\downarrow}) \tag{3.15}$$

where μ_1, μ_2 are Lagrange multipliers. The resulting wave-function can then be used to calculate the electronic properties. This model is specifically adapted to magnetic refinements, because unpaired electrons mostly occupy the valence orbitals which can be included in the chosen HOMOs to create the active space.

3.2.3 Application to $YTiO_3$

We here report our preliminary results using such a procedure for refining a 1-RDM model with a focus on a particular group of atoms. The work reported below aims at studying how simple a model can be to account for the essential features of a 1-RDM which can be retrieved from a magnetic Compton scattering (MCS) and polarized neutron diffraction (PND) joint refinement.

To our best knowledge, there is no experimental 1-RDM yet for ferromagnetic perovskite $YTiO_3$. It is thus essential to use an existing 1-RDM which can serve as a reference to assess the quality of our reconstruction procedure and model. From this reference 1-RDM, properties such as structure factors or DMCPS can be computed. These quantities will then be considered as pseudo experimental data. Here, the reference is computed from a CRYSTAL14 output using the PBE0-1/3[63] hybrid functional and atomic basis sets[84, 85], as proposed by the CRYSTAL14 package[18, 19]. To better mimic experimental data, a Gaussian noise was generated and added to theoretical DMCPs (Figure3.7) and magnetic structure factors. At this point no other modification was made (no resolution smearing or systematic bias). The refined 1-RDM result will eventually be compared with the reference computations, and, thereby, help us to assess the quality of the model, the pertinence of the procedure and the influence of a variety of parameters. A first test case was conducted on UREA[a] [146]. Here, we focus on $YTiO_3$ for which all experimental data are now available (*Chapter 1*), and the reference theoretical 1-RDM is obtained by means of the limited cluster construction method (*Chapter 2*). At the present time, Debye-Waller effects are not yet implemented in our code and it would be premature to envisage any reconstruction from any real experimental data. This is the purpose of the ongoing work. Moreover, as a first stage, the 1-RDM model needs to be pre-calibrated using well-mastered pseudo experimental data.

Cluster construction

The first step is a cluster model construction to conduct the molecular-like *ab initio* calculations. According to previous work, the Ti–O_1–Ti fragment is identified as playing a major role in spin delocalization and possibly the ferromagnetic coupling of metallic sites. As presented in Figure 3.6, the cluster is built on the experimental atomic positions. The atomic charges initial guess are +3, +3 and −2 for Y, Ti and O respectively, and atomic spin is $\frac{1}{2}$ per Ti atom. Two Ti–O_1–Ti fragments are considered as a possible spin-coupling pathways. Other atoms in the immediate neighbourhood are replaced by point charges to simulate the crystal environment for the cluster. The charge values can be fixed by the topological charges, i.e. the charges obtained from the integration in the atomic basins of

[a] a UREA crystal toy-model was thus created, and a spin value 1 per molecule was forced to conduct the SCF computation.

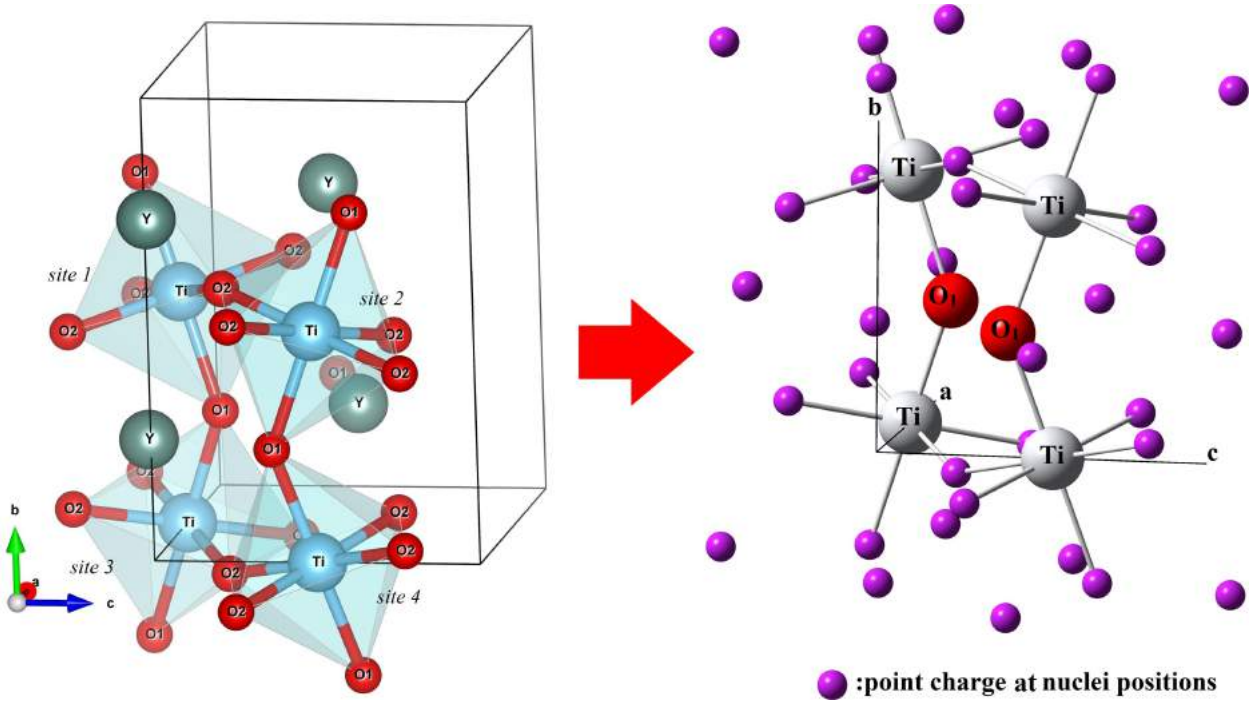

Figure 3.6: $YTiO_3$ 1-RDM cluster construction

an independent modelling[b].

Two points are worth mentioning for the cluster model construction:

- Atomic positions need to be those from the experimental structure. This is important for the $F_{mag}(\mathbf{Q})$ and $J_{mag}(\mathbf{u}, q)$ computations.
- Atomic charge and spin should respect atomic state in the solid, it means that the cluster can be charged. However, G09 can only take the total charge and as well as the total spin values, not that of atoms or basins[c].

Refinement parameters

A $\frac{1}{2}$ spin value per Ti atom was attributed as an initial guess. G09 calculation used HF[15] method and 6-31G basis set[25, 147–155]. The cluster charge and spin values are +8 (equal to $4 \times (+3) + 2 \times (-2)$) and 2 (equal to $4 \times (\frac{1}{2})$) respectively. The $3d$ electrons of Ti and $2p$ electrons of O are the focus of refinement. Given the asymmetry of the Ti environment in the model, it is expected that a perfect reproduction of the Ti contribution in the reference RDM will be difficult. To start with, the 3 HOMOs and 3 LUMOs are chosen to conduct the occupation refinement. 500 magnetic structure factors with $\frac{sin\theta}{\lambda}_{max} \approx 0.54\text{Å}^{-1}$ and 12

[b] In this case, it is computed by the TOPOND routine [66] available in CRYSTAL14). But experimental derived charges can obviously be also used.

[c] Except if fragments can be defined.

DMCPs have been generated to be used as pseudo-data values. Differences between refined and CRYSTAL14 results will be used to assess the method and the model.

Spin density and DMCP reproduction by 1-RDM refinement

The first objective is to reproduce the spin density and DMCPs. Spin density in plane Ti–O_1–Ti, O_1–Ti–O_2' and O_1–Ti–O_2 are calculated (with O_2 replaced by point charges). The latter is given in the appendix while Figure 3.8 and Figure 3.9 report spin density in planes Ti–O_1–Ti and O_1–Ti–O_2'.

The progression along $(a) \rightarrow (b) \rightarrow (c) \rightarrow (d)$ shows how the refinement model progressively approximates CRYSTAL14 results using a set of pseudo-experimental observations. Basis set optimization result (b) exhibits a dramatic improvement in the orbital descriptions, except the lack of blue contours around the O atoms. It is then corrected by occupation refinement (c), and ends up fairly close to the CRYSTAL14 results (d).

However, spin density in plane O_1–Ti–O_2 (Figure 3.10) does not succeed to reproduce the CRYSTAL14 distributions. Distribution around O_1 yields a similar result, but a problem arises in the vicinity of Ti. From previous works, the O_1–Ti–O_2 represents the xy plane in local axes and the d_{xy} population is reduced by crystal field effect. A cluster defined by two Ti–O_1–Ti fragments with point charges cannot reproduce the symmetry of an octahedron structure, nor corrects the crystal field effect (due to the lack of O_2 atoms). Another possible reason is that population refinement with only 3 HOMOs and 3 LUMOs (Figure 3.11, 3.12) cannot suffice to modify the d_{xy} populations. All the three planes (Figure 3.8, 3.9, 3.10) show several negative contours close to Ti atom along the Ti–O_1 direction in the refinement results, which are not present in the CRYSTAL14 figures. For this specific case, our objective is to refine the electronic behaviour in the vicinity of O_1. For the Ti case, another cluster such as TiO_6 with point charges around can be constructed so that crystal field effects are more adequately accounted for.

Spin density refinement with only magnetic structure factors can also be conducted. Figure C.4, Figure C.5 and Figure C.6 show the difficulty to reproduce the CRYSTAL14 results. In particular, the occupation refinement increases the difference for the interaction part between atoms. Comparing with the joint refinement (PND & MCS) case, DMCPs also have an influence on spin density refinement in position space. The objective is to refine the RDM (not only the electron densities in position space as in a multipolar model). The sole magnetic structure factors are just not enough. XRD or PND observations are more sensitive to localized electrons, while diffuse electrons are mainly described by the cross terms between atomic functions as numerously mentioned in the previous chapter. Once more, this shows the necessity of gathering multiple experiments to enrich the electron description in this solid.

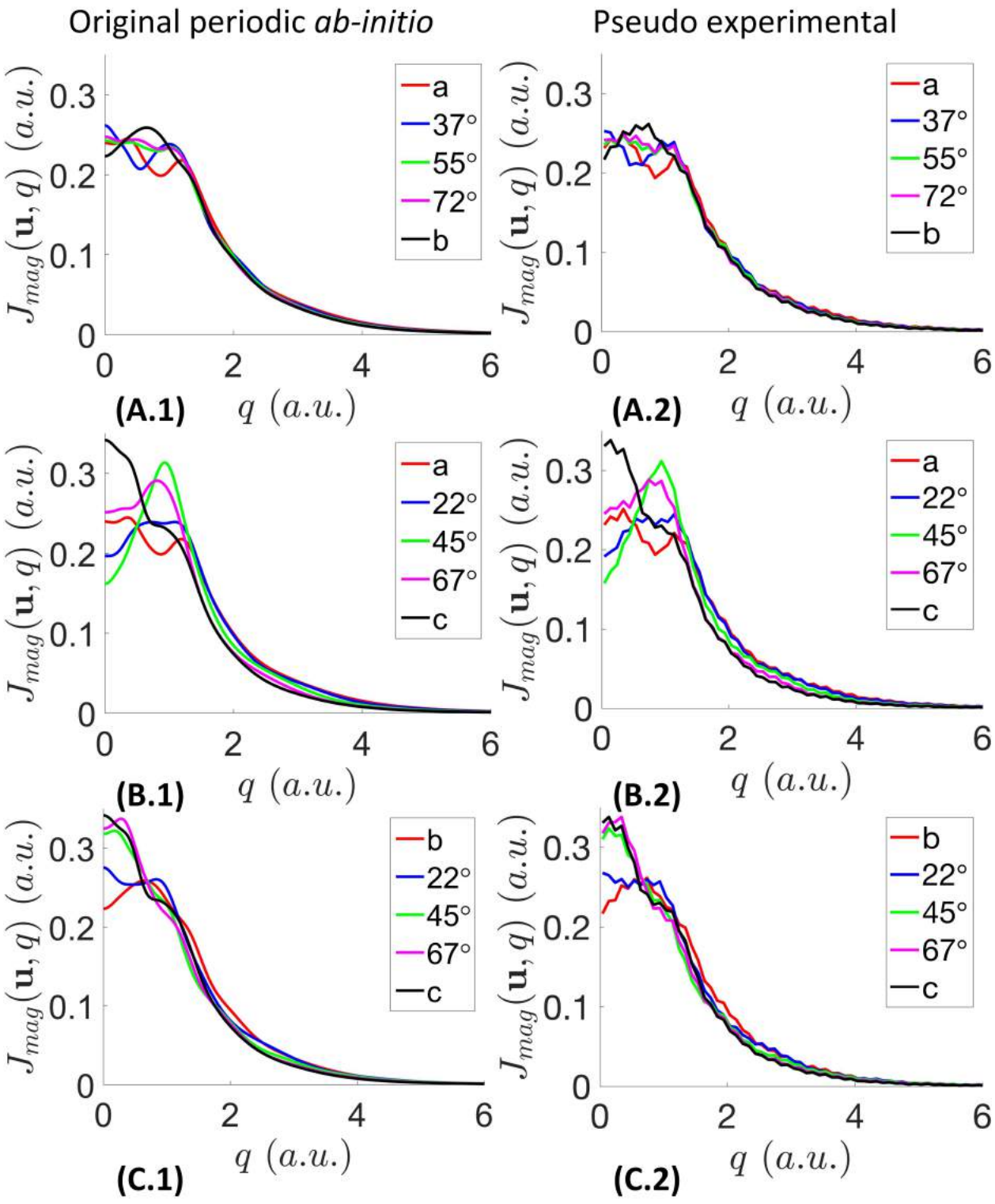

Figure 3.7: $YTiO_3$ DMCP with random noise
Directional magnetic compton profiles (DMCP) $J_{mag}(\mathbf{u}, q)$ for $YTiO_3$ for five non equivalent directions $\mathbf{u}$ in each plane. Each row corresponds to a set of DMCPs in a given plane: (A) (ab) plane; (B) (ac) plane; (C) (bc) plane. The spectra are in atomic units and normalized to one electron. Left column: original periodic *ab-initio* DMCP. Right column: periodic *ab-initio* DMCP, with random noise

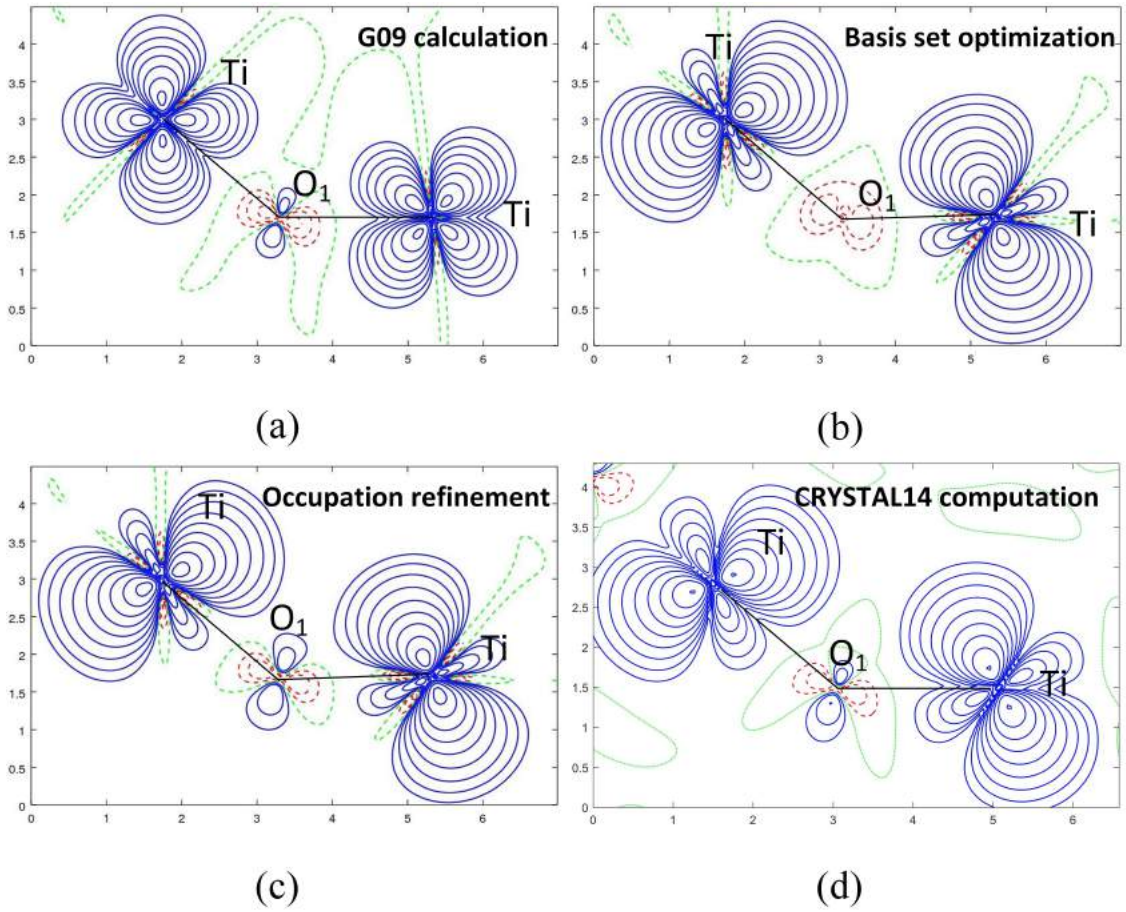

Figure 3.8: $YTiO_3$ spin density in plane Ti–O_1–Ti by 1-RDM refinement model (a) G09 calculation initial guess; (b) then after basis set optimization; (c) then after occupation refinement; (d) CRYSTAL14 computation. Contour at 0.01 $\times 2^n$, $(n = 0, \ldots, 12)$ $\mu_B \cdot$ Å^{-3}, positive (blue), negative (red) and neutral (green) lines.

From the DMCPs profiles (Figure 3.13 for the 3 principal crystallographic axes and Figure C.7 for the other directions in the three main crystallographic planes), the $\boldsymbol{b}$ direction (and directions close to $\boldsymbol{b}$) fairly reproduces CRYSTAL14 results. This corresponds to the Ti–O_1–Ti chemical bonds directions. Due to the lack of O_2 in the model, the other directions do not exhibit the same success. Nevertheless, this shows the sensitivity of Compton profiles to the chemical bond nature. Another remark is the weak difference between basis set optimization (red lines) and occupation refinement (blue lines) for the DMCPs result. The same remarks can be made concerning the 2D-MEMD reconstruction from DMCPs (Figure C.8, C.9, C.10). The $\boldsymbol{b}$ direction in (ab) and (bc) planes are very similar to the CRYSTAL14 results (Figure 1.30). However, (b) and (c) in Figure C.8, C.9, C.10 hardly show any change. This means that the occupation refinement does not modify significantly the RDM. A possible reason is the population refinement space cannot be limited to only 3 HOMOs and 3 LUMOs, which are quite delocalized. This is definitely not enough for having a satisfying impact on Ti $3d$ orbital rearrangement.

From the spin density and DMCPs results, electronic properties (related to the cluster structures) appear to be fairly well recovered by our oversimplified refinement model. *Ab*

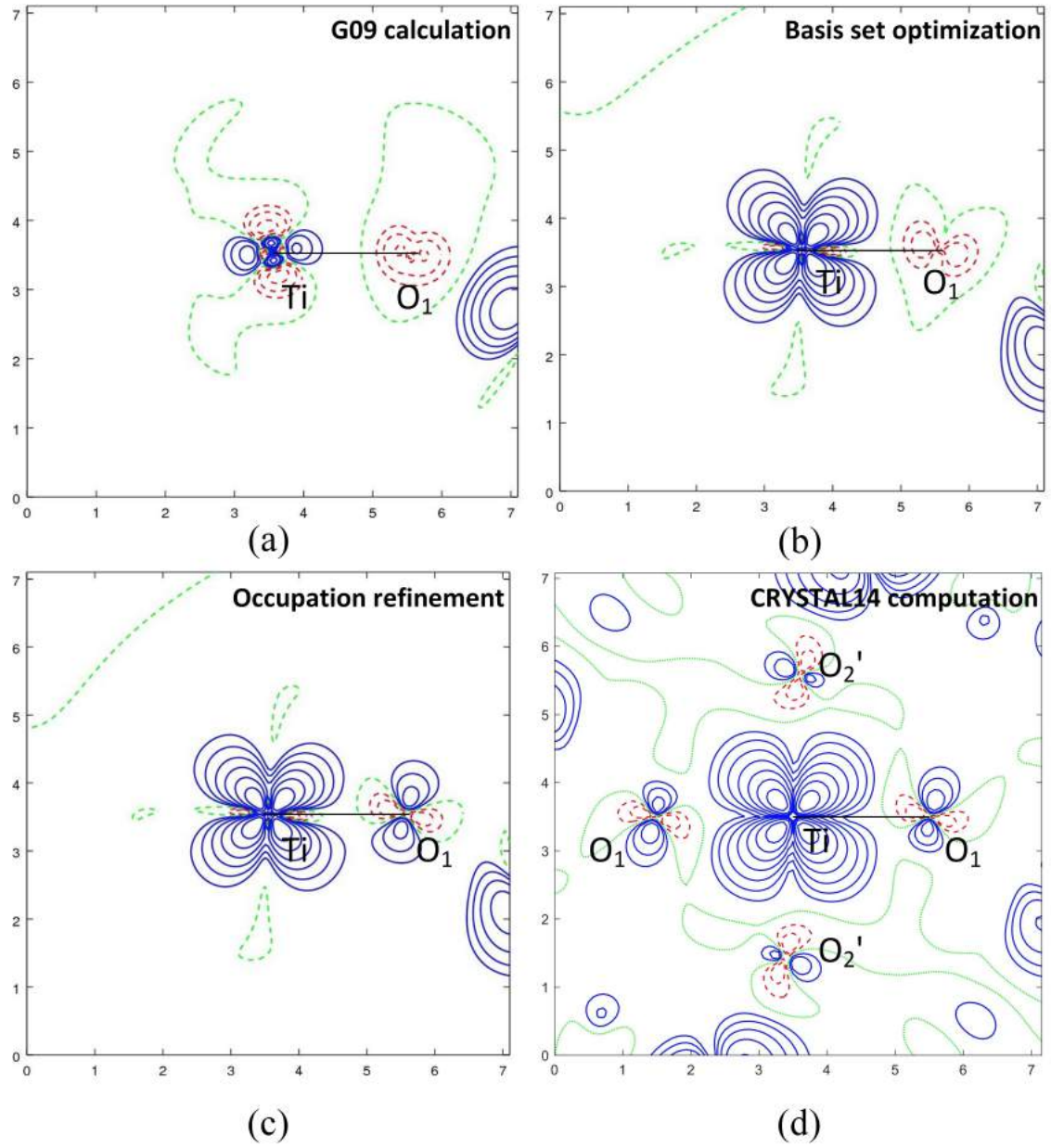

Figure 3.9: $YTiO_3$ spin density in plane O_1–Ti–O_2' by 1-RDM refinement model (a) G09 calculation initial guess; (b) then after basis set optimization; (c) then after occupation refinement; (d) CRYSTAL14 computation. Contour at 0.01 $\times 2^n$, $(n = 0, \ldots, 12)$ $\mu_B \cdot$ Å^{-3}, positive (blue), negative (red) and neutral (green) lines.

initio calculation (with G09 for our case) of the 6 atoms plus charges model can be improved using magnetic structure factors and DMCPs, so that it fairly reproduces the periodic state for position and momentum perspectives. The 1-RDM results can now be presented.

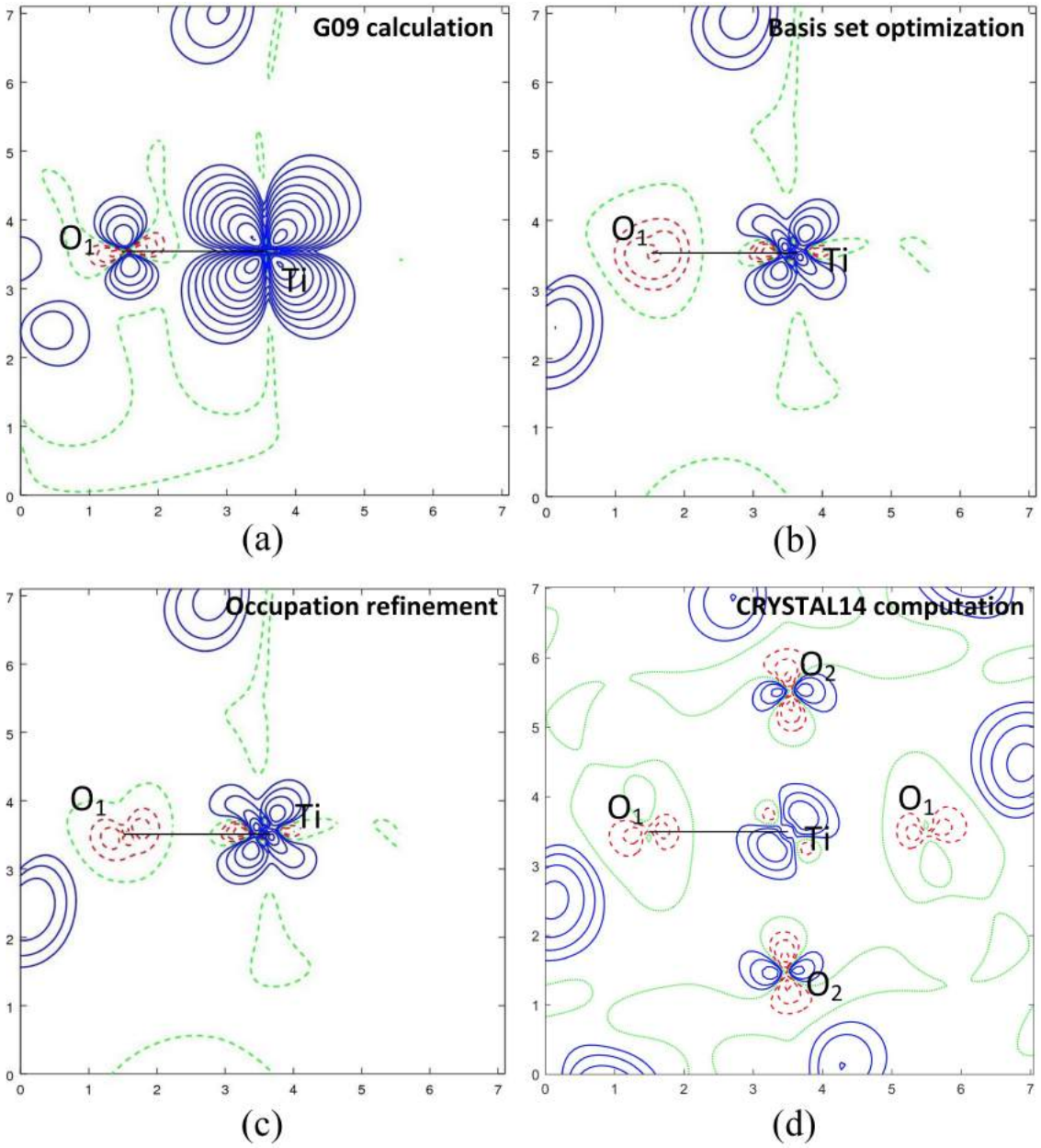

Figure 3.10: $YTiO_3$ spin density in plane O_1–Ti–O_2 by 1-RDM refinement model (a) G09 calculation initial guess; (b) then after basis set optimization; (c) then after occupation refinement; (d) CRYSTAL14 computation. Contour at 0.01 $\times 2^n$, $(n = 0, \ldots, 12)$ $\mu_B \cdot$ Å^{-3}, positive (blue), negative (red) and neutral (green) lines.

1-RDM refinement results

Spin-resolved 1-RDM along the chemical path Ti–O_1–Ti is displayed in Figure 3.14. According to the cluster definition, only the path between Ti atoms is worth considering. From Figure 3.14, there is a significant difference between G09 and CRYSTAL14 results. Both positive and negative contour numbers around O_1 atom (purple circles) are reduced from 3 to 2 by the basis set optimization. Furthermore, in TiO_1 interaction parts (orange triangles), the red contours number is reduced from 2 to 1. The occupation refinement slightly modifies the contour form, approaching the CRYSTAL14 maps. However, as

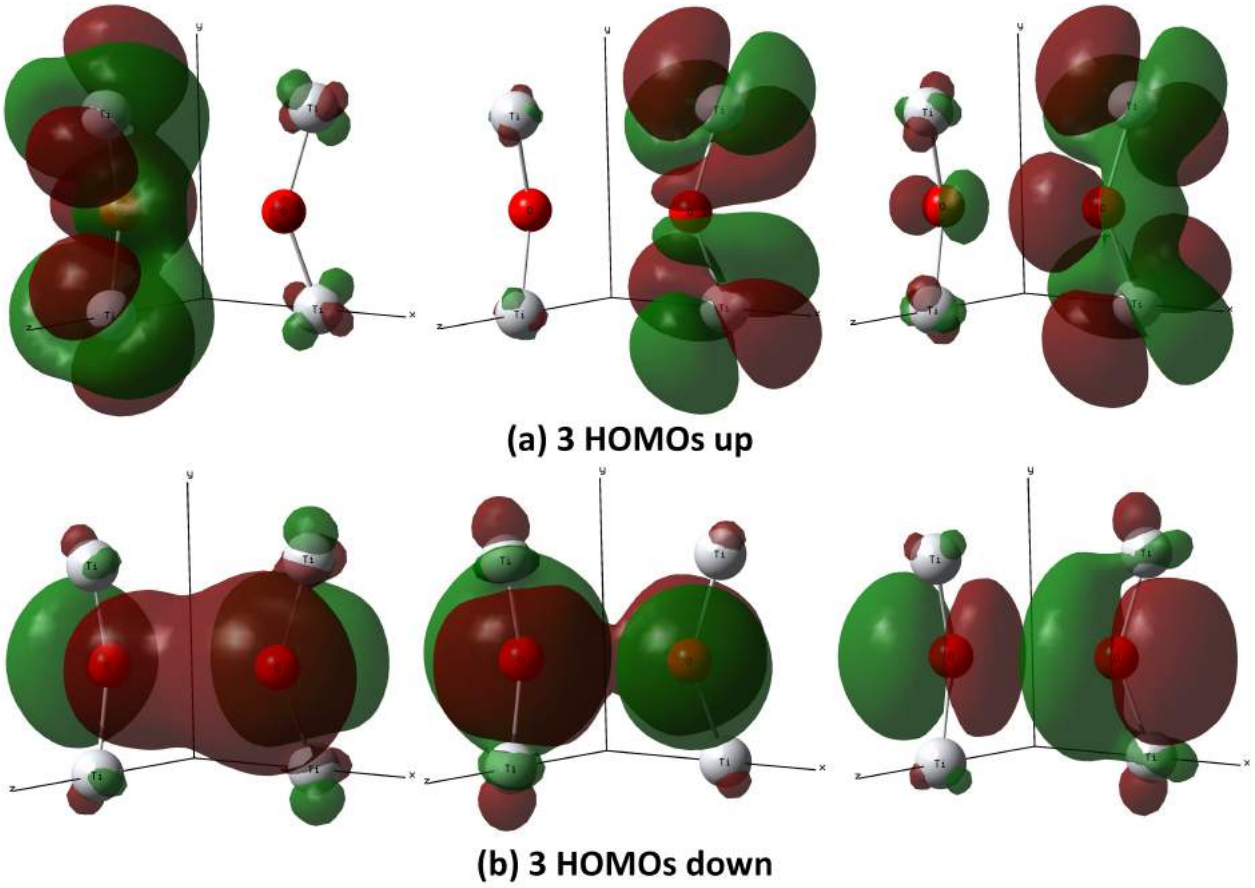

Figure 3.11: $YTiO_3$ 3 HOMOs
(a) 3 HOMOs up; (b) 3 HOMOs down. Isosurface value 0.01 a.u., positive (red), negative (green).

expected, a problem arises in the region close to Ti atom (black squares), where refinement and CRYSTAL14 results show inverse sign values. This problem can also be observed in the spin density maps along the Ti–O_1 path.

A refinement from magnetic structure factors only yields unsatisfying results (Figure C.11). The basis set optimization significantly improves the 1-RDM map (b), especially in regions around O_1. However, and rather surprisingly, the occupation refinement reduces the quality of the result (c) compared with the CRYSTAL14 computation (d), with an increased number of contours around O_1 atom and TiO_1 interaction regions increases. Even the spin density values (diagonal elements) cannot be correctly reproduced with only magnetic structure factors (as the spin density case). DMCPs have an impact not only on the off-diagonal elements but also on diagonal elements of the 1-RDM. This is because of the object of our model is not only the spin density refinement, but the complete electron information in the solid. A minimal number of magnetic structure factors and DMCPs are needed to achieve this goal by using a 1-RDM refinement model. However, the size of the active space is clearly too small and strategies have to be found to better act on specific regions of space.

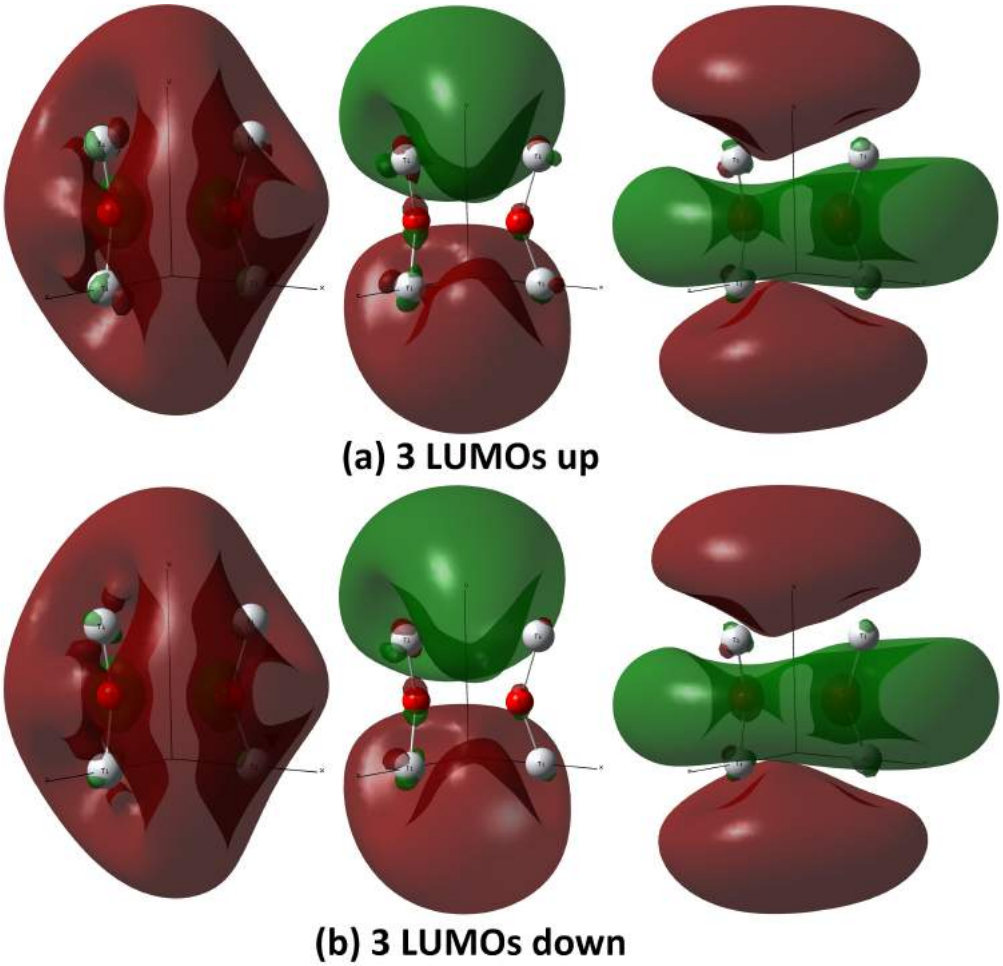

Figure 3.12: $YTiO_3$ 3 LUMOs
(a) 3 LUMOs up; (b) 3 LUMOs down. Isosurface value 0.01 a.u., positive (red), negative (green).

3.3 Discussions

From previous *section* 2.3.2, phase space functions can also be used to connect position and momentum representations. The Wigner and Moyal functions can be obtained from the 1-RDM refinement model, since all these quantities are based on the same wave-function (or density matrix). Wigner function bridges quantum and classical spaces, it associates **r** with **p** in phase space. Moyal function links directly to the experimental observables, but it is difficult to conduct a clear analysis as presented in *section* 2.3.2. However, the major problem is what additional information can be retrieved from the phase functions beyond the electron densities in position and momentum spaces or 1-RDM.

A discrete and limited set of data is available from scattering experiments. Error bars are conditioned by the measurement process. Refinement models are meant (and required to) to fit the data, but also help defining constraints for the refinement process and contribute to check the coherence between the different data based on the electronic state in a solid. For example, while HC concentrates on XRD data, the multipolar description is meant to

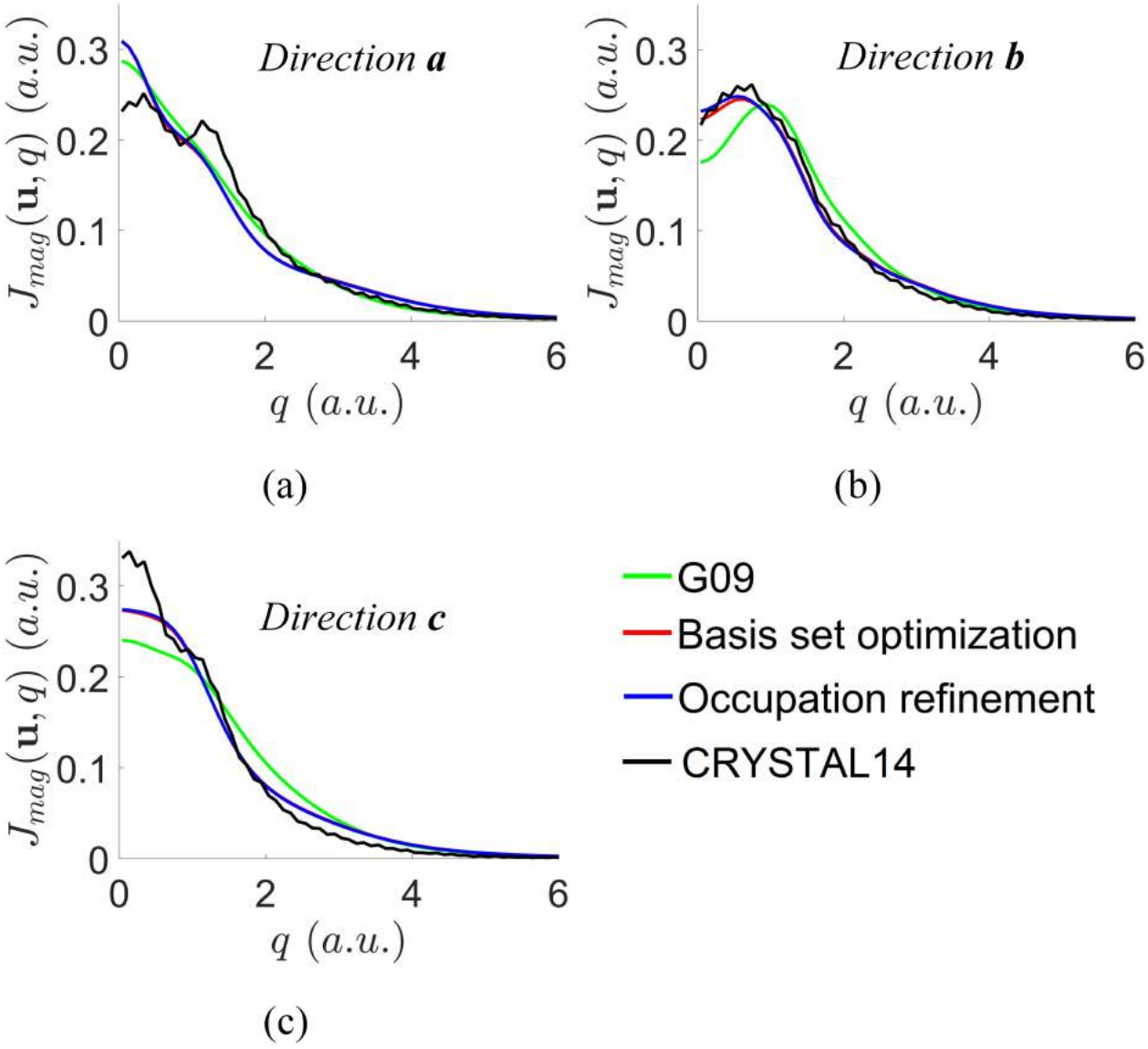

Figure 3.13: $YTiO_3$ DMCPs along 3 principal crystallographic axis by 1-RDM refinement model with DMCPs and magnetic structure factors
(a) Axis ***a***; (b) Axis ***b***; (c) Axis ***c***.

describe the entirety of the data and possibly eliminate outliers. Coherence between discrete XRD data can thus be preserved to fairly reproduce electron density in position space. The joint refinement (XRD & PND) model combines XRD and PND data, and not only considers individual coherences, but also between the two sets of data which have different origins. The goal is that the behaviours of electrons with spin up or down can be retrieved with better confidence. However, these two models are based on individual pseudo-atomic superpositions, interaction terms between atoms cannot be refined without additional information. This is available from Compton scattering experiments and a 1-RDM refinement model is now required to make the necessary connection between PND and MCS data (for the magnetic case). More global coherence and constraints between two different spaces (proved by "superposition" method) is introduced beyond internal PND or MCS data. It can thus reproduce

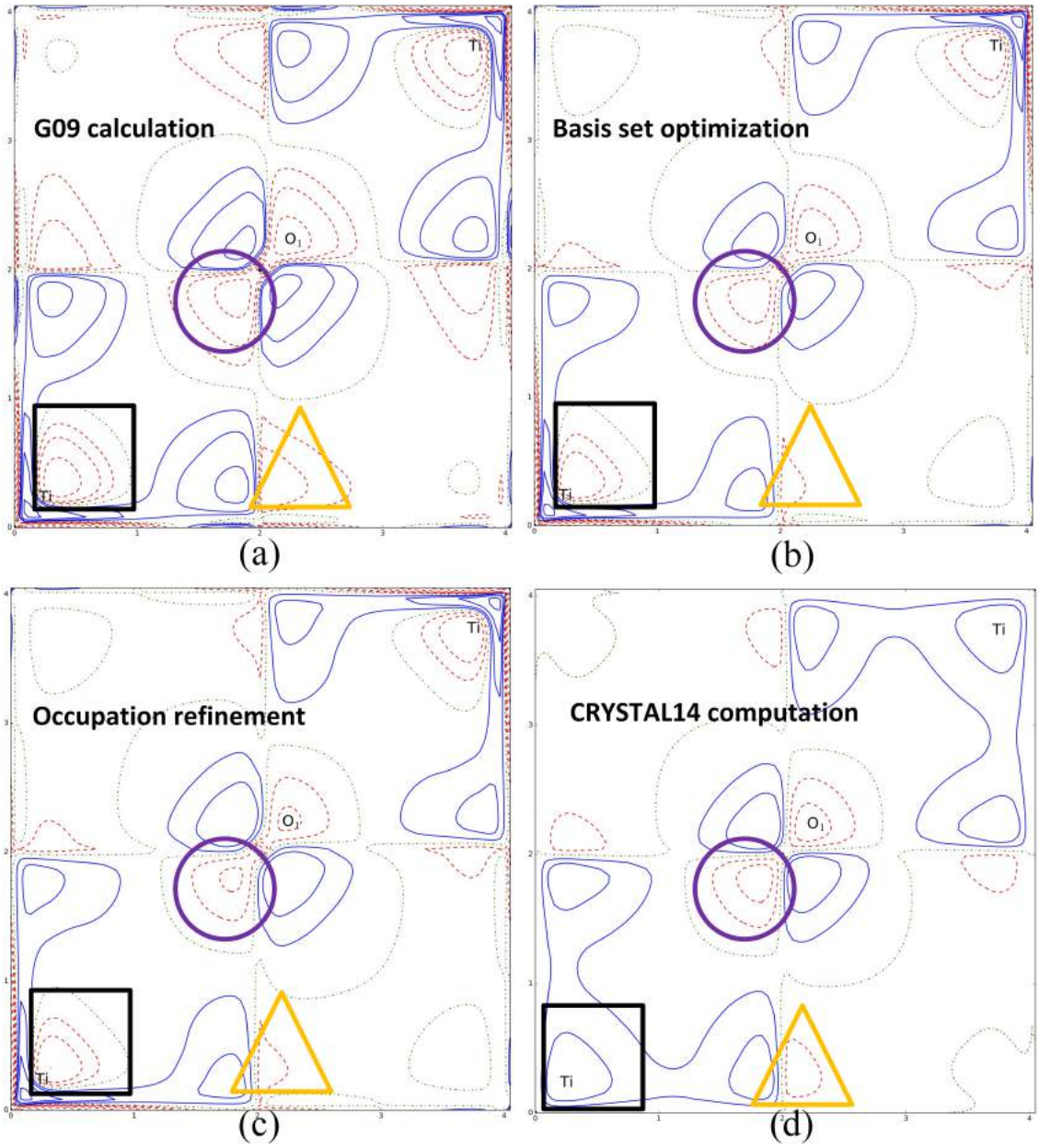

Figure 3.14: $YTiO_3$ 1-RDM along Ti–O_1–Ti by 1-RDM refinement model (a) G09 calculation initial guess; (b) then after basis set optimization; (c) then after occupation refinement; (d) Cluster model computation. Contours at $\pm 0.1 \times 2^n$ $(n = 0, ..., 20)$ $e{\cdot}\text{Å}^{-3}$ for total 1-RDM and $\pm 0.01 \times 2^n$ $(n = 0, ..., 20)$ $e{\cdot}\text{Å}^{-3}$ for spin 1-RDM, positive: blue lines, negative: red dashed lines and neutral: green dashed.

more detailed electronic information, including independent atoms and interactions between atoms contributions.

The model which has just been presented (for 1-RDM refinement) and the pseudo atom model concentrate on global and local contributions respectively. This first attempt in refining a 1-RDM model, with an initial guess from *ab initio* computation followed by basis set and occupation refinement aims at preserving the N-representability while staying coherent with several experimental data. The 1-RDM determination solely relies on

experimental observables (F_{mag} and J_{mag}) without recourse to energy minimization (during occupation refinement). Therefore, there are more degrees of freedom for parameters refinement based on experimental observations. However, the resulting 1-RDM is no longer idempotent. As preliminary results, this model is shown to fairly reproduce electronic properties in all representations (position and momentum). Nevertheless, further properties analysis based on electron density such as atomic charge and spin or topologies will require further work to reach the necessary degree of accuracy This work is still under progress.

Separation between atomic and interaction term contributions makes it more difficult and less flexible than a pseudo atom or near neighbour coupled atoms models. A population matrix modification (method of orbital separation in *Chapter 2*) can be considered in order to separate the atomic and interaction terms contribution. It is an additional difficulty that orbital populations with local axis can not be retrieved easily because, in this approach, a global axis system is imposed by the initial *ab initio* computation stage[a]. Moreover, the minimal cluster construction and choice of point charge values[b] should be based on more solid foundations. Obviously, the source function [44] is a possible tool to evaluate how the key atomic electrons are impacted by neighbouring atoms and assess their role as significant sources to the central cluster. Atoms with large weight values should be included in cluster construction. This is one of our current axes of possible development.

An *ab initio* calculation (HF or DFT) is of course a valuable method to obtain a system wave-function or 1-RDM. The objective is to minimize of the total system energy and no other quantity is accounted for in the SCF stage. A more general model based on *ab initio* with the constraint of experimental observations is of course possible. A very noticeable (and valuable) work in this spirit, using experimental XRD data only, was conducted by D. Jayatilaka [136, 141, 142]. Our approach is close to the latter but with a different philosophy. Energy is no longer the main criterion, no arbitrary Lagrange parameter is used and experimental data are the only reference to assess the 1-RDM pertinence. Both strategies are similar but they differ in their relation to energy minimisation. Jayatilaka's approach relies on a joint minimisation of the total energy and the weighted quadratic deviation between theoretical and experimental structure factors. The relative importance of both key quantities is driven by an arbitrary parameter, which is not a Lagrange parameter per se since it is not refined in the process. In the present work, energy minimisation is conducted in a mere initial stage to obtain molecular orbitals from which the experimental refinement is part of a post-processing work. Here the last word is given to the experiment, with all the possible freedom to constraint basis sets or occupation numbers.

[a] which causes a problem similar to that seen when deriving Ti($3d$) population in *Chapter 1*

[b] In the $YTiO_3$ case, two fragments are based on our previous work in *Chapter 1 and 2*, and point charge values are those derived from the theoretical topological analysis.

3.4 Summary

In this chapter, two methods are presented to connect the position and momentum spaces.

The "super-position" space approach is an indirect method. It allows a straightforward cross-checking between PND and MCS experiments. The performance of the "single atom model" is tested using a simple qualitative comparison of super-position and momentum densities. It helps clarifying the importance of different chemical bond path interaction from a comparison of results (between model, experimental and theoretical super-position density and 2D-MEMD): a good reproduction shows the negligible interaction of atoms. If not, significant interaction terms and possible magnetic coupling paths can be speculated. However, this method works better for magnetic properties of specific compounds (ideally with a single type of atom responsible for a major part of the spin density).

The 1-RDM refinement model is a direct and more general method. As it is based on an initial *ab-initio* computation, it makes it accessible for a larger class of compounds and, thereby, experimental data. Wave-function information in this model allows to refine not only the electron density in different spaces, but also the 1-RDM and other phase space distribution functions. The 1-RDM values along a chemical bond path can clarify the importance of the atomic sites interaction. It is sensitive to the nature of chemical bonds, and a spin resolved 1-RDM can be used to propose an elucidation of possible ferromagnetic pathways. It is worth emphasizing that, the cluster construction is the important and difficult part, especially for the metallic crystal compounds. Increasing the number of orbitals, or the size of the basis set, has a significant impact on the computation time and hinders our capacity to consider much more sophisticated models.

Both methods confirm the necessity of using momentum experimental data to obtain more complete electronic information in crystalline systems. The interaction between atoms is more easily clarified from the momentum perspective. As expected, the gathering of two spaces into a unique refinement yields more information, but brings more constraints, than the single representation traditional approach.

Conclusion and Perspectives

The purpose of this PhD work was to contribute to a description of electron density from a multiple representation perspective. *Ab initio* computation, on the theoretical side, and XRD, PND and MCS, on the experimental side, are used to investigate the electron behaviour in the solid from different aspects. Nevertheless it is now widely acknowledged that the combination of different experiments in position and momentum spaces can offer more precise and detailed information.

Pure *ab initio* computation, totally free of approximation, does not exist. It makes use of approximations in a variety of levels (determinants, functionals, perturbation orders) to estimate the electronic states in solids (or molecules). The comparison between experimental and theoretical results, in the Nit(SMe)Ph case, showed that standard DFT suffers from difficulties to reproduce the asymmetry of spin distribution between two NO groups. Mean field interaction approximations lacks precise electronic configuration information. They are problematic in specific cases, especially when spin density is involved, but it can be seen that the discrepancy already exists at the non spin resolved level. CASSCF for molecular cases and DFT+U for crystal cases are used to solve this problem. But it remains that disagreements between experimental and theoretical results must still encourage us to improve both experimental refinement models or theoretical computation techniques.

Electron density in position and momentum spaces can be analysed independently, and there is no doubt that today x-ray, electron or polarized neutron diffraction have reached a level of accuracy with which no other scattering experiment can compete. Their combination, with a joint refinement technique, brings us to another higher degree of accuracy as it pushes the boundaries of spin-resolved electron density in position space. Magnetic momentum density can be reconstructed from magnetic Compton scattering data. It is a valuable means for observing the most delocalized unpaired electrons. In the $YTiO_3$ case, investigations bring more details on the splitting of Ti $3d$ orbitals as they are subjected to crystal field effect in the TiO_6 octahedral structure. The $3d$ electrons occupy two t_{2g} state orbitals (d_{yz} and d_{xz}). It confirms that Ti atoms heavily contribute in the description of the unpaired electrons and thereby play an important role in magnetic properties. But this is not enough and a "simple" single site approach does not bring the full picture to ferromagnetism in such a

compound. It is necessary to better understand how the couplings are constructed and this requires a better description of how each Ti atom interacts with its neighbours. Such a more delocalized picture is also proven to be the key to describe momentum space properties. This is thus where a conjunction of approaches is expected to be the most fruitful.

In this respect, the "Super-position" density based on PND results is an indirect method to combine position and momentum spaces. It is the accumulation of spin densities from different atomic contributions translated to the same site. It can be projected onto any given plane and compared with 2D-MEMD. Geometrical similarities with 2D-MEMD are striking and confirm the coherence of different experiments. It thus offers a fast cross-checking method between PND and MCS experiments which usually requires a comparison with a third agent such as a theoretical computation reference. Quite paradoxically, the "isolated atom model" in its "super-position" representation and its 2D-MEMD, allows to analyse the role played by O atoms in magnetic properties for the $YTiO_3$ case. The strong sensitivity of momentum-space observables to delocalized electrons introduces significant discrepancies in planes involving Ti–O_1–Ti chemical bond directions. This very direction is thus identified as playing a major role in the spin delocalization and possibly the ferromagnetic coupling of metallic sites.

To reach another level of generality in the description, a l-RDM approach is valuable because it links position and momentum spaces by means of its diagonal and off-diagonal elements, respectively. Theoretical 1-RDM can be calculated based on periodic computations. 1-RDM contains not only the electron density information (diagonal elements), but also cross-term contributions between atoms (through the off-diagonal elements). These interaction effects are weak in position space, which confirms ignoring of cross-term contributions in position space is legitimate. However, the role played by these cross-term contributions becomes more apparent in momentum space.

In the $YTiO_3$ case, different roles for O_1 and O_2 can be clarified from DMCPs of TiO_1 and TiO_2 interaction contributions along Ti–O_1–Ti and Ti–O_2–Ti directions respectively. In 1-RDM maps, interactions are shown to contribute with a weight similar to that of independent atoms around atomic cross-region positions ($\Gamma(\mathbf{r}_{atomA}, \mathbf{r}_{atomB})$). The difference of TiO contributions shows that the Ti–O_1–Ti chemical bond constitutes a possible $Ti(3d)$–$O(2p)$–$Ti(3d)$ ferromagnetic coupling pathway.

Moyal function is useful to link experimental observations in position and momentum spaces. It corresponds directly to the Compton scattering at Bragg positions technique outcome. Nevertheless, this experiment is difficult to perform and a detailed interpretation scheme is still to be elaborated.

A 1-RDM refinement model allows a reconstruction from PND and MCS experimental data. The goal is not only to obtain the electron densitie in position or momentum spaces, but to

reach a level of description comparable to that of an experimental wave-function (providing that such a thing would exist). For $YTiO_3$, the model allows accounting for some coherent inter-atomic contributions, and includes weak magnetic contributions from O atoms.

Theoretical and experimental 1-RDM have been obtained by our two approaches. Some efforts are still ongoing and should be continued in the future to improve the accuracy and reliability of electronic information which can be obtained. On the theoretical side, more accurate computation quantum model beyond a mere standard HF or DFT approach (eg: CASSCF or DFT+U) should be considered to estimate the spin density in crystal. It is noteworthy that the impact of a CASSCF-like method on our *ab-initio* description of magnetic distribution in momentum representation has not yet been evaluated and would certainly be very instructive for future works on similar compounds.

To connect position and momentum spaces, probability distribution functions in phase space can be further developed by means of adapted cluster models with the hope that better analysis method can be developed to make full use of their respective specificities. On the experimental side, the "super-position" method needs to be extended to more general cases beyond single atom contributions to the major part of unpaired electron population.

Crystal field effects should be considered in a 1-RDM refinement model to provide a more realistic initial guess and thus allow for better final results regarding crystal properties. This will possibly involve a more flexible model where not only basis set functions and delocalized orbitals populations can be changed. Much of the effort will be put on this particular aspect in the immediate future.

Finally, Debye-Waller factors effects should be implemented in the (under development) refinement code. This will thus open a whole new range of possibilities for gathering experiments and better exploiting the richness of the ever increasing quality in experimental data.

Bibliography

[1] M. Deutsch, N. Claiser, S. Pillet, Y. Chumakov, P. Becker, J. M. Gillet, B. Gillon, C. Lecomte, and M. Souhassou. Experimental determination of spin-dependent electron density by joint refinement of x-ray and polarized neutron diffraction data. *Acta Crystallogr A*, 68(Pt 6):675–86, 2012.

[2] M. Deutsch, B. Gillon, N. Claiser, J. M. Gillet, C. Lecomte, and M. Souhassou. First spin-resolved electron distributions in crystals from combined polarized neutron and x-ray diffraction experiments. *IUCrJ*, 1(Pt 3):194–9, 2014.

[3] P. Macchi, J. M. Gillet, F. Taulelle, J. Campo, N. Claiser, and C. Lecomte. Modelling the experimental electron density: only the synergy of various approaches can tackle the new challenges. *IUCrJ*, 2(Pt 4):441–51, 2015.

[4] N. K. Hansen. Reconstruction of the electron momentum distribution from a set of directional compton profiles. Report, Hahn-Meitner-Institut fuer Kernforschung Berlin GmbH (Germany, 1980.

[5] L. Dobrzynski and A. Holas. Reconstruction of the electron momentum density distribution by the maximum entropy method. *Nuclear Instruments & Methods in Physics Research Section a-Accelerators Spectrometers Detectors and Associated Equipment*, 383(2-3):589–600, 1996.

[6] M. Cooper. *X-ray Compton scattering*. Oxford University Press on Demand, 2004.

[7] N. K. Hansen and P. Coppens. Electron population analysis of accurate diffraction data .6. testing aspherical atom refinements on small-molecule data sets. *Acta Crystallographica Section A*, 34(Nov):909–921, 1978.

[8] P. Coppens. *X-ray charge densities and chemical bonding*. International Union of Crystallography, 1997.

[9] P. J. Brown, J. B. Forsyth, and R. Mason. Magnetization densities and electronic states in crystals. *Philosophical Transactions of the Royal Society of London Series B-Biological Sciences*, 290(1043):481–495, 1980.

[10] Y. Sakurai, M. Ito, T. Urai, Y. Tanaka, N. Sakai, T. Iwazumi, H. Kawata, M. Ando, and N. Shiotani. An x-ray spectrometer for compton-scattering. *Review of Scientific Instruments*, 63(1):1190–1193, 1992.

[11] C. C. J. Roothaan. New developments in molecular orbital theory. *Rev. Mod. Phys.*, 23:69–89, Apr 1951.

[12] R. G. Parr and W. Yang. Density-functional theory of the electronic structure of molecules. *Annu Rev Phys Chem*, 46(1):701–28, 1995.

[13] W. Kohn and L. J. Sham. Self-consistent equations including exchange and correlation effects. *Physical Review*, 140(4A):A1133, 1965.

[14] Cesare Pisani, Roberto Dovesi, and Carla Roetti. *Hartree-Fock Ab Initio Treatment of Crystalline Systems*, volume 48. Springer Science & Business Media, 2012.

[15] C. C. J. Roothaan. Self-consistent field theory for open shells of electronic systems. *Reviews of Modern Physics*, 32(2):179–185, 1960.

[16] J. A. Pople and R. K. Nesbet. Self-consistent orbitals for radicals. *Journal of Chemical Physics*, 22(3):571–572, 1954.

[17] F. Ogliaro, M. Bearpark, JJ. Heyd, E. Brothers, KN. Kudin, VN. Staroverov, R. Kobayashi, J. Normand, K. Raghavachari, and A. Rendell. Gaussian 09, revision a. 02. gaussian. *Inc.: Wallingford, CT*, 2009.

[18] R. Dovesi, R. Orlando, A. Erba, C. M. Zicovich-Wilson, B. Civalleri, S. Casassa, L. Maschio, M. Ferrabone, M. De La Pierre, P. D'Arco, Y. Noel, M. Causa, M. Rerat, and B. Kirtman. Crystal14: A program for the ab initio investigation of crystalline solids. *International Journal of Quantum Chemistry*, 114(19):1287–1317, 2014.

[19] R. Dovesi, VR. Saunders, C. Roetti, R. Orlando, CM. Zicovich-Wilson, F. Pascale, B. Civalleri, K. Doll, NM. Harrison, IJ. Bush, et al. Crystal14 user's manual; university of torino: Torino, italy, 2014. *There is no corresponding record for this reference*, 2014.

[20] P. O. Löwdin. Quantum theory of many-particle systems. i. physical interpretations by means of density matrices, natural spin-orbitals, and convergence problems in the method of configurational interaction. *Physical Review*, 97(6):1474, 1955.

[21] R Stowasser and R Hoffmann. What do the kohn- sham orbitals and eigenvalues mean? *Journal of the american chemical society*, 121(14):3414–3420, 1999.

[22] J Foresman and A Frisch. Exploring chemistry with electronic structure methods: a guide to using gaussian. 1996.

[23] Cesare Pisani. *Quantum-mechanical ab-initio calculation of the properties of crystalline materials*, volume 67. Springer Science & Business Media, 2012.

[24] V. R. Saunders, C. Freyria-Fava, R. Dovesi, L. Salasco, and C. Roetti. On the electrostatic potential in crystalline systems where the charge-density is expanded in gaussian functions. *Molecular Physics*, 77(4):629–665, 1992.

[25] W. J. Hehre, R. Ditchfield, and J. A. Pople. Self—consistent molecular orbital methods. xii. further extensions of gaussian—type basis sets for use in molecular orbital studies of organic molecules. *The Journal of Chemical Physics*, 56(5):2257–2261, 1972.

[26] B. O. Roos, P. R. Taylor, and P. E. M. Siegbahn. A complete active space SCF method (CASSCF) using a density matrix formulated super-CI approach. *Chemical Physics*, 48(2):157–173, 1980.

[27] Per Siegbahn, Anders Heiberg, Björn Roos, and Bernard Levy. A comparison of the super-CI and the Newton-Raphson scheme in the complete active space SCF method. *Physica Scripta*, 21(3-4):323, 1980.

[28] P. E. M. Siegbahn, J. Almlof, A. Heiberg, and B. O. Roos. The complete active space SCF (CASSCF) method in a Newton–Raphson formulation with application to the HNO molecule. *Journal of Chemical Physics*, 74(4):2384–2396, 1981.

[29] J. Olsen. The CASSCF method: A perspective and commentary. *International Journal of Quantum Chemistry*, 111(13):3267–3272, 2011.

[30] B Roos. A new method for large-scale Cl calculations. *Chemical Physics Letters*, 15(2):153–159, 1972.

[31] F. Aquilante, J. Autschbach, R. K. Carlson, L. F. Chibotaru, M. G. Delcey, L. De Vico, I. Fdez Galvan, N. Ferre, L. M. Frutos, L. Gagliardi, M. Garavelli, A. Giussani, C. E. Hoyer, G. Li Manni, H. Lischka, D. Ma, P. A. Malmqvist, T. Muller, A. Nenov, M. Olivucci, T. B. Pedersen, D. Peng, F. Plasser, B. Pritchard, M. Reiher, I. Rivalta, I. Schapiro, J. Segarra-Marti, M. Stenrup, D. G. Truhlar, L. Ungur, A. Valentini, S. Vancoillie, V. Veryazov, V. P. Vysotskiy, O. Weingart, F. Zapata, and R. Lindh. Molcas 8: New capabilities for multiconfigurational quantum chemical calculations across the periodic table. *J Comput Chem*, 37(5):506–41, 2016.

[32] B. Dawson. Aspherical atomic scattering factors in crystal structure refinement. i. coordinate and thermal motion effects in a model centrosymmetric system. *Acta Crystallographica*, 17(8):990–996, 1964.

[33] R. F. Stewart. Valence structure from coherent x-ray scattering - fourier difference synthesis. *Journal of Chemical Physics*, 48(11):4882–4889, 1968.

[34] R. F. Stewart. Generalized x-ray scattering factors. *Journal of Chemical Physics*, 51(10):4569–+, 1969.

[35] R. F. Stewart. Electron population analysis with generalized x-ray-scattering factors - higher multipoles. *Journal of Chemical Physics*, 58(4):1668–1676, 1973.

[36] F. L. Hirshfeld. Differences densities by least-squares refinement - fumaramic acid. *Acta Crystallographica Section B-Structural Crystallography and Crystal Chemistry*, B 27(Apr15):769–+, 1971.

[37] M. T. Harel and FL. Hirshfeld. Difference densities by least-squares refinement. ii. tetracyanocyclobutane. *Acta Crystallographica Section B: Structural Crystallography and Crystal Chemistry*, 31(1):162–172, 1975.

[38] C. Jelsch, B. Guillot, A. Lagoutte, and C. Lecomte. Advances in protein and small-molecule charge-density refinement methods using mopro. *Journal of Applied Crystallography*, 38(1):38–54, 2005.

[39] A. Volkov, X. Li, T. Koritsanszky, and P. Coppens. Ab initio quality electrostatic atomic and molecular properties including intermolecular energies from a transferable theoretical pseudoatom databank. *Journal of Physical Chemistry A*, 108(19):4283–4300, 2004.

[40] V. Petricek, M. Dusek, and L. Palatinus. Crystallographic computing system jana2006: General features. *Zeitschrift Fur Kristallographie-Crystalline Materials*, 229(5):345–352, 2014.

[41] E. Clementi and D. L. Raimondi. Atomic screening constants from SCF functions. *Journal of Chemical Physics*, 38(11):2686–2689, 1963.

[42] E. Clementi and C. Roetti. Roothaan-Hartree-Fock atomic wavefunctions: Basis functions and their coefficients for ground and certain excited states of neutral and ionized atoms, Z$\leq$ 54. *Atomic data and nuclear data tables*, 14(3-4):177–478, 1974.

[43] J. Bentley and R. F. Stewart. Two-center calculations for x-ray scattering. *Journal of Computational Physics*, 11(1):127–145, 1973.

[44] C Gatti. The source function descriptor as a tool to extract chemical information from theoretical and experimental electron densities. In *Electron Density and Chemical Bonding II*, pages 193–285. Springer, 2011.

[45] RJ. Papoular and B. Gillon. Maximum entropy reconstruction of spin density maps in crystals from polarized neutron diffraction data. *EPL (Europhysics Letters)*, 13(5):429, 1990.

[46] P. Schleger, A. PuigMolina, E. Ressouche, O. Rutty, and J. Schweizer. A general maximum-entropy method for model-free reconstructions of magnetization densities from polarized neutron diffraction data. *Acta Crystallographica Section A*, 53(4):426–435, 1997.

[47] B. Gillon and P. Becker. *Magnetization densities in material science*, pages 277–302. Springer, 2011.

[48] P. Coppens, Z. Su, and PJ. Becker. *Analysis of charge and spin densities*, pages 713–734. Springer, 2006.

[49] P. J. Brown, A. Capiomont, B. Gillon, and J. Schweizer. Spin-densities in free-radicals. *Journal of Magnetism and Magnetic Materials*, 14(2-3):289–294, 1979.

[50] J. X. Boucherle, B. Gillon, J. Maruani, and J. Schweizer. Determination by polarized neutron diffraction of the spin density distribution in a non-centrosymmetrical crystal of DPPH: C6H6. *Journal De Physique*, 43(Nc-7):227–234, 1982.

[51] B. M. Bell, J. V. Burke, and A. Schumitzky. A relative weighting method for estimating parameters and variances in multiple data sets. *Computational Statistics & Data Analysis*, 22(2):119–135, 1996.

[52] J. M. Gillet, P. J. Becker, and P. Cortona. Joint refinement of a local wave-function model from compton and bragg scattering data. *Physical Review B*, 63(23), 2001.

[53] J. M. Gillet and P. J. Becker. Position and momentum densities. complementarity at work: refining a quantum model from different data sets. *Journal of Physics and Chemistry of Solids*, 65(12):2017–2023, 2004.

[54] A. B. Voufack, N. Claiser, C. Lecomte, S. Pillet, Y. Pontillon, B. Gillon, Z. Yan, J. M. Gillet, M. Marazzi, A. Genoni, and M. Souhassou. When combined x-ray and polarized neutron diffraction data challenge high-level calculations: spin-resolved electron density of an organic radical. *Acta Crystallographica Section B-Structural Science Crystal Engineering and Materials*, 73(4):544–549, 2017.

[55] S. Pillet, M. Souhassou, Y. Pontillon, A. Caneschi, D. Gatteschi, and C. Lecomte. Investigation of magnetic interaction pathways by experimental electron density measurements: application to an organic free radical, p-(methylthio)phenyl nitronyl nitroxide. *New Journal of Chemistry*, 25(1):131–143, 2001.

[56] Y. Pontillon, T. Akita, A. Grand, K. Kobayashi, E. Lelievre-Berna, J. Pecaut, E. Ressouche, and J. Schweizer. Experimental and theoretical spin density in a ferromagnetic molecular complex presenting interheteromolecular hydrogen bonds. *Journal of the American Chemical Society*, 121(43):10126–10133, 1999.

[57] Y. Pontillon, A. Caneschi, D. Gatteschi, A. Grand, E. Ressouche, R. Sessoli, and J. Schweizer. Experimental spin density in a purely organic free radical: Visualisation of the ferromagnetic exchange pathway in p-(methylthio)phenyl nitronyl nitroxide, nit(sme)ph. *Chemistry-a European Journal*, 5(12):3616–3624, 1999.

[58] Y. Zhao and D. G. Truhlar. The m06 suite of density functionals for main group thermochemistry, thermochemical kinetics, noncovalent interactions, excited states, and transition elements: two new functionals and systematic testing of four m06-class functionals and 12 other functionals. *Theoretical Chemistry Accounts*, 120(1-3):215–241, 2008.

[59] T. Yanai, D. P. Tew, and N. C. Handy. A new hybrid exchange-correlation functional using the Coulomb-attenuating method (CAM-B3LYP). *Chemical Physics Letters*, 393(1-3):51–57, 2004.

[60] A. D. Becke. Density-functional thermochemistry. iii. the role of exact exchange. *The Journal of chemical physics*, 98(7):5648–5652, 1993.

[61] T. H. Dunning Jr. Gaussian basis sets for use in correlated molecular calculations. i. the atoms boron through neon and hydrogen. *The Journal of chemical physics*, 90(2):1007–1023, 1989.

[62] J. P. Perdew, K. Burke, and M. Ernzerhof. Generalized gradient approximation made simple. *Phys Rev Lett*, 77(18):3865–3868, 1996.

[63] C. A. Guido, E. Bremond, C. Adamo, and P. Cortona. Communication: One third: A new recipe for the PBE0 paradigm. *J Chem Phys*, 138(2):021104, 2013.

[64] M. F. Peintinger, D. V. Oliveira, and T. Bredow. Consistent gaussian basis sets of triple-zeta valence with polarization quality for solid-state calculations. *J Comput Chem*, 34(6):451–9, 2013.

[65] TA. Keith. Aimall (version 10.07. 25). *Overland Park, KS, USA: TK Gristmill Software*, 2010.

[66] C Gatti and S Casassa. Topond14 user's manual. *CNR-ISTM Milano, Milano*, 2014.

[67] R. FW. Bader. *Atoms in molecules*. Wiley Online Library, 1990.

[68] C. Gatti. Chemical bonding in crystals: new directions. *Zeitschrift Fur Kristallographie*, 220(5-6):399–457, 2005.

[69] W. Tang, E. Sanville, and G. Henkelman. A grid-based bader analysis algorithm without lattice bias. *J Phys Condens Matter*, 21(8):084204, 2009.

[70] C. Gatti, G. Macetti, and L. Lo Presti. Insights on spin delocalization and spin polarization mechanisms in crystals of azido copper (ii) dinuclear complexes through the electron spin density source function. *Acta Crystallographica Section B: Structural Science, Crystal Engineering and Materials*, 73(4):565–583, 2017.

[71] M. I. Aroyo. International tables for crystallography, volume a, space-group symmetry. *Acta Crystallographica Section A: Foundations and Advances*, A(3), 2016.

[72] Boguslawski. K., C. R. Jacob, and M. Reiher. Can dft accurately predict spin densities? analysis of discrepancies in iron nitrosyl complexes. *Journal of chemical theory and computation*, 7(9):2740–2752, 2011.

[73] C. R. Jacob and M. Reiher. Spin in density-functional theory. *International Journal of Quantum Chemistry*, 112(23):3661–3684, 2012.

[74] A. C. Komarek, H. Roth, M. Cwik, W. D. Stein, J. Baier, M. Kriener, F. Bourée, T. Lorenz, and M. Braden. Magnetoelastic coupling in $r\mathrm{Tio}_3$ ($r = \mathrm{La}, \mathrm{Nd}, \mathrm{Sm}, \mathrm{Gd}, \mathrm{Y}$) investigated with diffraction techniques and thermal expansion measurements. *Physical Review B*, 75(22):224402, 2007.

[75] H Sawada and K Terakura. Orbital and magnetic orderings in localized t_{2g} systems, $YTiO_3$ and YVO_3: Comparison with a more itinerant e_g system $LaMnO_3$. *Physical Review B*, 58(11):6831, 1998.

[76] M. Mochizuki and M. Imada. Orbital physics in the perovskite Ti oxides. *New Journal of Physics*, 6(1):154, 2004.

[77] J. Akimitsu, H. Ichikawa, N. Eguchi, T. Miyano, M. Nishi, and K. Kakurai. Direct observation of orbital ordering in $YTiO_3$ by means of the polarized neutron diffraction technique. *Journal of the Physical Society of Japan*, 70(12):3475–3478, 2001.

[78] M. Ito, N. Tuji, F. Itoh, H. Adachi, E. Arakawa, K. Namikawa, H. Nakao, Y. Murakami, Y. Taguchi, and Y. Tokura. Observation of ordered orbital of $YTIO_3$ by the X-ray magnetic diffraction experiments. *Journal of Physics and Chemistry of Solids*, 65(12):1993–1997, 2004.

[79] JH Van Vleck. Theory of the variations in paramagnetic anisotropy among different salts of the iron group. *Physical Review*, 41(2):208, 1932.

[80] JR. Hester, K. Tomimoto, H. Noma, FP. Okamura, and J. Akimitsu. Electron density in $YTiO_3$. *Acta Crystallographica Section B: Structural Science*, 53(5):739–744, 1997.

[81] W. A. Harrison. *Electronic structure and the properties of solids: the physics of the chemical bond*. Courier Corporation, 2012.

[82] S. Dapprich, I. Komaromi, K. S. Byun, K. Morokuma, and M. J. Frisch. A new oniom implementation in gaussian98. part i. the calculation of energies, gradients, vibrational frequencies and electric field derivatives. *Journal of Molecular Structure-Theochem*, 461:1–21, 1999.

[83] S Piskunov, E Heifets, RI Eglitis, and G Borstel. Bulk properties and electronic structure of $SrTiO_3$, $BaTiO_3$, $PbTiO_3$ perovskites: an *ab initio* HF/DFT study. *Computational Materials Science*, 29(2):165–178, 2004.

[84] A. Erba, Kh E. El-Kelany, M. Ferrero, I. Baraille, and M. Rérat. Piezoelectricity of $SrTiO_3$: An *ab initio* description. *Physical Review B*, 88(3), 2013.

[85] A. Buljan, P. Alemany, and E. Ruiz. Electronic structure and bonding in $CuMO_2$(M = Al, Ga, Y) delafossite-type oxides: An ab initio study. *The Journal of Physical Chemistry B*, 103(38):8060–8066, 1999.

[86] A Holladay, P Leung, and P Coppens. Generalized relations between d-orbital occupancies of transition-metal atoms and electron-density multipole population parameters from x-ray diffraction data. *Acta Crystallographica Section A: Foundations of Crystallography*, 39(3):377–387, 1983.

[87] W A Sokalski and RA Poirier. Cumulative atomic multipole representation of the molecular charge distribution and its basis set dependence. *Chemical Physics Letters*, 98(1):86–92, 1983.

[88] A. Gukasov, A. Goujon, J. L. Meuriot, C. Person, G. Exil, and G. Koskas. Super-6T2, a new position-sensitive detector polarized neutron diffractometer. *Physica B-Condensed Matter*, 397(1-2):131–134, 2007.

[89] I. A. Kibalin, Z. Yan, A. B. Voufack, S. Gueddida, B. Gillon, A. Gukasov, F. Porcher, A. M. Bataille, F. Morini, N. Claiser, M. Souhassou, C. Lecomte, J. M. Gillet, M. Ito, K. Suzuki, H. Sakurai, Y. Sakurai, C. M. Hoffmann, and X. P. Wang. Spin density in $YTiO_3$: I. joint refinement of polarized neutron diffraction and magnetic x-ray diffraction data leading to insights into orbital ordering. *Physical Review B*, 96(5):054426, 2017.

[90] L. Lam and P. Platzman. Momentum density and compton profile of the inhomogeneous interacting electronic system. i. formalism. *Physical Review B*, 9(12):5122–5127, 1974.

[91] R. K. Pathak, A. Kshirsagar, R. Hoffmeyer, and A. J. Thakkar. Leading corrections to atomic impulse-approximation compton profiles: A density-functional approach. *Phys Rev A*, 48(4):2946–2951, 1993.

[92] J. R. Hart and A. J. Thakkar. Moments of the electron momentum density: Requirements for ab initio and density functional theory calculations. *International Journal of Quantum Chemistry*, 102(5):673–683, 2005.

[93] S. Ragot. Exact Kohn-Sham versus Hartree-Fock in momentum space: Examples of two-fermion systems. *J Chem Phys*, 125(1):014106, 2006.

[94] A. Erba, C. Pisani, S. Casassa, L. Maschio, M. Schutz, and D. Usvyat. Mp2 versus density-functional theory study of the compton profiles of crystalline urea. *Physical Review B*, 81(16), 2010.

[95] N. Hiraoka, T. Buslaps, V. Honkimäki, H. Minami, and H. Uwe. Fermi surface nesting inba1−xkxbio3observed by compton profile measurement. *Physical Review B*, 71(20), 2005.

[96] A. Koizumi, T. Nagao, N. Sakai, K. Hirota, and Y. Murakami. Coexistence of polaronic and band states in a bilayer manganite from two-dimensional reconstruction of magnetic compton profiles. *Physical Review B*, 74(1), 2006.

[97] Y. Sakurai, M. Itou, B. Barbiellini, P. E. Mijnarends, R. S. Markiewicz, S. Kaprzyk, J. M. Gillet, S. Wakimoto, M. Fujita, S. Basak, Y. J. Wang, W. Al-Sawai, H. Lin, A. Bansil, and K. Yamada. Imaging doped holes in a cuprate superconductor with high-resolution compton scattering. *Science*, 332(6030):698–702, 2011.

[98] N. K. Hansen, P. Pattison, and S. Jr. Analysis of the 3-dimensional electron-distribution in silicon using directional compton profile measurements. *Zeitschrift Fur Physik B-Condensed Matter*, 66(3):305–315, 1987.

[99] Y. Tanaka, N. Sakai, Y. Kubo, and H. Kawata. Three-dimensional momentum density of magnetic electrons in ferromagnetic iron. *Phys Rev Lett*, 70(10):1537–1540, 1993.

[100] W. Schulke, G. Stutz, F. Wohlert, and A. Kaprolat. Electron momentum-space densities of Li metal: A high-resolution Compton-scattering study. *Phys Rev B Condens Matter*, 54(20):14381–14395, 1996.

[101] J. M. Gillet, C. Fluteaux, and P. J. Becker. Analytical reconstruction of momentum density from directional compton profiles. *Physical Review B*, 60(4):2345–2349, 1999.

[102] Y. Tanaka, Y. Sakurai, A. T. Stewart, N. Shiotani, P. E. Mijnarends, S. Kaprzyk, and A. Bansil. Reconstructed three-dimensional electron momentum density in lithium: A compton scattering study. *Physical Review B*, 63(4), 2001.

[103] T. Nagao, Y. Kubo, A. Koizumi, H. Kobayashi, M. Itou, and N. Sakai. Momentum-density distribution of magnetic electrons in ferromagnetic nickel. *Journal of Physics-Condensed Matter*, 20(5):055201, 2008.

[104] R. J. Barlow. *Statistics: a guide to the use of statistical methods in the physical sciences*, volume 29. John Wiley & Sons, 1989.

[105] N Tsuji, M Ito, H Sakurai, K Suzuki, K Tanaka, K Kitani, H Adachi, H Kawata, A Koizumi, and H Nakao. Magnetic compton profile study of orbital ordering state of 3 d electrons in ytio3. *Journal of the Physical Society of Japan*, 77(2):023705, 2008.

[106] S. Huotari, K. Hamalainen, S. Manninen, S. Kaprzyk, A. Bansil, W. Caliebe, T. Buslaps, V. Honkimaki, and P. Suortti. Energy dependence of experimental be compton profiles. *Physical Review B*, 62(12):7956–7963, 2000.

[107] C. Adamo and V. Barone. Toward reliable density functional methods without adjustable parameters: The PBE0 model. *Journal of Chemical Physics*, 110(13):6158–6170, 1999.

[108] A. D. Becke. Density-functional exchange-energy approximation with correct asymptotic behavior. *Phys Rev A Gen Phys*, 38(6):3098–3100, 1988.

[109] T. M. Henderson, Artur F Izmaylov, Gustavo E Scuseria, and Andreas Savin. The importance of middle-range Hartree-Fock-type exchange for hybrid density functionals, 2007.

[110] T. M. Henderson, A. Izmaylov, and A. Scuseria, G.and Savin. The role of middle-range Hartree-Fock-type exchange in hybrid functionals. In *APS Meeting Abstracts*, volume 1, page 13004, 2008.

[111] A. V. Krukau, G. E. Scuseria, J. P. Perdew, and A. Savin. Hybrid functionals with local range separation. *J Chem Phys*, 129(12):124103, 2008.

[112] C. T. Lee, W. T. Yang, and R. G. Parr. Development of the colle-salvetti correlation-energy formula into a functional of the electron-density. *Physical Review B*, 37(2):785–789, 1988.

[113] C. Sternemann, G. Doring, C. Wittkop, W. Schulke, A. Shukla, T. Buslaps, and P. Suortti. Influence of lattice dynamics on electron momentum density of lithium. *Journal of Physics and Chemistry of Solids*, 61(3):379–382, 2000.

[114] J. M. Gillet, P. J. Becker, and G. Loupias. The refinement of anisotropic compton profiles and of momentum densities. *Acta Crystallographica Section A*, 51(3):405–413, 1995.

[115] J. M. Gillet. *Local Models for Joint Position and Momentum Density Studies*, pages 259–275. Springer, 2011.

[116] S Ragot. *Matrices Densité: Modélisation des Densités de Charge et d'Impulsion. Prédiction des Propriétés des Solides*. Thesis, Ecole centrale des arts et manufactures, Chatenay-Malabry, FRANCE, 2001.

[117] W. Yang and Z. Zhou. *Electronic structure of solid-state systems via the divide-and-conquer method*, pages 177–188. Springer, 1996.

[118] E. Wigner. On the quantum correction for thermodynamic equilibrium. *Physical review*, 40(5):749, 1932.

[119] J.E. Moyal. Quantum mechanics as a statistical theory. In *Mathematical Proceedings of the Cambridge Philosophical Society*, volume 45, pages 99–124. Cambridge Univ Press, 1949.

[120] D. Leibfried, T. Pfau, and C. Monroe. Shadows and mirrors: Reconstructing quantum states of atom motion. *Physics Today*, 51(4):22–28, 1998.

[121] H. L. Schmider. The structure of electronic Moyal functions, and their connection with experiment. *Zeitschrift Fur Physikalische Chemie-International Journal of Research in Physical Chemistry & Chemical Physics*, 215(10/2001):1289–1302, 2001.

[122] H. Schmider and J. P. Dahl. Nodal structure of the electronic Wigner function of many-electron atoms and molecules. *International Journal of Quantum Chemistry*, 60(1):439–452, 1996.

[123] W. Schulke, U. Bonse, and S. Mourikis. Compton-scattering at the bragg position. *Physical Review Letters*, 47(17):1209–1212, 1981.

[124] W. Schulke. Compton scattering of photons from standing wave fields in the bragg case of X-ray diffraction. *Physics Letters A*, 83(9):451–454, 1981.

[125] W. Schulke and S. Mourikis. Nondiagonal momentum density of Si by coherent inelastic X-ray scattering. *Acta Crystallographica Section A*, 42(2):86–98, 1986.

[126] Z. Yan, I. A. Kibalin, N. Claiser, S. Gueddida, B. Gillon, A. Gukasov, A. B. Voufack, F. Morini, Y. Sakurai, M. Brancewicz, M. Itou, M. Itoh, N. Tsuji, M. Ito, M. Souhassou, C. Lecomte, P. Cortona, and J. M. Gillet. Spin density in $YTiO_3$: II. momentum-space representation of electron spin density supported by position-space results. *Physical Review B*, 96(5):054427, 2017.

[127] R.S Mulliken. Electronic population analysis on LCAO–MO molecular wave functions. I. *The Journal of Chemical Physics*, 23(10):1833–1840, 1955.

[128] C. Gatti and P. Macchi. *Modern charge-density analysis*. Springer Science & Business Media, 2012.

[129] E. R Scerri. Have orbitals really been observed? *J. Chem. Educ*, 77(11):1492, 2000.

[130] J. C. Slater. Atomic shielding constants. *Physical Review*, 36(1):57, 1930.

[131] L.J. Clinton, W. L .and Massa. Determination of the electron density matrix from x-ray diffraction data. *Physical Review Letters*, 29(20):1363, 1972.

[132] L. Massa, M. Goldberg, C. Frishberg, R. F. Boehme, and S. J. La Placa. Wave functions derived by quantum modeling of the electron density from coherent x-ray diffraction: Beryllium metal. *Phys Rev Lett*, 55(6):622–625, 1985.

[133] Y. V. Aleksandrov, VG. Tsirelson, IM. Reznik, and RP. Ozerov. The crystal electron energy and compton profile calculations from x-ray diffraction data. *physica status solidi (b)*, 155(1):201–207, 1989.

[134] S. T. Howard, J. P. Huke, P. R. Mallinson, and C. S. Frampton. Density-matrix refinement for molecular crystals. *Phys Rev B Condens Matter*, 49(11):7124–7136, 1994.

[135] J. A. Snyder and E. D. Stevens. A wavefunction and energy of the azide ion in potassium azide obtained by a quantum-mechanically constrained fit to x-ray diffraction data. *Chemical Physics Letters*, 313(1-2):293–298, 1999.

[136] D. Jayatilaka and D. J. Grimwood. Wavefunctions derived from experiment. i. motivation and theory. *Acta Crystallogr A*, 57(Pt 1):76–86, 2001.

[137] J. M. Gillet. Determination of a one-electron reduced density matrix using a coupled pseudo-atom model and a set of complementary scattering data. *Acta Crystallogr A*, 63(Pt 3):234–8, 2007.

[138] W. Kohn. Density functional and density matrix method scaling linearly with the number of atoms. *Phys Rev Lett*, 76(17):3168–3171, 1996.

[139] S. Ragot, J. M. Gillet, and P. J. Becker. Interpreting compton anisotropy of ice I_h: A cluster partitioning method. *Physical Review B*, 65(23):235115, 2002.

[140] E Prince and A. J. C. Wilson. International tables for crystallography. 2004.

[141] D. Jayatilaka. Wave function for beryllium from x-ray diffraction data. *Physical Review Letters*, 80(4):798–801, 1998.

[142] D. Jayatilaka. Modern charge-density analysis, edited by C. Gatti & P. Macchi, 2012.

[143] A. Genoni. Molecular orbitals strictly localized on small molecular fragments from x-ray diffraction data. *J Phys Chem Lett*, 4(7):1093–9, 2013.

[144] A. Genoni. X-ray constrained extremely localized molecular orbitals: Theory and critical assessment of the new technique. *J Chem Theory Comput*, 9(7):3004–19, 2013.

[145] L.HR. Dos Santos, A. Genoni, and P. Macchi. Unconstrained and x-ray constrained extremely localized molecular orbitals: analysis of the reconstructed electron density. *Acta Crystallographica Section A: Foundations and Advances*, 70(6):532–551, 2014.

[146] S. Gueddida, Z. Yan, and J.-M. Gillet. Development of a joint refinement model for the spin-resolved one-electron reduced density matrix using different data sets. *Acta Crystallographica Section A*, 74(2):131–142, Mar 2018.

[147] RHWJ. Ditchfield, W. J. Hehre, and J. A. Pople. Self-consistent molecular-orbital methods. ix. an extended gaussian-type basis for molecular-orbital studies of organic molecules. *The Journal of Chemical Physics*, 54(2):724–728, 1971.

[148] P. C. Hariharan and J. A. Pople. The influence of polarization functions on molecular orbital hydrogenation energies. *Theoretical Chemistry Accounts: Theory, Computation, and Modeling (Theoretica Chimica Acta)*, 28(3):213–222, 1973.

[149] PC. Hariharan and J. A. Pople. Accuracy of AH_n equilibrium geometries by single determinant molecular orbital theory. *Molecular Physics*, 27(1):209–214, 1974.

[150] M. S. Gordon. The isomers of silacyclopropane. *Chemical Physics Letters*, 76(1):163–168, 1980.

[151] M. M Francl, W. J Pietro, W. J Hehre, J S Binkley, M. S Gordon, D. J DeFrees, and J. A Pople. Self-consistent molecular orbital methods. xxiii. a polarization-type basis set for second-row elements. *The Journal of Chemical Physics*, 77(7):3654–3665, 1982.

[152] RC. Binning and LA. Curtiss. Compact contracted basis sets for third-row atoms: Ga–Kr. *Journal of Computational Chemistry*, 11(10):1206–1216, 1990.

[153] J. P. Blaudeau, M. P. McGrath, L. A. Curtiss, and L. Radom. Extension of Gaussian-2 (G2) theory to molecules containing third-row atoms K and Ca. *The Journal of chemical physics*, 107(13):5016–5021, 1997.

[154] V. A. Rassolov, J. A. Pople, M. A. Ratner, and T. L. Windus. 6-31G* basis set for atoms K through Zn. *Journal of Chemical Physics*, 109(4):1223–1229, 1998.

[155] V. A. Rassolov, M. A. Ratner, J. A. Pople, P. C. Redfern, and L. A. Curtiss. 6-31g* basis set for third-row atoms. *Journal of Computational Chemistry*, 22(9):976–984, 2001.

Appendix A

This appendix gives additional information to *Chapter 1*. *Section A.1* uses G09 and CRYSTAL14 as examples to present the basic theoretical framework including the basis set and different types of basis function. It is technical but useful for the creation and implementation of our own models (*Chapter 2 and 3*). It is hoped to be of some help for whoever is interested in undertaking a similar work. *Section A.2* offers additional theoretical results using different functionals, gives the topology analysis tables and a selection of figures in vertical planes (i.e. perpendicular to the mean molecular plane) for the Nit(SMe)Pt case. *Section A.3* contains geometrical information of $YTiO_3$ for different experiments. $3d$ orbital populations are also presented. *Section A.4* gives theoretical DMCPs of $YTiO_3$ before and after convolution with experimental resolution.

A.1 *Ab-initio* computations

GTOs basis set

Molecular orbitals (MOs) φ_i are used to describe the electronic states of molecules, written as linear combinations of atomic orbitals (AO):

$$\varphi_i(\mathbf{r}) = \sum_j c_{ij}\chi_j(\mathbf{r}) \tag{A.1}$$

c_{ij} are MO coefficients, χ_j are the atomic orbitals (AO) defined as:

$$\chi_j(\mathbf{r}) = \sum_p^{N_j^{GTOs}} d_{jp}g_{jp}(\mathbf{r}) \tag{A.2}$$

N_j^{GTOs} is number of Gaussian functions used to define the j^{th} AO, and g_{jp} is the p^{th} Gaussian function:

$$g_{jp}(\mathbf{r}) = A_{jp}(x - X_{j0})^{l_1}(y - Y_{j0})^{l_2}(z - Z_{j0})^{l_3}e^{-\alpha_{jp}(\mathbf{r}-\mathbf{R_j})^2} \tag{A.3}$$

where the $\mathbf{R}_j$ is the atomic nuclei center of coordinates X_{j0}, Y_{j0}, Z_{j0}, and $\mathbf{r}$ is composed of x, y,and z. α_{jp} is the exponential coefficient, d_{jp} in (A.2) is the contraction coefficient, and A_{jp} is normalization coefficient for the primitive Gaussian function.

Normalization

In general, from the basis set input file, there is a linear dependence (or called overlap) between the N_j^{GTOs} primitive Gaussian functions which describe an atomic orbital. These Gaussian functions are not normalized. Two steps are thus necessary for the normalization.

(a) normalization of contraction coefficients to fix the linear dependence between the Gaussian functions, so that

$$\int |N_j \chi_j(\mathbf{r})|^2 = 1 \tag{A.4}$$

where

$$N_j = \left(\sum_{p,q}^{N_{GTOs}} d_{jp} d_{jq} \left(\frac{2\sqrt{\alpha_{jp} * \alpha_{jq}}}{\alpha_{jp} + \alpha_{jq}} \right)^{l+3/2} \right)^{-1/2} \tag{A.5}$$

where N_j is the linear dependence coefficient for the N_{GTOs} basis Gaussian functions (see Eq. (E.73) in Ref. [19]). Then $d_{jp}^{norm} = N_j d_{jp}$

(b) normalization of the primitive Gaussian functions, so that

$$\int |A_{jp} g_{jp}(\mathbf{r})|^2 = 1 \tag{A.6}$$

where

$$A_{jp} = (4\alpha_{jp})^{\frac{l}{2}+\frac{3}{4}} 2^{\frac{l}{2}-\frac{3}{4}} \left(\frac{1}{\pi} \right)^{\frac{3}{4}} \left(\frac{l_1! l_2! l_3!}{(2l_1)!(2l_2)!(2l_3)!} \right)^{1/2} \tag{A.7}$$

Additional information *If we want to use electronic information (basis set and MO coefficients) after a self-consistent field (SCF) computation to compute other properties (eg: Chapter 2), it is necessary to recognize the data format and to retrieve the data from the output file.*

Normally, step (a) is always conducted in the output file of ab initio program. Depending on different programs, step (b) is included in the computation process not in the output file. Moreover, pre-defined factor is also possibly added in the output data. Here, G09 and CRYSTAL14 are presented as examples:

(1) ***For G09*** *(fch file), step (a) is included, and there is no pre-defined factor.*

$$d_{jp}^{out} = d_{jp}^{norm}$$

*(**Tips:** Standard basis sets are mostly normalized, it means $d_{jp}^{norm} = d_{jp}$. If not (non standard case), G09 will carry out step (a) to eliminate any dependence, and write the d_{jp}^{norm} in the fch file. This process can be shown in log file by using keyword **gfprint**.)*

Before proceeding to any further computation using the population matrix and its associated basis set, it is necessary that normalization in step (b) is carried out.

(2) ***For CRYSTAL14*** *(output file generated by keyword* ***CRYAPI_OUT****), step (a) is included, and there is pre-defined factor (see Eq. (E.73–78) in Ref. [19]).*

$$d_{jp}^{out} = N_j d_{jp} F_{jp}^{pre}$$

where F_{jp}^{pre} *is the pre-defined factor depending on the* l *value (different type of shell: 0 for* s*, 1 for* p*, 2 for* d *etc.)*

$$F_{jp}^{pre} = (4\alpha_{jp})^{\frac{l}{2}+\frac{3}{4}} \left(\frac{1}{\pi}\right)^{\frac{3}{4}} \pi^{\frac{5}{8}} 2^{\frac{l}{2}-\frac{1}{2}} \left(\frac{l!}{(2l)!}\right)^{1/2} \tag{A.8}$$

As the output file does not change the α*, step (a) + (b) should be conducted before any further computations.*

Cartesian and Pure Basis Functions

Usually, Cartesian Gaussian basis functions, as in (A.3), have been used. $l = l_1 + l_2 + l_3$ is the angular momentum number. All possible basis functions (represent different shells eg: s, p_x, p_y, p_z, d_xy etc.) are related to different permutations and combinations of l_1, l_2, l_3. The number of basis functions or the number of polynomials, for a given angular momentum l, is $\frac{(l+1)(l+2)}{2}$. For the implementation, ordering of these polynomials is fixed. In CRYSTAL14 the ordering is simply alphabetical, while in G09 it is different: the first four angular momenta and the corresponding polynomials are listed in Table A.1 and Table A.2:

Symbol	Angular momentum	Number	Polynomials
S	0	1	1
P	1	3	x,y,z
D	2	6	xx,xy,xz,yy,yz,zz
F	3	10	xxx,xxy,xxz,xyy,xyz,xzz,yyy,yyz,yzz,zzz

Table A.1: Cartesian basis functions for CRYSTAL14

Symbol	Angular momentum	Number	Polynomials
S	0	1	1
P	1	3	x,y,z
D	2	6	xx,yy,zz,xy,xz,yz
F	3	10	xxx,yyy,zzz,xxy,xxz,xzz,yzz,yyz,yyz,xyz

Table A.2: Cartesian basis functions for G09

Occasionally, pure basis functions are used, especially for d and f orbitals, for which polynomials are those of real spherical harmonics. Unlike the cartesian case, the degeneracy for a given angular momentum l, is $2l + 1$. For the implementation, one must fix a certain ordering of these polynomials. The first four angular momenta and the corresponding polynomials are listed in Table A.3:

Symbol	Angular momentum	Number	Polynomials
S	0	1	$C_{00} = 1$
P	1	3	$C_{10} = z$,$C_{11} = x$,$S_{11} = y$
D	2	5	C_{20},C_{21},S_{21},C_{22},S_{22}
F	3	7	C_{30},C_{31},S_{31},C_{32},S_{32},C_{33},S_{33}

* C_{lm} and S_{lm} are cosine and sine-like spherical harmonics respectively.

Table A.3: Pure basis functions

As a matter of fact, in our computation, we mostly need to pay attention to d and f orbitals. It can be determined whether G09[a] use Cartesian or pure basis functions from the number of polynomials in the output file. If the pure option is chosen, the cartesian form basis set should be transformed to pure form, because the molecular coefficients are only compatible with pure functions. It is thus nessary to use the transformation matrix from cartesian to pure basis functions. For d and f the transformation matrix M_T is as follows (CRYSTAL14 case):

d orbitals:

$$\begin{pmatrix} X(C_{20}) \\ X(C_{21}) \\ X(S_{21}) \\ X(C_{22}) \\ X(S_{22}) \end{pmatrix} = \begin{pmatrix} -\frac{1}{2} & 0 & 0 & -\frac{1}{2} & 0 & 1 \\ 0 & 0 & 1 & 0 & 0 & 0 \\ 0 & 0 & 0 & 0 & 1 & 0 \\ \frac{1}{2}\sqrt{3} & 0 & 0 & -\frac{1}{2}\sqrt{3} & 0 & 0 \\ 0 & 1 & 0 & 0 & 0 & 0 \end{pmatrix} \begin{pmatrix} X(xx) \\ X(xy) \\ X(xz) \\ X(yy) \\ X(yz) \\ X(zz) \end{pmatrix}$$

f orbitals:

$$\begin{pmatrix} X(C_{30}) \\ X(C_{31}) \\ X(S_{31}) \\ X(C_{32}) \\ X(S_{32}) \\ X(C_{33}) \\ X(S_{33}) \end{pmatrix} = \begin{pmatrix} 0 & 0 & -\frac{3\sqrt{5}}{10} & 0 & 0 & 0 & 0 & -\frac{3\sqrt{5}}{10} & 0 & 1 \\ -\frac{\sqrt{6}}{4} & 0 & 0 & -\frac{\sqrt{30}}{20} & 0 & \frac{\sqrt{30}}{5} & 0 & 0 & 0 & 0 \\ 0 & -\frac{\sqrt{30}}{20} & 0 & 0 & 0 & 0 & -\frac{\sqrt{6}}{4} & 0 & \frac{\sqrt{30}}{5} & 0 \\ 0 & 0 & \frac{\sqrt{3}}{2} & 0 & 0 & 0 & 0 & -\frac{\sqrt{3}}{2} & 0 & 0 \\ 0 & 0 & 0 & 0 & 1 & 0 & 0 & 0 & 0 & 0 \\ \frac{\sqrt{10}}{4} & 0 & 0 & -\frac{3\sqrt{2}}{4} & 0 & 0 & 0 & 0 & 0 & 0 \\ 0 & \frac{3\sqrt{2}}{4} & 0 & 0 & 0 & 0 & -\frac{\sqrt{10}}{4} & 0 & 0 & 0 \end{pmatrix} \begin{pmatrix} X(xxx) \\ X(xxy) \\ X(xxz) \\ X(xyy) \\ X(xyz) \\ X(xzz) \\ X(yyy) \\ X(yyz) \\ X(yzz) \\ X(zzz) \end{pmatrix}$$

By using the transformation matrix M_T, the pure basis functions can be used with the resulting population matrix. It then becomes possible to compute properties such as charge, spin, density matrices.

Method	O1	N1	C1	O2	N2	O1+N1	O2+N2
M062x	0.33	0.33	-0.27	0.32	0.32	0.66	0.64
PBEXC	0.30	0.26	-0.11	0.30	0.25	0.56	0.55
PBE0-1/3	0.30	0.26	-0.11	0.30	0.25	0.56	0.55
B3LYP	0.33	0.30	-0.22	0.32	0.29	0.63	0.61

Table A.4: Nit(SMe)Ph Mulliken spin population by CRYSTAL14 with different functionals

A.2 Nit(SMe)Ph

The Nit(SMe)Ph periodic DFT computations with different functionals were conducted using CRYSTAL14. The Mulliken spin atomic populations are presented in Table A.4

Method	O1	N1	C1	O2	N2	O1+N1	O2+N2
U-B3LYP	0.3550	0.2648	-0.1994	0.3455	0.2547	0.6198	0.6002
U-CAM-B3LYP	0.3745	0.2937	-0.2894	0.3745	0.2843	0.6682	0.6498
U-M062X	0.3703	0.2848	-0.2686	0.3603	0.2745	0.6551	0.6348
ROHF	0.2125	0.2489	0.0157	0.2308	0.2563	0.4614	0.4871
RO-B3LYP	0.2839	0.2062	0.0104	0.2614	0.1891	0.4901	0.4505
RO-CAM-B3LYP	0.2958	0.2319	0.0017	0.2290	0.1856	0.5277	0.4146
RO-M062X	0.3054	0.2385	0.0123	0.2166	0.1796	0.5439	0.3962
Experiment (Joint Ref)	0.236(11)	0.327(13)	-0.144(18)	0.215(12)	0.287(12)	0.563	0.502

Table A.5: Nit(SMe)Ph monomer Mulliken spin population by G09 with different functionals

Method	O1	N1	C1	O2	N2	O1+N1	O2+N2
U-B3LYP	0.3550	0.2648	-0.1994	0.3455	0.2547	0.6198	0.6002
U-CAM-B3LYP	0.3745	0.2937	-0.2894	0.3655	0.2843	0.6682	0.6498
U-M062X	0.3702	0.2847	-0.2684	0.3603	0.2746	0.6549	0.6349
ROHF	0.2125	0.2489	0.0157	0.2308	0.2563	0.4614	0.4871
RO-B3LYP	0.2838	0.2062	0.0104	0.2614	0.1891	0.4900	0.4505
RO-CAM-B3LYP	0.2957	0.2318	0.0117	0.2291	0.1857	0.5275	0.4148
RO-M062X	0.3050	0.2383	0.0123	0.2169	0.1799	0.5433	0.3968
CASSCF(7,8)	0.2853	0.3234	-0.1742	0.2429	0.3120	0.6087	0.5549
Experiment (Joint Ref)	0.236(11)	0.327(13)	-0.144(18)	0.215(12)	0.287(12)	0.563	0.502

Table A.6: Nit(SMe)Ph monomer Mulliken spin population by MOLCAS with different functionals

[a]CRYSTAL14 uses pure functions

Bonding(x-y)	$d_{(x-y)}$ Å	$d_{(x-CP)}$ Å			$d_{(CP-y)}$ Å			$\Delta\rho(e\text{Å}^{-5})$			$\rho(e\text{Å}^{-3})$			ε		
		EXP	**G09**	**CRYSTAL14**	**EXP**	**G09**	**CRYSTAL14**	**EXP**	**G09**	**CRYSTAL14**	**EXP**	**G09**	**CRYSTAL14**	**EXP**	**G09**	**CRYSTAL14**
O2—N2	1.28	0.63	0.67	0.66	0.65	0.61	0.62	4.64	-18.21	-10.16	2.68	2.89	2.62	0.18	0.07	0.06
N1—O1	1.28	0.64	0.61	0.62	0.64	0.67	0.66	5.98	-18.05	-9.99	2.59	2.88	2.61	0.13	0.07	0.06
C1—N2	1.35	0.54	0.47	0.50	0.81	0.88	0.85	-19.30	-20.44	-22.54	2.19	2.18	2.19	0.28	0.31	0.30
C1—N1	1.36	0.55	0.47	0.52	0.81	0.88	0.83	-19.16	-21.24	-22.39	2.22	2.16	2.19	0.28	0.30	0.30
C2—C1	1.46	0.66	0.69	0.67	0.80	0.77	0.78	-13.30	-14.90	-18.70	1.79	1.81	1.87	0.10	0.11	0.10
C8—N1	1.50	0.65	0.59	0.60	0.86	0.91	0.90	-6.99	-12.52	-11.73	1.59	1.63	1.60	0.08	0.06	0.07
C8—C9	1.56	0.78	0.78	0.78	0.78	0.78	0.78	-10.14	-12.19	-14.14	1.59	1.60	1.62	0.08	0.02	0.02
C9—N2	1.50	0.66	0.59	0.60	0.85	0.91	0.91	-6.97	-12.48	-11.69	1.60	1.63	1.59	0.07	0.06	0.06
C4—C5	1.40	0.68	0.68	0.68	0.72	0.71	0.72	-19.61	-16.92	-21.05	2.10	2.02	2.08	0.17	0.19	0.17
C2—C3	1.40	0.67	0.71	0.71	0.74	0.69	0.69	-16.85	-16.90	-20.84	2.03	2.01	2.06	0.20	0.20	0.19
C6—C5	1.41	0.64	0.69	0.68	0.76	0.72	0.72	-18.59	-16.79	-20.66	2.08	2.01	2.06	0.21	0.18	0.17
C2—C7	1.41	0.68	0.71	0.71	0.72	0.70	0.69	-17.61	-16.81	-20.67	2.06	2.00	2.05	0.20	0.19	0.18
C3—C4	1.39	0.70	0.70	0.70	0.69	0.70	0.69	-17.26	-17.41	-21.46	2.02	2.05	2.10	0.24	0.21	0.19
C6—C7	1.39	0.68	0.70	0.69	0.71	0.69	0.69	-19.60	-17.70	-21.82	2.13	2.07	2.12	0.23	0.22	0.20
C11—C9	1.53	0.74	0.75	0.74	0.79	0.79	0.80	-9.56	-12.31	-14.48	1.60	1.63	1.65	0.10	0.02	0.02
C13—C9	1.52	0.74	0.74	0.73	0.78	0.78	0.79	-9.94	-12.82	-15.23	1.58	1.66	1.69	0.07	0.02	0.02
C10—C8	1.52	0.75	0.74	0.73	0.78	0.78	0.79	-11.18	-12.77	-15.18	1.62	1.66	1.68	0.04	0.01	0.01
C12—C8	1.53	0.70	0.75	0.74	0.82	0.78	0.79	-9.76	-12.50	-14.69	1.59	1.64	1.66	0.12	0.02	0.01
C5—S	1.76	0.85	0.89	1.07	0.91	0.86	0.69	-3.64	-9.76	-1.90	1.27	1.34	1.28	0.17	0.25	0.50
S—C14	1.80	0.91	0.94	0.75	0.89	0.86	1.05	-2.78	-8.25	-7.33	1.16	1.24	1.23	0.04	0.10	0.29

Table A.7: Nit(SMe)Ph topology analysis (complete) monomer for G09

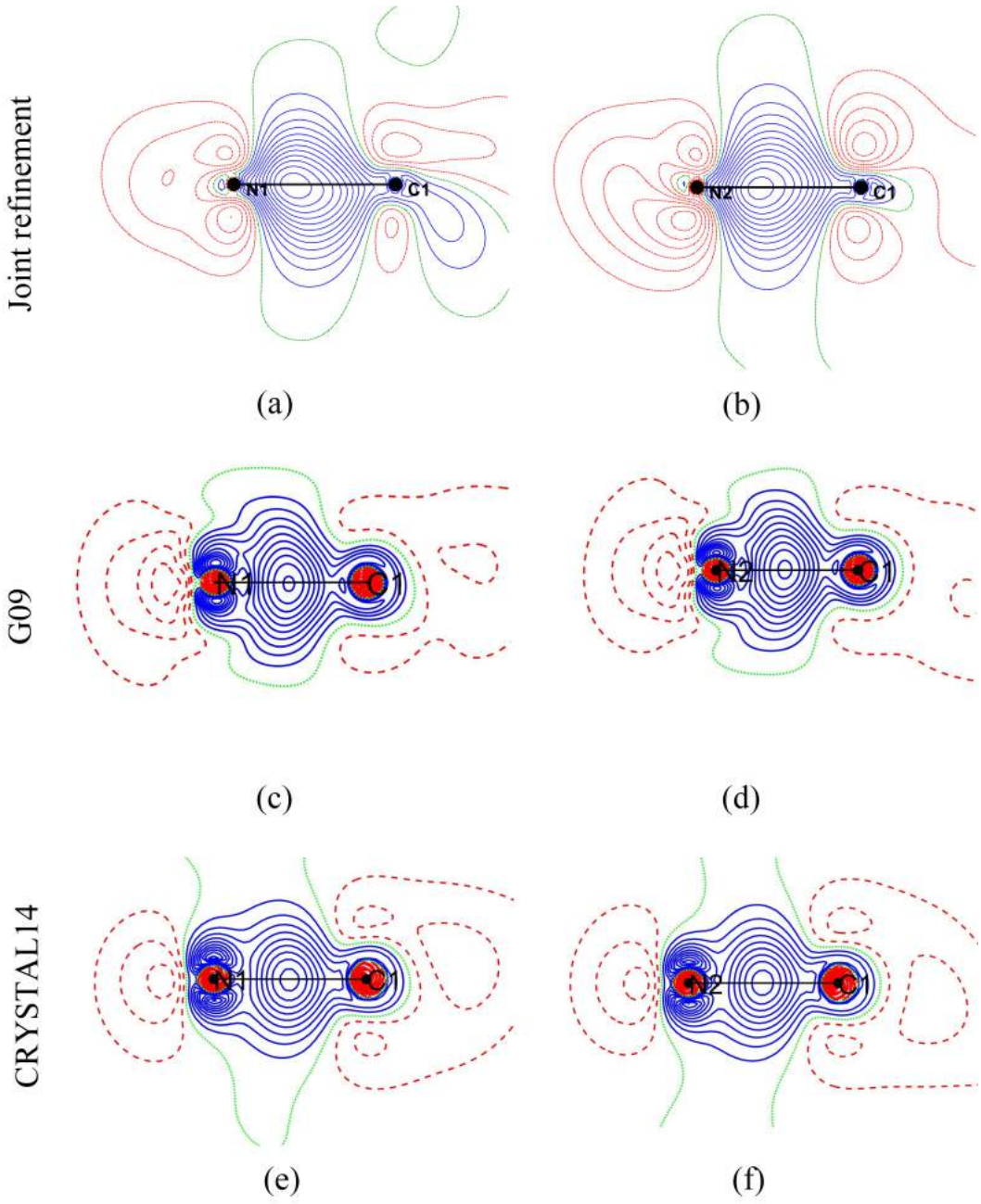

Figure A.1: Nit(SMe)Ph deformation density in the vertical plane containing bond C–N perpendicular to C1–N1–O1 plane (left) and C1–N2–O2 plane (right). Each row corresponds different methods: (a,b) joint refinement, (c,d) G09 (monomer), (e,f) CRYSTAL14. Contour intervals of 0.05 eÅ^{-3}, positive (blue), negative (red) and neutral (green) lines.

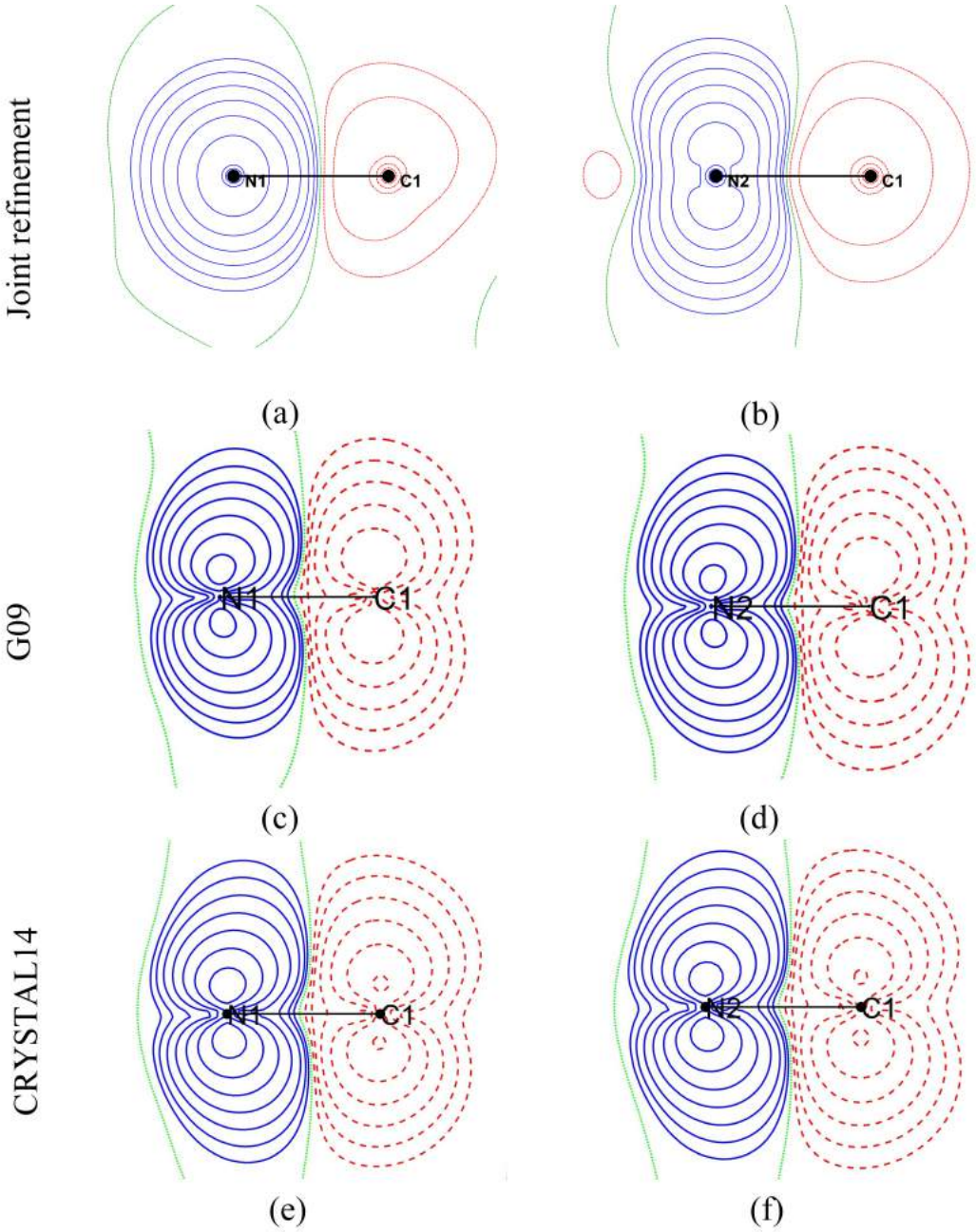

Figure A.2: Nit(SMe)Ph spin density in the vertical plane containing bond C–N perpendicular to C1–N1–O1 plane (left) and perpendicular to C1–N2–O2 plane (right). Each row corresponds different methods: (a,b) joint refinement, (c,d) G09 (monomer), (e,f) CRYSTAL14. Contour at 0.01 $\times 2^n$, $(n = 0, \ldots, 12)$ $\mu_B \cdot$ Å^{-3}, positive (blue), negative (red) and neutral (green) lines.

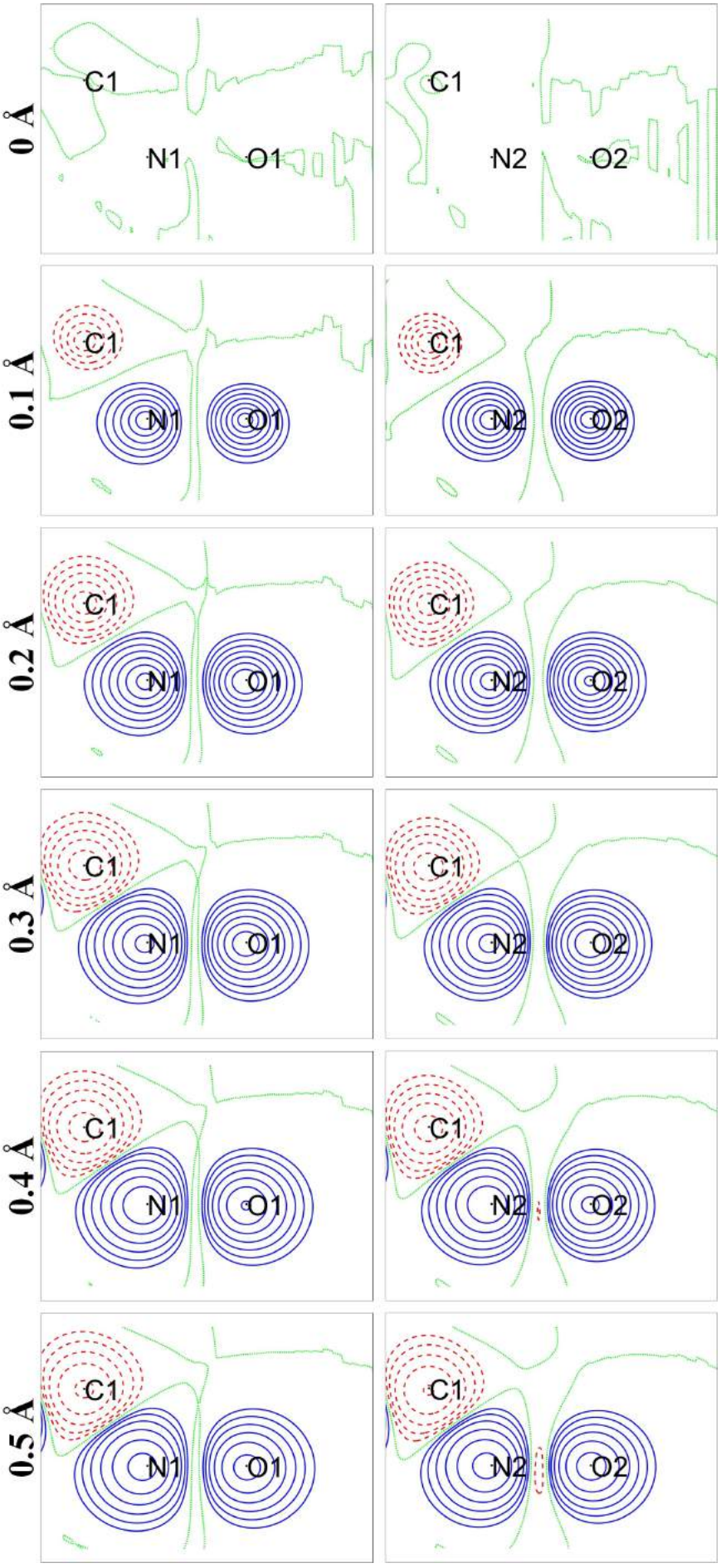

Figure A.3: Nit(SMe)Ph spin density from CASSCF additional C1–N1–O1 plane (left) and C1–N2–O2 plane (right). Each row corresponds to a different distance from the plane.Contour at 0.01 $\times 2^n$, $(n = 0, \ldots, 12)$ $\mu_B \cdot$ Å^{-3}, positive (blue), negative (red) and neutral (green) lines.

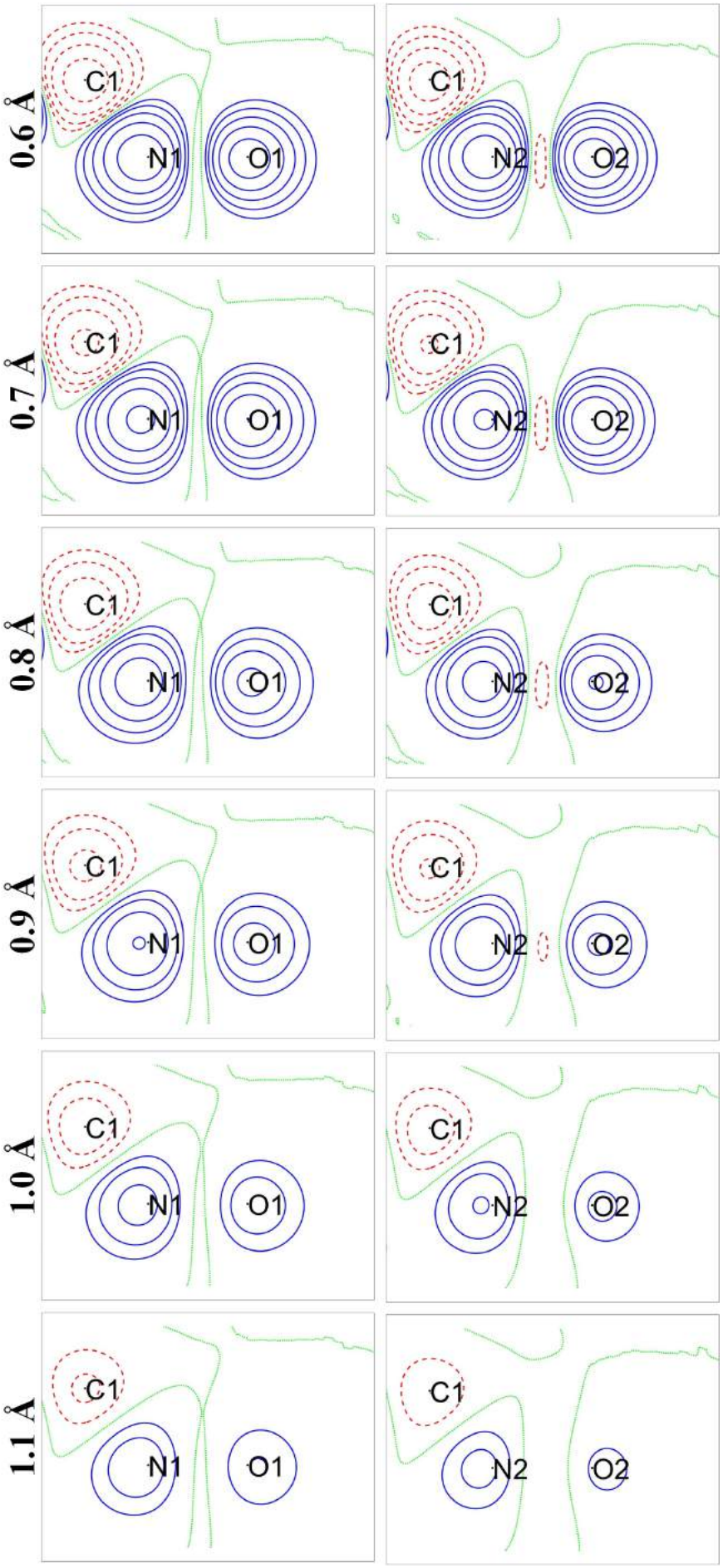

Figure A.4: Nit(SMe)Ph spin density from CASSCF additional C1–N1–O1 plane (left) and C1–N2–O2 plane (right). Each row corresponds to a different distance from the plane.Contour at 0.01 $\times 2^n$, $(n = 0, \ldots, 12)$ $\mu_B \cdot$ Å^{-3}, positive (blue), negative (red) and neutral (green) lines.

A.3 $YTiO_3$

	Y	Ti	O1	O2
x	0.07398(1)	0.500000	0.4577(1)	0.30949(9)
y	0.250000	0.000000	0.250000	0.05795(6)
z	0.97807(1)	0.000000	0.1209(1)	0.69065(9)

Table A.8: $YTiO_3$ fractional atomic coordinates from XRD at 100K

	Y	Ti	O1	O2
x	0.0739(1)	0.500000	0.4577(1)	0.3093(1)
y	0.250000	0.000000	0.250000	0.05801(5)
z	0.9780(1)	0.000000	0.12081(7)	0.69042(8)

Table A.9: $YTiO_3$ fractional atomic coordinates from UND at 40K

	PND	XMD	Joint PND & XMD	
			scheme 1	scheme 2
Ti(μB)	0.715(4)	0.597(47)	0.713(4)	0.708(5)
$\cdot$ P(xy)	0.0	0.0	0.0	0.0
P(xz)	0.39(3)	0.53(4)	0.44(2)	0.47(2)
P(yz)	0.61(6)	0.43(6)	0.55(4)	0.51(4)
P(z^2)	0.001(1)	0.03(1)	0.010(3)	0.022(4)
P($x^2 - y^2$)	0.0005(7)	0.003(3)	0.0000(1)	0.0000(1)
O_1(μB)	0.016(4)	0.054(43)	0.013(4)	0.009(5)
O_2(μB)	0.004(3)	-0.077(36)	0.005(3)	0.005(4)
Y(μB)	-0.047(4)	-0.136(38)	-0.049(4)	-0.053(5)
N_{obs}	286	62	348	348

Table A.10: $YTiO_3$ Ti $3d$ populations from PND and CRYSTAL14

A.4 DMCP for $YTiO_3$

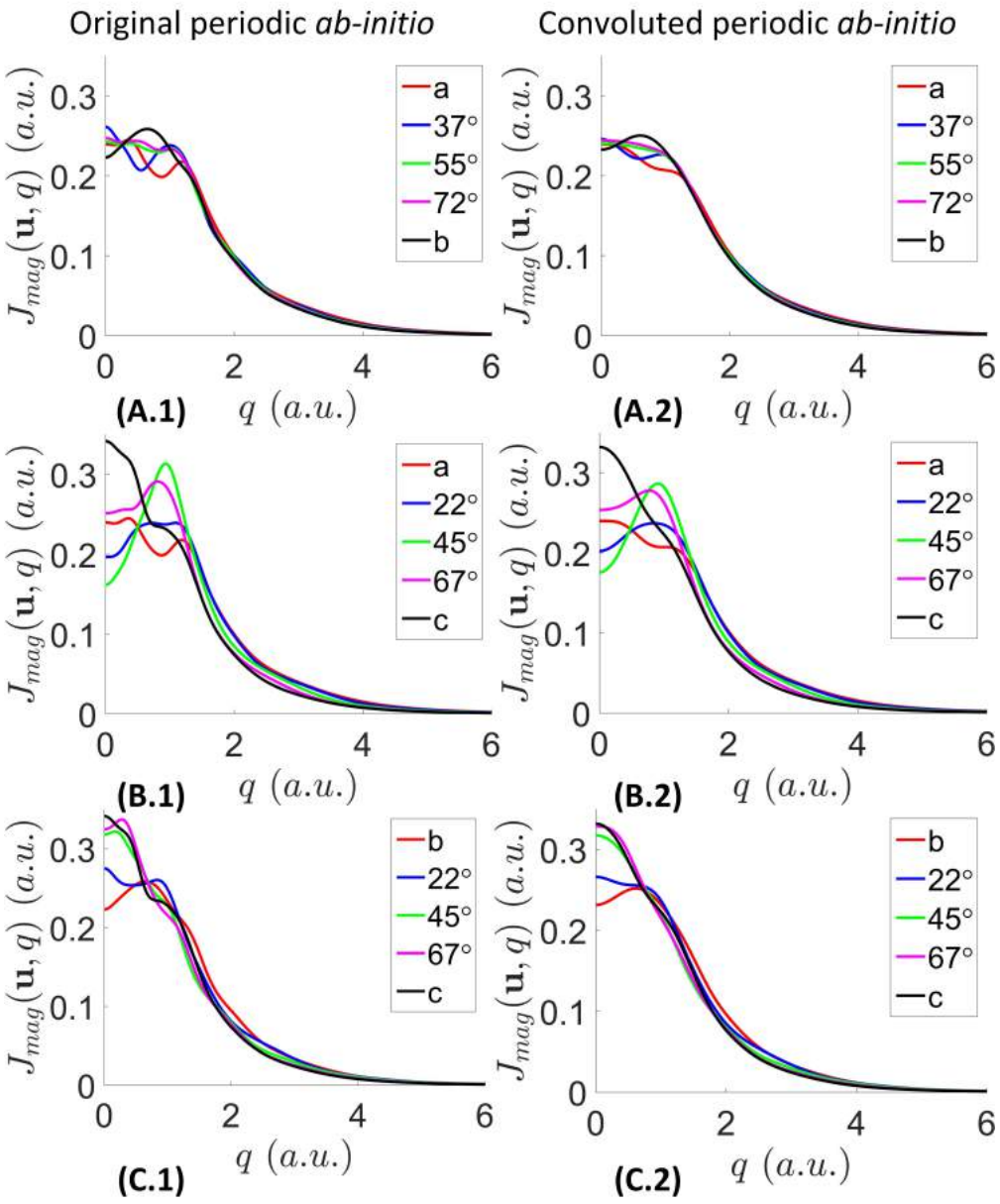

Figure A.5: $YTiO_3$ DMCPs
Directional magnetic compton profiles (DMCP) $J_{mag}(\mathbf{u}, q)$ for $YTiO_3$ for five non equivalent directions $\mathbf{u}$ in each plane. Each row corresponds to a set of DMCPs in a given plane: (A) (ab) plane; (B) (ac) plane; (C) (bc) plane. The spectra are in atomic units and normalized to one electron. Left column: original periodic *ab-initio* DMCP. Right column: periodic *ab-initio* DMCP, convoluted by a 0.4 a.u. wide Gaussian resolution function.

Appendix B

This appendix mainly presents the calculation technique details for the cluster construction. *Sections B.1*$\tilde{3}$ prepare the fundamental data for the cluster model, including G-vector (*Sections B.1*), cartesian population matrices (*Sections B.2*) and cluster population matrix definitions (*Sections B.3*). *Sections B.4*$\tilde{8}$ give calculation details for the cluster model, including reciprocal form factor $B(\mathbf{r})$ (*Sections B.4*), density matrix $\Gamma(\mathbf{r}, \mathbf{r}')$ (*Sections B.5*), Wigner function $W(\mathbf{x}, \mathbf{p})$ (*Sections B.6*), Moyal function $A(\mathbf{s}, \mathbf{k})$ (*Sections B.7*), and orbital separation for cross-terms analysis (*Sections B.8*). *Section B.9* presents the 2D Moyal function cross term results from the cluster construction.

B.1 G-vector list generation

G-vectors are used to define the cell positions in direct space. They only depend on cell parameters. To generate the G-vector list, the cell parameters a, b, c, α, β and γ are used.

The first method is using the function of CRYSTAL14

In the printing option $SETPRINT$, the subroutine 59 can output the G-vector values. Insert the following cards in the block 3 of the SCF input file (.d12).

```
SETPRINT
1
59 N
```

where N is the number of G-vectors. As the G-vectors are output with other data (eg. P(g) matrix...), the out file can be very large. The advice is to use a simple crystal to generate the list, for example, using the same cell parameters, but put only a H atom in the center of the cell.

The second method is makes use of the following algorithm:

As the G-vectors are based on the cell parameters, the list can be generated independently from the a, b, c, α, β and γ.

(a) Calculate the lattice vectors. The CRYSTAL14 convention is fixing the b axis, so

$$V = abc\sqrt{1 + 2cos(\alpha)cos(\beta)cos(\gamma) - cos^2(\alpha) - cos^2(\beta) - cos^2(\gamma)} \tag{B.1a}$$

$$\mathbf{a} = [a * sin(\gamma), b * cos(\gamma), 0] \tag{B.1b}$$

$$\mathbf{b} = [0, b, 0] \tag{B.1c}$$

$$\mathbf{c} = [\frac{c * (cos(\beta) - cos(\gamma) * cos(\alpha))}{sin(\gamma)}, c * cos(\alpha), \frac{V}{|\mathbf{a} \times \mathbf{b}|}] \tag{B.1d}$$

(b) List all possible G-vectors (m, k, $l \in \{-3, -2-1, 0, 1, 2, 3\}$), and calculate the norm values. As the G-vector space is center-symmetric, for m index only half will be accounted for ($m \in \{-3, -2-1, 0\}$) at the beginning. A 196 number G-vectors list with the module value $|G|$ will be obtained,

$$\begin{array}{ccc|c} -3 & -3 & -3 & |G_1| \\ \vdots & \vdots & \vdots & \vdots \\ m & k & l & |G_i| \\ \vdots & \vdots & \vdots & \vdots \\ 0 & 3 & 3 & |G_{196}| \end{array}$$

(c) Rank the list with $|G|$ ascending order.

(d) Double the list, insert the $-G$ just behind the G.

(e) Unique the list (the G with 0 could be listed several times).

Here an example coded by $MATLAB$:

```
%*****************************************************
clc
clear
close all
%input cell parameters
cell_a=5.69;
cell_b=7.609;
cell_c=5.335;
cell_alpha=90;
cell_beta=90;
cell_gamma=90;

%step a, Calculate the lattice vectors.
```

```
V_cell=cell_a*cell_b*cell_c*sqrt(1+2*cosd(cell_alpha)*...
    cosd(cell_beta)*cosd(cell_gamma)-cosd(cell_alpha)^2-...
    cosd(cell_beta)^2-cosd(cell_gamma)^2);

Vec_a=[cell_a*sind(cell_gamma),cell_a*cosd(cell_gamma),0];
Vec_b=[0,cell_b,0];
Vec_c=[cell_c*(cosd(cell_beta)-cosd(cell_gamma)*...
    cosd(cell_alpha))/sind(cell_gamma),cell_c*cosd(cell_alpha),...
    V_cell/norm(cross(Vec_a,Vec_b))];

%step b, List all possible G-vectors
G_vec_temps=zeros(196,4);
num_vec=0;
for m=-3:0
   for k=-3:3
      for l=-3:3
          num_vec=num_vec+1;
          G_vec_temps(num_vec,1:3)=[m k l];
          G_vec_temps(num_vec,4)=norm(Vec_a*m+Vec_b*k+Vec_c*l);
      end
   end
end

%step c, Rank the list
G_vec_temps=sortrows(G_vec_temps,4);

%step d, Double the list
G_vec_double=zeros(2*num_vec,3);

G_vec_double(1:2:2*num_vec-1,:)=G_vec_temps(:,1:3);
G_vec_double(2:2:2*num_vec,:)=-G_vec_temps(:,1:3);

%step e, Unique the list
G_vec=unique(G_vec_double,'rows','stable');
%*****************************************************
```

G_vec is the final G-vectors list.

B.2 Cartesian population matrix

As presented in *Appendix A*, there are cartesian and pure basis functions, which are compatible with cartesian and pure population matrices respectively. However, CRYSTAL14 offers only pure population matrices. It is thus necessary to define the cartesian population matrices by using transformation matrices.

If N_{orb} is the number of AOs (pure functions) per unit cell, the population matrix dimension is $N_{orb} \times N_{orb}$. A vector AOs of N_{orb} dimensions can be defined as:

$$\Phi_{pure}(\mathbf{r}) = [\chi'_1(\mathbf{r}), ..., \chi'_{N_{orb}}(\mathbf{r})] \tag{B.2}$$

Φ_{pure} can be obtained by the transformation matrix from the cartesian basis set definition (as presented in A.1). Suppose N_{Cart} is number of AOs (Cartesian functions), the vector AOs Φ_{Cart} is N_{Cart} dimensions,

$$\Phi_{Cart}(\mathbf{r}) = [\chi_1(\mathbf{r}), ..., \chi_{N_{Cart}}(\mathbf{r})] \tag{B.3a}$$

$$\Phi_{pure}(\mathbf{r}) = M_{TM} * \Phi_{Cart}(\mathbf{r}) \tag{B.3b}$$

where M_{TM} (of $N_{orb} \times N_{Cart}$ dimensions) is the transformation matrix[a], composed by the d, f orbitals transformation matrix (identity matrix for s and p orbitals). The 1-RDM can then be obtained from

$$\begin{aligned} \Gamma(\mathbf{r}, \mathbf{r}') &= \Phi^T_{pure}(\mathbf{r}) * P * \Phi_{pure}(\mathbf{r}') \\ &= (M_{TM} * \Phi_{Cart}(\mathbf{r}))^T(\mathbf{r}) * P * M_{TM} * \Phi_{Cart}(\mathbf{r}') \\ &= \Phi_{Cart}(\mathbf{r})^T * (M^T_{TM} * P * M_{TM}) * \Phi_{Cart}(\mathbf{r}') \end{aligned} \tag{B.4}$$

where P is the (pure) population matrix retrieved from the output file directly. The cartesian population matrix P_c can be defined as

$$P_c = M^T_{TM} * P * M_{TM} \tag{B.5a}$$

$$\Gamma(\mathbf{r}, \mathbf{r}') = \Phi_{Cart}(\mathbf{r})^T * P_c * \Phi_{Cart}(\mathbf{r}') \tag{B.5b}$$

The cartesian population matrix is directly compatible with the cartesian basis set.

B.3 Population matrix for the constructed cluster

CRYSTAL14 outputs the population matrices between cells. The population matrix *mat_cell* (composed by 27×27 population matrices) for the constructed cluster needs to be redefined. Here, the difference between G-vectors is used to define a relative position. The population

[a] the M_{TM} is identical for all cells

matrix for all kinds of relative cell positions can be generated from the 27 population matrices P_k where $k \in \{1, \ldots, 27\}$ and the G-vectors list (27 vectors) G. $mat\_cell(i, j)$, population matrix between cells i and j, where $i, j \in \{1, \ldots, 27\}$. $mat\_cell(i, j) = P_k$ means relative position between cells i and j is identical to the cell k with center cell. All population matrices in cluster population matrix mat_cell can be found in P_k or approximated to 0. A $Fortran$ program is used to calculate this population matrix:

(a) Calculate the relative cell positions

$$\mathbf{G}_{relative} = \mathbf{G}(\mathbf{i}) - \mathbf{G}(\mathbf{j}) \tag{B.6}$$

(b) Find the index num_row of $\mathbf{G}_{relative}$ in the G-vectors list.

This step serves to find the same relative positions between a given cell with the center cell. If num_row does not exist, then the relative cell positions indicates the fifth type, $mat\_cell(i, j) = 0$, and the interaction between the two cells is ignored. If num_row exits, means $num\_row \in \{0, \ldots 27\}$, then $mat\_cell(i, j) = P_{num\_row}$.

Finally, the mat_cell is a 27×27 matrix with elements $\{0, \ldots 27\}$, 0 means no interaction, and others using the corresponding population matrix retrieved from the output file. The following example is coded by $Fortran$:

```
!*******************************************************
num_cell=27

allocate(mat_cell(num_cell,num_cell))
!G_vec is the G-vector list

do i=1, num_cell
        do j=1,num_cell
                vec_dir(:)=G_vec(j,:)-G_vec(i,:)
                mat_cell(i,j)=num_row(vec_dir, G_vec(1:num_cell,:), num_cell)
        ENDDO
ENDDO

!find the row number of vector in a matrix
INTEGER FUNCTION num_row(x, Mat, num_cell)
        IMPLICIT NONE

        INTEGER, intent(in) :: num_cell

        INTEGER, DIMENSION(3) :: x
```

```
        INTEGER, DIMENSION(num_cell,3) :: Mat

        INTEGER :: i

        num_row=0d0

        do i=1,num_cell
                if (ALL(x(:) == Mat(i,:))) THEN
                        num_row=i
                        EXIT
                ENDIF
        ENDDO

ENDFUNCTION
!*****************************************************
```

For a larger cluster, the result can also be obtained by increasing the *num_cell* value, and using a new G-vectors list for the new cluster.

B.4 $B(\mathbf{r})$ computation

Based on (2.9a), the computation can be developed using the GTOs.

$$\begin{aligned} B(\mathbf{r}) &= \int \sum_{\mathbf{g}}^{N_{cells}} \Phi_{Cart}(\mathbf{s}) P_c^{\mathbf{g}} \Phi_{Cart}^{\mathbf{g}}(\mathbf{s}+\mathbf{r}) d\mathbf{s} \\ &= \sum_{n,m}^{N_{Cart}} \sum_{\mathbf{g}}^{N_{cells}} P_{c,nm}^{\mathbf{g}} \int \chi_n(\mathbf{s}) \chi_m^{\mathbf{g}}(\mathbf{s}+\mathbf{r}) d\mathbf{s} \\ &= \sum_{n,m}^{N_{Cart}} \sum_{\mathbf{g}}^{N_{cells}} P_{c,nm}^{\mathbf{g}} B_{nm}^{\mathbf{g}}(\mathbf{r}) \end{aligned} \tag{B.7}$$

where the $B_{nm}^{\mathbf{g}}(\mathbf{r}) = \int \chi_n(\mathbf{s}) \chi_m^{\mathbf{g}}(\mathbf{s}+\mathbf{r}) d\mathbf{s}$ is the contribution of two bi-center orbital cross contribution. Index $\mathbf{g}$ only changes the orbital center according to (2.3).

$$\begin{aligned} B_{nm}^{\mathbf{g}}(\mathbf{r}) = & \sum_{i=1}^{N_{GTOs}^n} \sum_{j=1}^{N_{GTOs}^m} d_n^i d_m^j \int \\ & (s_1 - X_n)^{l_1^n} (s_1 + x - X_m)^{l_1^m} e^{-\alpha_n^i (s_1 - X_n)^2 - \alpha_m^j (s_1 + x - X_m)^2} ds_1 \\ & (s_2 - Y_n)^{l_2^n} (s_2 + y - Y_m)^{l_2^m} e^{-\alpha_n^i (s_2 - Y_n)^2 - \alpha_m^j (s_2 + y - Y_m)^2} ds_2 \\ & (s_3 - Z_n)^{l_3^n} (s_3 + z - Z_m)^{l_3^m} e^{-\alpha_n^i (s_3 - Z_n)^2 - \alpha_m^j (s_3 + z - Z_m)^2} ds_3 \end{aligned} \tag{B.8}$$

where $[X_n, Y_n, Z_n]$ is the center position of χ_n, and $[X_m, Y_m, Z_m]$ for $\chi_m^{\mathbf{g}}$. The computation reduces to an integral of a bi-center wave-function product in GTOs format.

$$B^{\mathbf{g}}_{n,m,i,j,l}(x) = \int (s - X_n)^{l^n} (s + x - X_m)^{l^m} e^{-\alpha_n^i (s-X_n)^2 - \alpha_m^j (s+x-X_m)^2} ds \tag{B.9}$$

This key term can be developed to a polynomial expression by usaul mathematical methods for $l^n, l^m \in \{0, 1, 2, 3, \ldots\}$.

B.5 $\Gamma(\mathbf{r}, \mathbf{r}')$ computations

Starting from a given population matrix, a simple matrix operation can be applied to reduce the calculations.

(a) Define N sampling point along the path

$$\{\mathbf{r}_1, \mathbf{r}_2, \ldots, \mathbf{r}_N\}$$

(b) Calculate all the AO $\chi_i(\mathbf{r})$ for the N positions given above

$$\Psi = \begin{pmatrix} \chi_1(\mathbf{r}_1) & \chi_1(\mathbf{r}_2) & \cdots & \chi_1(\mathbf{r}_N) \\ \chi_2(\mathbf{r}_1) & \chi_2(\mathbf{r}_2) & \cdots & \chi_2(\mathbf{r}_N) \\ \vdots & \vdots & \cdots & \vdots \\ \chi_{N_{orb}}(\mathbf{r}_1) & \chi_{N_{orb}}(\mathbf{r}_2) & \cdots & \chi_{N_{orb}}(\mathbf{r}_N) \end{pmatrix}$$

where Ψ is a matrix with $N_{orb} \times N$ dimensions.

(c) Multiply the matrix to obtain the 1-RDM result along the path

$$\Gamma = \Psi^T * P * \Psi \tag{B.10}$$

where P is the population matrix with $N_{orb} \times N_{orb}$, so the result Γ is a matrix with $N \times N$ dimensions.

N_{orb} should change to N_{Cart} if the cartesian AOs and P_c are used. The total 1-RDM makes use of the total population matrix, and the spin population matrix for spin 1-RDM.

B.6 $W(\mathbf{x},\mathbf{p})$ computations

Based on (2.13) and (2.14), the $W_{n,m}(\mathbf{x},\mathbf{p})$ can be expressed in terms of GTOs:

$$\begin{aligned} W_{n,m}(\mathbf{x},\mathbf{p}) = & \sum_{i=1}^{N^n_{GTOs}} \sum_{j=1}^{N^m_{GTOs}} d^i_n d^j_m \int \\ & (x+\frac{s_1}{2}-X_n)^{l^n_1}(x-\frac{s_1}{2}-X_m)^{l^m_1} e^{-\alpha^i_n(x+\frac{s_1}{2}-X_n)^2-\alpha^j_m(x-\frac{s_1}{2}-X_m)^2+ip_x s_1} ds_1 \\ & (y+\frac{s_2}{2}-Y_n)^{l^n_2}(y-\frac{s_2}{2}-Y_m)^{l^m_2} e^{-\alpha^i_n(y+\frac{s_2}{2}-Y_n)^2-\alpha^j_m(y-\frac{s_2}{2}-Y_m)^2+ip_y s_2} ds_2 \\ & (z+\frac{s_3}{2}-Z_n)^{l^n_3}(z-\frac{s_3}{2}-Z_m)^{l^m_3} e^{-\alpha^i_n(z+\frac{s_3}{2}-Z_n)^2-\alpha^j_m(z-\frac{s_3}{2}-Z_m)^2+ip_z s_3} ds_3 \end{aligned} \tag{B.11}$$

So the problem becomes to calculate the integral:

$$W_{n,m,i,j}(x,p) = d^i_n d^j_m \int (x+\frac{s}{2}-X_n)^{l^n}(x-\frac{s}{2}-X_m)^{l^m} e^{-\alpha^i_n(x+\frac{s}{2}-X_n)^2-\alpha^j_m(x-\frac{s}{2}-X_m)^2+ips} ds \tag{B.12}$$

Similar to $B(\mathbf{r})$, this key term can be developed to a polynomial expression by math tools for $l^n, l^m \in \{0,1,2,3,\ldots\}$.

B.7 $A(\mathbf{s},\mathbf{k})$ computations

Based on (2.21) and (2.22), the $A_{n,m}(\mathbf{s},\mathbf{k})$ can be expressed in terms of GTOs:

$$\begin{aligned} A_{n,m}(\mathbf{s},\mathbf{k}) = & \sum_{i=1}^{N^n_{GTOs}} \sum_{j=1}^{N^m_{GTOs}} d^i_n d^j_m \int \\ & (x+\frac{s_1}{2}-X_n)^{l^n_1}(x-\frac{s_1}{2}-X_m)^{l^m_1} e^{-\alpha^i_n(x+\frac{s_1}{2}-X_n)^2-\alpha^j_m(x-\frac{s_1}{2}-X_m)^2+ik_x x} dx \\ & (y+\frac{s_2}{2}-Y_n)^{l^n_2}(y-\frac{s_2}{2}-Y_m)^{l^m_2} e^{-\alpha^i_n(y+\frac{s_2}{2}-Y_n)^2-\alpha^j_m(y-\frac{s_2}{2}-Y_m)^2+ik_y y} dy \\ & (z+\frac{s_3}{2}-Z_n)^{l^n_3}(z-\frac{s_3}{2}-Z_m)^{l^m_3} e^{-\alpha^i_n(z+\frac{s_3}{2}-Z_n)^2-\alpha^j_m(z-\frac{s_3}{2}-Z_m)^2+ik_z z} dz \end{aligned} \tag{B.13}$$

So the problem becomes to calculate the integral:

$$A_{n,m,i,j}(r,p) = d^i_n d^j_m \int (r+\frac{s}{2}-X_n)^{l^n}(r-\frac{s}{2}-X_m)^{l^m} e^{-\alpha^i_n(r+\frac{s}{2}-X_n)^2-\alpha^j_m(r-\frac{s}{2}-X_m)^2+ikr} dr \tag{B.14}$$

Similar to $B(\mathbf{r})$, this key term can be developed to a polynomial expression by math tools for $l^n, l^m \in \{0,1,2,3,\ldots\}$.

B.8 Orbitals separation

There are two methods to conduct the orbital separation for the cluster model computation.

The first method is conducted by three computations:
$\Gamma_1(\mathbf{r},\mathbf{r}')$: calculate only the contributions of orbitals defined by set 1
$\Gamma_2(\mathbf{r},\mathbf{r}')$: calculate only the contributions of orbitals defined by set 2 (there is no common orbitals between set 1 and set 2)
$\Gamma_{1+2}(\mathbf{r},\mathbf{r}')$: calculate only the contributions of orbitals defined by set 1 plus set 2

The cross term contribution is the difference between the total and the sum of set 1, set 2 independent results.

$$\Gamma_{cross}(\mathbf{r},\mathbf{r}') = \Gamma_{1+2}(\mathbf{r},\mathbf{r}') - (\Gamma_1(\mathbf{r},\mathbf{r}') + \Gamma_2(\mathbf{r},\mathbf{r}'))$$

The other method is more direct and used a modification in population matrix, the cross term between two set of orbitals $S_1 = \{i_1, i_2, ..., i_n\}$ and $S_2 = \{j_1, j_2, ..., j_m\}$. S_1 and S_2 satisfy,

$$S_1 \subset N^* \quad S_2 \subset N^*$$
$$S_1 \cap S_2 = \emptyset$$

Then, the population matrix can be modified like,

$$P_{ij} = 0, P_{ji} = 0 \quad if \quad i \notin S_1 \quad or \quad j \notin S_2$$

Suppose $i_n < j_1$, then the new population matrix is,

$$\mathbf{P} = \begin{array}{c} \\ 1 \\ \vdots \\ i_1 \\ \vdots \\ i_n \\ \vdots \\ j_1 \\ \vdots \\ j_m \\ \vdots \\ N \end{array} \begin{array}{c} \begin{array}{ccccccccccc} 1 & \dots & i_1 & \dots & i_n & \dots & j_1 & \dots & j_m & \dots & N \end{array} \\ \begin{pmatrix} & & & & & & 0 & & & & \\ & & & 0 & & & P_{i_1 j_1} & \dots & P_{i_1 j_m} & & \\ & & & & & & \vdots & \dots & \vdots & 0 & \\ & & & & & & P_{i_n j_1} & \dots & P_{i_n j_m} & & \\ & & & & & & & & & & \\ & 0 & P_{j_1 i_1} & \dots & P_{j_1 i_n} & & & & & & \\ & & \vdots & & \vdots & & & & & & \\ & & P_{j_m i_1} & \dots & P_{j_m i_n} & & & 0 & & & \\ & & & 0 & & & & & & & \\ & & & & & & & & & & \end{pmatrix} \end{array}$$

The cross terms contributions can be calculated using (1.12) and (1.15).

B.9 2D Moyal function cross term

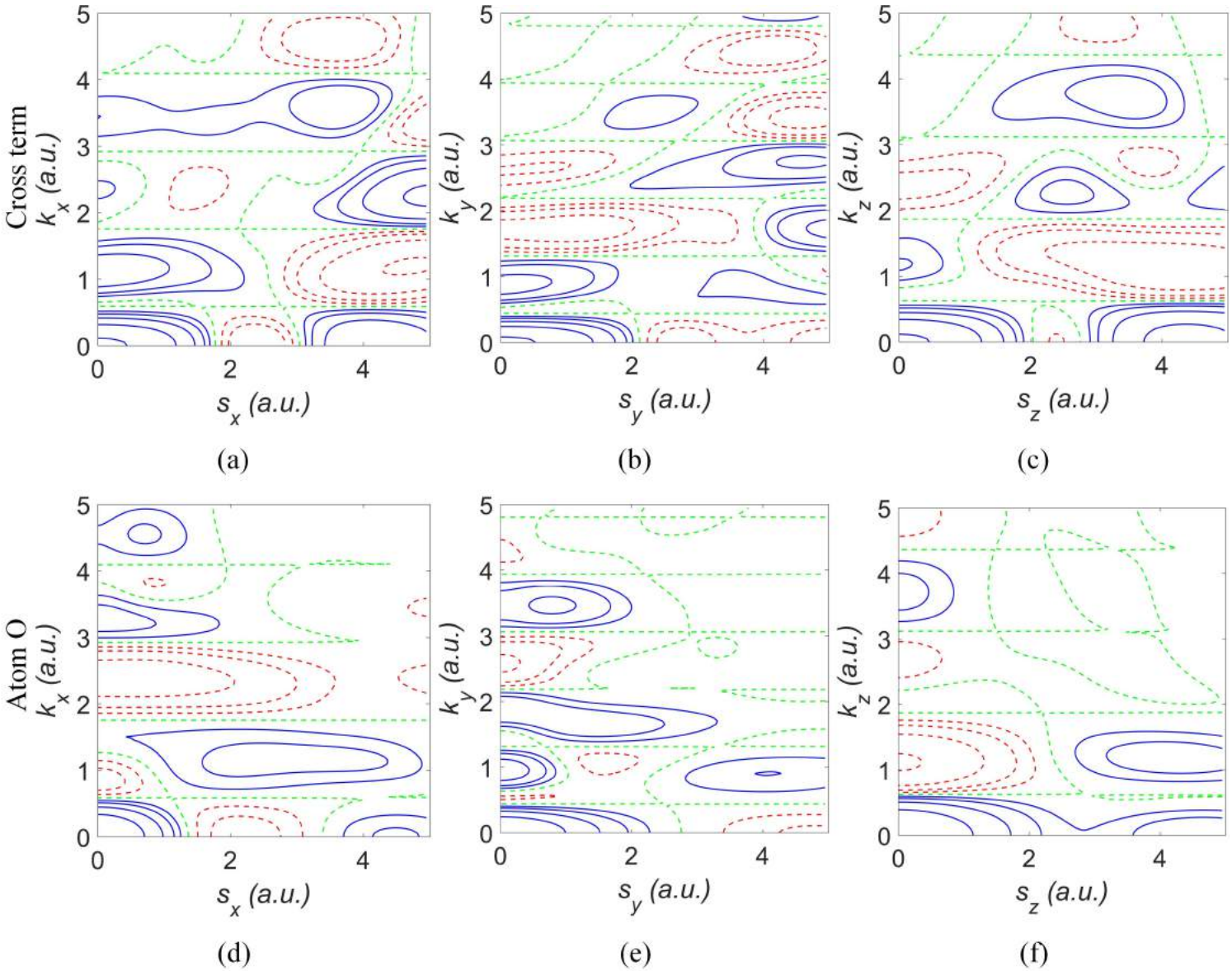

Figure B.1: $YTiO_3$ 2D magnetic Moyal function TiO cross term
Comparing with atom O contribution. Each column corresponds to a plane: (a,d) ($\mathbf{s}_x$ $\mathbf{k}_x$), (b,e) ($\mathbf{s}_y$ $\mathbf{k}_y$) and (c,f) ($\mathbf{s}_z$ $\mathbf{k}_z$). Row 1: TiO cross term contribution. Row 2: Atom O contribution. Contours at $\pm 0.1 \times 2^n$ $(n = 0, ..., 20)$ $e{\cdot}\text{Å}^{-3}$, positive: blue lines, negative: red dashed lines and neutral: green dashed.

Appendix C

This appendix contains additional results for two methods connecting both position and momentum spaces (presented in *Chapter 3*). *Section C.1* presents the "super position" spin density by adding the O_1 contributions. 2D-MEMD and "super position" spin density by an "single Ti model" using different d orbital coefficients are also calculated. *Section C.2* contains 1-RDM refinement model results using only magnetic structure factors. DMCPs and 2D-MEMD reconstruction results from 1-RDM refinement model reproduction results are also presented.

C.1 Super-position

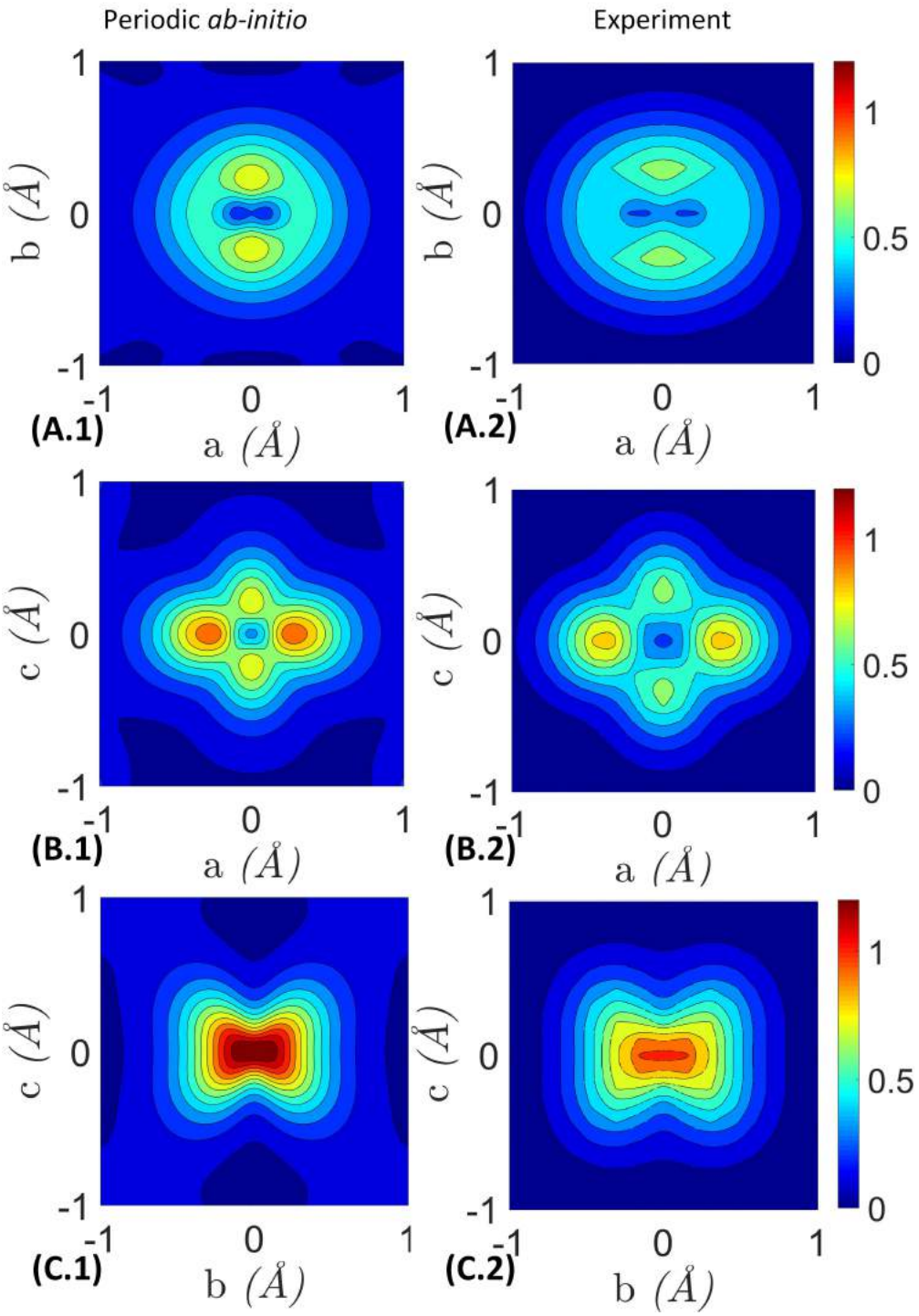

Figure C.1: $YTiO_3$ 2D super position spin density with O_1
Projections of the "super-position" spin density (in $\mu_B \cdot$ Å^{-2}) onto the three main crystallographic planes. Each row corresponds to a plane: (A) (ab) plane; (B) (ac) plane; (C) (bc) plane. Left column: periodic *ab-initio* results, with white solid lines indicating the projections of oxygen positions in "super-position" space. Right column: experimental data. Contours at intervals of 0.1 $\mu_B \cdot$ Å^{-2}. Colour bar scaling from 0 to 1.2 $\mu_B \cdot$ Å^{-2}.

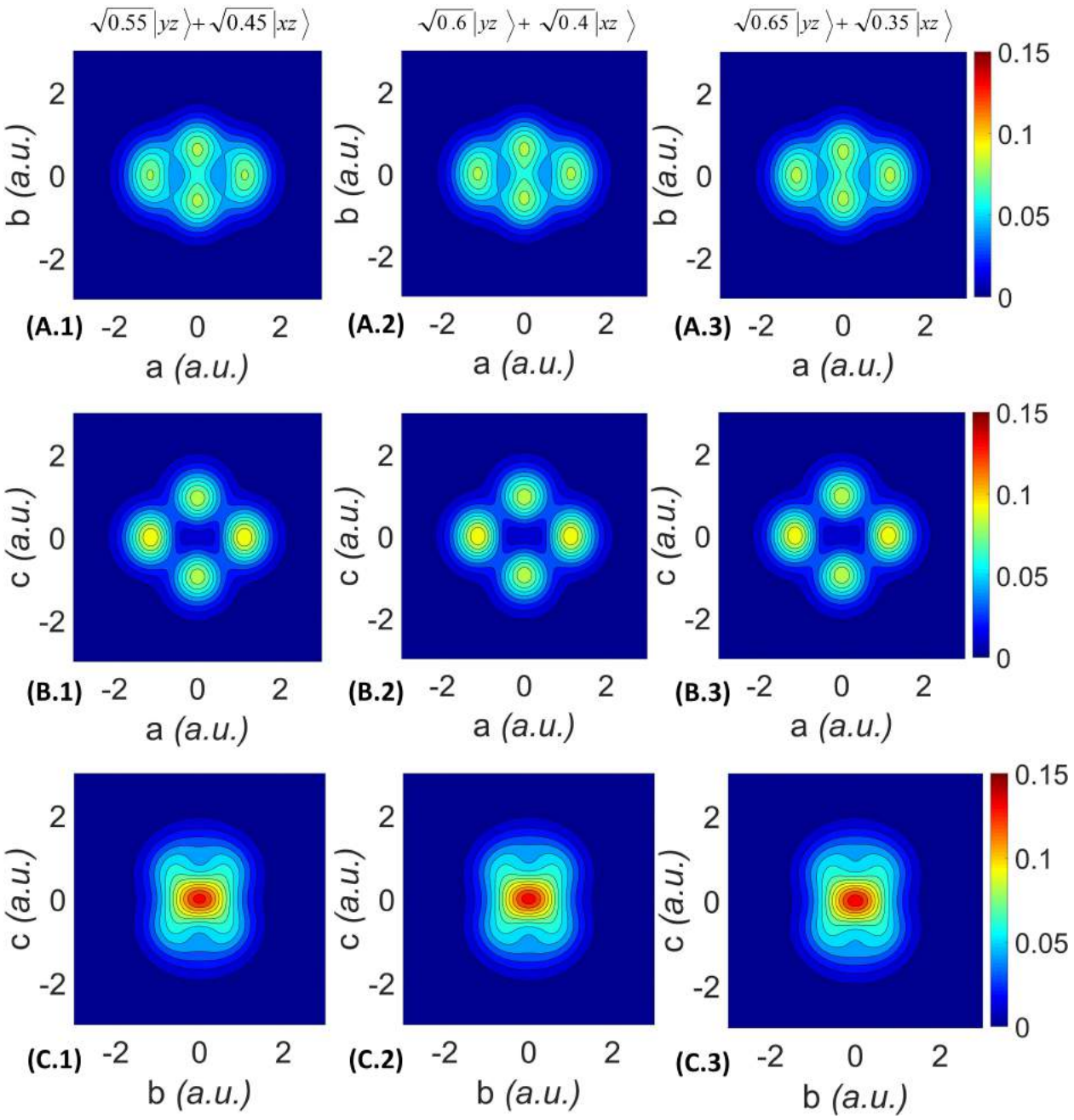

Figure C.2: $YTiO_3$ 2D-MEMD (additional)
Reconstructed spin density in momentum space (in a.u.), projected onto the three main crystallographic planes (2D-MEMD). Each row corresponds to a plane: (A) (ab) plane; (B) (ac) plane; (C) (bc) plane. Left column: $|\psi\rangle = \sqrt{0.55}|yz\rangle + \sqrt{0.45}|xz\rangle$. Middle column: $|\psi\rangle = \sqrt{0.6}|yz\rangle + \sqrt{0.4}|xz\rangle$. Right column: $|\psi\rangle = \sqrt{0.65}|yz\rangle + \sqrt{0.35}|xz\rangle$. Contour at intervals of 0.01 a.u. Color bar scaling from 0 to 0.15 a.u.

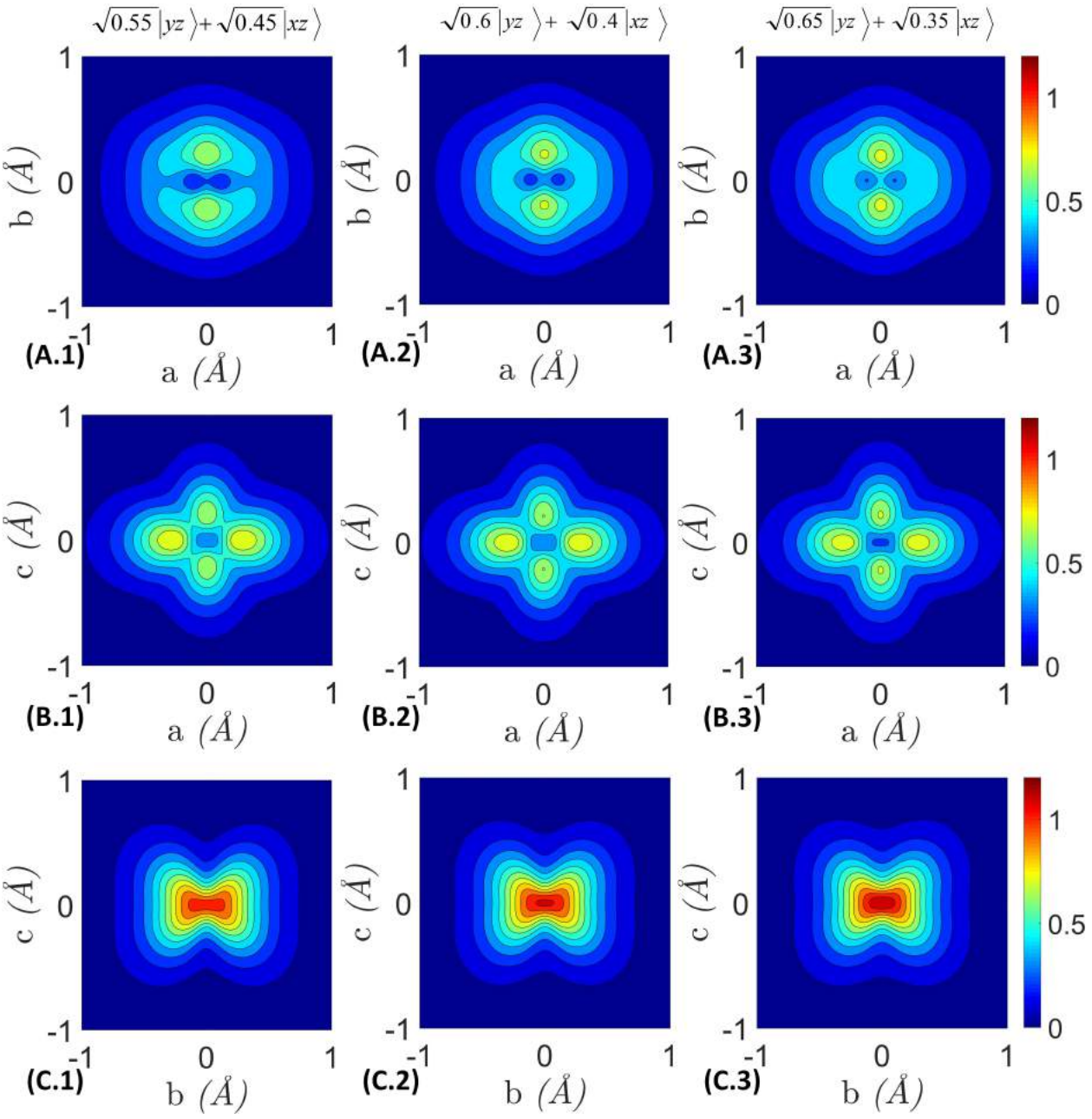

Figure C.3: $YTiO_3$ 2D super position spin density (additional)
Projections of the "super-position" spin density (in $\mu_B \cdot$ Å^{-2}) onto the three main crystallographic planes. Each row corresponds to a plane: (A) (ab) plane; (B) (ac) plane; (C) (bc) plane. Left column: $|\psi\rangle = \sqrt{0.55}|yz\rangle + \sqrt{0.45}|xz\rangle$. Middle column: $|\psi\rangle = \sqrt{0.6}|yz\rangle + \sqrt{0.4}|xz\rangle$. Right column: $|\psi\rangle = \sqrt{0.65}|yz\rangle + \sqrt{0.35}|xz\rangle$. Contours at intervals of 0.1 $\mu_B \cdot$ Å^{-2}. Colour bar scaling from 0 to 1.2 $\mu_B \cdot$ Å^{-2}.

C.2 1-RDM refinement

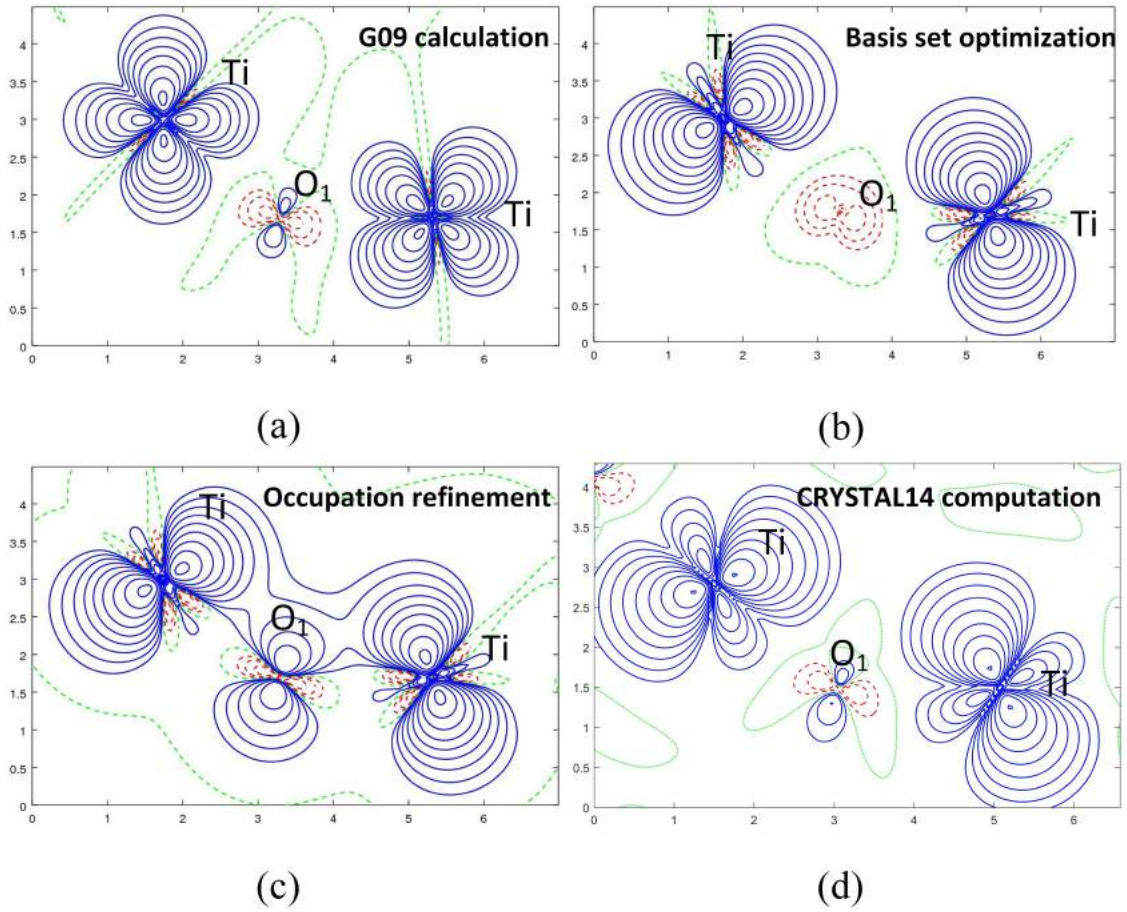

Figure C.4: $YTiO_3$ spin density in plane Ti–O_1–Ti by 1-RDM refinement model with magnetic structure factors only

(a) G09 calculation initial guess; (b) then after basis set optimization; (c) then after occupation refinement; (d) CRYSTAL14 computation. Contour at 0.01 $\times 2^n$, $(n = 0, \ldots, 12)$ $\mu_B \cdot$ Å^{-3}, positive (blue), negative (red) and neutral (green) lines.

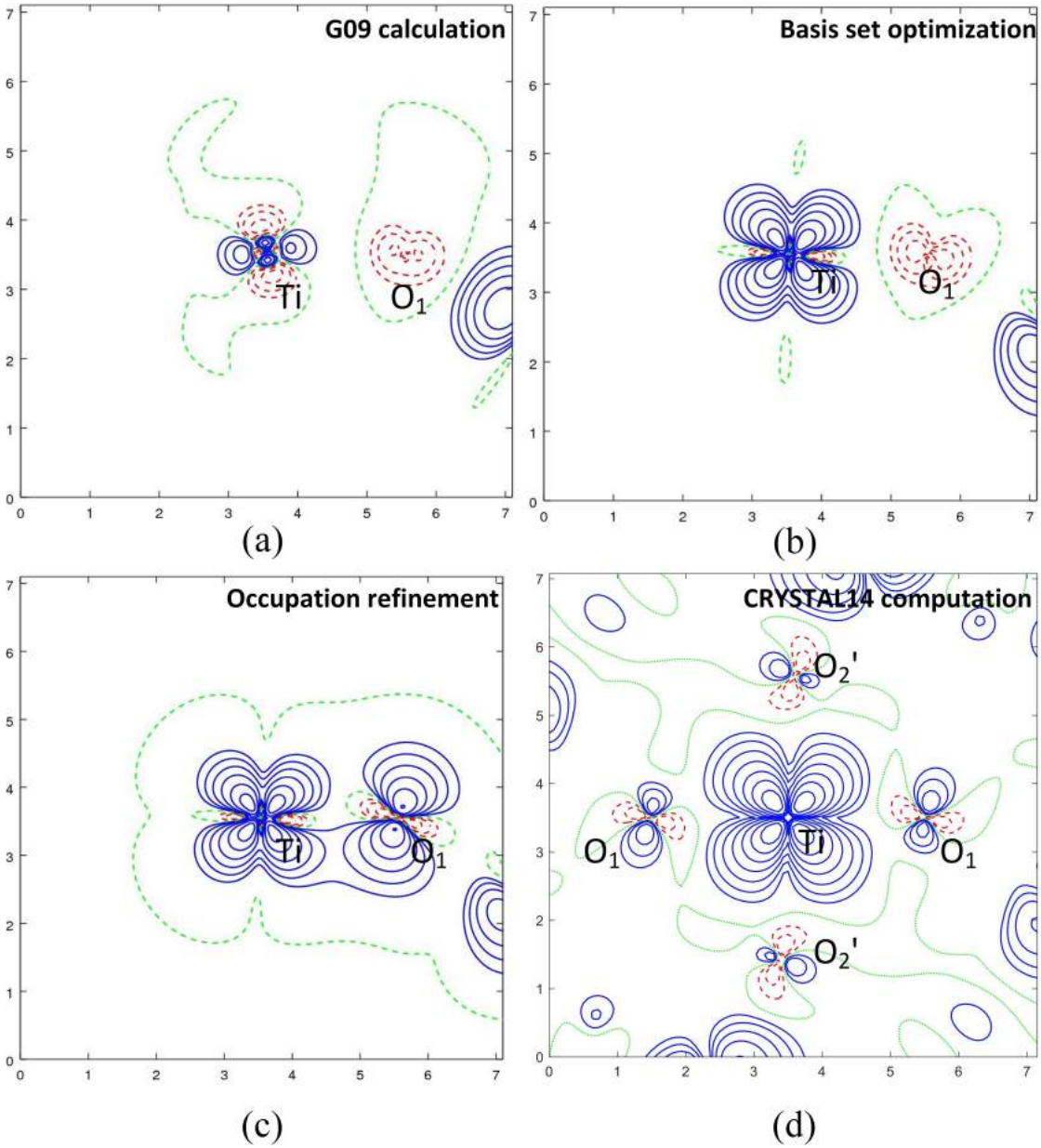

Figure C.5: $YTiO_3$ spin density in plane O_1–Ti–O_2' by 1-RDM refinement model with magnetic structure factors only

(a) G09 calculation initial guess; (b) then after basis set optimization; (c) then after occupation refinement; (d) CRYSTAL14 computation. Contour at 0.01 $\times 2^n$, $(n = 0, \ldots, 12)$ $\mu_B \cdot$ Å^{-3}, positive (blue), negative (red) and neutral (green) lines.

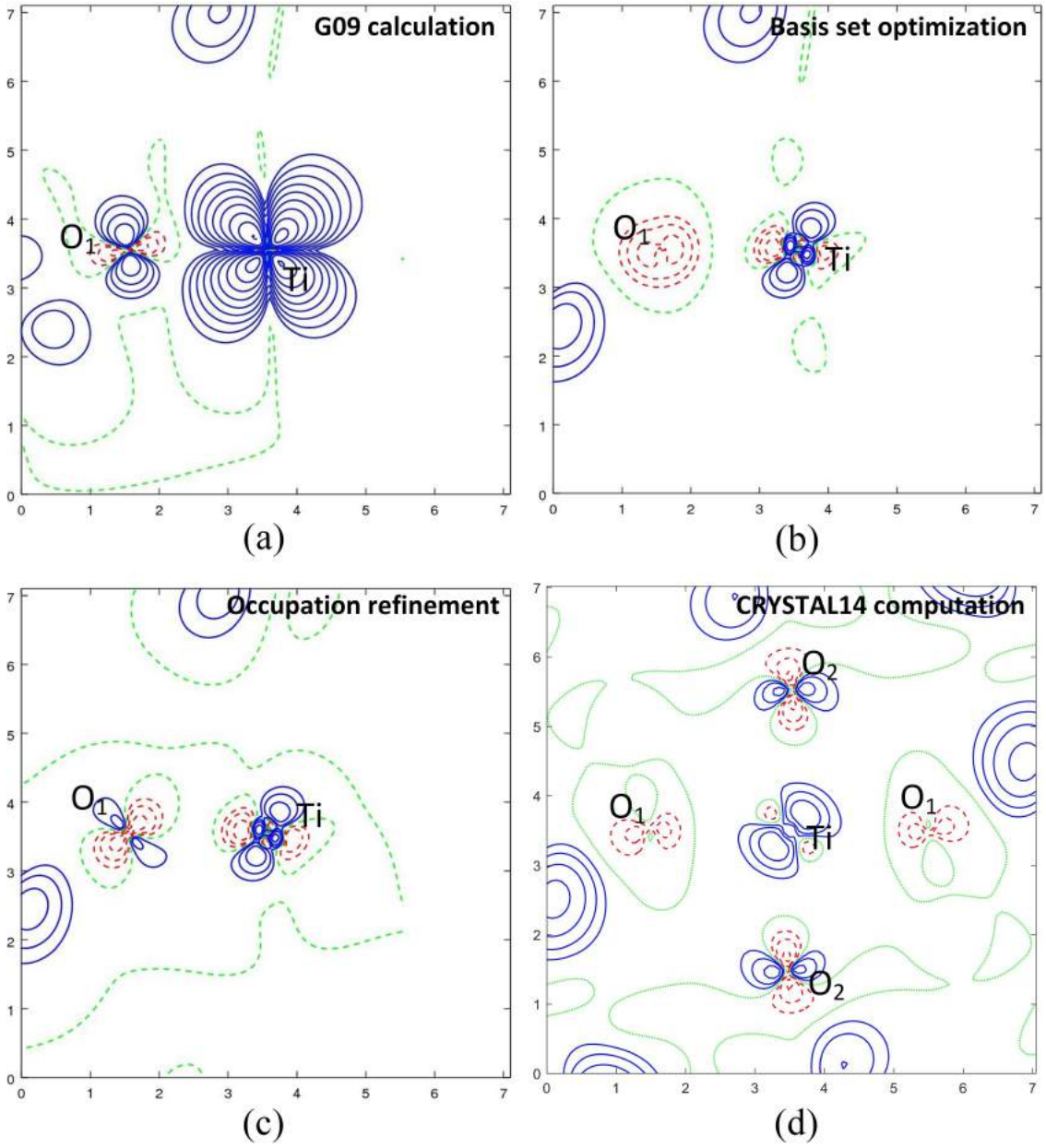

Figure C.6: $YTiO_3$ spin density in plane O_1–Ti–O_2 by 1-RDM refinement model with magnetic structure factors only

(a) G09 calculation initial guess; (b) then after basis set optimization; (c) then after occupation refinement; (d) CRYSTAL14 computation. Contour at 0.01 $\times 2^n$, $(n = 0, \ldots, 12)$ $\mu_B \cdot$ Å^{-3}, positive (blue), negative (red) and neutral (green) lines.

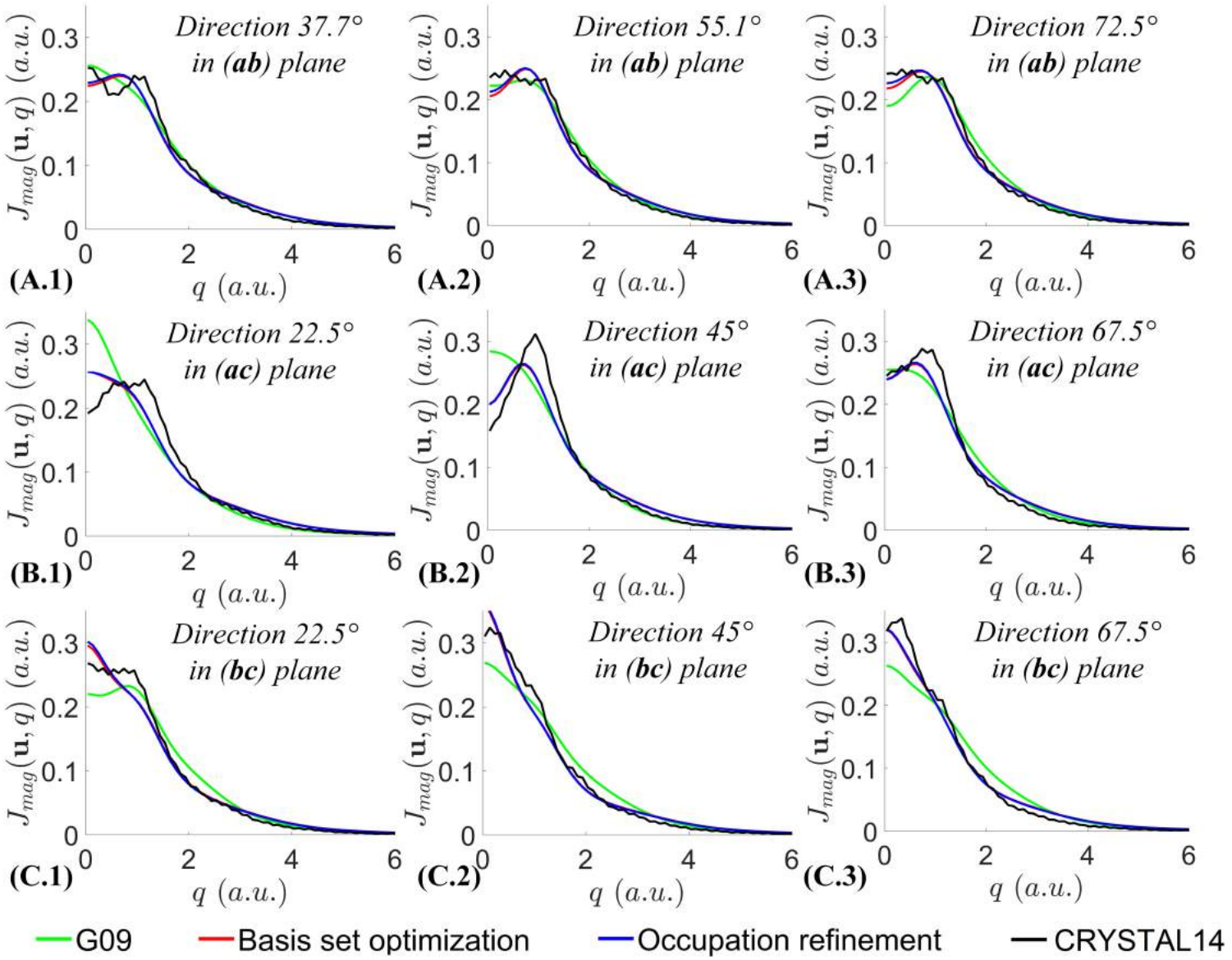

Figure C.7: $YTiO_3$ DMCPs along the directions in the three main crystallographic planes by 1-RDM refinement model with DMCPs and magnetic structure factors

Each row corresponds to a plane: (A) (ab) plane; (B) (ac) plane; (C) (bc) plane.

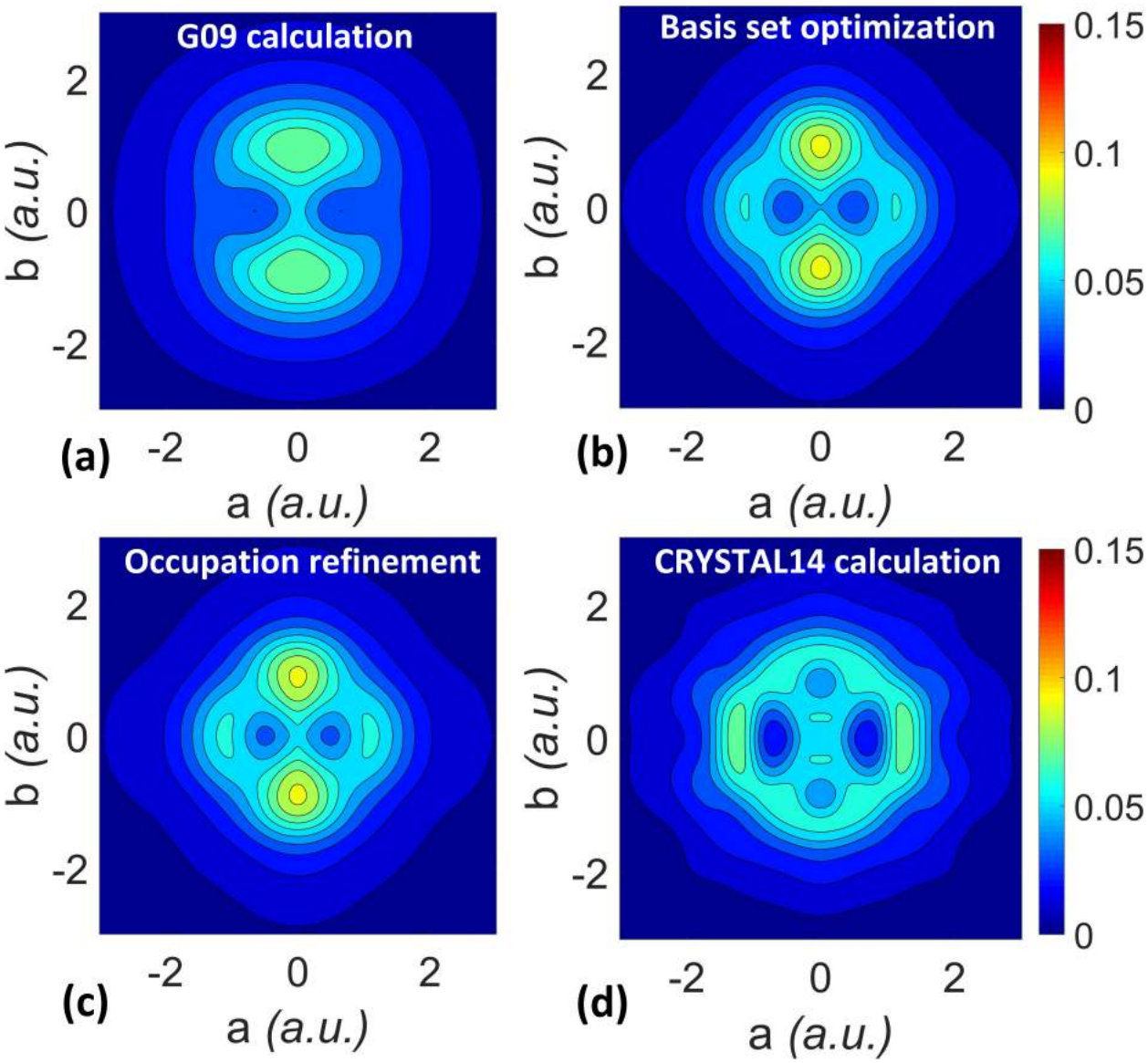

Figure C.8: $YTiO_3$ 2D-MEMD projected into (ab) plane by 1-RDM refinement model with DMCPs and magnetic structure factors
Reconstructed spin density in momentum space (in a.u.) from DMCP shown in Figure 3.13 and C.7. (a) G09 calculation initial guess; (b) then after basis set optimization; (c) then after occupation refinement; (d) CRYSTAL14 result. Contour at intervals of 0.01 a.u. Color bar scaling from 0 to 0.15 a.u.

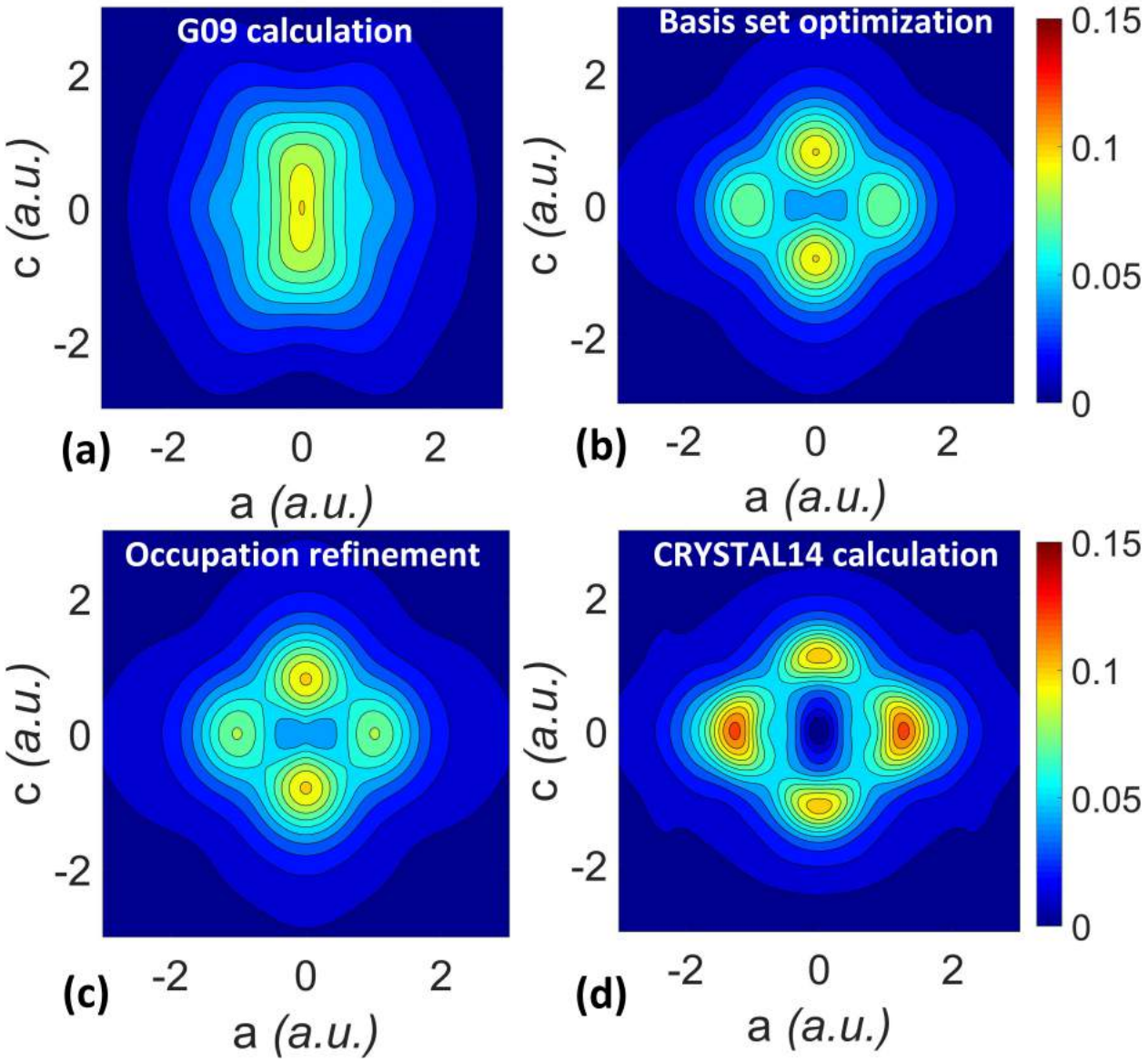

Figure C.9: $YTiO_3$ 2D-MEMD projected into (ac) plane by 1-RDM refinement model with DMCPs and magnetic structure factors
Reconstructed spin density in momentum space (in a.u.) from DMCP shown in Figure 3.13 and C.7. (a) G09 calculation initial guess; (b) then after basis set optimization; (c) then after occupation refinement; (d) CRYSTAL14 result. Contour at intervals of 0.01 a.u. Color bar scaling from 0 to 0.15 a.u.

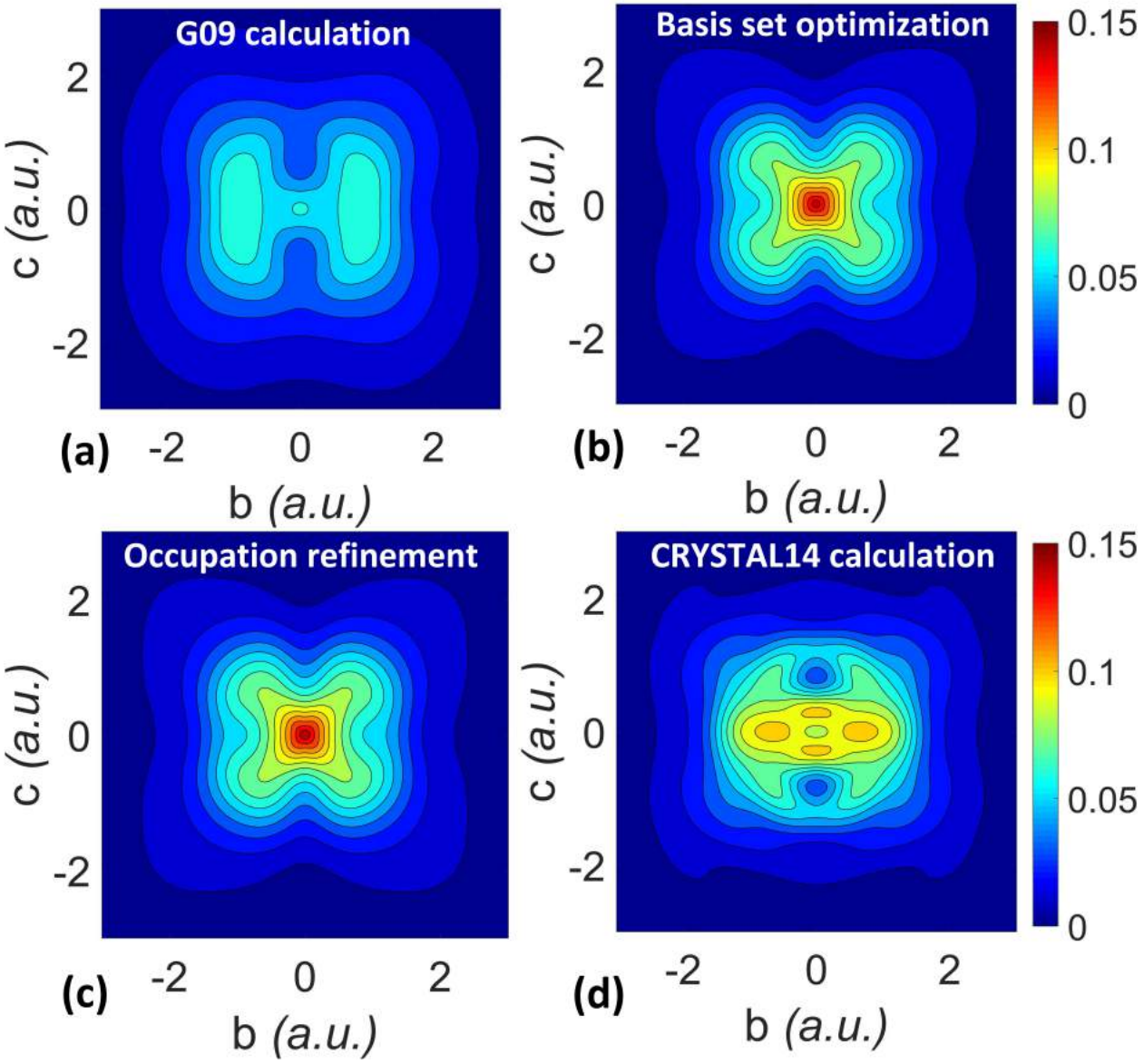

Figure C.10: $YTiO_3$ 2D-MEMD projected into (bc) plane by 1-RDM refinement model with DMCPs and magnetic structure factors
Reconstructed spin density in momentum space (in a.u.) from DMCP shown in Figure 3.13 and C.7. (a) G09 calculation initial guess; (b) then after basis set optimization; (c) then after occupation refinement; (d) CRYSTAL14 result. Contour at intervals of 0.01 a.u. Color bar scaling from 0 to 0.15 a.u.

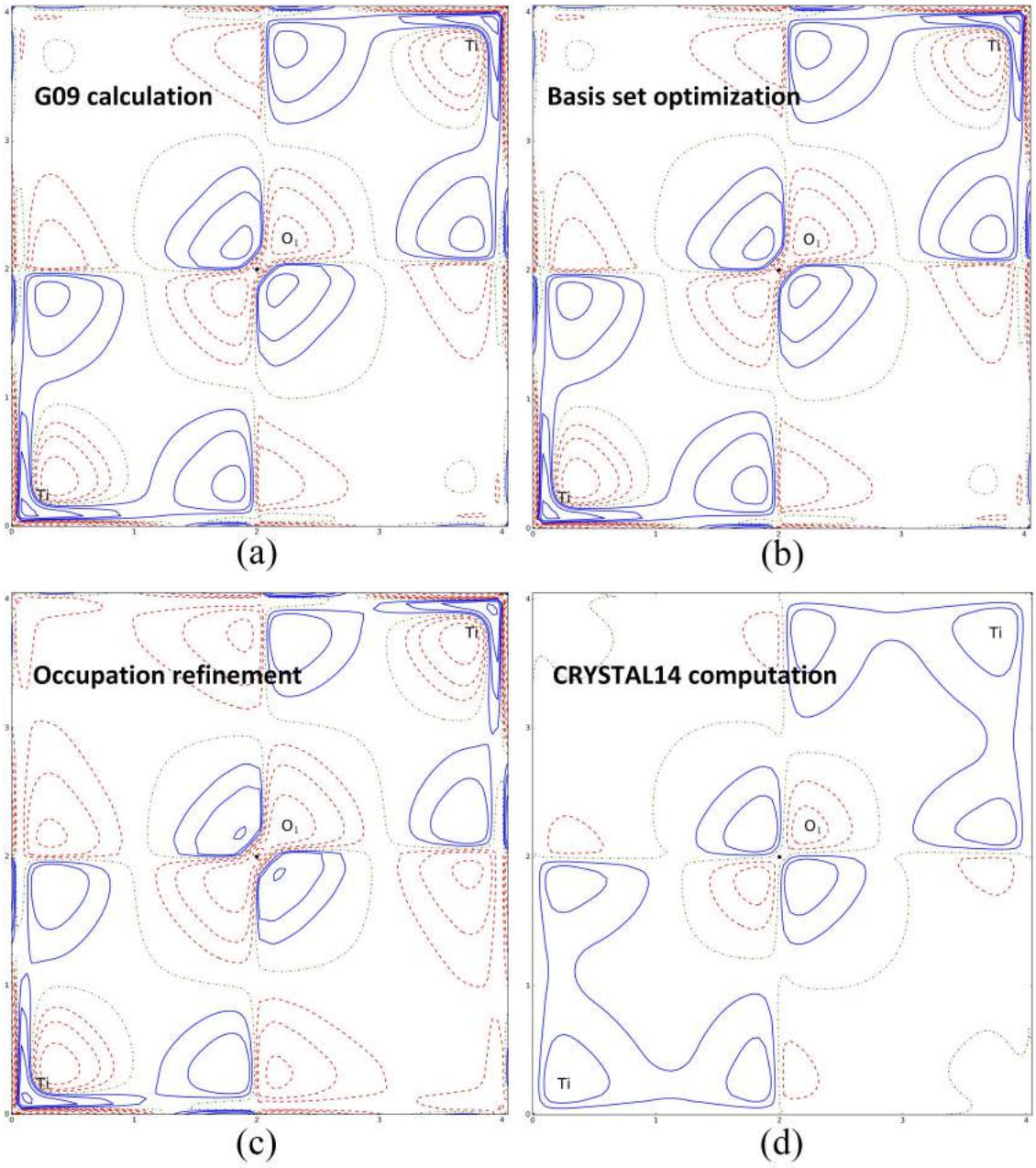

Figure C.11: $YTiO_3$ 1-RDM along Ti–O_1–Ti by 1-RDM refinement model with magnetic structure factors only

(a) G09 calculation initial guess; (b) then after basis set optimization; (c) then after occupation refinement; (d) Cluster construction (*chapter 2*). Contours at $\pm 0.1 \times 2^n$ $(n = 0, ..., 20)$ $e{\cdot}\text{Å}^{-3}$ for total 1-RDM and $\pm 0.01 \times 2^n$ $(n = 0, ..., 20)$ $e{\cdot}\text{Å}^{-3}$ for spin 1-RDM, positive: blue lines, negative: red dashed lines and neutral: green dashed.

Appendix D

Abstract in French

Titre : Reconstruction de densité d'impulsion et détermination de la matrice densité réduite à un électron

Mots clefs : densité d'électron, densité d'impulsion, diffraction des rayons X, diffraction des neutrons polarisés, matrice densité réduite à un électron

Résumé : La diffraction des rayons X à haute résolution (XRD) et celle des neutrons polarisés (PND) sont couramment utilisées pour modéliser les densités de charge $\rho(\mathbf{r})$ et de spin $\rho_{mag}(\mathbf{r})$ dans l'espace des positions [1, 2]. Par ailleurs, la diffusion Compton et diffusion Compton magnétique sont utilisées pour observer les plus diffus des électrons appariés et non appariés, en fournissant les profils Compton directionnels de charge (DCPs) $J(\mathbf{u}, q)$ et les profils Compton magnétiques directionnels (DMCPs) $J_{mag}(\mathbf{u}, q)$. Il est possible d'utiliser plusieurs DCPs et DMCPs non équivalents pour reconstituer la densité d'impulsion $n(\mathbf{p})$ et $n_{mag}(\mathbf{p})$ à deux ou trois dimensions. Puisque toutes ces techniques décrivent les mêmes électrons dans différentes représentations, nous nous concentrons sur l'association de $n(\mathbf{p})$ (resp. $n_{mag}(\mathbf{p})$), reconstituée par DCPs (DMCPs) avec $\rho(\mathbf{r})$ (resp. $\rho_{mag}(\mathbf{r})$), telle que déterminée à partir des données XRD (PND).

La confrontation théorie-experience, ou –plus rarement– entre différentes techniques expérimentales, requiert généralement les representations des densités reconstruites dans les espaces des positions et des impulsions. Le défi que pose la comparaison des résultats obtenus par calculs *ab-initio* et par des approches expérimentales (dans le cas de Nit(SMe)Ph) montre la nécessité de combiner plusieurs expériences et celle d'améliorer les modèles sur lesquels reposent les approches théoriques. Nous montrons que, dans le cas d'une densité de probabilité de présence d'électrons résolue en spin, une approche simple de type Hartree-Fock ou DFT [54] ne suffit pas. Dans le cas de $YTiO_3$, une analyse conjointe des espaces position et impulsion (PND & MCS) met en évidence un possible couplage ferromagnétique selon Ti–O_1-Ti [126]. Pour cela, une densité magnétique de " super-position" est proposée et s'avère permettre une vérification aisée de la cohérence

entre $\rho_{mag}(\mathbf{r})$ et $n_{mag}(\mathbf{p})$ déterminées expérimentalement, sans la nécessité d'une étape *ab-initio*. Pour aller plus loin, un modèle "d'atome de Ti isolé", basé sur des coefficients orbitaux affinés par PND, souligne l'importance du couplage cohérent métal-oxygène nécessaire pour rendre compte des observations dans l'espace des impulsions.

La matrice densité réduite à un électron (1-RDM) [20] est proposée comme socle de base permettant de systématiquement combiner les espaces des positions et des impulsions. Pour reconstruire cette 1-RDM à partir d'un calcul *ab-initio* périodique, une approche "cluster" est proposée. Il devient alors possible d'obtenir la 1-RDM théorique résolue en spin sur des chemins de liaison chimique particuliers. Ceci nous permet notamment de clarifier la différence entre les couplages Ti–O_1–Ti et Ti–O_2–Ti. Il est montré que l'importance des contributions du terme d'interaction entre les atomes (de métal et d'oxygène) est différente selon que l'on considère une représentation des propriétés dans l'espace des positions ou des impulsions. Ceci est clairement observé dans les liaisons chimiques métal-oxygène et peut être illustré par une analyse séparant les contributions par orbitales. Les grandeurs décrivant les électrons dans l'espace des phases comme la fonction de Moyal peuvent également être déterminées par cette construction en "cluster". Ceci peut revêtir un intérêt particulier si la technique de diffusion Compton aux positions de Bragg [123–125] pouvait être généralisée. Les premiers résultats d'un affinement de modèle simple de 1-RDM résolu en spin sont exposés. Le modèle respecte la N-représentabilité et est adapté pour plusieurs types de données expérimentales (telles que XRD, PND, CS, MCS ou XMD). Le potentiel de ce modèle n'est pas limité à une analyse en spin mais son usage est ici circonscrit à la description des électrons non appariés, ses limites sont identifiées et des voies d'amélioration future sont proposées.

Appendix E

Abstract in English

Title : Reconstruction of momentum densities and determination of one-electron reduced density matrix

Keywords : spin density, momentum density, X-ray diffraction, polarized neutron diffraction, one electron reduced density matrix

Abstract : High resolution X-ray diffraction (XRD) and polarized neutron diffraction (PND) are commonly used to model charge $\rho(\mathbf{r})$ and spin densities $\rho_{mag}(\mathbf{r})$ in position space [1, 2]. Additionally, Compton scattering (CS) and magnetic Compton scattering (MCS) are the main techniques to observe the most diffuse electrons and unpaired electrons by providing the "Directional Compton Profiles" (DCPs) $J(\mathbf{u}, q)$ and "Directional magnetic Compton Profiles" (DMCPs) $J_{mag}(\mathbf{u}, q)$, respectively. A set of such DCPs (DMCPs) can be used to reconstruct two-dimensional or three-dimensional electron momentum density $n(\mathbf{p})$ (resp. $n_{mag}(\mathbf{p})$). Since all these techniques describe the same electrons in different space representations, we concentrate on associating the $n(\mathbf{p})$ (resp. $n_{mag}(\mathbf{p})$) reconstructed from DCPs (resp. DMCPs) with $\rho(\mathbf{r})$ (resp. $\rho_{mag}(\mathbf{r})$) refined using XRD (resp. PND) data.

The confrontation between theory and experiment, or between different experiments, providing several sets of experimental data are available, is generally obtained from the reconstructed electron densities and compared with theoretical results in position and momentum spaces. The challenge of comparing the results obtained by *ab-initio* computations and experimental approaches (in the Nit(SMe)Ph case) shows the necessity of a multiple experiments joint refinement and also the improvement of theoretical computation models. It proves that, in the case of a spin resolved electron density, a mere Hartree-Fock or DFT approach[54] is not sufficient. In the $YTiO_3$ case, a joint analysis of position and momentum spaces (PND & MCS) highlights the possible ferromagnetic pathway along Ti–O_1–Ti [126]. Therefore, a "super-position" spin density is proposed and proves to allow cross-checking the coherence between experimental electron densities $\rho_{mag}(\mathbf{r})$ and $n_{mag}(\mathbf{p})$, without having recourse to *ab initio* results. Furthermore, an

"isolated Ti model" based on PND refined orbital coefficients emphasizes the importance of metal-oxygen coherent coupling to properly account for observations in momentum space.

A one-electron reduced density matrix (1-RDM)[20] approach is proposed as a fundamental basis for systematically combining position and momentum spaces. To reconstruct 1-RDM from a periodic *ab initio* computation, an "iterative cluster" approach is proposed. On this basis, it becomes possible to obtain a theoretical spin resolved 1-RDM along specific chemical bond paths. It allows a clarification of the difference between Ti–O_1–Ti and Ti–O_2–Ti spin couplings in $YTiO_3$. It shows that interaction contributions between atoms (metal and oxygen atoms) are different depending on whether the property is represented in position or momentum spaces. This is clearly observed in metal-oxygen chemical bonds and can be illustrated by an orbital resolved contribution analysis. Quantities for electron descriptions in phase space, such as the Moyal function, can also be determinered by this "cluster model", which might be of particular interest if Compton scattering in Bragg positions [123–125] could be generalized. The preliminary results of a simple spin resolved 1-RDM refinement model are exposed. The model respects the N-representability and is adapted for various experimental data (e.g.: XRD, PND, CS, MCS, XMD etc.). The potential of this model is not limited to a spin analysis but its use is limited here to the unpaired electrons description. The limitations of this model are analysed and possible improvements in the future are also proposed.

université PARIS-SACLAY
ÉCOLE DOCTORALE
INTERFACES
Approches Interdisciplinaires : Fondements, Applications et Innovation

Titre : Reconstruction de densité d'impulsion et détermination de la matrice densité réduite à un électron

Mots clés : densité d'électron, densité d'impulsion, diffraction des rayons X, diffraction des neutrons polarisés, matrice densité réduite à un électron

Résumé : La diffraction des rayons X à haute résolution (XRD) et celle des neutrons polarisés (PND) sont couramment utilisées pour modéliser les densités de charge $\rho(\boldsymbol{r})$ et de spin $\rho_{mag}(\boldsymbol{r})$ dans l'espace des positions [1, 2]. Par ailleurs, la diffusion Compton et diffusion Compton magnétique sont utilisées pour observer les plus diffus des électrons appariés et non appariés, en fournissant les profils Compton directionnels de charge (DCPs) $J(\boldsymbol{u}, q)$ et les profils Compton magnétiques directionnels (DMCPs) $J_{mag}(\boldsymbol{u}, q)$. Il est possible d'utiliser plusieurs DCPs et DMCPs non équivalents pour reconstituer la densité d'impulsion $n(\boldsymbol{p})$ et $n_{mag}(\boldsymbol{p})$ à deux ou trois dimensions. Puisque toutes ces techniques décrivent les mêmes électrons dans différentes représentations, nous nous concentrons sur l'association de $n(\boldsymbol{p})$ (resp. $n_{mag}(\boldsymbol{p})$), reconstituée par DCPs (DMCPs) avec $\rho(\boldsymbol{r})$ (resp. $\rho_{mag}(\boldsymbol{r})$), telle que déterminée à partir des données XRD (PND).
La confrontation théorie-expérience, ou --plus rarement-- entre différentes techniques expérimentales, requiert généralement les représentations des densités reconstruites dans les espaces des positions et des impulsions. Le défi que pose la comparaison des résultats obtenus par calculs *ab-initio* et par des approches expérimentales (dans le cas de Nit(SMe)Ph) montre la nécessité de combiner plusieurs expériences et celle d'améliorer les modèles sur lesquels reposent les approches théoriques. […]

Title : Reconstruction of momentum densities and determination of one-electron reduced density matrix

Keywords : spin density, momentum density, X-ray diffraction, polarized neutron diffraction, one electron reduced density matrix

Abstract : High resolution X-ray diffraction (XRD) and polarized neutron diffraction (PND) are commonly used to model charge $\rho(\boldsymbol{r})$ and spin densities $\rho_{mag}(\boldsymbol{r})$ in position space [1, 2]. Additionally, Compton scattering (CS) and magnetic Compton scattering (MCS) are the main techniques to observe the most diffuse electrons and unpaired electrons by providing the ``Directional Compton Profiles" (DCPs) $J(\boldsymbol{u}, q)$ and ``Directional magnetic Compton Profiles" (DMCPs) $J_{mag}(\boldsymbol{u}, q)$, respectively. A set of such DCPs (DMCPs) can be used to reconstruct two-dimensional or three-dimensional electron momentum density $n(\boldsymbol{p})$ (resp. $n_{mag}(\boldsymbol{p})$). Since all these techniques describe the same electrons in different space representations, we concentrate on associating the $n(\boldsymbol{p})$ (resp. $n_{mag}(\boldsymbol{p})$) reconstructed from DCPs (resp. DMCPs) with $\rho(\boldsymbol{r})$ (resp. $\rho_{mag}(\boldsymbol{r})$) refined using XRD (resp. PND) data. The confrontation between theory and experiment, or between different experiments, providing several sets of experimental data are available, is generally obtained from the reconstructed electron densities and compared with theoretical results in position and momentum spaces. The challenge of comparing the results obtained by *ab-initio* computations and experimental approaches (in the Nit(SMe)Ph case) shows the necessity of a multiple experiments joint refinement and also the improvement of theoretical computation models. […]

Université Paris-Saclay
Espace Technologique / Immeuble Discovery
Route de l'Orme aux Merisiers RD 128 / 91190 Saint-Aubin, France